ECOLE
POLYTECHNIQUE
DE BRUXELLES

Development of High Resolution Interferometric Inertial Sensors

Thesis presented by Binlei DING

with a view to obtaining a PhD Degree in Engineering Sciences and Technology (Docteur en Sciences de l'Ingénieur et Technologie)

Academic year 2020-2021

Supervisor: Professor Christophe COLLETTE

Thesis jury:

Prof. Christophe COLLETTE (Université libre de Bruxelles, Supervisor)
Prof. Pierre LAMBERT (Université libre de Bruxelles, Chair)
Prof. Arnaud DERAEMAEKER (Université libre de Bruxelles, Secretary)
Prof. Alessandro BERTOLINI (National Institute for Subatomic Physics)
Dr. Michel VAN CAMP (Royal Observatory of Belgium)

beams
Precision Mechatronics Laboratory

Acknowledgments

‘Time flies.’ is an expression that my promoter, prof. Christophe Collette, often refers to. As I complete my PhD thesis, the initial experience of joining the project seems to have taken place only yesterday. Indeed, time flies. In the near future, I will probably print this phrase, frame it and put it on my desk. As I reflect on the four years of my PhD study, I would like to sincerely thank all those who have helped me in any aspect.

Firstly, I want to thank my promoter, prof. Christophe Collette. I am very grateful to him for leading me into this field, so that I have had the honour to participate in this Nobel Prize winning related work. The project is interesting and involves optics, electronics, machinery, vacuum technology, etc., thus, it has been a considerable challenge for me. I have benefited from Christophe’s profound knowledge and innovative thinking. I am also very grateful for his careful guidance on how to think through and improve the experiments during the last four years, he has been an excellent mentor. Every experience that I learned from him has left a deep, lasting and beneficial impression on me.

Secondly, I would like to thank the members of the jury, prof. Arnaud Deraemaeker, prof. Alessandro Bertolini, dr. Michel Van Camp and prof. Pierre Lambert. They have provided me with valuable suggestions and comments on the revision of this thesis. I would also like to thank them for their guidance in the four years, whenever I encounter difficulties, they always took time out of their busy work schedule to listen and help me solve problems. Furthermore, they generously shared experimental instruments with me to improve my experimental results. Grateful thanks go to, Michel and his fellows from the Royal Observatory of Belgium and dr. Thomas Forbriger and ir. Edgar Wetzig from the Federal Institute for Geosciences and Natural Resources of Germany. They kindly lend us STS-1 seismometers which played a vital role in this project. I would especially thank the members of the LIGO Seismic Working Group for their comments and inspiring discussions, this thesis can be found as LIGO-P2000486.

Thirdly, I would like to thank my team members, they are dr. Guoying Zhao, dr. Cédric Dumoulin, Jennifer Watchi and Ameer Sider. Especially thanks to Guoying for his valuable discussions and help for improving the experiments. Thanks to all my fellow PhD students, colleagues and friends for a pleasant working environment. I hope that they all success in career and obtain fruitful results in research. Among them, I am especially grateful to dr. Jean-Charles Larrieu, dr. Loïc Blanc and Vicente Lafarga for their helps in lab and in Brussels. Meanwhile, I would like to thank the secretaries and technicians of the department for their help with my stay here. I appreciate ir. Axel Dero and ir. Michel Osée and Jean Salvatore Mele for producing components for experiments. I would like to thank everyone who helped me during the four years.

Finally, I want to thank my friends and families. Thanks to my friends for their encouragement and help. Thanks to my beloved father Yuejun Ding and mother Qingrong Wu, for their care and encouragement for me studying in Belgium. Thanks to my beloved wife, Qian Ye, for her accompanying, understanding and supporting during difficult times. Thank you!

Binlei Ding
January 13, 2021
in Brussels

Abstract

The gravitational wave observatory and many other large ground-based instruments need to be decoupled from the Earth's ever-present motion to improve their performance. In such scenarios, inertial sensors which measure the ground motion are necessary, especially those with a high resolution and a large dynamic range. This thesis aims to develop high performance inertial sensors which outperform the commercially available ones in terms of resolution and dynamic range in low frequency down to 0.01 Hz.

Inertial sensors essentially consist of two parts: a single-degree-of-freedom mechanism and a transducer which converts mechanical quantities into electrical quantities. In this work, a novel interferometric readout based on homodyne quadrature interferometer is proposed and examined. Experimental results show that its resolution is 1×10^{-11}, 1×10^{-12} and 2×10^{-13} $\mathrm{m}/\sqrt{\mathrm{Hz}}$ at 0.01, 0.1 and 1 Hz respectively. For the mechanical parts, the leaf spring pendulum and Lehman pendulum are used respectively as the restoring springs for the vertical and horizontal inertial sensors. With these, the resonance frequencies are made to 0.26 and 0.11 Hz, respectively. Combined with the interferometric readout, a Vertical Interferometric Inertial Sensor (VINS) and a Horizontal Interferometric Inertial Sensor (HINS) are developed. They are placed together in a vacuum chamber as an inertial unit to measure vertical and horizontal motion.

A critical investigation of the developed HINS and VINS is performed. The passive VINS and HINS are compared, firstly, with a commercial seismometer (Güralp 6T) the results showed that they provide equivalent seismograms in frequencies from tides to 10 Hz. Secondly, both simulations and measurements have been conducted in this study, a noise budget of the interferometric readout itself was constructed, which corresponds to the case when the proof-mass of the inertial sensors is blocked. At present, the resolution of the interferometric readout is found to be limited by the photodetector noise from 0.01 to 1 Hz. Moreover, huddle tests were conducted for the inertial units to examine their overall performance. However, extra experiments and simulations are performed and it is found that the resolution identified from the experimental means is worse than that from the simulation. Nevertheless, the mismatch can be reduced by reducing the magnitude of input ground vibration, by reducing undesired inputs and improving the stability of the interferometric readout output signal.

Keywords— Inertial unit, High resolution, Interferometric readout, Noise budgeting, Huddle test.

Contents

List of Figures

List of Tables

List of Abbreviations

Q factor	Quality Factor.
AC	Alternative Current.
aLIGO	Advanced LIGO.
ASD	Amplitude Spectral Density.
BS	Non-polarising Beam Splitter.
CAD	Computer Aided Design.
CC	Corner Cube.
CERN	European Organization for Nuclear Research.
CLIC	Compact Linear Collider.
COM	Centre of Mass.
DOF	Degree of Freedom.
ECS	Eddy Current Sensor.
EMF	Electromotive Force.
ET	Einstein Telescope.
FAST	Five-hundred-meter Aperture Spherical Telescope.
FBA	Force Balanced Accelerometer.
FD	Frequency Discriminator.
GAS	Geometric Anti-Springs.
GPS	Global Positioning System.
GSN	Global Seismographic Network.
HINS	Horizontal Interferometric Inertial Sensor.

LAT	Liquid Absolute Tilt-meter.
LBT	Large Binocular Telescope.
LEDs	Light-Emitting Diodes.
LIGO	Laser Interferometer Gravitational-Wave Observatory.
LNM	Low Noise Model.
LTIS	Linear Time-Invariant System.
LVDT	Linear Variable Differential Transducer.
MATLAB	Matrix Laboratory.
MEMS	Microelectromechanical systems.
NASA	National Aeronautics and Space Administration.
ODE	Ordinary Differential Equation.
OPD	Optical Path Difference.
PBS	Polarising Beam Splitter.
PD	Photodetector.
PSD	Power Spectral Density.
RIN	Relative Intensity Noise.
SNR	Signal to Noise Ratio.
STS1-H	STS1 Horizontal Seismometer.
STS1-V	STS1 Vertical Seismometer.
TF	Transfer Function.
VCA	Voice Coil Actuator.
VINS	Vertical Interferometric Inertial Sensor.
WPH	Half-Wave Plate.
WPO	Octadic-Wave Plate.
WPQ	Quarter-Wave Plate.

List of Symbols

c_c	The critical damping coefficient of a mass-spring-damper system.
c	Damping coefficient.
ε_0	Electric Permittivity of Vacuum.
ε_r	Relative Dielectric Constant.
F	The disturbing force applied on mass.
F_s	Force produced by spring.
F_d	Force produced by damper.
f_A	Force delivered by actuator.
f_0	Natural frequency.
g_a	Gain for acceleration feedback control.
g_v	Gain for velocity feedback control.
g_d	Gain for displacement feedback control.
M	Mass of the isolated platform.
k	Spring stiffness.
m	Proof mass of the inertial sensor.
n_s	Sensor noise.
n_{tm}	Thermomechanical noise.
n_a	Ambient noise.
n_i	Laser intensity noise.
n_f	Laser frequency noise.
n_p	Phase noise with respect to laser frequency noise.
n_s	Shot noise.
n_d	Dark current noise.

$n_{1/f}$	Flicker noise.
n_{te}	Thermo-electronical noise.
n_{q}	Quantisation noise.
T_{WX}	Transmissibility of a mass-spring-damper system.
T_{FX}	Compliance of a mass-spring-damper system.
V_{in}	Voltage Input.
$w(t)$	Displacement of ground motion in time domain.
$W(s)$	Displacement of ground motion in Laplace domain.
ω_{n}	Natural frequency in angular frequency.
$x(t)$	Displacement of the isolated platform in time domain.
ζ	Damping ratio of a mass-spring-damper system.

Chapter 1

Background

This thesis focuses on development of inertial sensors to fulfil the requirements of seismic isolation for large ground-based instruments. This chapter focuses on the background and motivation of this project. Section 1.1 introduces to large ground-based observatories, which require vibration isolation. Section 1.2 briefly discusses the working principles of vibration isolation system and the role of inertial sensors. Section 1.3 lists the contributions of the thesis to the states of art. Finally, Section 1.4 presents the contents of the following chapters in the thesis.

1.1 Large ground-based observatories

In 1970, Dr Ernst Stuhlinger was asked by Sister Mary Jucunda could he defend spending billions of dollars on exploration projects to Mars when millions of children were dying of hunger. His letter was later published by the National Aeronautics and Space Administration (NASA) and was named as *Why Explore Space?* [1] In it, Dr Ernst Stuhlinger briefly pointed out the importance of space projects in his thoughtful reply.

Firstly, space exploration requires the support of various disciplines, that in turn, promotes their development. In the 17$^{\text{th}}$ century, Newton inspired by Kepler's astronomical observations developed Newton's laws of motion. Nowadays, rockets are launched into space using these laws. Secondly, space exploration creates new markets and technologies to improve our daily life. Using a smartphone as an example, the Light-Emitting Diodes (LEDs) display the interfaces and indicate the working condition, the Microelectromechanical systems (MEMS) inertial sensors [2] measure the motion, and the Global Positioning System (GPS) unit shows the location. All these applications and technologies developed for space exploration are ultimately for civilian use. Thirdly, space exploration is also an important philosophical study which explores the origins and future of the universe, time and humanity. The photograph, *Earthrise*, enclosed with Dr Ernst Stuhlinger's letter continues to amaze people even today by the beauty and loneness of Earth (see Figure 1.1) and cause people to think about human–nature relationship [3].

Figure 1.1: Earthrise, taken on December 24, 1968 [4].

Observational astronomy is one of the methods used to explore space. Nowadays, the types of astronomical telescopes are differentiated according to the different electromagnetic spectrum. They follow the principle that the larger the size of the telescope aperture, the better the performance. With the development of engineering technology, the effective diameter of large optical telescopes can reach more than 10 meters, for instance, the Large Binocular Telescope (the LBT, see Figure 1.2a) [5]. The diameter of large radio telescopes can reach 500 meters, for example, the Five-hundred-meter Aperture Spherical Telescope (the FAST, see Figure 1.2c) [6]. However, Stars, black holes and even the atmosphere seriously affect the observation of electromagnetic waves.

An alternative method is to observe gravitational wave. Gravitational waves are 'ripples' in space-time which are generated by the motion of massive accelerating objects. These cosmic ripples propagate as waves outward from their source at the speed of light, and their propagation distorts space-time. Gravitational waves were first predicted by Einstein in 1916 [11]. Up until now, several observatories based on the Michelson interferometer have

(a) the LBT [7]

(b) the LIGO [8]

(c) the FAST [9]

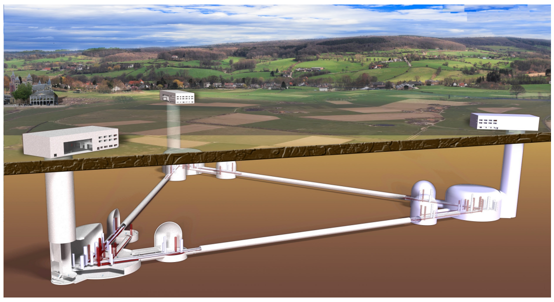

(d) the ET [10]

Figure 1.2: Large observatories: (a) the Large Binocular Telescope located in the Pinaleno Mountains of southeastern Arizona, United States. (b) the LIGO Livingston Observatory in Louisiana, United States. (c) the Five-hundred-meter Aperture Spherical Telescope located in the Dawodang depression in Guizhou, southwest China. (d) the Einstein Telescope, artistic review, in Europe.

been built to measure the strain of the ground stimulated by gravitational waves, for example, the Laser Interferometer Gravitational-Wave Observatory (the LIGO, see Figure 1.2b) [12] and Virgo detector of European Gravitational Observatory [13]. In order to improve their sensitivity, observatories have to be significantly large. The arm length of the interferometers is up to 4 km. As an emerging field of astronomy, Gravitational-wave astronomy has obtained outstanding results of observations and contributed to the cognition of the Universe. The 2017 Nobel Prize in Physics was awarded to the work of the Advanced LIGO (aLIGO) [14] for its detection of the gravitational waves, which were generated during the merge of black holes in the event GW150914 [15]. The third generation gravitational wave detector (the ET, see Figure 1.2d) is under development to achieve sensitivity improvements [16].

Building large ground-based telescopes faces challenges including budget, technology and manufacture [17, 18]. Among the challenges, the seismic activity at their site has a high impact on the cost and safety of the telescope [19]. High magnitude seismic motion are hazardous to ground-based telescopes [20]. Low magnitude seismic motion disturbs the measurement system of large telescopes, especially their optical system, and thus degrades the quality of measurements [21, 22, 23]. Even though the daily seismic activity is hard to feel, it happens all the time and everywhere [24]. Therefore, seismic vibration isolation systems are necessary for large ground-based telescopes [14, 25, 26, 27]. Section 1.2 will introduce principles of the active and passive vibration isolation system.

Matichard *et al.* [28] detailed the active-passive isolation platforms for the core optics and the auxiliary optics used in the aLIGO. Figure 1.3 shows the Computer Aided Design (CAD) model and the scheme of the platform isolating the core optics. The active-passive isolation platform includes three subsystems. The blue parts in the figure present the first subsystem. It is the hydraulic external pre-isolator and mainly focuses on the long-range positioning and alignment. Also, it gives active isolation for seismic vibration. The grey parts show the second subsystem. It is the internal seismic isolation platform with both active and passive isolation. The red parts indicate the third subsystem of quadruple pendulum suspensions [29], which is passive isolation. The third subsystem connects the second subsystem on its top side and the core optics on its bottom side. As a result of the isolation systems, the second subsystem provides the active isolation from 0.1 to 30 Hz in the frequency domain. The third subsystem provides passive isolation above 10 Hz.

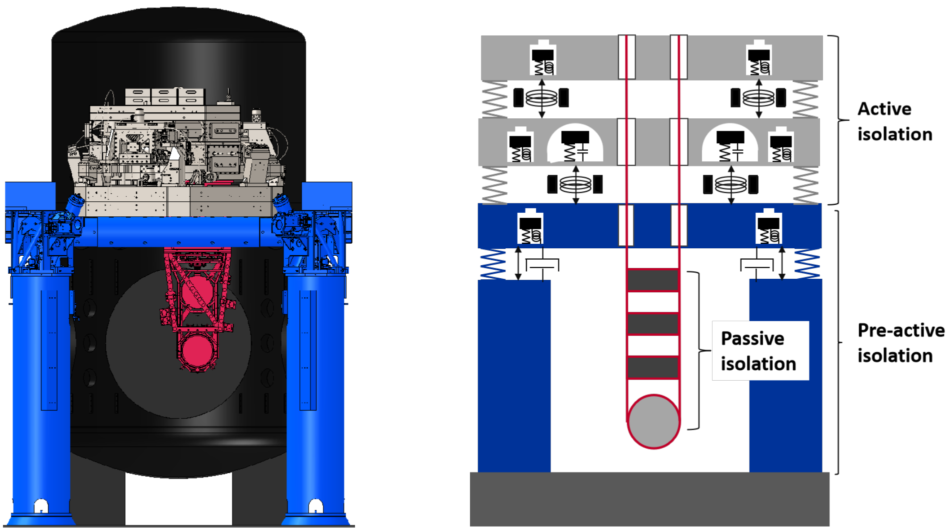

(a) **(b)**

Figure 1.3: The isolation systems supporting the core optics of aLIGO [28]: (a) The CAD model of isolation system, (b) The scheme of isolation system.

1.2 Vibration isolation

A perfect idea to minimise the effect of seismic vibration is to float large observatories in the air. Before advanced technologies are accessible, passive isolation and active isolation are still popular strategies. How the isolation strategies contribute to isolating seismic vibration in the frequency domain (from 0.01 to 10 Hz) is discussed hereafter.

1.2.1 Passive isolation strategy

Figure 1.4 shows a passive isolator expressed by a Mass-Spring-Damper system which is assumed as a single Degree of Freedom (DOF) system. The platform is rigid with a mass M, and it is suspended by a spring with a damper. The platform has displacement $x(t)$ which is excited by ground motion $w(t)$ or external disturbing force F.

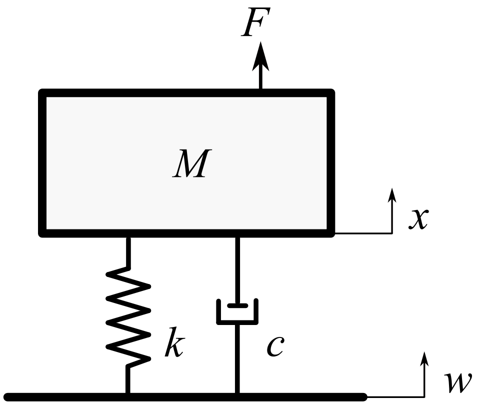

Figure 1.4: Sketch of a passive isolator: M: the mass of the platform, k: the stiffness of the spring, c: the damping coefficient of the damper, w: ground motion, F: disturbing force, x: platform motion.

This system is assumed as a Linear Time-Invariant System (LTIS), so the spring generates a force F_{s} according to Hook's law by

$$F_{\mathrm{s}} = -k(x - w) \tag{1.1}$$

where k is the stiffness of the spring. Meanwhile, the damping force F_{d} is

$$F_{\mathrm{d}} = -c(\dot{x} - \dot{w}) \tag{1.2}$$

where c is the damping coefficient proportional to the relative velocity between the platform and the ground. The symbols $\dot{w}$ and $\dot{x}$ denote the velocity of ground and the platform.

Gravity only changes the equilibrium position of the mass. Therefore, it is assumed that the effect of gravity is compensated. Taking the equilibrium position as the initial position, $x(0) = 0$, the force balance equation of the platform by Newton's law is

$$M\ddot{x} = \sum F = -F_{\mathrm{s}} - F_{\mathrm{d}} + F \tag{1.3}$$

where, F is the disturbing force. Merging equations (1.1), (1.2) and (1.3), a second-order Ordinary Differential Equation (ODE) is obtained by

$$M\ddot{x} + c(\dot{x} - \dot{w}) + k(x - w) = F \tag{1.4}$$

Equation (1.4) is also well known as the dynamic equation of the system. Characteristics of the system can be identified: $\omega_{\mathrm{n}}= \sqrt{k/M}$ is the natural frequency of the system. $c_{\mathrm{c}}= 2\sqrt{kM} = 2\zeta\omega_n$ is the critical damping coefficient and $\zeta= c/c_{\mathrm{c}}$ is the damping ratio of the system.

It is more convenient to express it in the frequency domain by transforming the ODE into an algebraic equation. After applying the Laplace transform and merging items, equation (1.4) becomes

$$\begin{aligned} X(s) &= \frac{cs + k}{Ms^2 + cs + k} W(s) + \frac{1}{Ms^2 + cs + k} F(s) \\ &= T_{\mathrm{WX}}(s)W(s) + T_{\mathrm{FX}}(s)F(s) \end{aligned} \tag{1.5}$$

where the Transfer Function (TF) $T_{\mathrm{WX}}(s)$ is the **transmissibility** of the system and $T_{\mathrm{FX}}(s)$ is the **compliance** of the system. Transmissibility indicates how ground motion (the displacement $W(s)$ in the example) transmits to the platform. Meanwhile, compliance represents how the disturbing force $F(s)$ disturbs the platform.

The isolation performance of a passive isolator depends on the parameters k, c and M. Figures 1.5, 1.6 and 1.7 show the comparison between the passive isolator with different parameters. Table 1.1 lists the value of the parameters modelling the passive isolator. When the platform is rigidly mounted on ground, the ground motion at each frequency fully transmits to the platform $|T_{\mathrm{WX}}| = 1$ (dash-dot black curves in Figures 1.5, 1.6 and 1.7). The transmissibility and compliance of the original passive isolator are shown by solid blue curves in Figures 1.5, 1.6 and 1.7. The isolator is assumed to have the resonance frequency at 1 Hz. The objective of vibration isolation is to decrease both transmissibility and compliance in the interested frequency range.

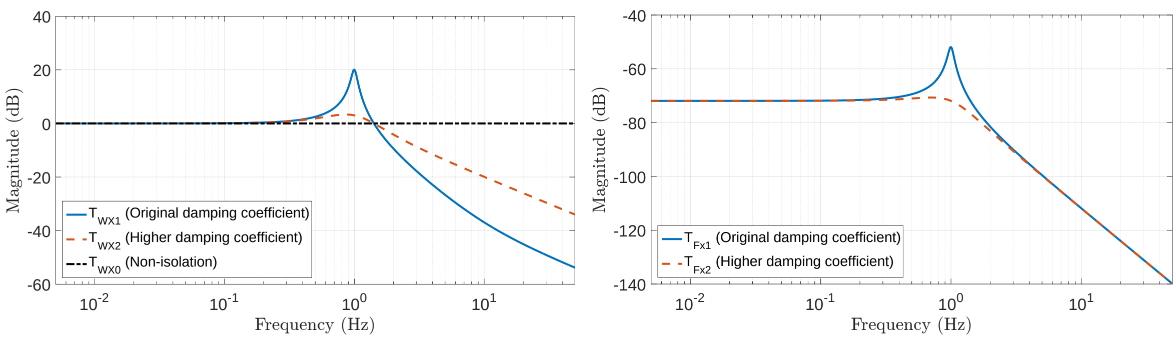

(a) **(b)**

Figure 1.5: Comparison between the transmissibility and compliance of the isolator by increasing the damping coefficient c, while keeping k and M: (a) Transmissibility, (b) Compliance.

Concerning the original isolator in Figure 1.5, above its resonance, the transmissibility $|T_{\mathrm{WX}}| < 1$, with a slope of -2 in logarithmic scale, means that the platform is more insensitive to the ground motion in higher frequencies. At its resonance, an overshooting appears with $|T_{\mathrm{WX}}| > 1$, thus the system amplifies ground motion. Below its resonance, $|T_{\mathrm{WX}}| = 1$ means that the ground motion is fully transmitted. Concerning its compliance, because the disturbing force excites the system, the system is desired to have compliance with the low magnitude or to be isolated from the disturbing force.

Figure 1.5 also shows the comparison between passive isolators with respect to different damping coefficients. The dash red curves show the transmissibility and compliance of the isolator with a higher damping coefficient c^*. The magnitude of the overshooting decreases in both of its transmissibility and compliance. However, the new transmissibility above the resonance frequency increases indicating the isolation performance decreases. One solution is to use a relaxation isolator [30], which keeps the isolation performance while increasing the damping coefficient.

Figure 1.6 shows the comparison between passive isolators with respect to different value of stiffness. The dash red curves show the performance of the isolator with lower stiffness k^*. The isolation performance is extended from the blue curve (original isolator) to the red curve (low stiffness isolator). Because reducing the stiffness of the system decreases the critical damping $c_{\mathrm{c}} = 2\sqrt{kM}$, the damping ratio increases and thus the overshooting decreases a bit. However, its transmissibility is not improved below the resonance frequency and its compliance is degraded in the same frequency bandwidth.

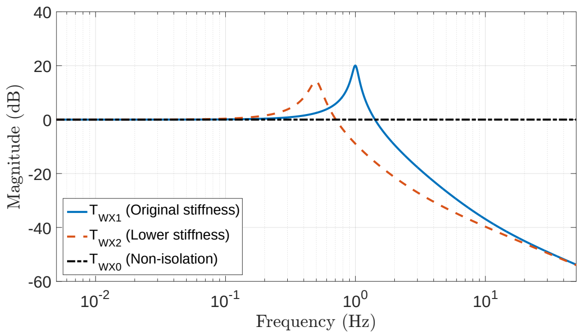

(a)

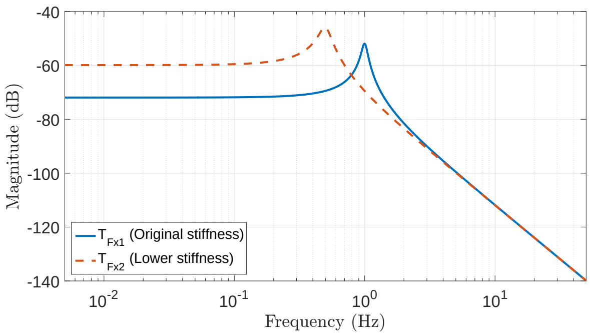

(b)

Figure 1.6: Comparison between the transmissibility and compliance of the isolator by decreasing the stiffness k, while keeping c and M: (a) Transmissibility, (b) Compliance.

Figure 1.7 shows the comparison between passive isolators with respect to different values of mass. The transmissibility and the compliance of the new isolator with extra mass are shown by dash red curves. By comparing with the original isolator, it achieves limited performance improvement. Adding mass changes the damping ratio, so the magnitude of the overshooting increase a bit. Different from the degradation of the compliance with less stiffness (see Figure 1.6b), the compliance of the system with higher mass is not degraded

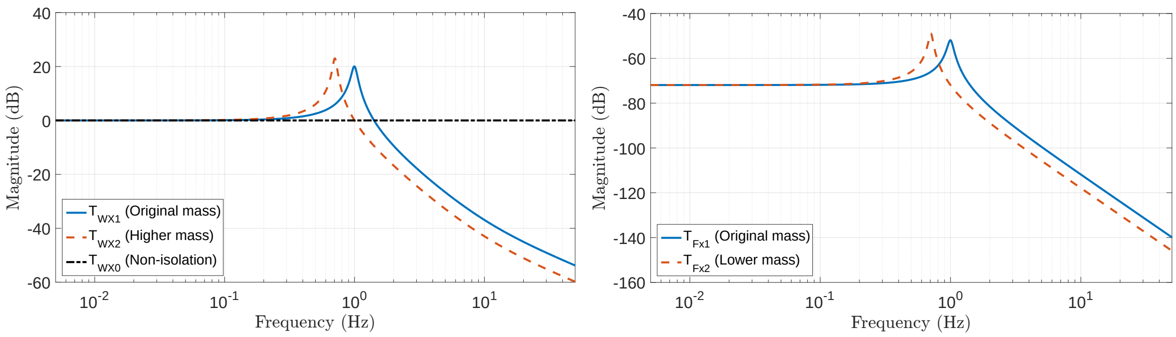

(a) **(b)**

Figure 1.7: Comparison between the transmissibility and compliance of the isolator by increasing the mass M, while keeping c and k: (a) Transmissibility, (b) Compliance.

below the resonance frequency (see Figure 1.7b). However, the improvement by adding mass is hard to be applied on a heavy platform. For example, decreasing the resonance frequency from 1 to 0.01 Hz requires that the new mass M^* is as 1×10^4 times heavier than the original mass.

In conclusion, the passive isolator acts in the frequency band which is above its resonance frequency. Using passive isolator only to perform isolation in the low-frequency domain is challenging.

Table 1.1: Parameters modelling the passive isolator.

Situation	Parameters	Symbol	Value	Unit
Original system	Mass of the isolated platform	M	100	kg
	Damping coefficient	c	62.83	Ns/m
	Spring stiffness	k	3.948×10^3	N/m
	Resonance frequency	f_0	1	Hz
Increase damping (Figure. 1.5)	New damping coefficient	c^*	628.32	Ns/m
	New resonance frequency	$f_0{}^*$	1	Hz
Decrease stiffness (Figure. 1.6)	New spring stiffness	k^*	986.96	N/m
	New resonance frequency	$f_0{}^*$	0.5	Hz
Increase mass (Figure. 1.7)	New mass of the isolated platform	M^*	200	kg
	New resonance frequency	$f_0{}^*$	0.7071	Hz

1.2.2 Active isolation strategy

Based on a passive isolator, the active isolation system achieves the goal of isolation by employing a control system. Depending on different objectives, different types of systems can be used. Amongst them, the inertial feedback control shows advantages in improving both the transmissibility and compliance [31].

Figure 1.8 shows a sketch of an active isolator based on the passive isolator with an inertial feedback control. A sensor S, actuator A and controller $H(s)$ are marked in red.

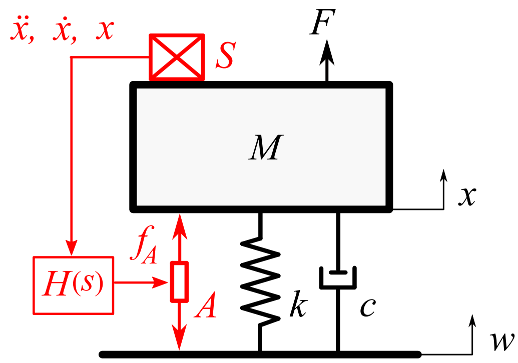

Figure 1.8: Working principle of an active isolator: S: the inertial sensor, A: the actuator, $H(s)$: the controller, f_A: the force generated by the actuator.

Sensors and actuators are assumed to have perfect dynamics in the discussion. The sensor measures either the displacement $x(t)$, velocity $\dot{x}(t)$ or acceleration $\ddot{x}(t)$ of the platform. In order to simplify the discussion, constant gains are applied to the measured signals, and the force f_A delivered by the actuator can be expressed by

$$f_\mathrm{A} = g_\mathrm{a}\ddot{x} + g_\mathrm{v}\dot{x} + g_\mathrm{d}x \tag{1.6}$$

where g_a, g_v and g_d are gains of proportional controllers for acceleration, velocity and displacement feedback. With the actuator force, equation (1.3) becomes

$$M\ddot{x} = \sum F = -F_\mathrm{s} - F_\mathrm{d} - f_\mathrm{A} + F \tag{1.7}$$

Substituting equations (1.1) and (1.2) into equation (1.7), the dynamic equation of the system in the Laplace domain is

$$\begin{aligned} X(s) &= \frac{(cs+k)W(s) + F(s)}{(M+g_a)s^2 + (c+g_v)s + (k+g_d)} \\ &= T_\mathrm{WX}W(s) + T_\mathrm{WF}F(s) \end{aligned} \tag{1.8}$$

Equation (1.8) shows the transmissibility T_WX and compliance T_WF of the active isolator. Table 1.2 lists the value of parameters modelling the active isolator.

Figure 1.9 shows a comparison among different controllers. The transmissibility and compliance of the original passive isolator (solid blue curves) is shown for comparison. The effect of acceleration feedback (dash-dot red curves) is similar to increasing virtual mass on the passive isolator (see Figure 1.7). The effect of velocity feedback (dotted yellow curves) dampens the overshooting while keeping the isolation performance in frequencies above its

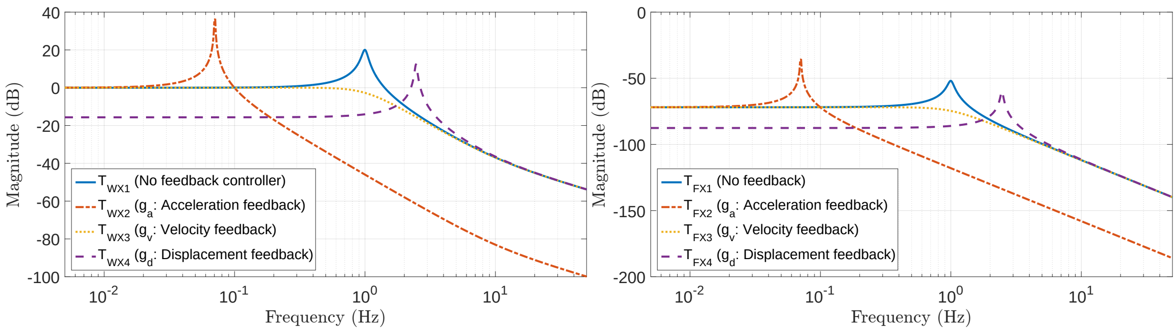

Figure 1.9: Comparison between the transmissibility and compliance of the active isolation system by using different gain: (a) Transmissibility, (b) Compliance.

resonance. It is also called sky-hook damper because the effect of the actuator equals to that of a damper linking the mass to an imaginary point fixed in the sky. The effect of displacement feedback (dash purple curves) implements isolation performance in the low-frequency range and improves the compliance to disturbing force. It is also called a sky-hook spring because the actuator acts as a spring linking the mass to an imaginary point fixed in the sky. Most of the active isolation strategies are based on a combination of a sky-hook spring and a sky-hook damper [32].

In conclusion, both displacement feedback and acceleration feedback can be implemented for the isolation of low-frequency vibrations. However, a larger control bandwidth, especially towards extremely low frequencies, can be achieved with the displacement feedback given the controller is the same for the two control strategies. Therefore, the displacement feedback strategy is recommended for active seismic vibration isolation.

Table 1.2: Parameters in simulation of active isolation.

Continued to table 1.1			
Situation	Parameters	Symbol	Value
Acceleration feedback	Gain for acceleration feedback	g_a	2×10^4
Velocity feedback	Gain for velocity feedback	g_v	8×10^2
Displacement feedback	Gain for displacement feedback	g_d	2×10^4

The performance of the active isolator is limited by the noise of the applied sensor. Assuming that the applied sensor is a displacement sensor with noise n_s, equation (1.6) becomes

$$f_\mathrm{A} = -g_\mathrm{d}(x + n_\mathrm{s}) \tag{1.9}$$

Substituting this new actuator force into equation (1.7), the dynamic equation of the system in the Laplace domain becomes

$$X(s) = \frac{(cs + k)W(s) + F(s) - g_{\mathrm{d}}N_{\mathrm{s}}(s)}{Ms^2 + cs + k + g_{\mathrm{d}}} \tag{1.10}$$

where $N_{\mathrm{s}}(s)$ is the Laplace transform of the sensor noise n_{s}. As previously discussed, isolation performance can be improved by increasing the control gain. Ultimately, with large values of the control gain, equation (1.10) becomes

$$\lim_{g_{\mathrm{d}} \to \infty} X(s) = -N_{\mathrm{s}}(s) \tag{1.11}$$

where the motion of the platform $X(s)$ is dominated by the sensor noise.

In conclusion, the active isolator applied proportional displacement feedback control achieves the goal of isolation in the low-frequency domain. A displacement sensor is preferred but its noise limits the performance of the active isolation.

In order to achieve the observation of gravitational waves, the aLIGO used unprecedented multi-stage platforms to meet the sensitivity required for observation. Through developments, the current multi-stage platform achieves low-frequency vibration isolation by the active isolation, and high-frequency vibration isolation by the passive isolation. Compared with an single stage platform, the multi-stage platform has an improved performance [28]. However, the vibration isolation effectiveness at very low frequency, for example from 0.01 to 10 Hz, still needs to be improved, and it is essentially limited by the resolution of the feedback inertial sensors. Therefore, the development of inertial sensors with high-resolution is conducted in this study.

Inertial sensor for active isolation

The typical sensors applied to the seismic isolation system of aLIGO are seismometers and geophones, their general working principles will be discussed in Chapter 2. By recalling the isolation system used in the aLIGO, seismometers, Streckeisen (STS2) [33] and Trillium (T240) [34], are used in the first and second subsystems (see Figure 1.3), and Geophones, Geotech (GS13) [35] and Sercel (L4C) [36], are used in the second subsystem and all other subsystems. Figure 1.10a compares the four inertial sensors by their appearances. Their heights range from more than 10 centimetres to nearly 40 centimetres, and their weights range from 2 kilograms to nearly 15 kilograms.

According to equation (1.11) the performance of the isolation is limited by the sensor noise, Figure 1.10b shows the comparison among the noises of the sensors. The sensor noise is detailed in the next chapter. Here, the curves represent the Amplitude Spectral Density

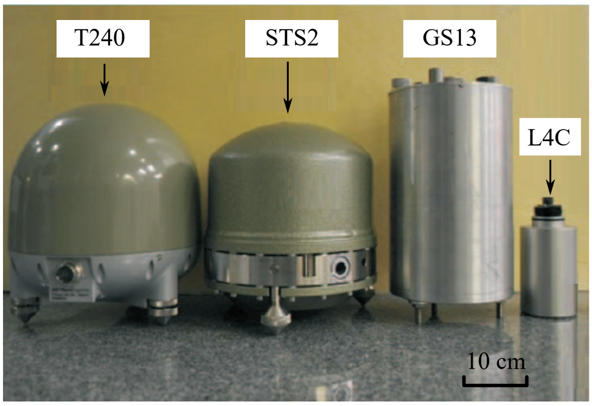

(a)

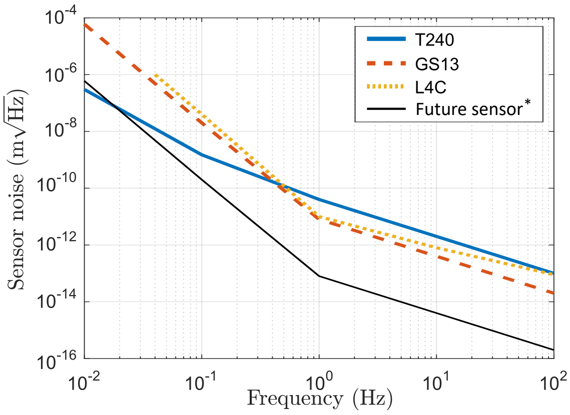

(b)

Figure 1.10: The inertial sensors used in aLIGO and their noise: (a) The seismometers and geophones used in aLIGO [37]. (b) The comparison between the theoretical noise of the inertial sensors [38]. (*) The noise of future sensor is estimated by decreasing the noise of GS13 with a factor of 100 [39].

(ASD) of the sensor noise which is

$$\mathrm{A_{nn}} = \sqrt{\mathrm{P_{nn}}} \tag{1.12}$$

where $\mathrm{A_{nn}}$ denotes the one-sided ASD of the sensor noise in the unit of $\mathrm{m}/\sqrt{\mathrm{Hz}}$, $\mathrm{P_{nn}}$ denotes the one-sided Power Spectral Density (PSD) of the sensor noise in the unit of $\mathrm{m^2/Hz}$. Therefore, a good sensor means that the ASD of its noise is low in the figure. The noise of T240 (solid blue curve), GS13 (dashed red curve) and L4C (dotted yellow curve), which are estimated by Lantz and Kissel [38], are compared in the figure. Among them, the seismometer (T240) has less noise in the low-frequency range and the geophone (GS13) is better in the high-frequency range.

The aLIGO requires an inertial sensor with the noise performance roughly by a factor of 100 better than today's GS13 from 0.01 to 10 Hz to improve the seismic isolation [39]. The solid black curve in Figure 1.10b shows the expected noise performance of the desired sensor. Once this upgrade is completed, the quality of signal obtained by aLIGO is expected to have an improvement in the related frequency range. Moreover, the development of high-performance sensors is not only beneficial to improve the results of astronomical observations but also high-precision physical experiments. High precision seismic isolation is also required by ground-based precision instruments such as the Compact Linear Collider (CLIC) [40] in the European Organization for Nuclear Research (CERN) [41].

1.3 Contributions

The main contributions of the thesis are:

- Development of high resolution interferometric inertial sensors, including both the Vertical Interferometric Inertial Sensor (VINS) and the Horizontal Interferometric Inertial Sensor (HINS). The inertial sensors are placed in a vacuum chamber to measure both vertical and horizontal motion. Several tests including ring-down test, blocked-mass test, huddle test are performed to analyse the performance of the inertial sensors.
- Development of high resolution interferometric readout for the displacement measurement, including:
  - (i) the development of long-range interferometric readout with using three photodetectors for reducing laser intensity noise,
  - (ii) both analytical and experimental investigations to identify the noise sources of the readout which allows to better understand the limitation of the current design.
- Development of the mechanics of the inertial sensor, including:
  - (i) the development of the model of Lehman pendulum with negative stiffness to decrease its resonance frequency,
  - (ii) the development of in-depth models for characterizing the dynamics of the inertial sensors in the presence of gravity.
- Theoretical and experimental characterisation of the resolution of the inertial sensors, consisting of:
  - (i) the development of model and noise budgeting of the inertial sensors,
  - (ii) examination and validation of the resolution with blocked-mass test and huddle test,
  - (iii) the investigations of the simulated huddle test to find more physical insight for the residual in the huddle test.
- Assembly of both inertial sensors in the vacuum environment for measurements.

Combined, these contributions provide a framework for developing high-resolution inertial sensors with interferometric displacement readout.

1.4 Thesis overview

In order to fulfil the requirements of active isolation, vertical interferometric inertial sensors (VINS) and horizontal interferometric inertial sensors (HINS) are under development. Both of have good noise performance (high resolution) in the low-frequency domain (from 0.01 to 10 Hz). They are assembled in a vacuum chamber as an inertial unit to measure the motion on both of vertical and horizontal directions. This thesis presents the interferometric readouts, mechanics, noise performance and validation experiments of these inertial sensors.

Chapter 2 introduces the working principle of inertial sensors. Firstly, the chapter discusses the general working principles of passive and active inertial sensors. Secondly, methods to improve sensor resolution are discussed. One primary method is to improve the sensing part of the inertial sensor, which is mainly discussed in Chapter 3. The other primary method is to improve the mechanics, which is presented in Chapter 4.

Following the discussion in Chapter 2, Chapter 3 focuses on the sensing part of the inertial sensor. Different displacement sensing technologies are compared at the beginning of the chapter. The interferometric readout is selected because it has good noise performance. Next, the optical path of the interferometric readout is demonstrated and is modelled by the Jones matrix. Then, the data processing method is discussed. Finally, the performance of the interferometric readout is validated with an Eddy current sensor. The resolution of the readout reaches 0.2 pm/$\sqrt{\mathrm{Hz}}$ at 1 Hz.

Chapter 4 discusses the mechanics of the inertial sensor. Firstly, some flexure hinges used in inertial sensors for low-frequency measurement are compared. The mechanics of the HINS and VINS are respectively developed from the Lehman pendulum and the leaf spring pendulum. Secondly, the working principles and the dynamics of the mechanics are discussed. Thirdly, the assemblies of HINS and VINS are presented and validated with Güralp 6T seismometers. The resonance frequencies of mechanics are 0.11 and 0.26 Hz, respectively.

Chapter 5 discusses the noise sources of the HINS and VINS. Firstly, a general model of the HINS and VINS combining noises sources are presented. These noise sources come from the optoelectronic system, mechanical system and the environment. Secondly, the models of these noise sources are separately discussed. Meanwhile, the estimations of the noise are discussed. Thirdly, the noise budgeting of the inertial sensor is presented.

Chapter 6 discusses the resolution of the inertial sensors estimated by the huddle test. In the first section, the working principle of the huddle test is demonstrated. The second section of the chapter presents the results of the huddle test. In the third section, non-linearities in the measurement and incoherent excitations are discussed as the two reasons of the high residual in the huddle test.

Chapter 2

Inertial sensor

This chapter introduces the working principle of inertial sensors. In Section 2.1, the working principle of the passive inertial sensor are demonstrated, the primary methods to improve the sensor in terms of resolution are discussed, one is to improve the resolution of the readout and the other is to extend bandwidth of the mechanics. Section 2.2 presents the working principle of the active sensor with possible improvements for extending the bandwidth or increasing the dynamic range. Moreover, a comparison in terms of resolution shows that either using an active or passive inertial sensor is a trade-off between the resolution and the linearity.

2.1 Passive inertial sensor

Inertial sensors can be of different types [31, 42]. Figure 2.1 shows a sketch of the mechanical system of a passive inertial sensor measuring ground motion. This mechanical system is called the **mechanics** in the thesis. The movable mass m is called the **proof-mass**. Friction-less joints support the proof-mass from its frame. The stiffness and the damping coefficient of the system are denoted by k and c, respectively.

The dynamic equation of the mechanical system is

$$m\ddot{x} + c(\dot{x} - \dot{w}) + k(x - w) = 0 \tag{2.1}$$

where gravity is exclusive because x is counted from the static equilibrium of the proof-mass. The method to compensate gravity is discussed in Chapter 4. Equation (2.1) in the Laplace

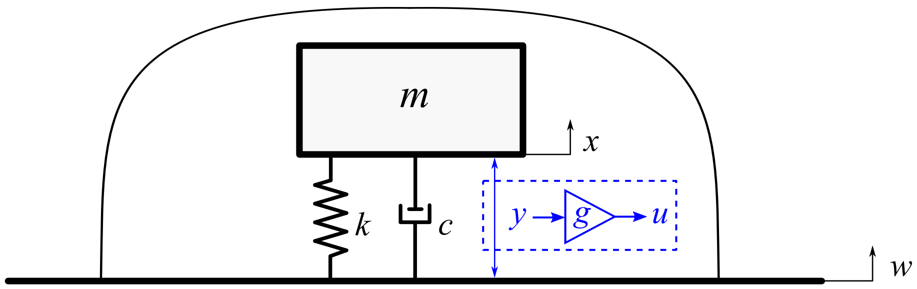

Figure 2.1: Working principle of a passive inertial sensor: m: proof-mass of the inertial sensor, k: the stiffness, c: the damping coefficient, w: ground motion, x: the motion of the proof-mass, y: the relative motion of the proof-mass, g: the sensitivity of the readout u: the voltage output of the readout.

domain is

$$ms^2Y + csY + kY = -ms^2W \tag{2.2}$$

where $y = x - w$ is the relative motion between its frame and the proof-mass. Therefore, the transmissibility of the mechanics is

$$T_{\mathrm{WY}} = \frac{Y}{W} = \frac{-ms^2}{ms^2 + cs + k} \tag{2.3}$$

The blue part in Figure 2.1 represents the sensor measuring this relative motion y. This embedded sensor is defined as the **readout** of the inertial sensor in this thesis. A readout can be one of contactless motion sensors, such as the capacitive displacement sensor. However, only sensors to measure displacement are studied in this thesis. The voltage outputs U of the readout is

$$U = gY \tag{2.4}$$

where g is the sensitivity of the readout and is regarded as a gain in the unit of V/m. Because this readout couples with the mechanics, thus equation (2.4) and (2.3) can be merged. The new transfer function of the inertial sensor T_{WU} is

$$T_{\mathrm{WU}} = \frac{U}{W} = gT_{\mathrm{WY}} = \frac{-gms^2}{ms^2 + cs + k} \tag{2.5}$$

where $T_{\mathrm{WU}} = gT_{\mathrm{WY}}$ is the sensitivity of the inertial sensor which converts ground displacement W to voltage output U in the unit of V/m.

Alternatively, this system can directly measure ground acceleration by

$$T_{\mathrm{W_aU}} = \frac{U}{s^2W} = \frac{-gm}{ms^2 + cs + k} \tag{2.6}$$

where $T_{\mathrm{W_aU}}$ represent the sensitivity of the sensor which converts ground displacement W_{a} to voltage output U in the unit of V/ms^{-2}.

Figure 2.2 shows the comparison between the two sensitivities expressed by equations (2.5) and (2.6), and the used parameters are listed in Table 2.1. The solid blue curve represents T_{WU}, for frequencies larger than the resonance frequency, a flat transfer function can be obtained, which is perfect to estimate ground motion.

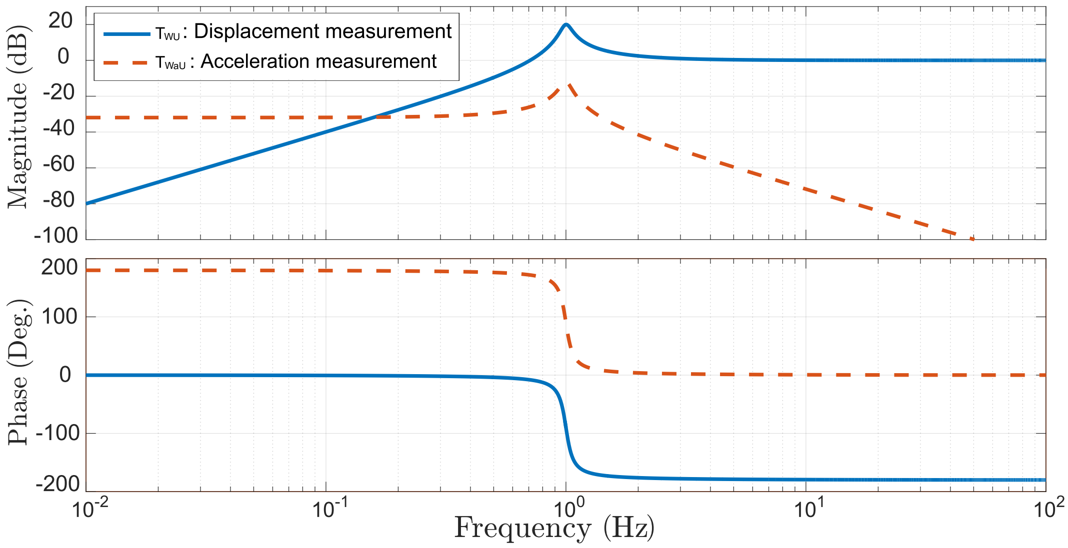

Figure 2.2: The Bode plots of sensitivities of the inertial sensor to measure displacement and acceleration: the unit (dB) of solid blue curve and dash red curve are respective to ($\frac{1\,\mathrm{V}}{1\,\mathrm{m}}$) and ($\frac{1\,\mathrm{V}}{1\,\mathrm{ms}^{-2}}$) because g (in equations (2.5) and (2.6)) is assumed to be 1 V/m.

Table 2.1: Parameters of passive and active inertial sensors.

Sensor type	Parts	Parameters	Symbol	Value	Unit
Passive (Figure 2.2)	Mechanics	Proof-mass	m	1	kg
		Damping coefficient	c	0.6283	Ns/m
		Spring stiffness	k	39.48	N/m
		Resonance frequency	f_0	1	Hz
	Readout	TF (Gain)	g	1	[V/m]
Active (Figure 2.7 & 2.8)	Actuator	TF (Gain)	B	1	N/A
	Controller #1[a]	TF (Gain)	H_1	-38	A/V
	Controller #2[b]	TF (Gain)	H_2	380	A/V

[a] The controller for the displacement measurement with relative displacement feedback;
[b] The controller for the acceleration measurement with relative displacement feedback.

The dash red curve indicates the sensitivity $T_{\mathrm{W_aU}}$ for acceleration measurement. At the frequencies smaller than its resonance frequency, a constant transfer function estimates the ground acceleration, which is the working principle of an accelerometer. However, its magnitude is scaled by $1/(2\pi f_0)^2$. Therefore, the design of an accelerometer is a trade-off between its bandwidth and sensitivity.

There is also a type of inertial sensor to measure velocity, which is called geophone. The readout of the inertial sensor normally is a voice coil, which measure the relative velocity between the frame and the proof-mass of the inertial sensor. They are out of the discussion here because the velocity readout is required to implement their mechanism [31].

Improvement

Figure 2.3 presents a block diagram of the passive inertial sensor. The input of the sensor is ground motion w and the inevitable noise n_s. Here, the noise is the deviation from the expected response under the ground excitation, and it is contributed by different noise sources which are discussed in Section 5.2. The output of the sensor is the voltage signal u.

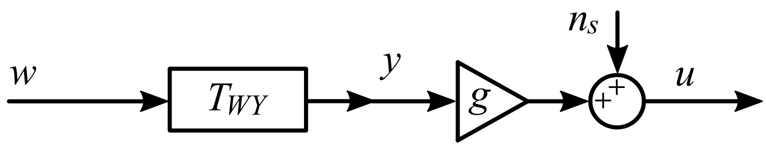

Figure 2.3: Block diagram of a passive inertial sensor: w: ground motion, T_WY: the transmissibility of the mechanics, y: relative motion, g the sensitivity of the readout, n_s: sensor noise, u: voltage output of the sensor.

According to Figure 2.3, the voltage output of the passive sensor in the Laplace domain is

$$U = gT_\mathrm{WY}W + N_\mathrm{s} \tag{2.7}$$

The measured ground motion can be expressed by

$$\begin{aligned}\hat{W} = \frac{U}{gT_\mathrm{WY}} &= \frac{gT_\mathrm{WY}W + N_\mathrm{s}}{gT_\mathrm{WY}} \\ &= W + \frac{N_\mathrm{s}}{gT_\mathrm{WY}}\end{aligned} \tag{2.8}$$

where the measured motion $\hat{W}$ contains the ground motion W and the noise $\frac{N_\mathrm{s}}{gT_\mathrm{WY}}$. The **Resolution** of the inertial sensor is

$$R = \frac{N_{\mathrm{s}}}{gT_{\mathrm{WY}}} \tag{2.9}$$

where R is the smallest physical quantity that the inertial sensor can measure. The readout noise is scaled by the sensitivity of the readout and the transmissibility of the mechanics in the measurement. The ASD of the resolution can be expressed by

$$\mathrm{A_R} = \frac{\mathrm{A_{nn}}}{|gT_{\mathrm{WY}}|} \tag{2.10}$$

where $\mathrm{A_R}$ is the ASD of the inertial sensor resolution and $\mathrm{A_{nn}}$ is the ASD of readout noise n_{s}, also is the resolution of the readout.

Generally, there are two main possibilities to improve the resolution of an inertial sensor in the low-frequency domain. One way is to improve the mechanics for extending the bandwidth in the low-frequency domain. Improvements was focused on decreasing the resonant frequency of the mechanics, such as the development of folded pendulum [43, 44, 45]. Among them, Barone *et al.* [45] reported that the resonance frequency reached 0.06 Hz. Another way is to decrease the noise floor of the readout. Compared to the non-interferometric sensing technologies [46], the interferometric sensing technology demonstrates more advantages in noise performance [47].

Figure 2.4 shows the comparison between the resolution with respect to different transmissibility of mechanics. The solid red curve shows an assumed displacement to be measured. Two different inertial sensors are compared. They have the same readouts with the gain $g = 1$ V/m and the same ASD of noise $n_{\mathrm{s}} = 1 \times 10^{-10}$ V/$\sqrt{\mathrm{Hz}}$. However, the two inertial sensors have different mechanics in terms of resonance. The original mechanics has

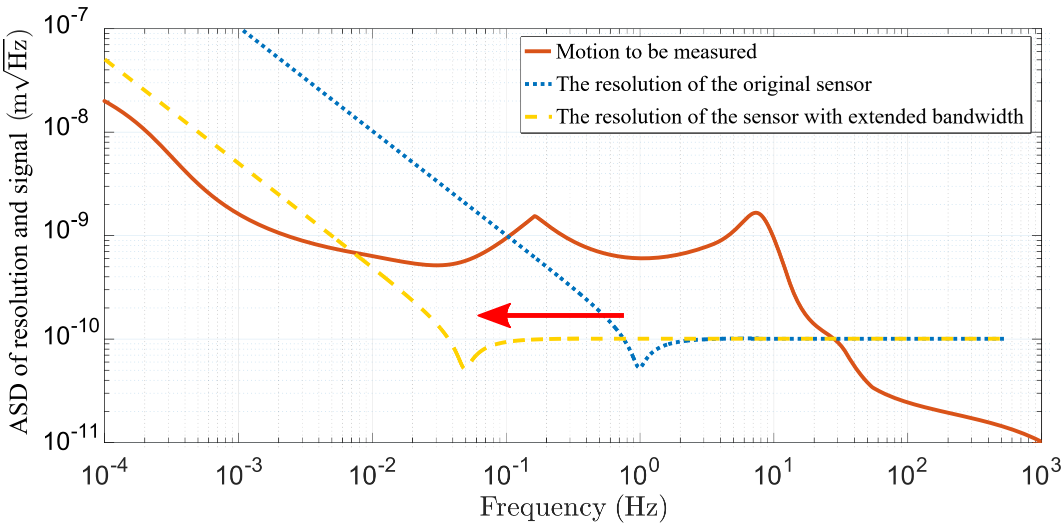

Figure 2.4: Effect of an improvement of the bandwidth on the resolution of the inertial sensor.

the resonance frequency of 1 Hz. According to equation (2.10), the ASD of its resolution is shown as the dotted blue curve. Because the sensor only measures ground motion larger than its resolution, its reliable measurement is from 0.1 to 30 Hz. In contrast, the mechanics with extended bandwidth has a resonance frequency of 0.05 Hz. Its ASD of sensor resolution is the dash yellow curve. The reliable measurement of the improved sensor is from 0.01 to 30 Hz, which is better than the original sensor in the low-frequency domain.

Figure 2.5 shows the comparison between the resolution with respect to different readout noise. The original sensor and improved one are used to measure the same ground motion (solid red curve). Both have the same mechanics, but different readouts. The resolution of the original sensor is as the same as described in Figure 2.4. The readout noise of the improved sensor is $n_s = 2 \times 10^{-11}$ V$/\sqrt{\text{Hz}}$, which is lower than that of the original one. Consequently, the resolution of the improved sensor (dash green curve) is better because of an extended reliable measurement (0.04 to 100 Hz).

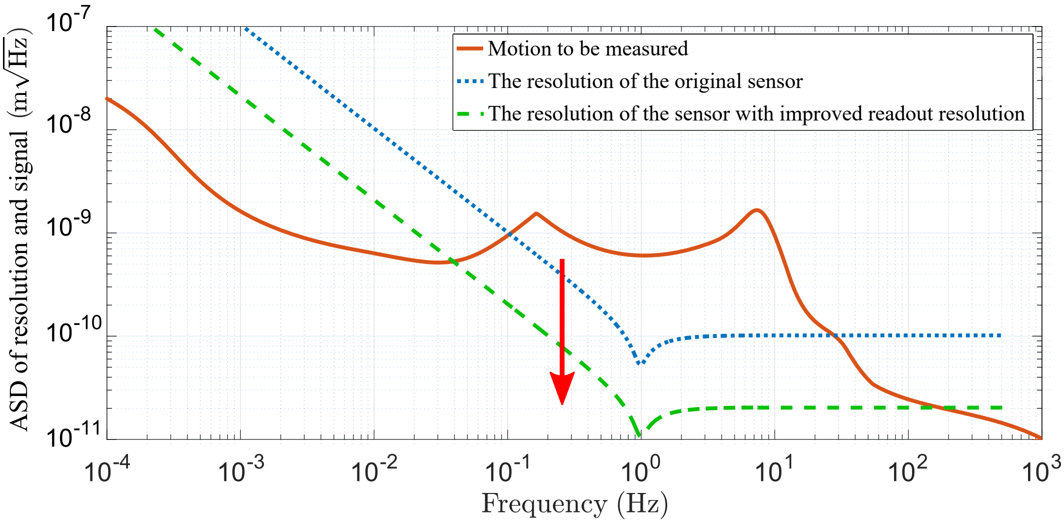

Figure 2.5: Effect of an improvement of the readout resolution on the resolution of the inertial sensor.

Once the inertial sensor has high-resolution in the low-frequency domain, it has the limitation of the tilt-horizontal coupling [48]. Due to gravity, the mechanics are sensitive to both translation and rotation. Reference [49] is a comprehensive review of the tilt-horizontal coupling of inertial sensors. Reference [50] presented this phenomenon observed by using STS1 Horizontal Seismometer (STS1-H) and STS1 Vertical Seismometer (STS1-V) [51] in the seismic monitoring, and the STS1-H was reported more sensitive to the problem. One solution is to decrease the sensitivity of the inertial sensor to the tilting by additional mechanical parts reported by references [52, 53]. However, the weight of the prototype is significantly increased. An alternative solution is to remove the tilting signal in measurements. The tilting signal can be obtained by the high-performance tilt-meter [54] or multiple sensors [55]. A Liquid Absolute Tilt-meter (LAT) is under development to measure tilting signal in our laboratory, which is discussed in Appendix A.

2.2 Active inertial sensor

Figure 2.6 shows a sketch of an active inertial sensor. An actuator A and a controller H_i (i = 1 or 2 depends on the measurement of the inertial sensor) in red have been applied to the original passive sensor. The control force imposes the proof-mass to move with the input motion, which is known as the force balance principle [56].

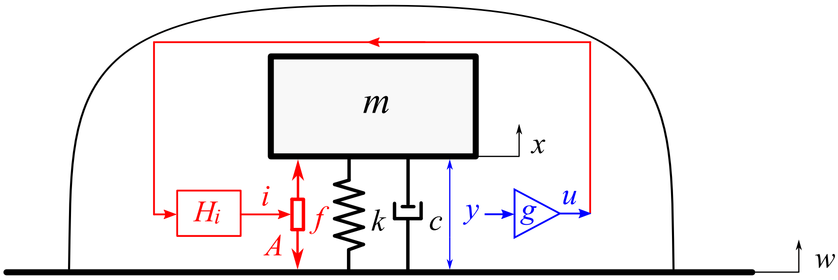

Figure 2.6: Working principle of an active inertial sensor: H_i: the controller, i = 1 or 2 depends on the measurement of the inertial sensor, i: the fedback current, A: the actuator, f: the force generated bu the actuator.

According to the voltage output of the readout u, the driven current i generated by the controller is

$$i = H_\mathrm{i} u \tag{2.11}$$

The actuator is mounted between the proof-mass and the frame of the inertial sensor. Here, a contactless Voice Coil Actuator (VCA) is used, and it generates force f by

$$f = Bi \tag{2.12}$$

where B is the force constant of the VCA in the unit of N/A. The relationship between the input force and proof-mass motion can be expressed by the compliance which is

$$T_\mathrm{FY} = \frac{1}{ms^2 + cs + k} \tag{2.13}$$

Therefore, the relative motion of the proof-mass Y is

$$Y = T_\mathrm{WY} W - T_\mathrm{FY} F \tag{2.14}$$

where W is ground motion and F is the driving force. Merging equations (2.3), (2.4), (2.11), (2.12), (2.13) and (2.14) in the Laplace domain, it yields

$$
\begin{aligned}
T_{\mathrm{WU}} = \frac{U}{W} &= \frac{gT_{\mathrm{WY}}}{1 + gH_1BT_{\mathrm{FY}}} \\
&= \frac{-gms^2}{ms^2 + cs + k + gH_1B}
\end{aligned}
\tag{2.15}
$$

where T_{WU} defines the sensitivity of an active inertial sensor. H_1 is simplified as a controller with a constant gain.

Figure 2.7 shows the comparison between the sensitivities of the passive and active inertial sensors for displacement measurement. The parameters used to plot the figure are listed in Table 2.1. By comparing the the sensitivity of the passive sensor (solid blue curve) with the sensitivity of the active sensor (dash red curve), it shows that the bandwidth extends to the lower frequency. This is the basic working principle of a broadband seismometer [57].

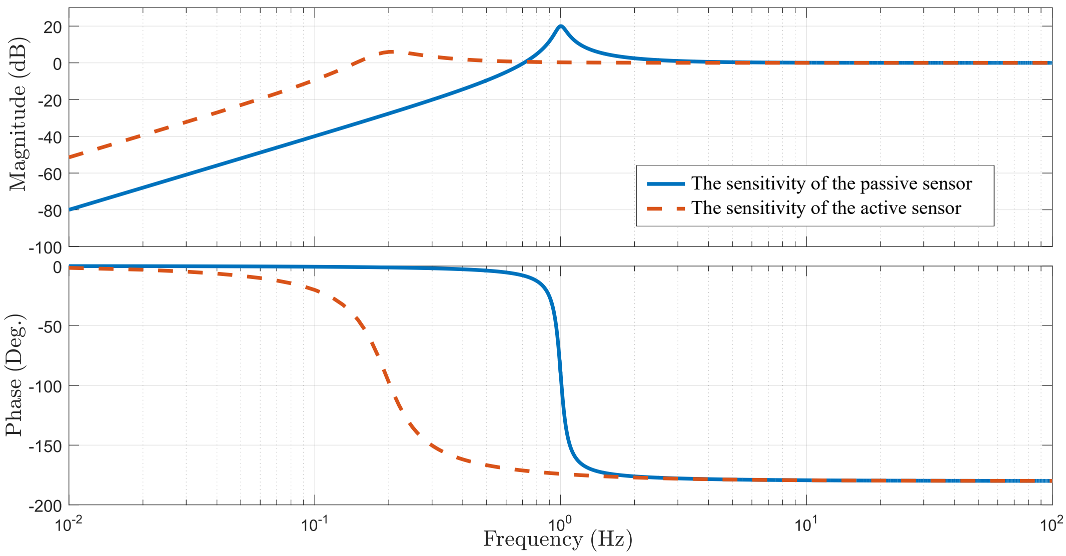

Figure 2.7: The Bode plots of passive and active inertial sensors to measure displacement: the unit (dB) with respect to ($\frac{1\,\mathrm{V}}{1\,\mathrm{m}}$) and $g = 1$ V/m (in equations (2.5) and (2.15)).

This active inertial sensor can measure acceleration as well. The sensitivity $T_{\mathrm{W_aU}}$ is

$$
\begin{aligned}
T_{\mathrm{W_aU}} = \frac{U}{s^2W} &= \frac{gT_{\mathrm{W_aY}}}{1 + gH_2BT_{\mathrm{FY}}} \\
&= \frac{-gm}{ms^2 + cs + k + gH_2B}
\end{aligned}
\tag{2.16}
$$

where H_2 is a new proportional controller used to feedback the relative displacement for the acceleration measurement.

Figure 2.8 shows the comparison between the sensitivities of the passive and active inertial sensor for acceleration measurement. The parameters used to plot the figure are listed in Table 2.1. The sensitivity of the passive inertial sensor (solid blue curve) changes to the

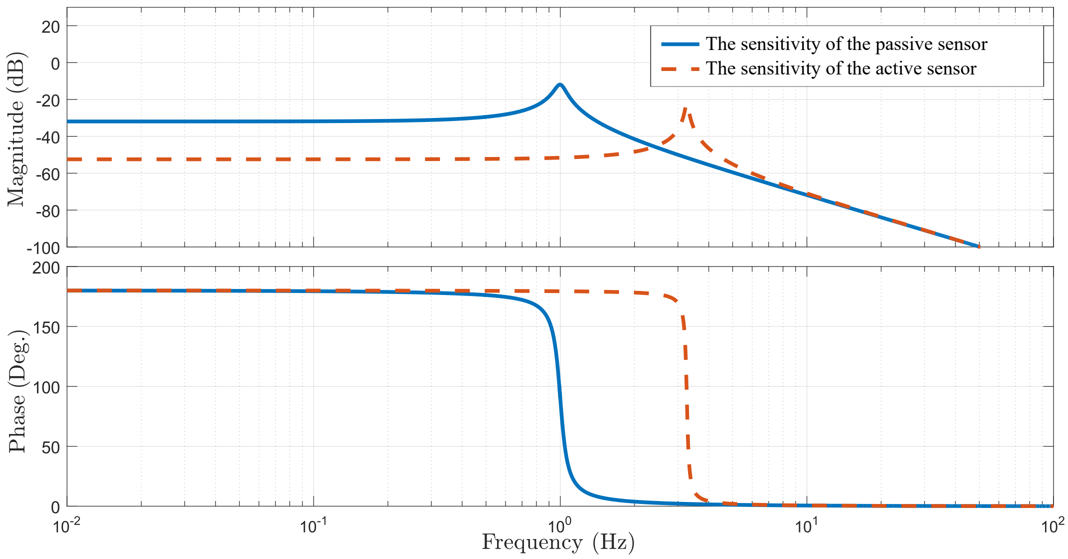

Figure 2.8: The Bode plots of passive and active inertial sensors to measure acceleration: the unit (dB) with respect to ($\frac{1\,\mathrm{V}}{1\,\mathrm{ms}^{-2}}$) and $g = 1$ V/m (in equations (2.6) and (2.16)).

sensitivity of the active inertial sensor (dash red curve). In the useful frequency range, the feedback forces impose the proof-mass to move with the ground motion, thus to increase the dynamic range. It means that the sensor measures with a small relative motion of the proof-mass, which improves the linearity of the measurement. However, the magnitude of its flat sensitivity is degraded. A force-feedback accelerator is often called as the Force Balanced Accelerometer (FBA), which is commonly used in commercial wideband seismometers or custom prototypes [58].

Improvement

Because the resolution of the inertial sensor is critical, the resolution of the active inertial sensor is compared with that of the passive inertial sensor. In order to facilitate the discussion of the noise, the noise of the readout n_s and the actuator n_a are introduced in the active inertial sensor. Figure 2.9 presents a block diagram of an active inertial sensor with the noise sources.

According to the block diagram shown in Figure 2.9, in the Laplace domain, the relationship between the sensor output and the inputs is

$$\begin{aligned} U &= g\big(T_{\mathrm{WY}}W - T_{\mathrm{FY}}(N_a + BHU)\big) + N_\mathrm{s} \\ &= \frac{gT_{\mathrm{WY}}}{1 + gT_{FY}BH}W - \frac{1}{1 + gT_{\mathrm{FY}}BH}(T_{\mathrm{FY}}N_\mathrm{a} - N_\mathrm{s}) \\ &= T_{\mathrm{WU}}W + T_{\mathrm{FU}}(T_{\mathrm{FY}}N_\mathrm{a} - N_\mathrm{s}) \end{aligned} \tag{2.17}$$

where T_{WY} is the transmissibility (equation (2.3)) and T_{FY} is the compliance (equation (2.13)). T_{WU} and T_{FU} are transfer functions between the motion w or force f and output u. The

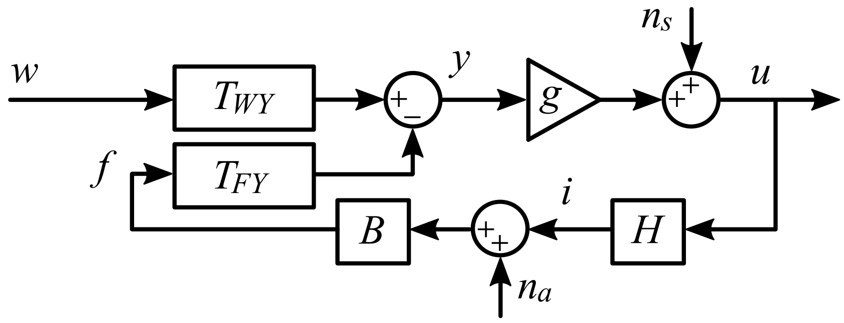

Figure 2.9: Block diagram of an active inertial sensor with noise sources: w: ground motion, y: relative motion of the proof-mass, u: the voltage output, i: the fedback current, f: the driven force, T_{WY}: the sensitivity of the original passive inertial sensor, T_{FY}: the compliance of the original passive inertial sensor, g: the sensitivity of the readout, H: the controller, B: the force constant of the actuator.

measured motion from the active inertial sensor $\hat{W}$ is

$$\begin{aligned}\hat{W} = \frac{U}{T_{\mathrm{WU}}} &= \frac{T_{\mathrm{WU}}W}{T_{\mathrm{WU}}} - \frac{T_{\mathrm{FU}}(T_{\mathrm{FY}}N_{\mathrm{a}} - N_{\mathrm{s}})}{T_{\mathrm{WU}}} \\ &= W - \frac{T_{\mathrm{FY}}N_{\mathrm{a}} - N_{\mathrm{s}}}{gT_{\mathrm{WY}}}\end{aligned} \tag{2.18}$$

According to equation (2.18), the resolution of the active inertial sensor is

$$R = \frac{N_{\mathrm{s}} - T_{\mathrm{FY}}N_{\mathrm{a}}}{gT_{\mathrm{WY}}} \tag{2.19}$$

Comparing this resolution with that of the passive inertial sensor (equation (2.9)), there is an extra item contributed by the actuator noise $\frac{T_{\mathrm{FY}}N_{\mathrm{a}}}{gT_{\mathrm{WY}}}$. Since the actuator noise N_{a} and readout noise N_{s} are incoherent, the added actuator obviously increases the noise of the inertial sensor unless it is ignorable. Therefore, closing the loop of an inertial sensor inject more noise into the system, but improve the linearity.

In conclusion, whether to modify a passive inertial sensor to an active one is a trade-off between the noise and non-linearity. In order to have possibilities of choosing between passive and active inertial sensors in the future, the installation of the actuator has included in the design of the mechanics.

2.3 Conclusion

This chapter introduced to the working principle of the inertial sensor and determined its development direction. The working principles of inertial sensors were analysed. For low-frequency applications, it was found that inertial sensors measuring the displacement quantity are superior in terms of the achievable sensitivity compared to those measure velocity and acceleration quantities. It was discussed that the modification of the type of inertial sensor in terms of resolution, which can be improved by reducing the resonance frequency of its mechanics and improving the resolution of its readout from the design viewpoint. In order to better regulate the dynamic behaviours of inertial sensors such as extending its bandwidth, or increasing its dynamic range and linearity, the active inertial sensor can be used. It was compared that the resolution of the active inertial sensor to that passive, the results indicated that either using an active or passive inertial sensor is a trade-off between the resolution and the linearity.

In conclusion, the development of the inertial sensor focuses on developing an interferometric readout with high-resolution and mechanics with low resonance frequency. The installation of the actuator will be considered in the design of the mechanical system.

Chapter 3

Inertial sensor readout

This chapter presents the readout technology used in the inertial sensor. Section 3.1 compares different contactless displacement readouts. Amongst them, the interferometric readout is selected because of high-resolution. The prototype of the readout is sensitive to polarisation states of laser beams, thus has an extended the measurement range. Section 3.2 shows the prototype and the working principle of the interferometric readout. Section 3.3 presents the mathematical model of the readout by the Jones matrices and mathematically shows the signals measured by photodetectors of the interferometric readout. Section 3.4 details the data processing for recovering the measured relative displacement. Section 3.5 presents the experimental validation of the interferometric readout.

3.1 Readout mechanism

As discussed in Section 2.1, one essential part of an inertial sensor is the displacement readout. There are many readouts measuring displacement with different sensing technologies [46, 59]. Amongst them, the selected readout should have the following features: high resolution, sufficient bandwidth at low frequency (0.01 to 10 Hz), and sufficient measurement range, which is large enough to measure microseisms [60] (about 6.5×10^{-6} m at 0.15 Hz). Moreover, because the selected readout is eventually coupled with the mechanics, the features of compactness and contactless are also important.

3.1.1 Inductive readout

The Linear Variable Differential Transducer (LVDT) [61] is a type of transformer used for measuring displacement. The original readout in the STS1 seismometer is a type of LVDT.

Figure 3.1 shows a typical working principle of the LVDT. It consists of essential parts: one primary fixed windings (middle), two secondary fixed windings (left and right) and a movable ferromagnetic core (the grey bar). The primary winding connects with an AC voltage source V_{in} in series. They generate a magnetic flux Φ. The two secondary windings have the same length L and turns of coils N, their negative poles (left side) are shunted together, and the positive poles (right side) output the voltage signal. The Electromotive Force (EMF) V_{a}

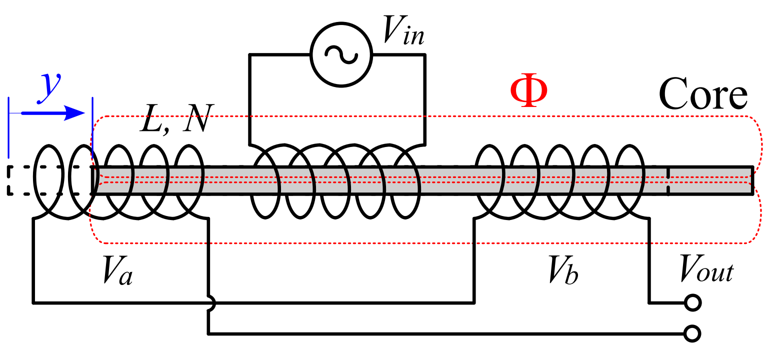

Figure 3.1: The working principle of the Linear Variable Differential Transducer: The dash block is the original position of the core.

and V_b on the two secondary windings are

$$V_\mathrm{a} = -\frac{L-y}{L} N \frac{\mathrm{d}\Phi}{\mathrm{d}t} \tag{3.1}$$

$$V_\mathrm{b} = -N \frac{\mathrm{d}\Phi}{\mathrm{d}t} \tag{3.2}$$

where, y is the position of the core. By combining equations (3.1) and (3.2), the output voltage is

$$\begin{aligned} V_\mathrm{out} = V_\mathrm{a} - V_\mathrm{b} &= -\frac{L-y}{L} N \frac{\mathrm{d}\Phi}{\mathrm{d}t} + N \frac{\mathrm{d}\Phi}{\mathrm{d}t} \\ &= \frac{y}{L} N \frac{\mathrm{d}\Phi}{\mathrm{d}t} \end{aligned} \tag{3.3}$$

where the output V_out is proportional to the position y. The quality of the magnetic flux Φ is important in terms of signal quality. Tariq [62] and Braccini [63] reported prototypes with resolution reached 1×10^{-12} m/$\sqrt{\mathrm{Hz}}$ at 1 Hz.

When this readout is used in an inertial sensor, the long ferromagnetic core has to be mounted on the proof-mass. Therefore, the mass of the proof-mass increases because of adding the core. The difficulty of this mounting is the alignment of the long ferromagnetic core, because enough clearance between the movable core and the fixed windings is required.

The Eddy Current Sensor (ECS) is also an inductive sensor commonly used in the positioning system. A prototype with resolution reached 100 nm was reported by [64]. Because its resolution is not better than the LVDT, its working principle is not discussed.

3.1.2 Capacitive readout

Capacitive sensing technology measures displacement by the variation of capacitance. This type of readouts is commonly used in seismometers such as the STS2 and T240. Figure 3.2 shows a basic working principle by using two conductive plates to measure the distance between each other.

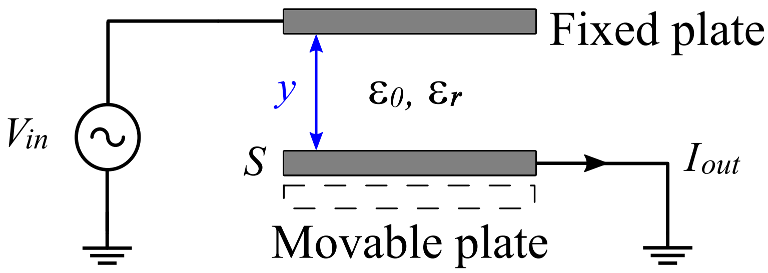

Figure 3.2: The working principle of the capacitor readout [65]: The dash block is the original position of the movable plate.

The geometry of the two conductive plates are the same, one plate is fixed and the other moves with the proof-mass. The distance between two plates is y. These two plates consist of a capacitor with effective area S, the electric permittivity of vacuum is $\varepsilon_0 = 8.854\,187\,8 \times 10^{-12}$ F/m and the relative dielectric constant is $\varepsilon_r = 1$. The capacitance is

$$C = \frac{\varepsilon_0 \varepsilon_r S}{y} \tag{3.4}$$

The capacitive reactance of the capacitor is $X_C = 1/\omega C$, where ω is angular frequency. When a supply charges the plate by voltage V_{in}, the output current I_{out} of the system is

$$I_{out} = \frac{V_{in}}{X_C} = V_{in} \omega \varepsilon_0 \varepsilon_r \frac{S}{y} \tag{3.5}$$

where the output I_{out} is inversely proportional to the distance y. The signal quality of a capacitance readout strongly relates to its sensing circuit and structure [65]. A capacitive readout reaching the resolution of 1×10^{-12} m/$\sqrt{\text{Hz}}$ at 1 Hz was reported by [66].

In order to use a capacitive readout in an inertial sensor, the movable plate is mounted on the proof-mass. The mass of the plate is ignored when compared to that of the proof-mass. Moreover, for improving its resolution, the movable plate is normally connected to the sensing circuit via wires for either power supplying, signal outputting or grounding. The flexibility of the wire is important because a stiff wire may change the dynamics of the mechanics.

3.1.3 Optical linear encoder

Many non-interferometric optical sensing technologies can be used to measure displacement [67]. Among them the optical linear encoder has outperforming resolution. It measures displacement by scanning the encoded positions.

Figure 3.3 shows a basic working principle of optical linear encoders. The encoder includes two parts: a ruler and a scanning head. As shown in the figure, the scanning head generates an incident beam to the detected area and receives the reflected beam from the ruler containing the encoded information of the position. When the scanning head moves with y, the new position can be detected. Optical linear encoders can have resolution with a sub-nanometre level [68].

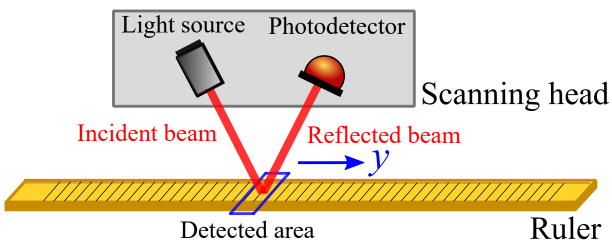

Figure 3.3: The working principle of the linear encoder.

Normally, the mass of the ruler is less than that of the scanning head. Therefore, mounting the scale on the proof-mass is easier than mounting the scanning head. A study presented that the assembly of using an optical linear encoder in an inertial sensor [69]. The main advantages are high-resolution of sub-nanometre and simple alignment.

3.1.4 Michelson interferometric readout

Several interferometric displacement measurement mechanisms were discussed in the references [47, 70]. Of these, the Michelson interferometric readout is a basic configuration. It measures the change in optical power caused by the Optical Path Difference (OPD) thus presents the displacement of the movable optical retro-reflector in a Michelson interferometer.

Figure 3.4 presents the basic working principle of a Michelson interferometer. The laser source generates a laser beam, which can be presented by its electric field vector E

$$E = E_0\, e^{i(\omega t + \phi_\mathrm{L})} \tag{3.6}$$

where E_0 is the initial electric field generated by the laser source, ω is the optical angular frequency. The phase ϕ_L is [70]

$$\phi_\mathrm{L} = \frac{2\pi n L}{\lambda} \tag{3.7}$$

where $n \simeq 1$ is the refractive index of the optical path, λ is the wavelength of the laser beam in the vacuum and L is the physical optical path length that the beam travelled.

When the laser beam goes through the 50-50 beam-splitter cube (BS), it is separated equally into reflected and transmitted laser beams with an amplitude coefficient of $1/\sqrt{2}$. Then, the reflected beam goes to the measurement arm whose length is L_x, and the transmitted beam goes to the reference arm whose length is L_y.

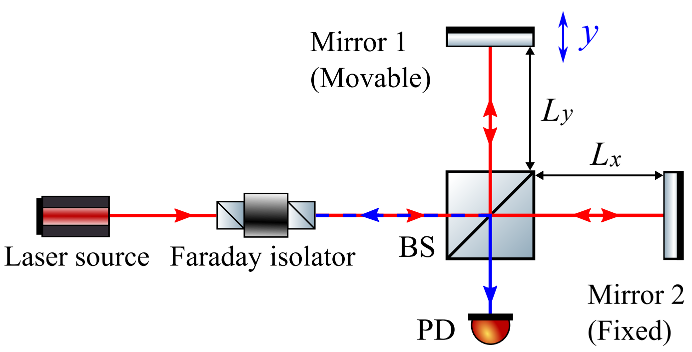

Figure 3.4: The working principle of simple Michelson interferometer: The red lines are single laser beams, the blue lines are multiple laser beams; The arrows indicate the direction of propagation.

The length of the two arms is equal, $L_{\mathrm{x}} = L_{\mathrm{y}}$, in a perfect alignment. When the movable mirror (mirror 1) moves, the optical path varies with the displacement y and cause optical path differences in the two arms. The reflection of the mirrors doubles the travelling of the beams in the arms, by combining equation (3.7), the phase of the beams on the round-trip are

$$\phi_{\mathrm{L_x}} = \frac{4\pi n L_{\mathrm{x}}}{\lambda} \tag{3.8}$$

$$\phi_{\mathrm{L_y}} = \frac{4\pi n (L_{\mathrm{x}} + y)}{\lambda} \tag{3.9}$$

where $\phi_{\mathrm{L_x}}$ the phase on a round-trip with respect to the reference arm, and $\phi_{\mathrm{L_y}}$ is the phase with respect to the measurement arm.

The electric field is used to describe the laser beam and the transmitted and reflected beams entering BS on the return-trip are

$$E_{\mathrm{x}} = \frac{E_0}{\sqrt{2}} e^{i(\omega t + \phi_{\mathrm{L_x}})} \tag{3.10}$$

$$E_{\mathrm{y}} = \frac{E_0}{\sqrt{2}} e^{i(\omega t + \phi_{\mathrm{L_y}})} \tag{3.11}$$

At BS, both the returned beams are again half reflected and transmitted. The electric field of beams measured by the photodetector E_{PD} is

$$\begin{aligned} E_{\mathrm{PD}} = \frac{1}{\sqrt{2}} E_{\mathrm{x}} + \frac{1}{\sqrt{2}} E_{\mathrm{y}} &= \frac{E_0}{2} e^{i(\omega t + \phi_{\mathrm{L_x}})} + \frac{E_0}{2} e^{i(\omega t + \phi_{\mathrm{L_y}})} \\ &= E_0 \, e^{i(\omega t + \frac{\phi_{\mathrm{L_x}}}{2} + \frac{\phi_{\mathrm{L_y}}}{2})} \cos\left(\frac{\phi_{\mathrm{L_y}} - \phi_{\mathrm{L_x}}}{2}\right) \\ &= E_0 \, e^{i(\omega t + \frac{\phi_{\mathrm{L_x}}}{2} + \frac{\phi_{\mathrm{L_y}}}{2})} \cos\left(\frac{2\pi n \cdot y}{\lambda}\right) \end{aligned} \tag{3.12}$$

where $2\pi n y / \lambda$ is the OPD of the two arms on the return-trip. Similar to equation (3.12), the electric field of the unmeasured beams E_{loss} is

$$E_{\mathrm{loss}} = E_0 \, e^{i(\omega t + \frac{\phi_{\mathrm{L_x}}}{2} + \frac{\phi_{\mathrm{L_y}}}{2})} \sin\left(\frac{2\pi n \cdot y}{\lambda}\right) \tag{3.13}$$

which is set-apart by the Faraday isolator. The power of the laser beams at the photodetector P_{PD}, and the unmeasured laser power P_{loss} are

$$P_{\mathrm{PD}} = |E_{\mathrm{PD}}|^2 = P_0 \cos^2\left(\frac{2\pi n \cdot y}{\lambda}\right) \tag{3.14}$$

$$P_{\mathrm{loss}} = |E_{\mathrm{loss}}|^2 = P_0 \sin^2\left(\frac{2\pi n \cdot y}{\lambda}\right) \tag{3.15}$$

$$P_0 = |E_0|^2 = P_{\mathrm{PD}} + P_{\mathrm{loss}} \tag{3.16}$$

where P_0 is the initial laser power from the laser source. As $|e^{i\phi}| = 1$, the finally measured laser power depends only on the OPD and is not affected by the length of the common-path. Once P_{PD} is measured by the photodetector, the phase of the OPD can be calculated. Equation (3.14) can be rewritten by

$$P_{\mathrm{PD}} = \frac{P_0}{2}\left[1 + \cos\left(\frac{4\pi n \cdot y}{\lambda}\right)\right] \tag{3.17}$$

By knowing P_0 and combining with equation (3.7), the relationship between the relative motion y and the measured laser power P_{PD} is

$$\hat{y} = \frac{\arccos(2\frac{P_{\mathrm{PD}}}{P_0} - 1)\lambda}{4\pi n} \tag{3.18}$$

where $\hat{y}$ is the measured relative motion. The inverse trigonometric function only returns the measured phase within a range of π, thus the measurement range is limited in $\lambda/4$. In order to expand the measurement range, the long the wavelength of the laser is expected. Therefore, the interferometric readout using 1550 nm laser has the measurement range of 387.5 nm. However, the resolution of the Michelson interferometer is excellent and the reported resolution was at the level of sub-pico metre [71].

In order to use an interferometric readout in an inertial sensor, the movable mirror must be mounted onto the proof-mass, which in turn increases the weight of the proof-mass.

3.1.5 Comparison

Figure 3.5 compares the readouts in terms of their resolution and typical measurement range. The resolution here is the root mean square value from DC to high frequencies. A readout with a high resolution and a large measurement range locates at the top-left corner

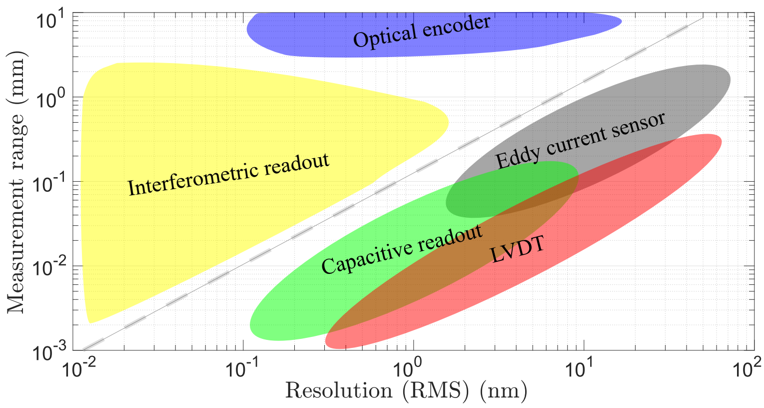

Figure 3.5: Comparison among readouts.

of the figure. The LVDT and capacitive readout have good resolution and measurement range, so they are commonly used in commercial seismometers to monitor earthquakes [72]. However, the inertial sensors used for the active isolation prefers higher resolution. The optical encoder has better resolution than the LVDT and capacitive readout. One example is the prototype developed by Hellegouarch *et al.* [69], whose readout was the optical encoder (LIP281 Heidenhain [68]). The interferometric readout has the best resolution as well as a large measurement range. Among them, the measurement range of a simple Michelson interferometer is limited. Reference [58, 71] presented inertial sensors implemented with simple Michelson interferometric readout. Alternatively, a Michelson interferometer can be modified to extend its measurement range, for example, the interferometric readout presented in Otero's prototype [73]. Consequently, the interferometric readout has been selected because of its high-resolution and large measurement range.

3.2 Long-range interferometric readout

In order to extend the measurement range of a simple Michelson interferometric readout, the large phase must be unambiguously extracted over more than one cycle (more than 2π), which is not possible by using equation (3.17). Alternatively, it is possible to recover large phase by using quadrature signals which can be carried by the two polarisations states of the beam or by two transverse modes of the beam profile.

3.2.1 Polarisation state based readout

In order to have quadrature signals, a phase different $\pi/2$ can be introduced by beams with two polarisation states. The discussion involves the polarisation properties of laser beam, which are briefly introduced in Appendix B. In order to facilitate discussion, p-polarisation (parallel polarisation) and s-polarisation (perpendicular, 'senkrecht' in German, polarisation) are defined, and are respectively parallel and perpendicular to the plane of incidence.

Figure 3.6 shows diagram of a long-range Michelson interferometric readout (homodyne interferometer) with polarisation states. The dot on the beam indicates the s-polarised beam and the perpendicular line, the p-polarised beam. The beam is split by a non-polarising beam splitter and then one polarisation is delayed in the arm of the fixed mirror. An Octadic-Wave Plate WPO placed in the arm provides a differential (round-trip) phase shift of $\pi/2$ between two linear polarisations [74, 73, 75]. In fact, this creates two co-located Michelson interferometers, one in each polarisation, that measure the target mirror. The outputs of these interferometers are then separated by using a polarizing beam splitter. After recombining at the beam splitter, the two polarisations measured at the photodetector PD1 and PD2 are

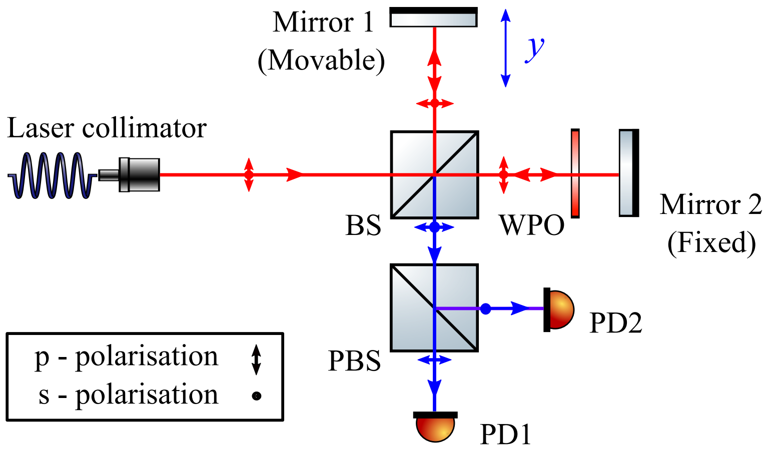

Figure 3.6: Diagram of a long-range Michelson interferometric readout with the polarisation states: The red lines show single polarised laser beams, the blue lines shows the interfered recombined beam. The WPO in the arm of fixed mirror has its fast axis aligned with the s- (or p-) polarisation, effectively creating two co-incident Michelson interferometers. The Polarising Beam Splitter (PBS) splits the two outputs onto the photodetectors PD1 and PD2.

$$P_{\mathrm{PD1}} = P_0(1 + \sin(2\phi_{\mathrm{y}})) \tag{3.19}$$

$$P_{\mathrm{PD2}} = P_0(1 + \cos(2\phi_{\mathrm{y}})) \tag{3.20}$$

where P_0 is determined by the optical power and the fraction of it that reaches the sensors. ϕ_{y} is the phase with respect to the OPD. Tracking the phase of the two quadrature signals, an arbitrarily large phase can be calculated using

$$\hat{\phi}_{\mathrm{y}} = \frac{\mathrm{arctan2}(P_{\mathrm{PD1}} - P_0, P_{\mathrm{PD2}} - P_0)}{2} \tag{3.21}$$

where $\hat{\phi}_{\mathrm{y}}$ is the measured phase. $\mathrm{arctan2}(\sin(\phi), \cos(\phi))$ is the four-quadrant inverse tangent function which returns the value of the phase ϕ within the range [-π,π]. If the amplitude of the phase ϕ exceeds the range [-π, π], the function returns the wrapped phase ϕ_{w} within the range. In this case, the phase unwrapping operation is required to track the phase, and it returns the unwrapped phase $\phi_{\mathrm{u}} = \phi$. The four-quadrant inverse tangent and phase tracking are implemented by the **atan2** and **unwrap** functions of MATLAB, and they are discussed in Appendix C. An interferometric readout of this kind has been mounted in a seismometer [74, 73], and it had a resolution of around 1 pm/$\sqrt{\mathrm{Hz}}$ at 1 Hz.

Several modifications of the optical path have been introduced to reduce noises and hence improve the interferometer resolution. The first way is to increase the number of reflections in the arm of the movable mirror [76, 77]. In comparison with a single-bounce interferometric readout, the resolution of the prototype is improved by a factor which is the number of reflections. An optimum number of reflections is adjustable as explained in reference [78]. The second way is to decrease the number of optical components to avoid unwanted extra reflections. An interferometer that uses beam splitter plates has been developed [79], and BS, PBS and WPO in Figure 3.6 can be replaced by two slightly wedged plates coated with a three-layer metal film [80]. The third way to use an additional photodetector to delete the DC component P_0 in equations (3.19) and (3.20). A Quarter-Wave Plate (WPQ) can also introduce the required phase shift in the system, and an additional photodetector can easily be implemented on the configuration. There were many kinds of interferometric readout using WPQ [81, 82, 83, 84, 85, 86]. A novel prototype developed from Ponceau's prototype [81] is presented in thesis.

Some prototypes with pico-metre level resolution at 1 Hz are listed in Figure 3.7. All cited prototype use the wave-plate to generate quadrature signals, as well as the prototype presented in the thesis. In order to improve the performance of the readout, the researches generally included modifications of the data processing to decrease noise [74, 75, 87], improvements of the noise performance of components used in interferometric readouts, such as laser source and photodetectors [88, 89], and reductions of the external noise [90, 91].

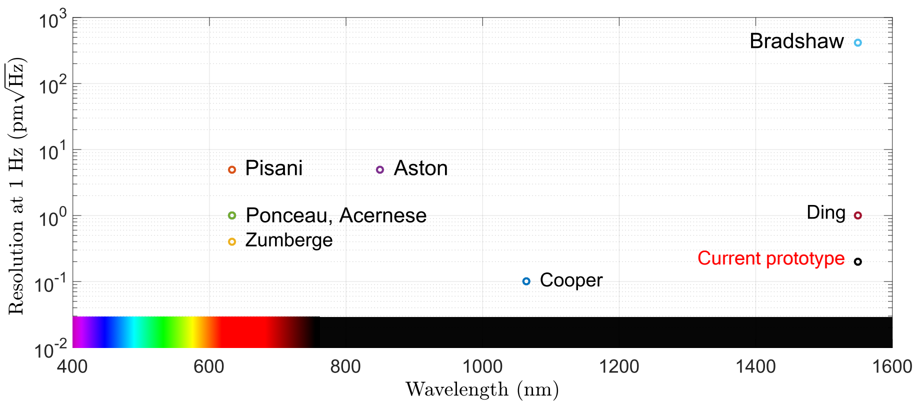

Figure 3.7: Comparison among resolution of interferometric readouts against wavelength: The colourful bar indicates the colour of visible laser beams and the near infrared beam. Pisani [76], Ponceau [81], Aston [82], Bradshaw [83], Ding [85], Cooper [86], Zumberge [92], Acernese [93].

Due to the operation of phase tracking, the wavelength becomes a non-critical parameter. In this case, a laser source with low intensity noise and frequency noise [1] is preferred. Therefore, the infrared laser source, Koheras X15 (the specification is in Appendix E), is selected.

The prototype presented in the thesis combines the different advantages. It has an innovative optical path, a more compact structure, and can be easily aligned. Corner cubes [2], used as the retro-reflectors, reduce the impact of the retro-reflector tilting. The signals of the three photodetectors can be used to reduce the impact of laser intensity noise.

[1]The noise sources are discussed in Section 5.2.3
[2]The corner cube is introduced in Section 3.2.3

3.2.2 Transverse electromagnetic mode based readout

Moreover, a phase shift of $\pi/2$ can be generated between two modes of the beam profile [94]. In fact, the profile can be seen as a superposition of Transverse Electromagnetic Modes (TEM) [95]. When all optics are well aligned with the cavity of the laser, the intensity distribution of the beam has a Gaussian profile, defined as the TEM_{00} mode [96]. By slightly tilting the mirror of the interferometer, the intensity distribution becomes the sum of a TEM_{00} mode and a TEM_{01} mode. When propagating, these modes accumulate a different phase, called a Gouy phase [95, 97]. After travelling, a phase shift of $\pi/2$ can be obtained. Consequently, two quadrature signals are measured by placing one photodiode at the maximum intensity of each mode. Figure 3.8 shows a diagram of such a device.

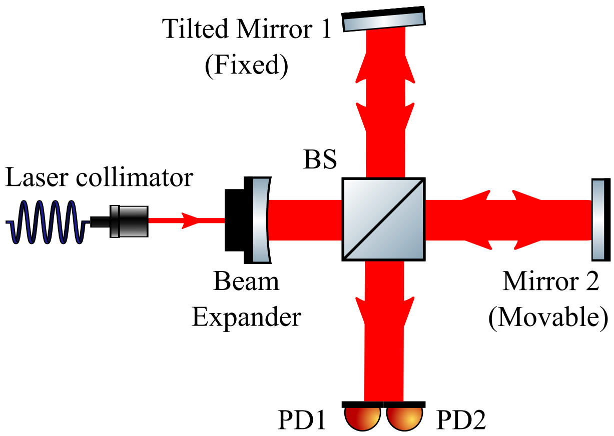

Figure 3.8: Diagram of an interferometric readout with transverse electromagnetic modes: BS: non-polarising beam splitter, PD1&2: photodetectors.

The beam expander plays two roles. First, it allows being in the condition where the phase shift between the two modes is $\pi/2$ [95]. Second, it eases the positioning of the two photodiodes. However, no resolution using this method is found in the literature. Consequently, its performance will not be discussed.

3.2.3 Prototype of long-range compact interferometric readout

Figure 3.9 exhibits the prototype of the interferometric readout under development. The dimension of the prototype is $140 \times 100\ \mathrm{mm}^2$. The laser source (Koheras X15) generates a linearly polarised laser beam, whose wavelength and beam intensity are 1550 nm and 4 mW. This laser beam passes through the polarisation-maintaining fibre of the laser source and is collimated by the collimator (1). The beam diameter of the laser is 1.6 mm.[3] The setting of the gain of the photodetectors is 20 dB.

Figure 3.10 shows the optical path of the interferometric sensing section. Because the

[3]The beam diameter is 2 mm with a distance of 1 m from the collimator. `https://www.thorlabs.com/newgrouppage9.cfm?objectgroup_id=1696`

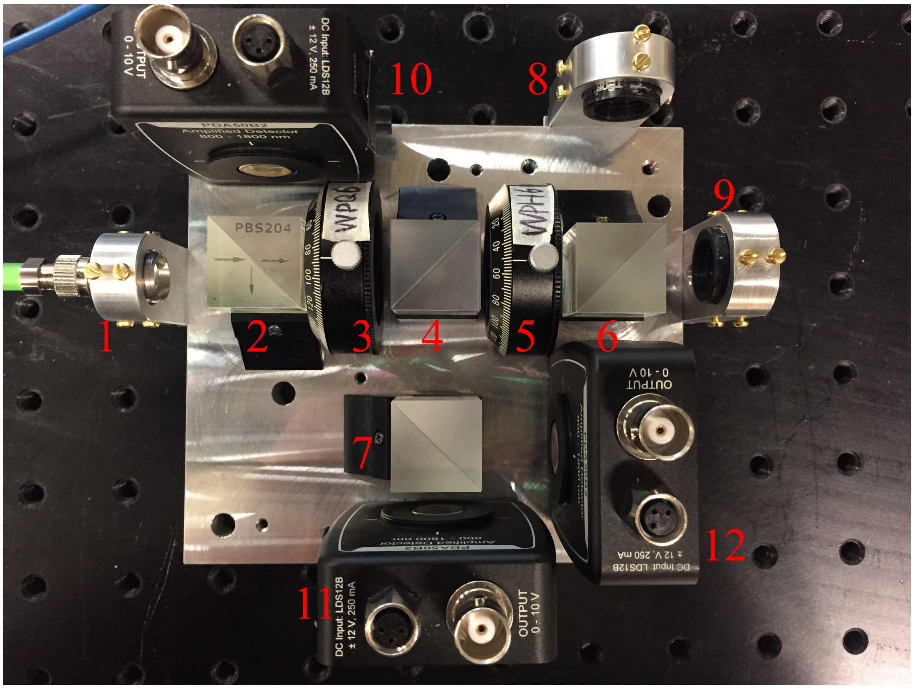

Figure 3.9: The prototype of the interferometric readout: 1: the collimator (F240APC), 2&6&7: the Polarising Beam Splitter Cubes (PBS1,2&3; PBS204), 3: the Quarter-Wave Plate (WPQ; WPQ10E), 4: the Non-Polarising Beam Splitter Cube (BS; BS018), 5: Half-Wave Plate (WPH; WPH10E), 8&9: the Corner Cubes (CC1&2; PS974M-C), 10&11&12: the Switchable Gain Amplified Photodiodes (PD1,2&3; PDA50B2).

fibre outputs a linearly polarised beam, rotating the collimator connected to the fibre will change the angle of the linear polarisation state. The perfect alignment of the laser collimator allows the laser beam to present as a pure p-polarised beam. At PBS1, only the laser beam with p-polarisation state is transmitted, thus here, PBS1 works as a filter. If the alignment of

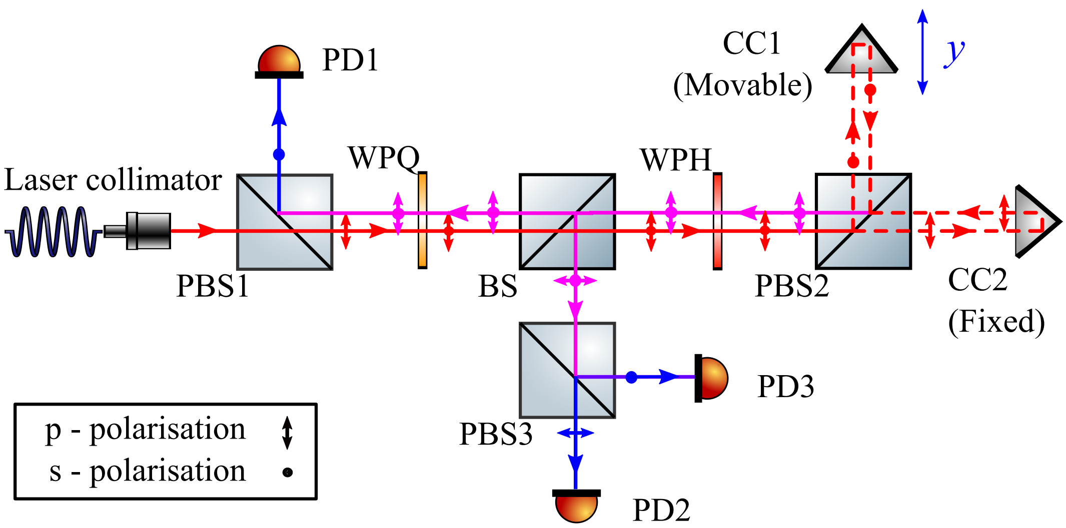

Figure 3.10: The optical path of the interferometric sensing part: Arrows indicate the direction of propagation. The red lines show single laser beams in different polarisation states, the solid purple lines represent the recombined beams and the solid blue line shows the interfered recombined beams.

the collimator is imperfect, the laser beam with s-polarisation state is reflected, and the power is lost. The transmitted laser beam propagates to WPQ.

At WPQ, the fast axis of WPQ is rotated in an anticlockwise direction from the axis of s-polarisation state with an angle of $45°$. Therefore, the electric field of the incident p-polarised laser beam projects equally onto the fast axis and slow axis of WPQ. Due to the function of WPQ, the transmitted laser beam propagates to BS with a circular polarisation state.

At BS, this non-polarising beam splitter divides the incident laser beam equally into the transmitted and reflected laser beam without any change to the polarisation state. It is inevitable that the optical system loses the laser power of the reflected laser beam, which has half-power of the incident laser beam. The transmitted laser beam propagates to WPH with the same circular polarisation state.

At WPH, the fast axis of WPH is rotated in an anticlockwise direction from the axis of s-polarisation state with an angle of $22.5°$. According to the orientation of WPH, the electric field of the incident laser beam is also rotated, and thus the transmitted laser beam now has a circular polarisation state. This circular polarisation state consists of a p-polarisation state and an s-polarisation state. After which, the transmitted beam propagates to PBS2.

At PBS2, the polarising beam splitter separates the incident laser beam, sending it to the movable corner cube (CC1), and a p-polarised laser beam to the fixed CC2. The dash red lines indicate the two laser beams. The arm containing movable CC1 is the measurement arm, and the one containing fixed CC2 is the reference arm. The corner cube, also called a corner reflector, it is a type of retro-reflector which ensures that the reflected beam remains parallel to the incident beam. The benefit is that the corner cube is insensitive to angular motion when compared to a plane mirror. Therefore, the corner cube does not require the mechanics to provide a translational motion. However, the drawback is that the corner cube introduces an undesirable polarisation into the two arms [98]. Movable CC1 adds an extra phase to the s-polarised laser beam. This extra phase can be converted into the motion of CC1 y after data processing.

On the return trip, the two laser beams do not interfere with each other because of their different polarisation states. The p-polarised laser beam and the s-polarised laser beam (with extra phase) are recombined at PBS2. The electric fields of the p- and s-polarised laser beams compose the electric field of the recombined beams. Then, WPH rotates in an anticlockwise direction the p-polarised state and s-polarised state (with extra phase) by the same angle of $45°$. BS divides the beam into the transmitted and reflected beams.

The rotated p-polarised state of the transmitted beam is on the slow axis of WPQ, and is delayed. The rotated s-polarised state (with extra phase) is on the fast axis of WPQ. At PBS1, the two electric fields of the incident laser beam project onto the axis of the s-polarisation state and axis of the p-polarisation state (with the extra phase). PD1 measures the power of the s-polarised interfered laser beam.

Concerning the reflected laser beam from BS, it incidents on PBS3 with the $45°$ anticlockwise rotated p-polarised state and s-polarised state (with extra phase). At PBS3, the two electric fields of the incident laser beam project onto the axis of the s-polarisation state and axis of the p-polarisation state. PD2 measures the power of the p-polarised interfered laser beam, and PD3 measures the power of the s-polarised interfered laser beam.

3.3 Prototype modelling

The Jones matrices expresses the polarisation characteristics of optical components. Therefore, the prototype can be mathematically expressed by the Jones calculus. Table 3.1 lists Jones matrices for the employed optical components [99].

The output laser beam of the collimator is linearly polarised. By assuming that the orientation of the collimator causes laser beam with the pure p-polarisation state, equation (3.6) becomes

$$E = \begin{bmatrix} E_{\mathrm{p}} \\ E_{\mathrm{s}} \end{bmatrix} = E_0 \, e^{i(\omega t + \phi_{\mathrm{L}})} \begin{bmatrix} 1 \\ 0 \end{bmatrix} \tag{3.22}$$

where, E is the electric field of the laser beam, E_{p} and E_{s} are the electric fields of p-polarised and s-polarised beams and ϕ_{L} is the phase with respect to the common-path travelled. As discussed in Section 3.1.4, the measured laser power only depends on the OPD. Therefore, the phase change with respect to the common-path is not discussed. According to Table 3.1, the electric field of the laser beam propagates to PBS2 $E_{(\Rightarrow \mathrm{PBS2})}$ is

$$\begin{aligned} E_{(\Rightarrow \mathrm{PBS2})} &= WPH_{22.5°} \cdot BS_{\mathrm{t}} \cdot WPQ_{45°} \cdot PBS1_{\mathrm{t}} \cdot E \\ &= \frac{i}{\sqrt{2}} \begin{bmatrix} 1 & 1 \\ 1 & -1 \end{bmatrix} \cdot \frac{1}{\sqrt{2}} \begin{bmatrix} 1 & 0 \\ 0 & 1 \end{bmatrix} \cdot \frac{1}{\sqrt{2}} \begin{bmatrix} 1 & i \\ i & 1 \end{bmatrix} \begin{bmatrix} 1 & 0 \\ 0 & 0 \end{bmatrix} \begin{bmatrix} E_{\mathrm{p}} \\ E_{\mathrm{s}} \end{bmatrix} = \frac{1}{2\sqrt{2}} \begin{bmatrix} i-1 \\ i+1 \end{bmatrix} E_{\mathrm{p}} \end{aligned} \tag{3.23}$$

In the reference arm of the interferometric readout, the electric field of the laser beam in return-trip $E_{(\mathrm{ref.arm})}$ is

$$\begin{aligned} E_{(\mathrm{ref.arm})} &= PBS2_{\mathrm{t}} \cdot PBS2_{\mathrm{t}} \cdot E_{(\Rightarrow \mathrm{PBS2})} \\ &= \begin{bmatrix} 1 & 0 \\ 0 & 0 \end{bmatrix} \cdot \begin{bmatrix} 1 & 0 \\ 0 & 0 \end{bmatrix} \cdot \frac{1}{2\sqrt{2}} \begin{bmatrix} i-1 \\ i+1 \end{bmatrix} E_{\mathrm{p}} = \frac{1}{2\sqrt{2}} \begin{bmatrix} i-1 \\ 0 \end{bmatrix} E_{\mathrm{p}} \end{aligned} \tag{3.24}$$

The electric field of the laser beam in return-trip of the measurement arm $E_{(\text{mea.arm})}$ is

$$\begin{aligned} E_{(\text{mea.arm})} &= PBS2_{\text{r}} \cdot e^{i2\phi_{\text{y}}} \cdot PBS2_{\text{r}} \cdot E_{(\Rightarrow \text{PBS2})} \\ &= \begin{bmatrix} 0 & 0 \\ 0 & 1 \end{bmatrix} \cdot e^{i2\phi_{\text{y}}} \cdot \begin{bmatrix} 0 & 0 \\ 0 & 1 \end{bmatrix} \cdot \frac{1}{2\sqrt{2}} \begin{bmatrix} i-1 \\ i+1 \end{bmatrix} E_{\text{p}} = \frac{e^{i2\phi_{\text{y}}}}{2\sqrt{2}} \begin{bmatrix} 0 \\ i+1 \end{bmatrix} E_{\text{p}} \end{aligned} \tag{3.25}$$

where ϕ_{y} is the phase due to the OPD between the measurement arm and the reference arm, this is the phase requiring measurement. According to equation (3.7), it is related to y by $\phi_{\text{y}} = 2\pi y/\lambda$. Due to the reflection, the laser beam travels this OPD twice. Therefore, a coefficient 2 to double the phase ϕ_{y} is required in equation (3.25).

Table 3.1: Jones matrices of optical components.

No.	Components	Jones matrices: Transmission	Jones matrices: Reflection
1	PBS	$PBS_{\text{t}} = \begin{bmatrix} 1 & 0 \\ 0 & 0 \end{bmatrix}$	$PBS_{\text{r}} = \begin{bmatrix} 0 & 0 \\ 0 & 1 \end{bmatrix}$
2	BS	$BS_{\text{t}} = \frac{1}{\sqrt{2}} \begin{bmatrix} 1 & 0 \\ 0 & 1 \end{bmatrix}$	$BS_{\text{r}} = BS_{\text{t}}$
		Transmission	
3	WPQ at 0°[(a)]	$WPQ_{0^\circ} = e^{i\frac{\pi}{4}} \begin{bmatrix} 1 & 0 \\ 0 & -i \end{bmatrix}$	
4	WPH at 0°[(a)]	$WPH_{0^\circ} = \begin{bmatrix} i & 0 \\ 0 & -i \end{bmatrix}$	
	Rotation matrix (R)	$R(\theta) = \begin{bmatrix} \cos(\theta) & \sin(\theta) \\ -\sin(\theta) & \cos(\theta) \end{bmatrix}$	
5	WPQ at 45°[(b)]	$WPQ_{45^\circ} = R(-45^\circ) \cdot WPQ_{0^\circ} \cdot R(45^\circ) = \frac{1}{\sqrt{2}} \begin{bmatrix} 1 & i \\ i & 1 \end{bmatrix}$	
6	WPH at 22.5°[(c)]	$WPH_{22.5^\circ} = R(-22.5^\circ) \cdot WPH_{0^\circ} \cdot R(22.5^\circ) = \frac{i}{\sqrt{2}} \begin{bmatrix} 1 & 1 \\ 1 & -1 \end{bmatrix}$	

(a) The angle between the fast axis and the axis of s-polarisation state is 0°;
(b) The angle between the fast axis and the axis of s-polarisation state is 45°, anticlockwise;
(c) The angle between the fast axis and the axis of s-polarisation state is 22.5°, anticlockwise.

At PBS2 on the return-trip, the returned laser beams recombined and propagate out of PBS2. The electric field of the recombined laser beam $E_{(\Leftarrow \text{PBS2})}$ is

$$\begin{aligned} E_{(\Leftarrow \text{PBS2})} &= E_{(\text{ref.arm})} + E_{(\text{mea.arm})} \\ &= \frac{1}{2\sqrt{2}} \begin{bmatrix} i-1 \\ 0 \end{bmatrix} E_{\text{p}} + \frac{e^{i2\phi_{\text{y}}}}{2\sqrt{2}} \begin{bmatrix} 0 \\ i+1 \end{bmatrix} E_{\text{p}} = \frac{1}{2\sqrt{2}} \begin{bmatrix} i-1 \\ e^{i2\phi_{\text{y}}}(i+1) \end{bmatrix} E_{\text{p}} \end{aligned} \tag{3.26}$$

This recombined laser beam propagates to the three PD.

When the recombined laser beam propagates back to the laser collimator, the fast axes of WPQ and WPH are still $45°$ and $22.5°$ in the anticlockwise direction from the axis of s-polarisation state. Therefore, the Jones matrices of WPQ at $45°$ $WPQ_{45°}$ and WPH at $22.5°$ $WPH_{22.5°}$ are still valid.

Laser power measured by PD1

As discussed previously, the laser propagating to PD1 passes consecutively through the half-wave plate, the non-polarising beam splitter (transmission), the quarter-wave plate and the polarising beam splitter (reflection). Therefore, the electric field E_{PD1} reaching PD1 is

$$\begin{aligned} E_{\mathrm{PD1}} &= PBS1_{\mathrm{r}} \cdot WPQ_{45°} \cdot BS_{\mathrm{t}} \cdot WPH_{22.5°} \cdot E_{(\Leftarrow \mathrm{PBS2})} \\ &= \begin{bmatrix} 0 & 0 \\ 0 & 1 \end{bmatrix} \cdot \frac{1}{\sqrt{2}} \begin{bmatrix} 1 & i \\ i & 1 \end{bmatrix} \cdot \frac{1}{\sqrt{2}} \begin{bmatrix} 1 & 0 \\ 0 & 1 \end{bmatrix} \cdot \frac{i}{\sqrt{2}} \begin{bmatrix} 1 & 1 \\ 1 & -1 \end{bmatrix} \cdot \frac{1}{2\sqrt{2}} \begin{bmatrix} i-1 \\ e^{i2\phi_{\mathrm{y}}}(i+1) \end{bmatrix} E_{\mathrm{p}} \\ &= \frac{1}{2} e^{i(\phi_{\mathrm{y}} - \frac{\pi}{2})} \begin{bmatrix} 0 \\ \cos(\phi_{\mathrm{y}}) \end{bmatrix} E_{\mathrm{p}} \end{aligned} \tag{3.27}$$

The photodetector measures the laser power, which is

$$\begin{aligned} P_{\mathrm{PD1}} = |E_{\mathrm{PD1}}|^2 &= |\frac{1}{2} e^{i(\phi_{\mathrm{y}} - \frac{\pi}{2})}|^2 \cdot \Big(|0|^2 + |\cos(\phi_{\mathrm{y}})|^2 \Big) \cdot |E_{\mathrm{p}}|^2 \\ &= \frac{1}{8} P_0 \Big(1 + \cos(2\phi_{\mathrm{y}}) \Big) \end{aligned} \tag{3.28}$$

where $P_0 = |E|^2$ is the initial laser power from the collimator. According to equation (3.22), as the orientation of the collimator is perfect and guarantees a purely p-polarised laser beam, E_{p} can express the initial laser power by $P_0 = |E_{\mathrm{p}}|^2$.

Laser power measured by PD2

The laser propagating to PD2 passes in turn, through the half-wave plate, the non-polarising beam splitter (reflection) and the polarising beam splitter (transmission). Therefore, the electric field E_{PD2} reaching PD2 is

$$\begin{aligned} E_{\mathrm{PD2}} &= PBS1_{\mathrm{t}} \cdot BS_{\mathrm{r}} \cdot WPH_{22.5°} \cdot E_{(\Leftarrow \mathrm{PBS2})} \\ &= \begin{bmatrix} 1 & 0 \\ 0 & 0 \end{bmatrix} \cdot \frac{1}{\sqrt{2}} \begin{bmatrix} 1 & 0 \\ 0 & 1 \end{bmatrix} \cdot \frac{i}{\sqrt{2}} \begin{bmatrix} 1 & 1 \\ 1 & -1 \end{bmatrix} \cdot \frac{1}{2\sqrt{2}} \begin{bmatrix} i-1 \\ e^{i2\phi_{\mathrm{y}}}(i+1) \end{bmatrix} E_{\mathrm{p}} \\ &= \frac{1}{2} e^{i(\phi_{\mathrm{y}} - \frac{\pi}{2})} \begin{bmatrix} \sin(\phi_{\mathrm{y}} + \frac{\pi}{4}) \\ 0 \end{bmatrix} E_{\mathrm{p}} \end{aligned} \tag{3.29}$$

The power of the laser beam reaching PD2 P_{PD2} is

$$\begin{aligned} P_{\text{PD2}} = |E_{\text{PD2}}|^2 &= |\frac{1}{2}e^{i(\phi_{\text{y}}-\frac{\pi}{2})}|^2 \cdot \Big(|\sin(\phi_{\text{y}}+\frac{\pi}{4})|^2 + |0|^2\Big) \cdot |E_{\text{p}}|^2 \\ &= \frac{1}{8}P_0\Big(1+\sin(2\phi_{\text{y}})\Big) \end{aligned} \tag{3.30}$$

The key items in equation (3.28) and equation (3.30) are $\cos$ function and $\sin$ function, respectively. The employed data processing method requires an extra signal to remove the item of P_0 which contains noise in practice.

Laser power measured by PD3

The laser propagating to PD3 passes sequentially through the half-wave plate, the non-polarising beam splitter (reflection) and the polarising beam splitter (reflection). The only difference between the optical path of reaching PD3 and PD2 is the reflection or transmission at PBS3. The electric field E_{PD3} attaining PD3 is

$$\begin{aligned} E_{\text{PD3}} &= PBS1_{\text{r}} \cdot BS_{\text{r}} \cdot WPH_{22.5^\circ} \cdot E_{(\Leftarrow\text{PBS2})} \\ &= \begin{bmatrix} 0 & 0 \\ 0 & 1 \end{bmatrix} \cdot \frac{1}{\sqrt{2}} \begin{bmatrix} 1 & 0 \\ 0 & 1 \end{bmatrix} \cdot \frac{i}{\sqrt{2}} \begin{bmatrix} 1 & 1 \\ 1 & -1 \end{bmatrix} \cdot \frac{1}{2\sqrt{2}} \begin{bmatrix} i-1 \\ e^{i2\phi_{\text{y}}}(i+1) \end{bmatrix} E_{\text{p}} \\ &= \frac{1}{2}e^{i(\phi_{\text{y}}-\frac{\pi}{2})} \begin{bmatrix} 0 \\ \cos(\phi_{\text{y}}+\frac{\pi}{4}) \end{bmatrix} E_{\text{p}} \end{aligned} \tag{3.31}$$

The power of the laser beam reaching PD3 P_{PD3} is

$$\begin{aligned} P_{\text{PD3}} = |E_{\text{PD3}}|^2 &= |\frac{1}{2}e^{i(\phi_{\text{y}}-\frac{\pi}{2})}|^2 \cdot \Big(|0|^2 + |\cos(\phi_{\text{y}}+\frac{\pi}{4})|^2\Big) \cdot |E_{\text{p}}|^2 \\ &= \frac{1}{8}P_0\Big(1-\sin(2\phi_{\text{y}})\Big) \end{aligned} \tag{3.32}$$

The key item in the equation is the $-\sin$ function.

The above discussion is based on a movable CC1. In Figure 3.10, if CC1 is fixed and CC2 is movable, the s-polarised electric field contains the information of the extra phase. Therefore, the electric fields on three photodetectors are different from the electric fields expressed by equations (3.27), (3.29) and (3.31). However, the measured laser powers are equal to those expressed by equations (3.28), (3.30) and (3.32). In conclusion, either CC1 or CC2 can be used to measure the motion of the proof-mass, and does not affect the data processing of the interferometric readout.

Quadrature signals

By subtracting equation (3.32) from (3.28), and equation (3.30) from (3.28), the quadrature signals with respect to the sine and cosine function $Q_{\sin}$ and $Q_{\cos}$ are

$$\begin{aligned} Q_{\sin} = P_{\mathrm{PD1}} - P_{\mathrm{PD3}} &= \frac{1}{8}P_0\Big(1+\cos(2\phi_{\mathrm{y}})\Big) - \frac{1}{8}P_0\Big(1-\sin(2\phi_{\mathrm{y}})\Big) \\ &= \frac{\sqrt{2}P_0}{8}\sin(2\phi_{\mathrm{y}}+\frac{\pi}{4}) \end{aligned} \tag{3.33}$$

$$\begin{aligned} Q_{\cos} = P_{\mathrm{PD1}} - P_{\mathrm{PD2}} &= \frac{1}{8}P_0\Big(1+\cos(2\phi_{\mathrm{y}})\Big) - \frac{1}{8}P_0\Big(1+\sin(2\phi_{\mathrm{y}})\Big) \\ &= \frac{\sqrt{2}P_0}{8}\cos(2\phi_{\mathrm{y}}+\frac{\pi}{4}) \end{aligned} \tag{3.34}$$

where the DC offset $\frac{1}{8}P_0$ contains laser intensity noise (in Section 5.2.3) is removed. However, A DC phase offset $\pi/4$ and the gain factor $\sqrt{2}$ are introduced from the subtraction. By using the arctan2 function discussed in Section 3.2, the measured phase $\hat{\phi}_{\mathrm{y}}$ is extracted by

$$\hat{\phi}_{\mathrm{y}} = \frac{\mathrm{arctan2}(Q_{\sin}, Q_{\cos}) - \frac{\pi}{4}}{2} \tag{3.35}$$

where the gain factor $\frac{\sqrt{2}P_0}{8}$ is cancelled off, and the item $-\pi/4$ on the right side compensates the DC phase offsets induced by subtractions (equations (3.33) and (3.34)). According to equation (3.7) and (3.35), the displacement of the movable corner cube is

$$\begin{aligned} \hat{y} &= \frac{\lambda}{2\pi n}\cdot\hat{\phi}_{\mathrm{y}} \\ &= \frac{\lambda}{4\pi n}\big(\mathrm{arctan2}(Q_{\sin}, Q_{\cos}) - \frac{\pi}{4}\big) \end{aligned} \tag{3.36}$$

where $\lambda = 1550$ nm is the wavelength of the laser beam and $n \simeq 1$ is the index of refraction. Equation (3.36) indicates that the developed interferometric readout has an theoretically infinite measurement range. Moreover, because demodulating the phase needs processing time, the data processing has the problem of data age if the motion of the proof-mass is too fast [70].

Another method designed to constitute quadrature signals was to remove the item of P_0 in equation (3.28) and (3.30) [81]. A monitoring photodetector detects the loss power at BS in Figure (3.10). If PD1, PD2 and this additional photodetector are of the same type, the power measured on PD1 and PD2 varies from 0 to $P_0/4$ mW but the power measured on the additional photodetector is constant at $P_0/2$ mW. Because of the unbalanced power in measurements, the maximum power on PD1 and PD2 can only be half of their measurement range. In contrast, the presented configuration has the same maximum measured power on PD1, PD2 and PD3.

3.4 Data processing

In practice, the output signal of the photodetectors are voltage signals. The electronic elements of the photodetector convert the laser power to response voltage. However, the procedure is imperfect. The imperfect voltage signals on the three photodetectors V_{PD1}, V_{PD2} and V_{PD3} are

$$V_{\mathrm{PD1}} = G_1\mathfrak{R}_1 \cdot \eta_1 A_1 I_1 \cdot \frac{P_0}{8}\Big(1 + \cos(2\phi_{\mathrm{y}} + \phi_1)\Big) + B_1 \tag{3.37}$$

$$V_{\mathrm{PD2}} = G_2\mathfrak{R}_2 \cdot \eta_2 A_2 I_2 \cdot \frac{P_0}{8}\Big(1 + \sin(2\phi_{\mathrm{y}} + \phi_2)\Big) + B_2 \tag{3.38}$$

$$V_{\mathrm{PD3}} = G_3\mathfrak{R}_3 \cdot \eta_3 A_3 I_3 \cdot \frac{P_0}{8}\Big(1 - \sin(2\phi_{\mathrm{y}} + \phi_3)\Big) + B_3 \tag{3.39}$$

where, G_{i}, $\mathrm{i} = 1, 2$, and 3 are the amplifying factors of the circuit in each photodetector. They convert laser power into photocurrent. According to the manual of the photodetector [100], the gain factor at 20 dB setting is 1.5×10^4 V/A $\pm 2\%$. $\mathfrak{R}_{\mathrm{i}}$, $\mathrm{i} = 1, 2$, and 3 are the responsivity of the photodetector. The typical value is 0.85 A/W. B_{i}, $\mathrm{i} = 1, 2$, and 3 are the offsets of the photodetector, and it varies between ±20 mV at 20 dB setting. G_{i}, $\mathfrak{R}_{\mathrm{i}}$ and B_{i} of the three photodetectors are different from each other. η_{i}, $\mathrm{i} = 1, 2$, and 3 are the overall power loss factors of each optical path. The optical components are listed in Appendix D, the individual loss factor of the components can be found in their data-sheet. Moreover, the alignment of the optical components is critical, as it affects the phase offset and the magnitude of the signal, for instance, the orientation of the quarter-wave plate. ϕ_{i}, $\mathrm{i} = 1, 2$, and 3 are the phase offsets caused by the misalignment of the optical components. A_{i}, $\mathrm{i} = 1, 2$, and 3 are the magnitude coefficients caused by the misalignment. Moreover, η_{i}, ϕ_{i}, A_{i} and I_{i} of the three photodetectors are different from each other. I_{i}, $\mathrm{i} = 1, 2$, and 3 are the fringe contrast which indicates the quality of interference on each photodetectors. It is effected by the alignment and can be evaluated by [70]

$$I_{\mathrm{i}} = \frac{P_{\mathrm{PDi}}(\max) - P_{\mathrm{PDi}}(\min)}{P_{\mathrm{PDi}}(\max) + P_{\mathrm{PDi}}(\min)} = \frac{V_{\mathrm{PDi}}(\max) - V_{\mathrm{PDi}}(\min)}{V_{\mathrm{PDi}}(\max) + V_{\mathrm{PDi}}(\min)} \tag{3.40}$$

where $V_{\mathrm{PDi}}(\max)$ and $V_{\mathrm{PDi}}(\min)$ denote the maximum and minimum values of the interference measured. The perfect fringe contrast equals to 1 and it is acceptable to have it down to 0.9 [73]. The fringe contrast of the developed prototype is around 0.95.

Equation (3.37), (3.38) and (3.39) can be simplified by

$$V_{\mathrm{PD1}} = g_1 \cdot \cos(2\phi_{\mathrm{y}} + \phi_1) + b_1 \tag{3.41}$$

$$V_{\mathrm{PD2}} = g_2 \cdot \sin(2\phi_{\mathrm{y}} + \phi_2) + b_2 \tag{3.42}$$

$$V_{\mathrm{PD3}} = -g_3 \cdot \sin(2\phi_{\mathrm{y}} + \phi_3) + b_3 \tag{3.43}$$

where $g_{\text{i}} = G_{\text{i}}\Re_{\text{i}} \cdot \eta_{\text{i}} A_{\text{i}} I_{\text{i}} \cdot \frac{P_0}{8}$, $b_{\text{i}} = G_{\text{i}}\Re_{\text{i}} \cdot \eta_{\text{i}} A_{\text{i}} I_{\text{i}} \cdot \frac{P_0}{8} + B_{\text{i}}$ and ϕ_{i} respectively present gains, offsets and phase offsets of the signals, with $\text{i} = 1, 2$ and 3.

Reference [101] presented a study of several data-processing methods with a two-detector homodyne interferometer and reported that the phase with the least non-linearity was extracted by the bias-corrected ellipse fitting. Based on that, the data processing of this three-detector homodyne interferometer includes the normalisation in order to minimise gains and offsets, and the ellipse fitting in order to minimise phase offset.

3.4.1 Normalisation

The function of normalisation is to minimise the unbalanced gains and offsets in each measurement. Therefore, obtaining the minimum value (destructive interference) and the maximum value (constructive interference) is essential. If the motion of the corner cube is minor, the measured phase with respect to the motion is insufficient. Therefore, calibration signals containing the minimum and maximum values of the three signals are required.

$$\bar{g_{\text{i}}} = \frac{V_{\text{PDi}}(\text{max}) - V_{\text{PDi}}(\text{min})}{2}; \quad \text{i} = 1,\ 2\,\text{and}\,3 \tag{3.44}$$

where $V_{\text{PDi}}(\text{max})$ and $V_{\text{PDi}}(\text{min})$ denote the maximum and minimum values, the $\bar{g_{\text{i}}}$ is the estimated gain in measurements from PDi. The offset can be estimated by

$$\bar{b_{\text{i}}} = \frac{V_{\text{PDi}}(\text{max}) + V_{\text{PDi}}(\text{min})}{2}; \quad \text{i} = 1,\ 2\,\text{and}\,3 \tag{3.45}$$

where $\bar{b_i}$ is the estimated offset in measurements from PDi. By combining equation (3.44) and (3.45), equation (3.41), (3.42) and (3.43) become

$$N_{\text{PD1}} = \frac{g_1}{\bar{g_1}} \cos(2\phi_{\text{y}} + \phi_1) + \frac{b_1 - \bar{b_1}}{\bar{g_1}} \tag{3.46}$$

$$N_{\text{PD2}} = \frac{g_2}{\bar{g_2}} \sin(2\phi_{\text{y}} + \phi_2) + \frac{b_1 - \bar{b_2}}{\bar{g_2}} \tag{3.47}$$

$$N_{\text{PD3}} = -\frac{g_3}{\bar{g_3}} \sin(2\phi_{\text{y}} + \phi_3) + \frac{b_1 - \bar{b_3}}{\bar{g_3}} \tag{3.48}$$

where $N_{\text{PDi}}, \text{i} = 1,\ 2$ and 3 are the three normalised signals which vary from -1 to 1.

Figure 3.11 shows the performance of normalisation by Lissajous curves. The dash curves present those of the raw signals (V_{PD1} against V_{PD2} and V_{PD1} against V_{PD3}), and in contrast, the solid curves present those of the normalised signals (N_{PD1} against N_{PD2} and N_{PD1} against N_{PD3}). It is obvious that normalisation cannot correct the phase offset of the signals.

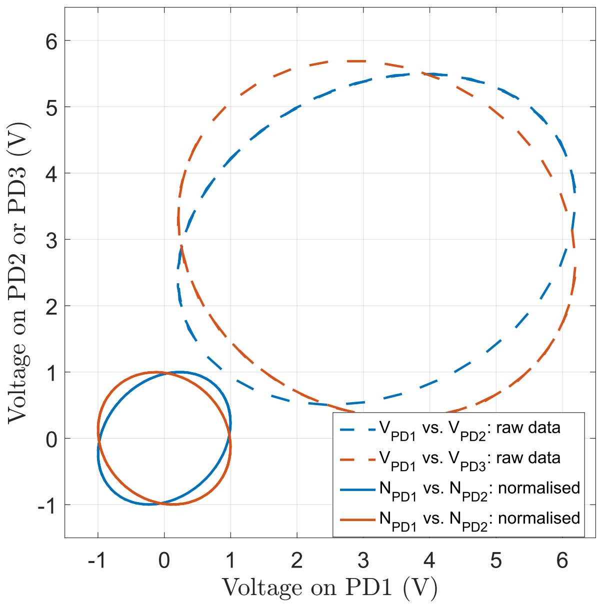

Figure 3.11: The effect of the normalisation on Lissajous curves.

The normalised signals can be subtracted with each other to obtain the quasi-quadrature signals with a phase difference. The quality of the parameters estimated in the normalisation is important. Errors of the estimated parameters cause insufficient intensity noise suppression. In the case of the desired estimation, the main benefit of obtaining quadrature signals from three photodetectors is to reduce the intensity noise (in Section 5.2.3), the quasi-quadrature signals Q_1 and Q_2 are

$$\begin{aligned} Q_1 = N_{\mathrm{PD1}} - N_{\mathrm{PD3}} &= 2\sin\left(\frac{\pi}{4} + \frac{\phi_3 - \phi_1}{2}\right)\sin\left(2\phi_{\mathrm{y}} + \frac{\pi}{4} + \frac{\phi_3 - \phi_1}{2}\right) \\ &= k_1 \sin\left(2\phi_{\mathrm{y}} + \frac{\pi}{4} + \frac{\phi_2 - \phi_1}{2} + \phi_0\right) \end{aligned} \tag{3.49}$$

$$\begin{aligned} Q_2 = N_{\mathrm{PD1}} - N_{\mathrm{PD2}} &= 2\cos\left(\frac{\pi}{4} + \frac{\phi_2 - \phi_1}{2}\right)\cos\left(2\phi_{\mathrm{y}} + \frac{\pi}{4} + \frac{\phi_2 - \phi_1}{2}\right) \\ &= k_2 \cos\left(2\phi_{\mathrm{y}} + \frac{\pi}{4} + \frac{\phi_2 - \phi_1}{2}\right) \end{aligned} \tag{3.50}$$

where $k_1 = 2\sin(\frac{\pi}{4} + \frac{\phi_3-\phi_1}{2})$ and $k_2 = 2\cos(\frac{\pi}{4} + \frac{\phi_2-\phi_1}{2})$ are the gains resulting from the subtraction, and $\phi_0 = \frac{\phi_3-\phi_2}{2}$ is the phase difference between the two quasi-quadrature signals.

3.4.2 Ellipse fitting

The function of the ellipse fitting is to fit an ellipse to data and to correct for a unit circle [102]. Therefore, it corrects the phase offsets of the signals. According to the trigonometric identity of $\cos^2(\theta) + \sin^2(\theta) = 1$, Q_1 and Q_2 from equations (3.49) and (3.50) can be combined as

$$\frac{1}{{k_1}^2}{Q_1}^2 - \frac{2\sin(\phi_0)}{k_1 k_2}Q_1 Q_2 + \frac{1}{{k_2}^2}{Q_2}^2 - \cos^2(\phi_0) = 0 \tag{3.51}$$

because of $(\frac{2\sin(\phi_0)}{k_1 k_2})^2 - 4\frac{1}{{k_1}^2}\frac{1}{{k_2}^2} < 0$, the points Q_1, Q_2 of the Lissajous curve lie on an rotated ellipse and satisfies a general ellipse equation as

$$Ax^2 + Bxy + Cy^2 + Dx + Ey + F = 0 \tag{3.52}$$

where $A = 1/{k_1}^2$, $B = -2\sin(\phi_0)/k_1 k_2$, $C = 1/{k_2}^2$, $D = E = 0$ and $F = -\cos^2(\phi_0)$ are the parameters of the ellipse. As the envelope of the ellipse is fixed by the points (Q_1, Q_2), parameters of the ellipse can be estimated, therefore, the value of $\bar{k_1}$, $\bar{k_2}$, $\sin(\bar{\phi_0})$ and $\cos(\bar{\phi_0})$ can be calculated in the procedure. The quasi-quadrature signals eventually can be corrected to quadrature signals by

$$\begin{aligned}
Q_{\sin} &= \frac{Q_1}{\bar{k_1}\cos(\bar{\phi_0})} - \frac{Q_2}{\bar{k_2}}\tan(\bar{\phi_0}) \\
&= \frac{k_1\sin(2\phi_\mathrm{y} + \frac{\pi}{4} + \frac{\phi_2-\phi_1}{2} + \phi_0)}{\bar{k_1}\cos(\bar{\phi_0})} - \frac{k_2\cos(2\phi_\mathrm{y} + \frac{\pi}{4} + \frac{\phi_2-\phi_1}{2})}{\bar{k_2}}\tan(\bar{\phi_0}) && (3.53)\\
&= \sin(2\phi_\mathrm{y} + \frac{\pi}{4} + \frac{\phi_2-\phi_1}{2})Q_{\cos} && = \frac{Q_2}{\bar{k_2}} \\
&= \frac{k_2\cos(2\phi_\mathrm{y} + \frac{\pi}{4} + \frac{\phi_2-\phi_1}{2})}{\bar{k_2}} && (3.54)\\
&= \cos(2\phi_\mathrm{y} + \frac{\pi}{4} + \frac{\phi_2-\phi_1}{2})
\end{aligned}$$

where $Q_{\sin}$ and $Q_{\cos}$ are the quadrature signals to extract the measured phase. The quality of the quadrature signals highly depends on the quality of the parameter estimation.

Figure 3.12 presents the effect of the ellipse fitting on quasi-quadrature signals by Lissajous curve. The gains k_1 and k_2 of the quasi-quadrature signals $Q1$ and $Q2$ are normalised for comparison. Observing the difference between the Lissajous curve of quasi-quadrature signals (Q_1 against Q_2, dotted red circle) and the unit circle (dash black circle), it shows that the Lissajous curve presents a rotated ellipse, which indicates a clear phase offset. On the contrary, the Lissajous curve of quadrature signals ($Q_{\sin}$ against $Q_{\cos}$, solid blue circle) and the unit circle is overlapped, which shows the phase offsets are corrected.

According to the quadrature signals, the measured phase $\hat{\phi_\mathrm{y}}$ can be calculated by

$$\begin{aligned}
\hat{\phi_\mathrm{y}} = \frac{\mathrm{arctan2}(Q_{\sin}, Q_{\cos}) - \frac{\pi}{4}}{2} &= \frac{(2\phi_\mathrm{y} + \frac{\pi}{4} + \frac{\phi_2-\phi_1}{2}) - \frac{\pi}{4}}{2} \\
&= \phi_\mathrm{y} + \frac{\phi_2-\phi_1}{4}
\end{aligned} \tag{3.55}$$

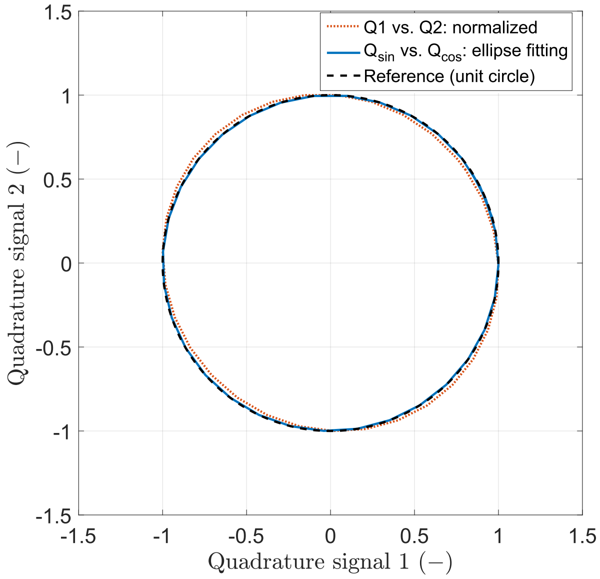

Figure 3.12: The effect of ellipse fitting on Lissajous curves.

where, ϕ_y is the true phase and $(\phi_2 - \phi_1)/4$ is a DC phase offset injected by the ellipse fitting. Because the original phase offsets ϕ_1, ϕ_2 and ϕ_3 in equation (3.46) to (3.48) are actually unknown, the unknown DC phase offset remains in the measured phase and eventually contributes to a DC offset in the measurement of displacement.

Figure 3.13a presents a comparison between the measured phases $\hat{\phi}_y$ from quasi-quadrature signals and quadrature signals. The measured phase from Q_1 and Q_2 (dash red curve) comparing with the true phase (ϕ_y, dash black curve) shows that the measured phase

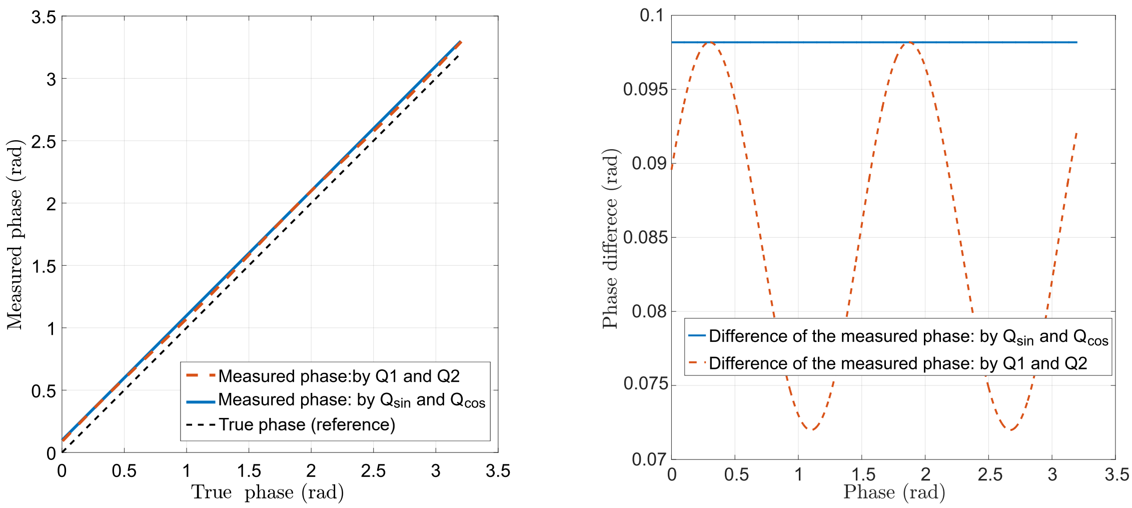

(a) **(b)**

Figure 3.13: Comparison between measured phases from the data processing: Quasi-quadrature signals Q_1 and Q_2 obtained without ellipse fitting, and quadrature signals $Q_{\sin}$ and $Q_{\cos}$ obtained with ellipse fitting. (a) Measured phases with or without the ellipse fitting against the true phase, (b) The difference between the measured phases and the true phase.

is non-linear. The related phase differences ($\hat{\phi}_{\mathrm{y}}$ - ϕ_{y}) against the true phase is shown by Figure 3.13b. On the contrary, the measured phase from Q_{sin} and Q_{cos} (solid blue curve) is parallel to the true phase, and the phase difference (solid blue curve) is an DC offset in Figure 3.13b. The difference between the measured phase and the true phase is the unknown DC phase offset $(\phi_2 - \phi_1)/4$. Because the interferometric inertial sensor finally measures AC signals, this constant offset is not an issue. Consequently, the difference between the solid blue curve and the dash red curve indicates the importance of the ellipse fitting.

In conclusion, the parameters estimated from the normalisation and ellipse fitting are important to measurement. Normally, the calibration and the parameter estimation are conducted before every measurement. The reasons for insufficient parameter estimation and the related non-linearity are discussed in Section 6.3.2.

3.5 Experimental validation

In this section, the interferometric readout is experimental validated. The experiments include the validation of its working principle and the measurement of its resolution. The results show that the interferometric readout correctly measures the relative displacement with a high-resolution of 2×10^{-13} m/$\sqrt{\mathrm{Hz}}$ at 1 Hz.

3.5.1 Working principle validation

Figure 3.14 shows the setup to validate the working principle of the interferometric readout. The interferometric readout (1) is fixed onto the frame (5). The movable corner cube (2) of the readout is mounted on a piezo actuator (3), Cedrat, APA100M [103]. An open-loop piezo controller (Thorlabs, MDT693B [104]) drives the piezo actuator. The other end of the piezo actuator is mounted on the frame (5). The piezo provides reciprocating motion to the movable corner cube. Meanwhile, an eddy current readout (Lion Precision, U8B [105]) measures the signal for comparison. Its probe (4) targets the movable corner cube. The probe is driven by the driver (6), Lion Precision, ECL101 [105]. This sensor is used because it is a well calibrated displacement sensor with good linearity and a resolution of 1×10^{-8} m/$\sqrt{\mathrm{Hz}}$ at 1 Hz. The setup is placed inside a vacuum chamber (7) with 1 mbar. The electrical feed-through and the optical feed-through (Appendix F) on the vacuum chamber connect the setup inside and instruments outside.

Two experiments are performed with the setup. The first one is to validate that the interferometric readout implements the displacement measurement. The input signal is white noise with a low-pass filter, which has a cut-off frequency at 10 Hz. The interferometric readout and eddy current sensor measure the displacement of the corner cube driven by the input signal. The signals are recorded by the data acquisition system, NI PXIe-4497, with

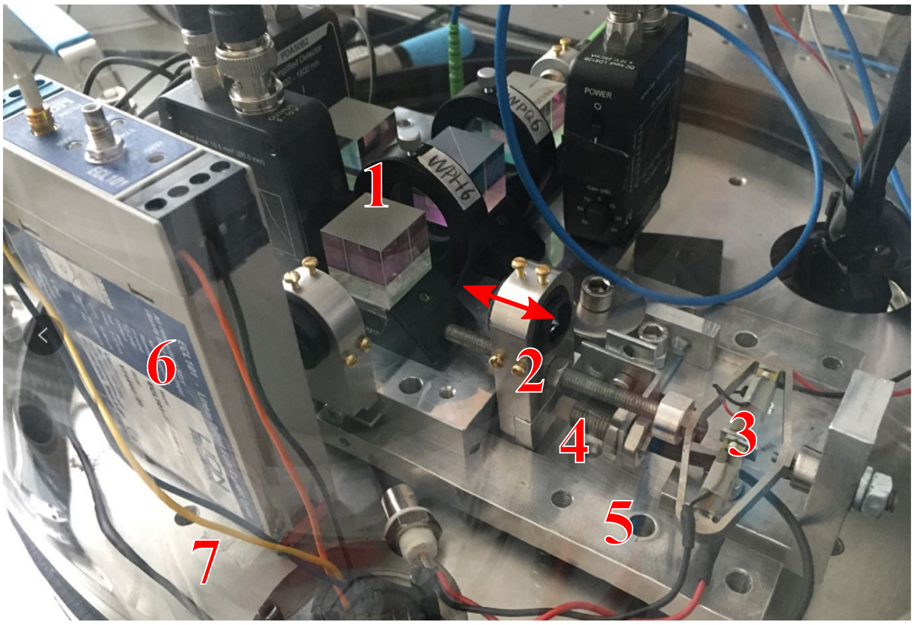

Figure 3.14: Setup to validate the interferometric readout with an eddy current displacement sensor: 1: the interferometric readout, 2: the movable corner cube of the readout, 3: the piezo actuator, 4: the probe of the eddy current displacement sensor, 5: the frame for mounting, 6: the driver of the eddy current sensor, 7: the base of the vacuum chamber. The red arrows indicate the motion of the corner cube.

sampling frequency of 10 kHz.

Figure 3.15 shows the ASD of the three signals. The ASD of the input signal (dash blue curve) is compensated with a factor 2.05×10^{-6} to facilite the comparison, its value is shown by the left vertical axis. The input signal is filtered above 10 Hz. The ASD of the signal from the interferometric readout (solid red curve) is different from the ASD of the input

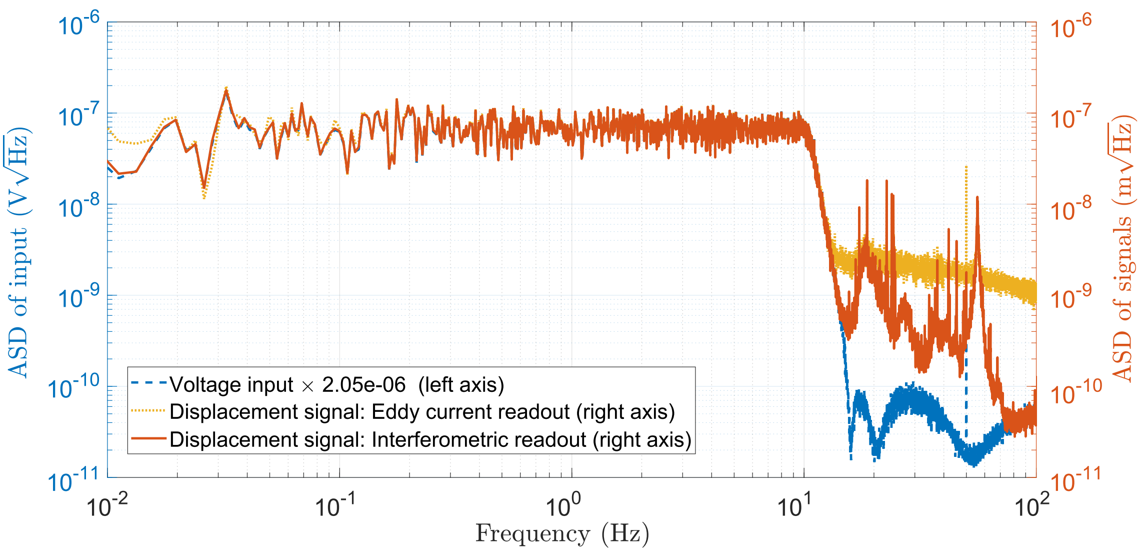

Figure 3.15: Amplitude spectral density of signals from the white noise excitation experiment: left vertical axis: ASD of input, right vertical axis: ASD of signals.

signal above 15 Hz, as the mounting of the corner cube senses ground motion. The ASD of the signal from the eddy current sensor (dotted yellow curve) is different from the ASD of the signal from the interferometric readout above 15 Hz, which dues to the low resolution of the eddy current sensor.

Figure 3.16 shows coherence between the signals from 0.01 to 20 Hz. The input signal and the signal of the interferometric readout (solid red curve) are coherent below 10 Hz, the coherence decreases above 15 Hz because the interferometric readout senses ground motion. The coherence between the input signal and the signal of the eddy current sensor (dotted yellow curve) drops below 0.1 Hz and above 15 Hz, which due to the low resolution of the eddy current sensor. Therefore, the coherence between the signals of the interferometric readout and the eddy current sensor (dash blue curve) is low below 0.1 Hz and above 15 Hz.

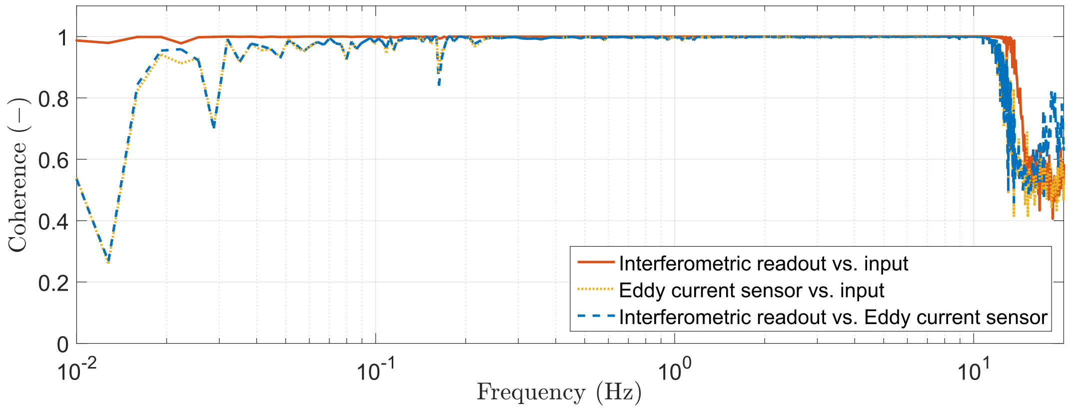

Figure 3.16: Coherence of the input signal and the measured signals from the white noise excitation experiment.

Figure 3.17 shows the transfer function between the signals of the interferometric

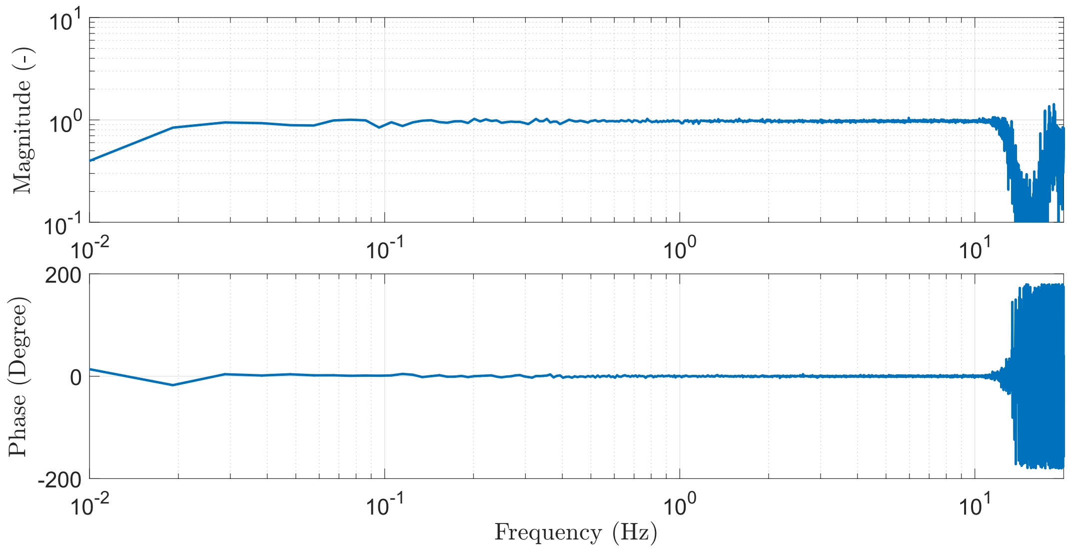

Figure 3.17: Transfer function between the measured signals from the white noise excitation experiment: the top figure shows the magnitude of the transfer function and the lower

readout and the eddy current sensor. It shows that the amplitude of the signals equals one from 0.01 to 10 Hz, which proves that the measurement of the interferometric readout correctly measures the displacement. The magnitude of the transfer function drops due to the noise of the eddy current sensor.

Then, the linearity of the measurement is checked by the sine sweep experiment, in which the corner cube is driven by a chirp signal (blue curve in Figure 3.18) whose frequency increases with time in the experiment. The amplitude of the driving chirp signal is 0.1 V with frequencies being swept from 0.01 to 10 Hz during 3500 s. The amplitude of the measured displacement is about 0.4 µm. The signals is recorded by the data acquisition system, NI PXIe-4497, with a sampling frequency of 1×10^4 Hz. When the signal of the interferometric readout (red curve) is compared to the signal of the eddy current sensor (yellow curve), the latter is noiser. These signals are converted to show their time-frequency distributions in Figure 3.19.

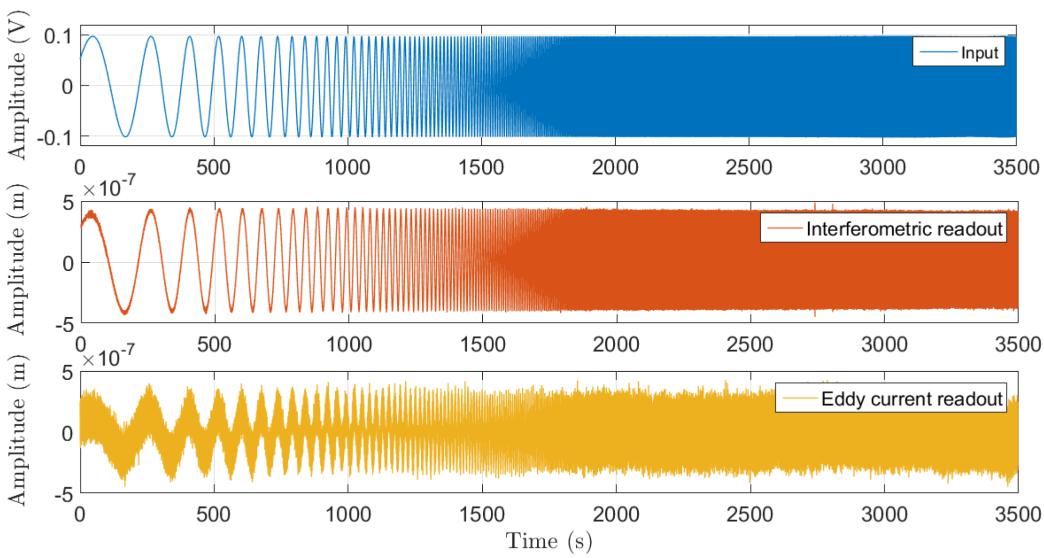

Figure 3.18: Signals from the sine sweep experiment in the time domain.

The time-frequency distribution plots the amplitude of a signal against its time and frequency components. The vertical bars on the right of the figures show the amplitude of the signal. The brilliant yellow colour means high amplitude and the dark blue means no energy. As the frequency of the chirp signal is from 0.01 to 10 Hz during 3500 s, its curve is a diagonal in Figure 3.19a, and has no obvious energy on the other frequencies. Figure 3.19b is the time-frequency distribution of the signal measured by the interferometric readout. Compared to the input signal, the figure has no difference and thus it presents that the readout measures the displacement linearly. However, the curve of the eddy current sensor (see Figure 3.19c) is less brilliant, and the background is uneven dark blue, which indicates a higher noise than that of the interferometer readout. Therefore, Figure 3.19 shows that the measurement of interferometric readout is linear in frequencies from 0.01 to 10 Hz at the chosen excited level

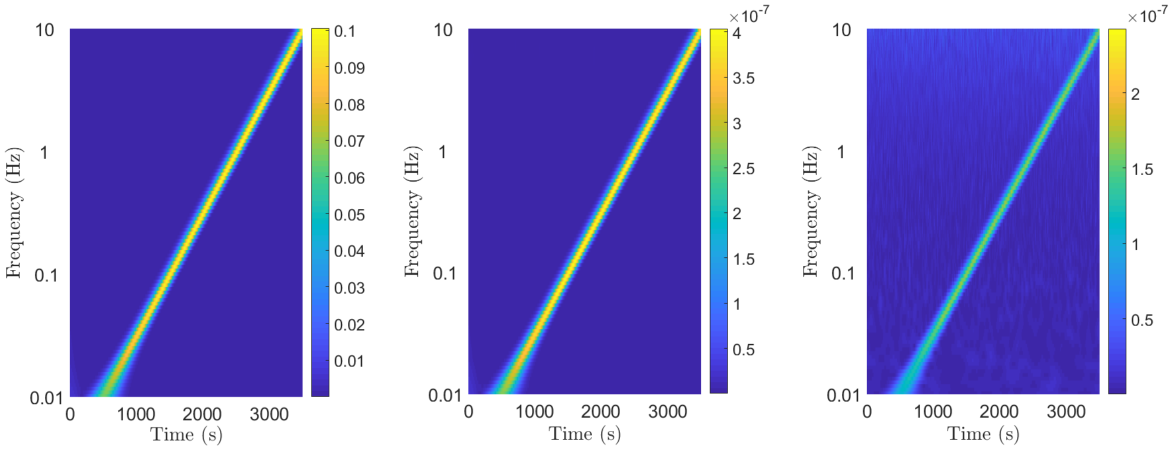

(a) (b) (c)

Figure 3.19: Time-frequency distribution figures of signals from the sine sweep experiment: (a) Time-frequency distribution of the chirp input signal, (b) Time-frequency distribution of the signal measured by the interferometric readout, (c) Time-frequency distribution of the signal measured by the eddy current sensor.

and the developed sensor outperforms the eddy current sensor in terms of the resolution.

3.5.2 Resolution characterisation

The resolution of the interferometric readout is estimated by the blocked-mass test. The working principle of the blocked-mass test is demonstrated in Section 5.3. Figure 3.20 shows

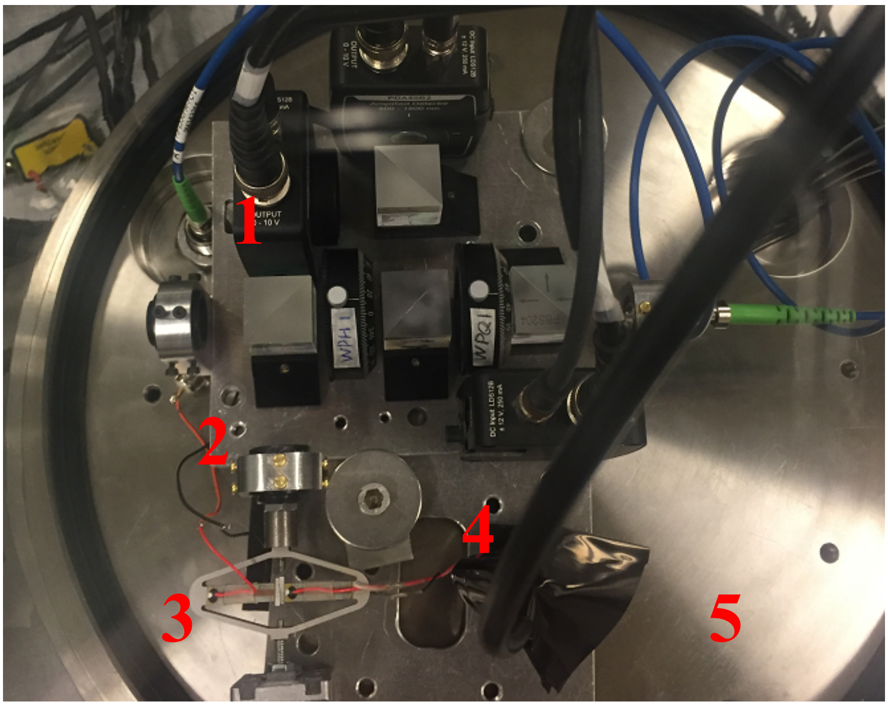

Figure 3.20: Setup for measuring the resolution of the interferometric readout: 1. the interferometric readout, 2. the corner cube, 3. the piezo actuator, 4. the base of the setup, 5. the vacuum chamber

the setup for the experiment. The setup is inside a vacuum chamber (5) with 1 mbar. The interferometric readout (1) is mounted on the base (4). Both of the corner cubes are fixed onto the frame of the interferometric readout for improving the rigidity. This decreases the effect of the ground motion on the readout. Because the signals in the resolution measurement are too weak to generate a full Lissajous circle, a calibration procedure to generate a full Lissajous circle is required. In order to do so, one corner cube is required with a high amplitude motion. A piezo actuator (3) is mounted between the frame (4) and the holder of the corner cube (2), and it provides enough motion on the corner cube in the calibration. The input signal used to generate the calibration signal is a sinusoid with the amplitude of 2 V with frequency of 0.5 Hz. After the calibration, the measurement to estimated the resolution is performed without input signals. The signal is processed with the parameters estimated from the calibration.

Figure 3.21 shows the estimated resolution of the interferometric readout. The gain factor of the photodetectors are 20 dB. The output laser intensity of the laser source is 4 mW. The sampling frequency of the measurement is 10 kHz, and the measurement length is 1000 s. The blue curve in the figure shows the resolution of the interferometric readout. The resolution of the optical readout is around 1×10^{-11} m/$\sqrt{\text{Hz}}$ at 0.01 Hz, 1×10^{-12} m/$\sqrt{\text{Hz}}$ at 0.1 Hz, and 2×10^{-13} m/$\sqrt{\text{Hz}}$ at 1 Hz. This result will be further discussed with noise budgeting in Chapter 5. Moreover, this readout is sensitive to the seismic vibration between 2 to 100 Hz. The reason is that the optical-component holders including the frame of the corner cube with the piezo actuator are not sufficiently rigid. Therefore, improving the rigidity of the readout is a possibility to decrease the effect of the seismic vibration on the structure, which is further discussed in Section 5.3.1.

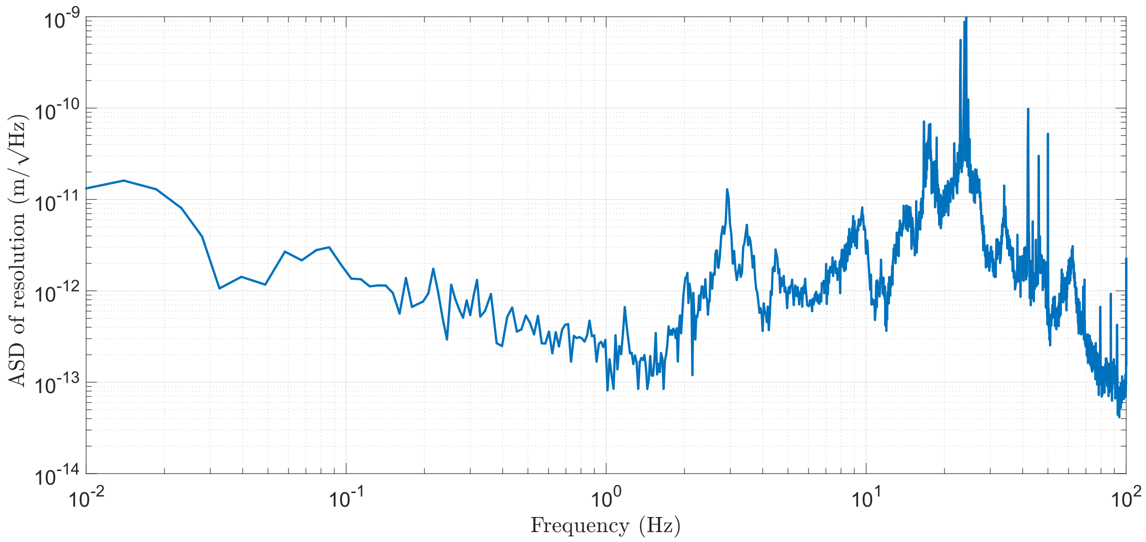

Figure 3.21: Resolution of the interferometric readout.

3.6 Conclusion

This chapter discussed the development of the readout of the inertial sensors. Different readouts for measuring relative displacements were reviewed. It was found that interferometric readouts are superior among candidates in terms of the resolution. However, its measurement range is limited within a quarter wavelength. The methods to extend the measurement range by quadrature signals were compared. A long-range interferometric readout generating quadrature signals by polarisation states of the laser was presented. Its working principle was demonstrated by using Jones matrices. Moreover, the importance of the employed data-processing was analysed in terms of noise and non-linearities reduction. The performance of the interferometric readout was also experimentally investigated in comparison with a benchmark eddy current sensor (Lion Precision, U8B). It was shown that the interferometric outperforms the eddy current sensor in terms of the resolution, and it behaves linearly in a measurement range of 0.4 μm from 0.01 to 10 Hz.

The resolution of the interferometric readout was identified by the blocked-mass test, as 2e-13 $\mathrm{m}/\sqrt{\mathrm{Hz}}$ at 1 Hz. However, its resolution showed a degradation at high frequencies from 2 to 100 Hz because of the flexibilities of the optical components. One improvement can be done by mounting optical components of the interferometric readout more rigidly. The in-depth discussion of its resolution is in Chapter 5, combining the noise budgeting.

Chapter 4

Inertial sensor mechanics

This project requires inertial sensors to measure separately, both horizontal and vertical motions. Therefore, two types of mechanics are required. In Section 4.1, some flexure hinges used in inertial sensors for low-frequency measurement are compared. Amongst them, the Lehman pendulum (in the Horizontal Interferometric Inertial Sensor (HINS)) and Leaf spring pendulum (in the Vertical Interferometric Inertial Sensor (VINS)) combining cross-spring hinges are good candidates. Section 4.2 presents the mechanics of the Horizontal Interferometric Inertial Sensor (HINS) including its dynamic behaviours and the experimental characterisation. Section 4.3.1 presents the mechanics of the Vertical Interferometric Inertial Sensor (VINS) including its dynamic behaviours and the experimental characterisation.

The resonance frequencies of the mechanics of the HINS and VINS are 0.11 and 0.26 Hz, respectively. Section 4.4 shows the inertial unit which consists both the HINS and VINS are placed in a vacuum chamber in a compact fashion.

4.1 Flexure joint

The mechanics requires a low resonance frequency to improve the sensor resolution in the low-frequency domain. Many models of low-frequency oscillators were presented by Wanner [106]. One challenge of implementing the models is to develop the suitable kinematic joints which provides the desired relative motion between the proof-mass and the frame.

Ball-bearings and linear sliders are common examples of kinematic joints used for rotational and translational motion. Their structures block the undesired Degree of Freedom (DOF). Their advantage is that they facilitate motion with a large range and a heavy load, and thus are often used in industry. However, they have the disadvantages of friction. Therefore, they are not suitable for inertial sensors.

Alternatively, flexure hinges can be used as joints. These rely on the elastic properties of the material and have interesting features including extremely low and uniform friction, low stiffness, no backlash and smooth motion. Its disadvantage is the range-limited motion, but it is not a problem to the mechanics of the inertial sensors.

4.1.1 Clamped-plate hinge

Figure 4.1 presents a basic flexure hinge is an assembly of frames with a clamped elastic plate. The two ends of the elastic plate are clamped by a fixed frame A and a movable frame B, respectively. Its effective length is l. Frame A normally has two parts screwed together to hold the elastic plate by friction. By the same method, frame B clamps the opposite end of the plate.

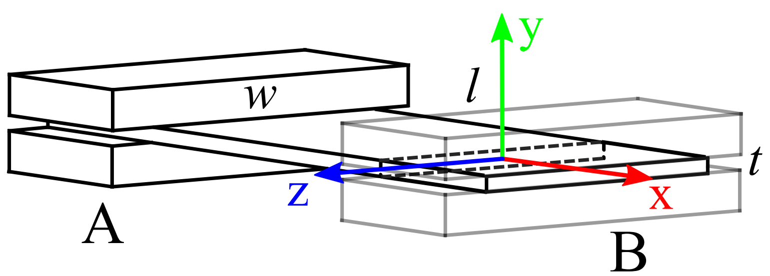

Figure 4.1: The sketch of a clamped elastic plate: l: the effective length, w: the width of the strip, t the thickness of the strip.

A Cartesian coordinate system is oriented in the the middle of the end clamped by the frame B. For a clamped-plate hinge with a short effective length, the commonly desired deflection of the plate is θ_z, a rotation about the z-axis. The rotational stiffness of the hinge can be estimated by the beam theory [107], which is

$$k_{\theta_z} = \frac{EI_z}{l} \tag{4.1}$$

where k_{θ_z} is the rotational stiffness, E is Young's modulus of the material, $I_z = wt^3/12$ is the area moment of inertia, l is the effective length, w is the width of the strip and t is the thickness of the strip.

Mechanics with clamped-plate hinge

Figure 4.2a shows a simple pendulum combining clamped-plate hinge with its model. When the frame is excited by translational motion w, a relative angle θ is generated between the pendulum and the frame. The black ball represents the point of the pendulum's centre of mass COM. L is the effective length of the pendulum between the hinge and the COM.

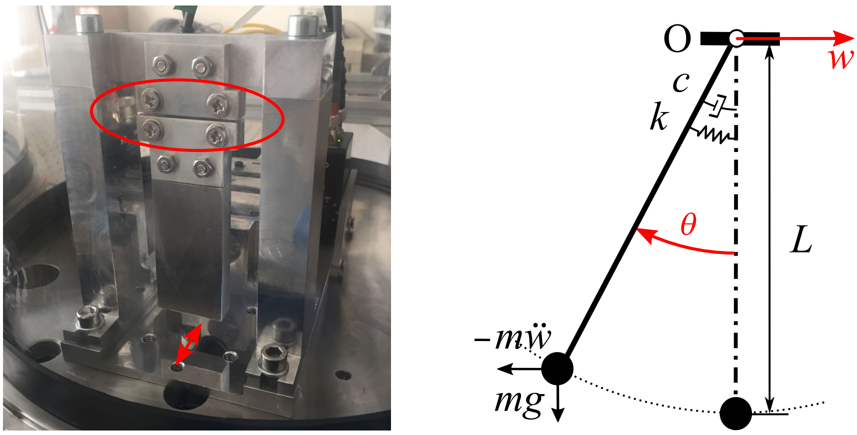

(a) **(b)**

Figure 4.2: A simple pendulum using clamped-plate hinge: (a) the prototype of the pendulum. Its clamped-plate hinge is shown in the red circle, the thickness of the plate is a 50 µm, made of Cu-Be material. The resonance of the system is around 7 Hz. Double arrow indicates the direction of the pendulum motion. (b) The model of the pendulum: O: the rotation centre, L: the effective length of the pendulum, m: the mass, c: the rotational damping, k: the rotational stiffness, w: ground motion, θ: the relative motion.

Applying Newton's second law of rotation about the hinge O, the dynamic equation of the mechanics under translational excitations can be derived as

$$I\ddot{\theta} = -c\dot{\theta} - k\theta + m\ddot{w}L\cos(\theta) - mg\sin(\theta)L \tag{4.2}$$

where, I is the moment of inertia with respect to the rotation centre O. The relative angle θ is small in the oscillation regime, therefore, it is assumed $\sin(\theta) \approx \theta$ and $\cos(\theta) \approx 1$. equation (4.2) expressed in the Laplace domain is

$$\Theta(s) = \frac{mLs^2}{Is^2 + cs + (k + mgL)} W(s) \tag{4.3}$$

where, $\Theta(s)$ and $W(s)$ are the relative rotation θ and ground motion w in the Laplace domain. The resonance frequency of the mechanics is

$$f_0 = \frac{1}{2\pi}\sqrt{\frac{k + mgL}{I}} \tag{4.4}$$

Typical methods to decrease the resonance frequency of the pendulum are to decrease the stiffness of the hinge and increase the inertia of the pendulum. Moreover, if the stiffness of the hinge is ignored $f_0 = \frac{1}{2\pi}\sqrt{g/L}$ with $I = mL^2$, which is often used to describe the resonance frequency of a pendulum.

Figure 4.3a shows a mechanics based on the leaf spring pendulum, which is developed from the LaCoste pendulum [108]. The hinge in the red circle links the frame and the pendulum. The bent blade (in the green circle), also known as the leaf spring or zero-length spring, is used to balance the weight of the pendulum without contributing extra restoring force [109]. The mechanics has the resonance frequency around 6 Hz and is coupled with an interferometric readout.

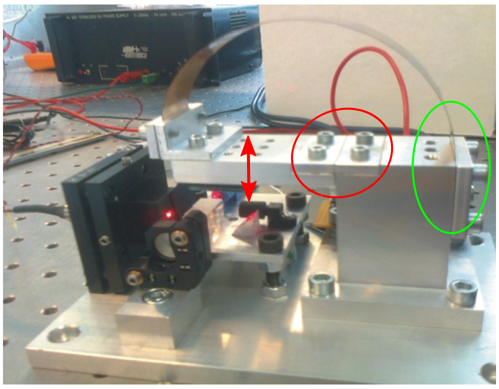

(a)

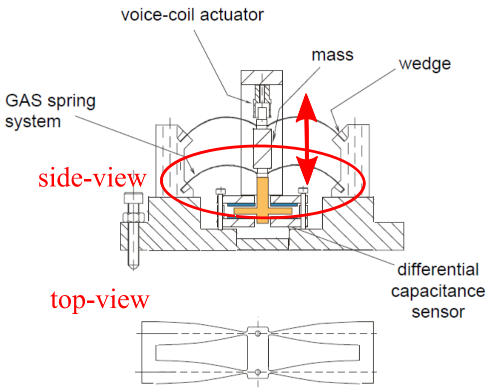

(b)

Figure 4.3: Examples of sensors using clamped-plate hinges in the mechanics: (a) A leaf spring pendulum [110], (b) Geometric anti-springs (GAS) [111]. Red circles mark the hinges and green circle marks the leaf spring of the pendulum. Double arrows indicate the direction of the motion.

Figure 4.3b presents the mechanics of an accelerometer based on the Geometric Anti-Springs (GAS) mechanism [111]. The GAS mechanism has been developed for the active seismic isolation of the Virgo detector [112], and its working principle is based on the negative-stiffness-mechanism [113]. Here, the size of GAS is reduced for the accelerometer mechanics. The bent blades (one pair of them is marked in red circle) have the stiffnesses in the vertical and horizontal directions. The stiffness of the blade was investigated by Cella *et al.* [114]. The blades are applied with static horizontal loads. When the proof-mass moves away its equilibrium, the component of the horizontal loads on the vertical direction compensates the vertical restoring force. Consequently, the resonance frequency of the mechanics is reduced. The mechanics has the estimated resonance frequency about 1 Hz and is coupled with a capacitive readout.

4.1.2 Cross-spring hinge

The cross-spring hinge, also known as the cross-spring pivot, is an alternative to the clamped-plate hinge for rotation. It can either be assembled by individual clamped-plate hinges or made from a monolithic material.

Figure 4.4 presents the configuration of an assembled symmetric cross-spring hinge from different views. The two strips cross each other at the middle with a crossing angle, $\alpha = 90°$. A Cartesian coordinate system is oriented on the crossing point. The hinge is symmetric about the x-axis. The designed motion is a rotation about the z-axis. Wittrick [115] reported that the axial load (along x-axial) affects the rotational stiffness of a cross-spring hinge. One estimation of the rotational stiffness with axial load (with the rotational motion is less than $15°$), was given by [116]

$$k_{\theta z} = \frac{2Ewt^3}{3l}(3c^2 - 3c + 1) + \left[\frac{2(9c^2 - 9c + 1)}{15\cos(\frac{\alpha}{2})} + c\cos(\frac{\alpha}{2})\right] P_x l \tag{4.5}$$

where E is the Young's modulus of the material, P_{x} is the axial load along x-axis, w is the widths of the strip, l is effective length of the strip, t is the thickness of the strip and α is the crossing angle of two strips. $c = 1/2$ is geometric parameter indicating the crossing position of the plates at the midpoint, which is the common configuration. In the case that the hinge is free from axial load $P_{\mathrm{x}} = 0$, equation (4.5) can be simplified to

$$k_{\theta z} = \frac{2EI_z}{l} \tag{4.6}$$

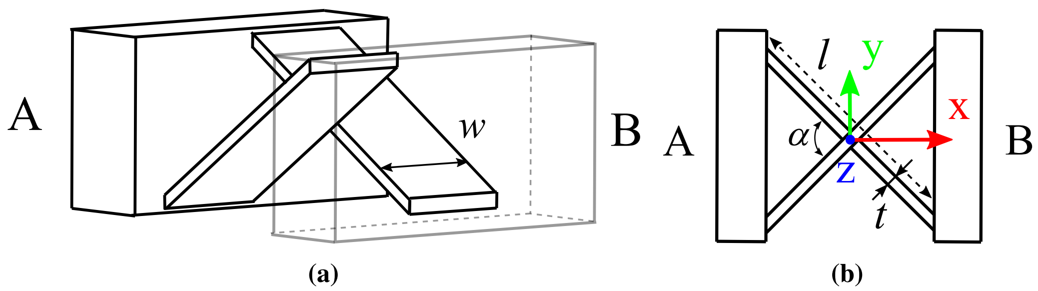

Figure 4.4: The sketch of a cross-spring hinge: (a) Perspective view of the hinge, (b) Side view of the hinge. w: the widths of the strip, l: effective length of the strip, t: the thickness of the strip, α: the crossing angle of two strips.

where $I_z = wt^3/12$ is the area moment of inertia. Compared with equation (4.1), the stiffness $k_{\theta z}$ is the sum of rotational stiffness of two individual clamped-plate hinges. Eventually, the deflection of a cross-spring hinge is the common deflections of the two clamped-plate hinges about the z-axis, and the undesired deflections of an individual clamped-plate are limited.

A cross-spring hinge can be made from a monolithic material. The strips intersects each other at the crossing position. This type of hinge is specifically called a cartwheel hinge. The stiffness of the hinge in different DOFs was presented by Kang and Gweon [117]. Pei *et al.* [118] presented the modelling of the general cartwheel hinge to analyse their kinematic motion.

Mechanics with cross-spring hinge

Figure 4.5 presents two examples of mechanics using cross-spring hinges. They are parts of commercial STS1 seismometers, which were produced in the 1970s. In the field of seismology, one STS1-V and two STS1-H seismometers are used as a group in order to measure vertical motion, east-west, and north-south horizontal motions. In recent years, these seismometers have been gradually replaced by seismometers with the compact structure (for example the symmetric triaxial seismometer [119]) and the improved readout.

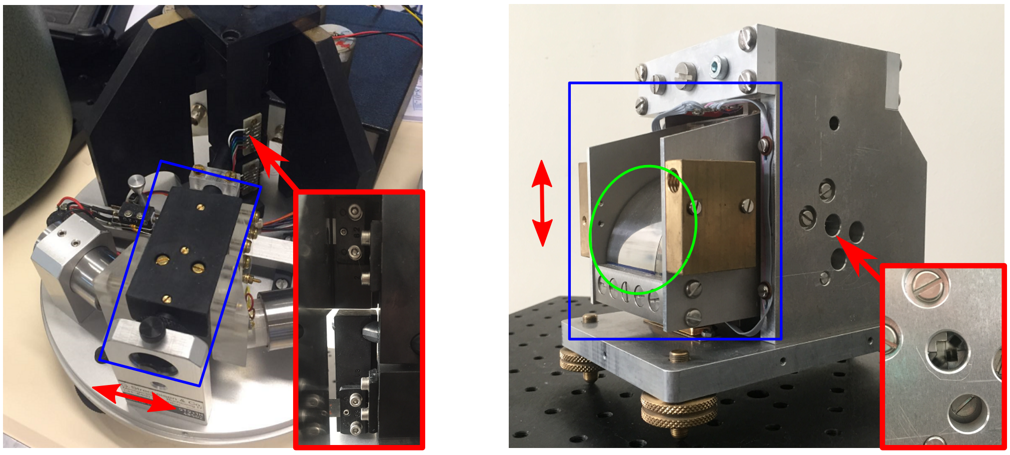

(a) **(b)**

Figure 4.5: Examples of sensors using cross-spring hinge: (a) The mechanics of a STS1-H seismometer, (b) the mechanics of STS1-V seismometer. Blue rectangles mark the pendulum of the structure, red rectangles give zoom-in views of the hinges and green circle marks the additional leaf-spring. Double arrows indicate the direction of the pendulum motion.

Figure 4.5a shows the mechanics of an STS1-H, which is developed from the Lehman pendulum (or garden-gate pendulum) [120]. Its pendulum (in blue rectangle) oscillates horizontally. The zoom-in figure in the red rectangle shows the one pair of cross-spring hinges. The resonance frequency of the system is around 0.25 Hz.

Figure 4.5b presents the mechanics of an STS1-V. The structure is leaf spring pendulum which is developed from the LaCoste pendulum [57]. Its pendulum (in blue rectangle) oscillates vertically. The yellow components on the pendulum are used to tune the inertia of the pendulum. The leaf-spring clamped onto the end of the pendulum is shown in the green circle. The other end of the leaf spring is clamped onto the frame. Different from the mechanics in Figure 4.3a, the applied joint is a cross-spring hinge, which is shown in the zoom-in figure in the red rectangle. The use of the hinge helps to support a heavy mass (600 g) without unwanted deflections. Consequently, its resonance frequency is 0.25 Hz, and the parasitic frequency is 70 Hz. Zumberge and Otero [73, 92] presented a modified prototype, which has a resonance frequency of 0.02 Hz and a parasitic frequency of 4 Hz.

4.1.3 Notch hinge

The notch hinges are made from monolithic materials. Therefore, it avoids problems come from assembling such as the internal deformation or misalignment. Figure 4.6 presents a symmetrical-circular notch hinge. Side A is assumed the fixed end, and side B is the free end. A Cartesian coordinate system is oriented on the geometric centre of the hinge, the designed deflection is the bending about the z-axis.

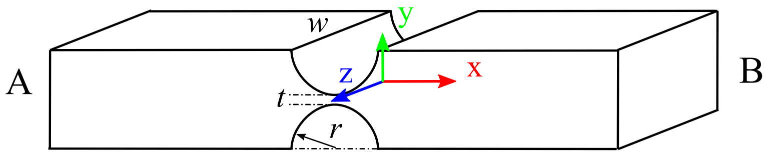

Figure 4.6: The sketch of a symmetric circular notch hinge: r: The radius of the notch, t: the thickness of minimal distance between the notches, w the width.

The notches shown in the figure are half-circle symmetrically aligned. The estimation of its bending stiffness depends highly on the ratio between t/r. Young *et al.* [121] presented several empirical formulations and report that the most accurate empirical formulation in the range of $0.05 \leqslant t/r \leqslant 0.65$ (with errors less than 2.5 %) is given by [122]

$$k_{\theta z} = \frac{Ewt^2}{12}\Big(-0.0029 + 1.3556\sqrt{\frac{t}{2r}} - 0.5227\big(\sqrt{\frac{t}{2r}}\big)^2\Big) \tag{4.7}$$

For different requirements, the notches of a hinge can be in different shapes, for example the rectangular, elliptical or polynomial profile. Moreover, they can be symmetric or non-symmetric for different usage. Notch hinges can be produced as individual units, but more commonly, the mechanics and notch hinges are fabricated together as a monolithic structure.

Mechanics with notch hinge

Figure 4.7 presents two monolithic mechanics used in horizontal inertial sensors. Figure 4.7a shows a structure of a double parallelogram mechanics (in red rectangular) connected to an external arm [69]. The readout of the sensor is a linear encoder and mounted on the synchronization lever (pointed by green arrow). Concerning the double parallelogram mechanics (in red rectangular), the primary stage (marked by dash red lines) moves horizontally with the vertical parasitic motion. The secondary stage (marked by dash green lines) is an improvement to limit the parasitic motion [123]. Its resonance frequency is around 7 Hz. Moreover, an interesting mechanics based on a parallelogram flexure structure has been developed by Hines *et al.* [124]. The structure made of fused silica and has a resonance frequency of 3.76 Hz.

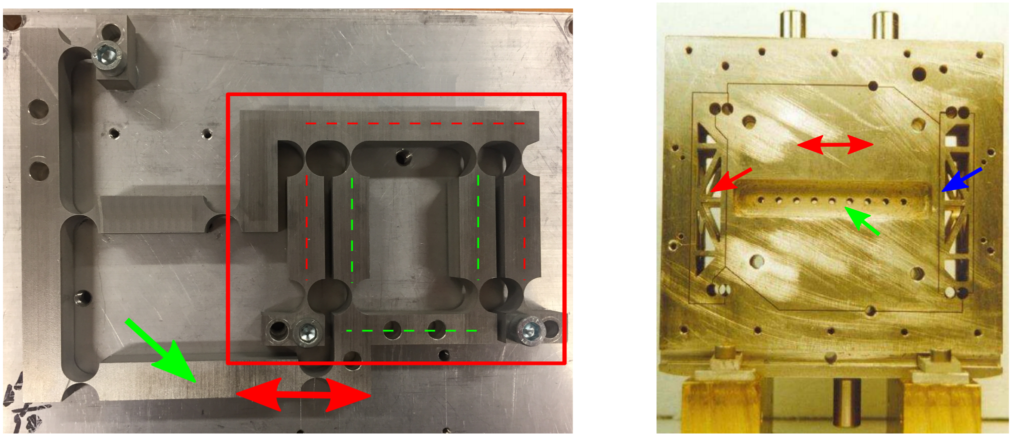

(a) **(b)**

Figure 4.7: Examples of sensors using notch hinges: (a) Parallelogram mechanics [69]: the green arrow points the synchronization lever, dash red lines marks the primary stage, dash green lines mark the secondary stage; (b) Folded pendulums structure [125]: red arrow points the inverse pendulum, green arrow points the proof-mass and blue arrow points the pendulum. Double arrows indicate the direction of the motion.

Figure 4.7b presents a Watt's linkage which is also called a folded pendulum structure [126]. Because the structure is compact and tunable, it is a good candidate to be used as a mechanics [43, 45, 127]. The structure has three parts; its proof-mass (marked by green arrow) is supported by a pendulum (marked by blue arrow) and an inverse pendulum (marked by red arrow). The proof-mass has a groove in the middle to mount an extra mass. By tuning the position of the extra mass, the inertia of the moving part can be tuned. The resonance frequency is [43]

$$f_0 = \frac{1}{2\pi}\sqrt{\frac{g}{(m_1+m_2)}\left(\frac{m_1}{L_1}-\frac{m_2}{L_2}\right)+k_0} \tag{4.8}$$

where, the pendulum has the equivalent mass m_1 at the free end and its length is L_1, and the inverse pendulum has the equivalent mass m_2 at the free end and its length is L_2. k_0 represents the effect of cumulative stiffness of the flexure joints [43]. By tuning m_2, the force from the inverse pendulum compensates the restoring force of the pendulum, thus the folded pendulum can reach very low resonance frequency. Typically, it reaches 0.5 Hz, and its parasitic frequency is higher than 1000 Hz. The lowest resonance frequency of 0.06 Hz was reported by Barone and Giordano [45].

Moreover, the mechanics of the Microelectromechanical systems (MEMS) inertial sensor can be fabricated from monolithic materials including silicon wafers. A MEMS inertial sensor designed to measure horizontal motion was introduced by Li *et al.* [128] and has a natural frequency of 15.2 Hz and a parasitic frequency of 92 Hz. The negative-stiffness technology can be used in the MEMS inertial sensors as well. Middlemiss *et al.* [129] presented a MEMS inertial sensor that employed the negative-stiffness technology. Its natural frequency is 20 Hz for horizontal measurements. Due to the effect of negative-stiffness, its natural frequency is 2.3 Hz for vertical measurements. The parasitic frequency of the structure is 10.2 Hz. The MEMS inertial sensor introduced by Boom *et al.* [130] has the mechanism to adjust the effect of negative-stiffness, its natural frequency can be adjusted from 102 Hz to 28.1 Hz in several steps.

4.1.4 Spiral flexure

Typical springs such as helical springs have non-linearity problems which are created by the material, axial or torsional deformation [131]. More than that, a helical spring does not have any guide. Alternatively, a spiral flexure can be used, which has high radial stiffness and low axial stiffness by spiral slots.

Figure 4.8 presents the spiral flexure used in an L4C geophone. The spiral flexure suspends the moving coil of the geophone, and this same spring is mounted on the bottom to support the coils [132]. The proof-mass oscillates vertically and has a resonance frequency of about 1 Hz [133]. A team at the University of Birmingham developed interferometric inertial sensors with the mechanics constructed of L4C geophones [134].

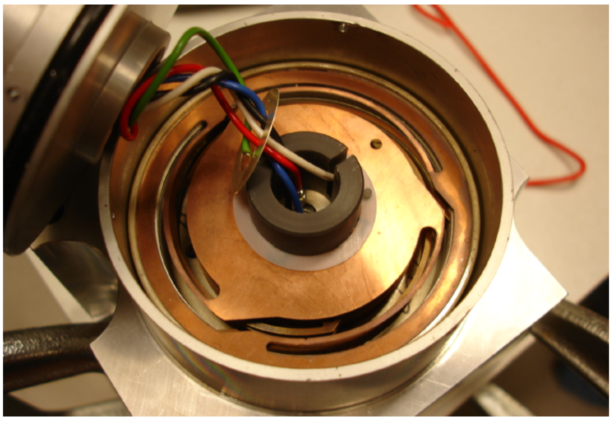

Figure 4.8: A photograph of the spiral flexure used in a L4C geophone. [135]

The estimation of axial stiffness depends on its material, geometry and the profile of the slots. Multiple spiral flexures can be used in series by the coaxial alignment, which reduces stiffness fluctuations in radial directions and rejects spurious resonances in the high frequency band. Chen *et al.* [136] reported a comparison between a thick spiral flexure and a stack of thin spiral flexures, their total thickness is the same, but the cumulative stiffness of the stacked one is far lower than the stiffness of the single one.

4.1.5 Comparison

Table 4.1 presents detailed information about the mentioned mechanics. Figure 4.9 shows a comparison of some mechanics by their resonance frequency against their dimension, and it shows that bigger mechanics can be easier to achieve lower resonance. Besides the dimension, the stiffness of the hinge and the mechanism of the mechanics are important to further decrease the resonance. In this thesis, the mechanics are developed from the Lehman pendulum and the leaf spring pendulum. The cross-spring hinges are used as joints because they are more reliable than the clamped-plate hinges, and easier to produce than the notch hinge. Additionally, with minor modifications to the frames, the strips can be produced using alternative materials. This gives access to the study of the thermomechanical noise [137] of the inertial sensor with respect to the material of the hinge. Moreover, there are other mechanisms can be used as the joint, for example, a Rolamite joint for translation [138]. However, its structure is more complex than the structures of the discussed joints, but it can be regarded as a candidate for the development in future.

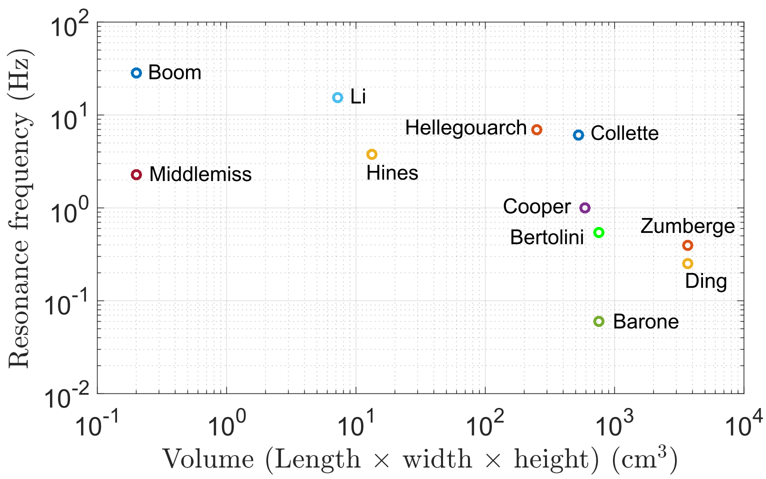

Figure 4.9: Comparison of the resonance frequencies for different dimensions.

Thanks go to dr. Michel Van Camp from the Royal Observatory of Belgium, dr. Thomas Forbriger and ir. Edgar Wetzig from the Federal Institute for Geosciences and Natural Resources of Germany, from whom we borrowed STS-1 seismometers no longer used in the service of the seismic monitoring. The mechanics used in this thesis have been developed from these seismometers.

Table 4.1: List of mechanics using the hinges.

Ref.	Hinge			Mechanics						Readout
	Type	Material	t (µm)	Type	Direction	m (g)	Size[b] (cm)	f_0 (Hz)	f_P (Hz)	Type
/	Clamped-plate	Cu-Be	50	Simple pendulum	H[a]	60	10×3×14	7	/	Interferometric readout
Collette [110]		Cu-Be	90	leaf spring pendulum	V	55	15×7×5	6	>100	Interferometric readout
Bertolini [111]		Cu-Be	100	GAS	V	36	scalable	1	>300	Capacitive readout
Hellegouarch [69]	Notched	Aluminium	50	Parallelogram	H	/	18×14×1	7	>300	Optical encoder
Hines [124]		Fused silica	83	Parallelogram	H	2.2	9.2×4.8×0.3	3.76	/	Interferometric readout
Bertolini [43]		Aluminium	50	Folded pendulum	H	830	14×4×13.4	0.54	>1000	Capacitive readout
Acernese [127]		Aluminium	100	Folded pendulum	H	1000	/	0.5	>1000	Interferometric readout
Barone [45]		Aluminium	100	Folded pendulum	H	/	14×4×13.4	0.06	>1000	Inductive readout
Li [128]		Silicon	500	MEMS	H	0.31	4.45×3.22×0.5	15.2	92	Capacitive readout
Middlemiss [129]		Silicon	200	MEMS	H & V	/	1×1×0.2	2.3[c]	10.2	Optical shadow readout
Boom [130]		Silicon	50	MEMS	H & V	0.033	2×2×0.05	28.1	/	Capacitive readout
Zumberge [73, 92]	Cross-spring	steel	51	leaf spring pendulum	V	350	18×12×17	0.4	4	Interferometric readout
Ding [139]		steel	/	leaf spring pendulum	V	600	18×12×17	0.25	70	Interferometric readout
Cooper [134]	Spiral flexure	/	/	/	V	1000	13×7.6	1	>1000	interferometric readout

t: Thickness of the hinge; m: Proof-mass of the mechanics; f_0: Resonance frequency; f_P: Parasitic frequency;
/: unknown;
[a] V: Vertical, H: Horizontal;
[b] The size of overall frame: Length×Width×Height or Height×Diameter,
[c] Resonance frequency for vertical measurement: 2.3 Hz, Resonance frequency for horizontal measurement: 20 Hz.

4.2 HINS mechanics

Because the volume of a STS1-H is too large, a modified mechanics has been developed. Figure 4.10a shows the prototype of the Horizontal Interferometric Inertial Sensor (HINS). The dimensions of the mechanics are about 200×140×150 mm^3. One pair of home-made cross-spring hinges (see Figure 4.11) defines the rotation axis of the horizontal pendulum. A corner cube (3) is mounted at the end of the pendulum, and is coupled with the interferometric readout (1). A voice coil actuator (4, LVCM-022-013) is mounted on the pendulum, and it either damps the pendulum with a resistive shunt or is used in a feedback loop. The three screws on the base of the mechanics can be used to adjust the tilting angle between the support and the ground.

Figure 4.10b shows the Computer Aided Design (CAD) model of the prototype. Some components are transparently treated to display the optical path and the pendulum. The laser beam passes through from the collimator (1), and continues to PBS2 (2). The reference beam goes to the fixed corner cube (3), and the measurement beam to the movable corner cube (4). Consequently, the motion of the pendulum can be measured by the interferometric readout.

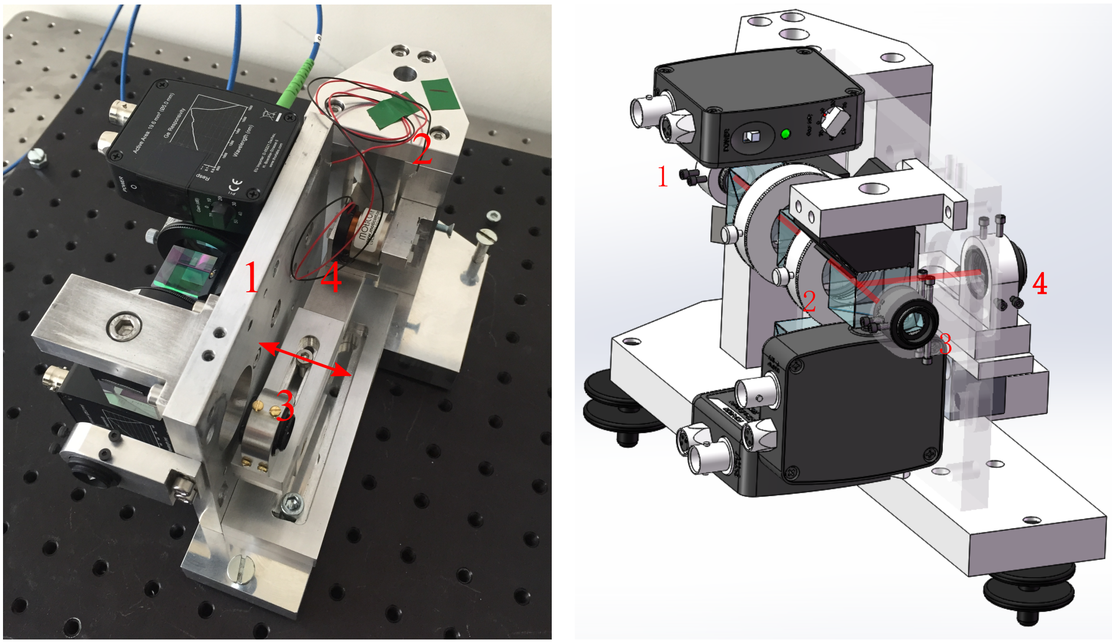

(a) **(b)**

Figure 4.10: Prototype of the HINS and its optical path to corner cubes: (a) Prototype of the HINS: 1: interferometric readout, 2: mechanics, 3: pendulum with corner cube, 4: voice coil actuator; (b) Optical path in the HINS: 1: the laser collimator, 2: PBS2, 3: fixed CC, 4: movable CC mounted on the pendulum. The red lines show the optical path from the laser collimator to PBS2, and from PBS2 to the fixed CC and movable CC. Double arrow indicates the direction of the pendulum motion.

Figure 4.11a shows one cross-spring hinges. It is assembled by two hinge supports (1), four spring-holders (2) and two strips (in 300 series stainless steel) (3). The length of one strip is around 50 mm, and the hinge supports and strip-holders clamp it. The effective length after clamping is 5 mm. Its width and thickness are 12.5 mm and 0.038 mm. The two hinge supports are the same, but they have a 2 mm height shift after assembling.

Figure 4.11b presents one pair of hinges which are vertically mounted with the mechanics. The hinge supports (A1&B1) of the two crossed-spring hinges are fixed on the stable frame (1) and the base (3) of the mechanics. The supports (A2&B2) are fixed with the pendulum (2). The dash-dot line indicates the rotation axis of the pendulum.

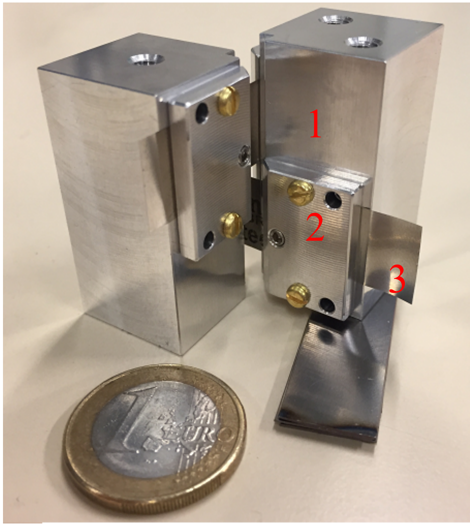

(a)

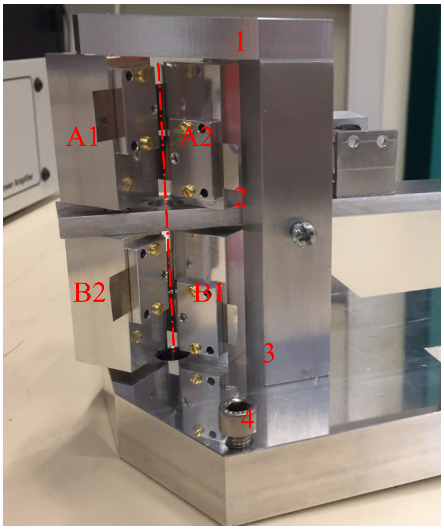

(b)

Figure 4.11: Joints of the HINS: (a) One pair of hinge used in the HINS: 1: hinge support, 2: strip-holder, 3: stainless steel strip; (b) Two hinges assembled in a the HINS: 1: support, 2: pendulum, 3: base, 4: screws, A1&A2 and B1&B2: two pairs of hinge supports. Dash-dot red line: rotational axis of the pendulum.

4.2.1 Modelling

A simple method to estimate the resonance frequency of the garden-gate pendulum without the joint stiffness was discussed by Wielandt [140]. A model with the stiffness of the hinge is presented hereafter to better discuss the resonance frequency of the pendulum.

Figure 4.12a presents the model of the mechanics. Ψ is a reference plane referring to the ground, which is perpendicular to gravity. O refers to the rotational centre of the pendulum and is the origin of a Cartesian coordinate system. X-axis is defined the direction of the initial position of the pendulum (dash line); Z-axis defines the opposite direction of gravity. When the pendulum rotates around point O, the rotation is in the Ω plane. The rotation range of the pendulum in practice is within $\pm 1°$. Due to the cross-spring hinges, it is assumed that the proof-mass m only oscillates within the Ω plane. ω denotes the rotation of the pendulum with a damping coefficient c and stiffness k. The length between the corner cube and the rotational centre is L_c and the length between the mass centre and the rotational centre is L.

The gravitational force $G = [0,\ 0,\ -mg]^\top$ is applied at the centre of the mass.

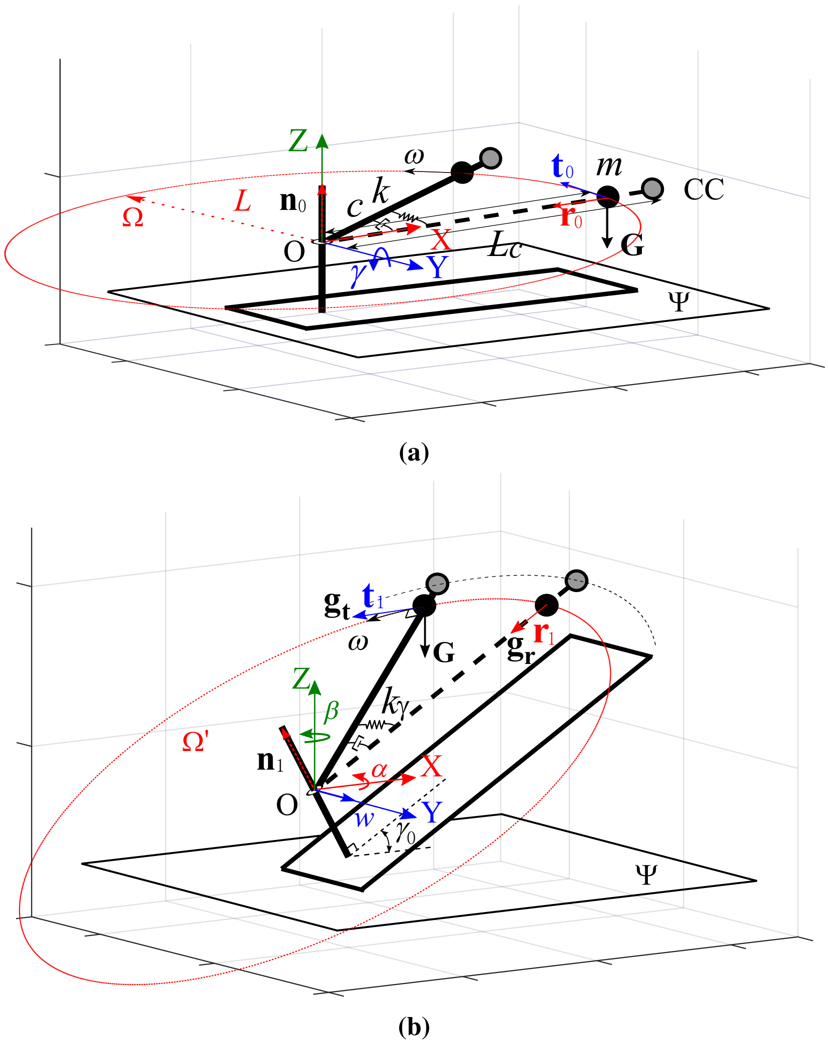

Figure 4.12: The model of the Lehman pendulum: (a) The model without tilting, the proof-mass rotates in the Ω plane; (b) The model with the tilting γ_0 about Y-axis, the proof-mass rotates in the $\boldsymbol{\Omega}\mathbf{n}'$ plane. The joint O presents the cross-spring hinge allowing oscillations. Black dots present the mass centre of the pendulum, and grey dots present the mounting of the corner cube. The dashed line denotes the initial position of the pendulum. The translation w along Y-axis as well as rotational motions $\boldsymbol{\alpha}$, $\boldsymbol{\gamma}$ and $\boldsymbol{\beta}$ about X-axis, Y-axis and Z-axis of the frame can be defined on the point O.

The unit vector $\mathbf{n_0}$ presents the normal direction of the Ω plane. At the initial position shown in Figure 4.12a, vectors $\mathbf{r_0}$ and $\mathbf{t_0}$ respectively present the radial and tangent directions of motion of the proof-mass. They are

$$\mathbf{n_0} = [0,\ 0,\ 1]^\top \tag{4.9}$$

$$\mathbf{r_0} = [-1,\ 0,\ 0]^\top \tag{4.10}$$

$$\mathbf{t_0} = [0,\ -1,\ 0]^\top \tag{4.11}$$

where the vectors $\mathbf{n_0}$, $\mathbf{r_0}$ and $\mathbf{t_0}$ are defined in the Cartesian coordinate system (XYZ).

When the mechanics is not tilted, the restoring force of the joint pushes the pendulum back to the equilibrium with the stiffness k. It is possible to compensate the restoring force by the gravitational force as the mechanics tilted with angle γ_0. The tilting direction is inverse to the typical tilting direction of a Lehman pendulum, thus it provides a negative-stiffness effect. Therefore, the tilt angle γ_0 can be used to adjust the compensation of the restoring force and thus to tune the resonance frequency.

Figure 4.12b presents the whole mechanics tilted about Y-axis with an angle γ_0. The Ω' plane (marked with red circle) presents the rotation plane of the proof-mass after tilting. Rotation matrices are used in the derivation, and they are given by [141]

$$R_x(\alpha) = \begin{bmatrix} 1 & 0 & 0 \\ 0 & \cos(\alpha) & \sin(\alpha) \\ 0 & -\sin(\alpha) & \cos(\alpha) \end{bmatrix} \quad R_y(\gamma) = \begin{bmatrix} \cos(\gamma) & 0 & -\sin(\gamma) \\ 0 & 1 & 0 \\ \sin(\gamma) & 0 & \cos(\gamma) \end{bmatrix} \quad R_z(\beta) = \begin{bmatrix} \cos(\beta) & \sin(\beta) & 0 \\ -\sin(\beta) & \cos(\beta) & 0 \\ 0 & 0 & 1 \end{bmatrix} \tag{4.12}$$

where $R_x(\alpha)$, $R_y(\gamma)$ and $R_z(\beta)$ are the rotation matrices of the proof-mass rotating about the point O. For space-fixed rotations, the normal vector $\mathbf{n_0}$ after tilting is

$$\mathbf{n_1} = R_y(\gamma_0) \cdot \mathbf{n_0} = \big[-\sin(\gamma_0),\ 0,\ \cos(\gamma_0) \big]^\top \tag{4.13}$$

The radial vector $\mathbf{r_0}$ after tilting is

$$\mathbf{r_1} = R_y(\gamma_0) \cdot \mathbf{r_0} = \big[-\cos(\gamma_0),\ 0,\ -\sin(\gamma_0) \big]^\top \tag{4.14}$$

The gravitational force of the proof-mass $\mathbf{G} = (0,\ 0,\ -mg)^\top$ has a projection on the vector $\mathbf{r_1}$ and it is

$$\begin{aligned} \mathbf{g_r} &= \mathbf{proj}_{\mathbf{r_1}}\mathbf{G} = \frac{\mathbf{r_1} \cdot \mathbf{G}}{||\mathbf{r_1}||^2} \cdot \mathbf{r_1} \\ &= -mg\sin(\gamma_0) \cdot \big[\cos(\gamma_0),\ 0,\ \sin(\gamma_0) \big]^\top \end{aligned} \tag{4.15}$$

where, the vector $\mathbf{g_r}$ is the projection. $\mathbf{proj}_{\mathbf{r_1}}\mathbf{G}$ indicates the operation of projecting the vector $\mathbf{G}$ onto the vector $\mathbf{r_1}$, and $||\mathbf{r_1}||$ is the magnitude of the vector. The vector $\mathbf{g_r}$ points the rotation point in the Ω' plane, and its magnitude g_r is

$$g_\mathrm{r} = ||\mathbf{g_r}|| = mg\sin(\gamma_0) \tag{4.16}$$

As discussed in Section 4.1.2, g_r is the axial load applied on the joint. According to equation (4.5), the rotational stiffness of the joint can be estimated, and it is denoted by k_γ. The variation of the stiffness k_γ during oscillation is not addressed in the following discussion.

When the mechanics is tilted, the motion of the proof-mass causes the variation of potential energy. Therefore, the contribution of the gravitational force is taken into account. The tangent vector is used to find the component of the gravitational force in the Ω' plane. For space-fixed rotations, the tangent vector containing tilting angle γ_0 and rotation ω is

$$\mathbf{t_1} = R_y(\gamma_0)R_z(\omega) \cdot \mathbf{t_0} = -\left[\sin(\omega)\cos(\gamma_0),\ \cos(\omega),\ \sin(\omega)\sin(\gamma_0)\right]^\top \tag{4.17}$$

The projection of the vector $\mathbf{G}$ on the vector $\mathbf{t_1}$ is

$$\begin{aligned}\mathbf{g_t} &= \mathbf{proj}_{\mathbf{t_1}}\mathbf{G} = \frac{\mathbf{t_1}\cdot\mathbf{G}}{\|\mathbf{t_1}\|^2}\cdot\mathbf{t_1} \\ &= -mg\sin(\gamma_0)\sin(\omega)\cdot\left[\sin(\omega)\cos(\gamma_0),\ \cos(\omega),\ \sin(\omega)\sin(\gamma_0)\right]^\top\end{aligned} \tag{4.18}$$

where, $\mathbf{g_t}$ is the component of the gravitational force in the Ω' plane and its magnitude g_t is

$$g_\mathrm{t} = \|\mathbf{g_t}\| = mg\sin(\gamma_0)\sin(\omega) \tag{4.19}$$

Moreover, Figure 4.12b shows that several excitations cause the rotation of the proof-mass about the point O. They are the translational motion w along Y-axis, rotational motion β about Z-axis and rotational motion α about X-axis. As the rotation of the proof-mass can be studied in the Ω' plane, Figure 4.13 shows the motion of the proof-mass under different excitations in the Ω' plane.

Response to translational motion w

Even through the pendulum is tilted about Y-axis, the projection of the translational motion w is the same in the Ω' plane. As shown in Figure 4.13a, the rotation of the proof-mass ω in equation (4.19) equals to the relative motion θ between the frame and the pendulum. Applying Newton's second law of rotation about the hinge O in the Ω' plane (see Figure 4.12b), the sum of torque about the hinge O is given by

$$I\ddot{\theta} = \sum\tau = -\tau_\mathrm{s} - \tau_\mathrm{d} + F_\mathrm{w}L\cos(\theta) + g_\mathrm{t}L \tag{4.20}$$

where I is the moment of inertia with respect to the rotation centre O, $\tau_\mathrm{s} = k_\gamma\theta$ is the rotational spring torque, $\tau_\mathrm{d} = c\dot{\theta}$ is the rotational damping torque, $F_\mathrm{w} = m\ddot{w}$ is the reaction force on the centre of mass and $g_\mathrm{t}L$ is contributed by the gravitational force. Combining equations (4.19) and (4.20) with $\omega = \theta$, its dynamic equation is

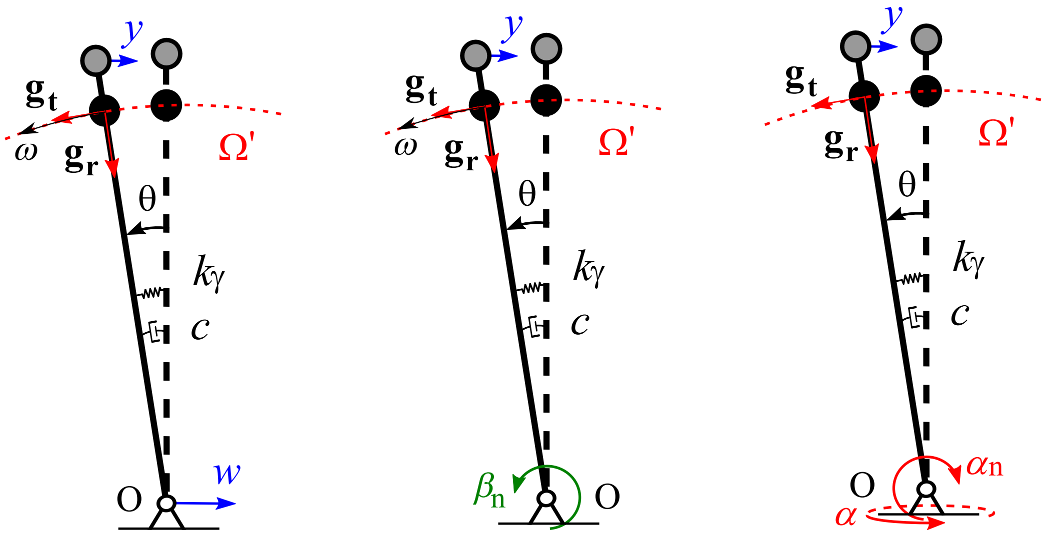

Figure 4.13: Motion of the proof-mass under different excitations: the unmarked geometric parameters are defined in Figure 4.12. θ is the relative rotation between the pendulum and the frame. (a) the proof-mass is excited by w in the Ω' plane; (b) the proof-mass is excited by $\boldsymbol{\beta}$: β_{n} is the projection of $\boldsymbol{\beta}$ in the Ω' plane; (c) the whole mechanics tilting by the angle α. Because the pendulum is tilted, the proof-mass is excited by $\boldsymbol{\alpha}$: α_{n} is the projection of $\boldsymbol{\alpha}$ in the Ω' plane.

$$I\ddot{\theta} = -c\dot{\theta} - k_\gamma \theta + m\ddot{w}L\cos(\theta) + mgL \cdot \sin(\gamma_0)\sin(\theta) \tag{4.21}$$

As the relative angle θ is small in the oscillation regime, the relative motion y of the corner cube along Y-axis is assumed to be linear. The interferometric readout measures this relative motion y with respect to θ by

$$y = -\sin(\theta)L_{\mathrm{c}} = -\theta L_{\mathrm{c}} \tag{4.22}$$

where approximation $\sin(\theta) \approx \theta$ is applied. Substituting equation (4.22) into (4.21), yields

$$I\ddot{y} + c\dot{y} + \left(k_\gamma - mg\sin(\gamma_0)L\right)y = -m\ddot{w}LL_{\mathrm{c}} \tag{4.23}$$

where approximation $\cos(\theta) \approx 1$ is applied. Using Laplace transform, equation (4.23) becomes

$$T_{\mathrm{WY}} = \frac{Y(s)}{W(s)} = \frac{-mLL_{\mathrm{c}}s^2}{Is^2 + cs + \left(k_\gamma - mg\sin(\gamma_0)L\right)} \tag{4.24}$$

where T_{WY} is the transmissibility of the HINS to the translational motion W.

Response to rotational motion β

As shown in Figure 4.13b, the scalar projection of the vector $\boldsymbol{\beta} = [0,\ \beta,\ 0]^\top$ on the $\boldsymbol{\Omega}'$ plane is given by

$$\begin{aligned}\beta_\mathrm{n} &= \|\mathbf{proj}_{\mathbf{n_1}}\boldsymbol{\beta}\| = \|\frac{\mathbf{n_1}\cdot\boldsymbol{\beta}}{\|\mathbf{n_1}\|^2}\cdot\mathbf{n_1}\| \\ &= \beta\cos(\gamma_0)\end{aligned} \tag{4.25}$$

where β_n denotes the counter-clockwise rotation of the frame in the $\boldsymbol{\Omega}'$ plane. Because both of the frame and the proof-mass rotates in the $\boldsymbol{\Omega}'$ plane. The relationship between rotations is

$$\omega = \theta - \beta\cos(\gamma_0) \tag{4.26}$$

where ω is the rotation of the proof-mass and θ is the relative angle between the frame and the proof-mass. Therefore, combining equation (4.26), the magnitude of the vector $\mathbf{g_t}$ is

$$g_\mathrm{t} = \|\mathbf{g_t}\| = mg\sin(\gamma_0)\sin\big(\theta - \beta\cos(\gamma_0)\big) \tag{4.27}$$

Applying Newton's second law of rotation about the hinge O in the $\boldsymbol{\Omega}'$ plane, the sum of torque about the hinge O is given by

$$I\ddot{\theta} = \sum\tau = -\tau_\mathrm{s} - \tau_\mathrm{d} - I\ddot{\beta}_\mathrm{n} + g_\mathrm{t}L \tag{4.28}$$

where $\tau_\mathrm{s} = k_\gamma\theta$ is the torque generated by the rotational spring, $\tau_\mathrm{d} = c\dot{\theta}$ is the rotational damping torque, $I\ddot{\beta}_\mathrm{n}$ is the reaction torque and $g_\mathrm{t}L$ is the contribution of the gravitational force. Combining equations (4.25), (4.27 and (4.28), the dynamic equation of the mechanics under this rotational excitation can be derived by

$$I\ddot{\theta} = -c\dot{\theta} - k_\gamma\theta - I\ddot{\beta}\cos(\gamma_0) + mgL\cdot\sin(\gamma_0)\sin\big(\theta - \beta\cos(\gamma_0)\big) \tag{4.29}$$

Applying approximation $\sin\big(\theta - \beta\cos(\gamma_0)\big) \approx \theta - \beta\cos(\gamma_0)$, and substituting equation (4.22) into (4.29), yields

$$I\ddot{y} + c\dot{y} + \big(k_\gamma - mgL\sin(\gamma_0)\big)y = L_\mathrm{c}\cos(\gamma_0)\big(I\ddot{\beta} + mgL\sin(\gamma_0)\beta\big) \tag{4.30}$$

where approximations $\sin(\theta) \approx \theta$ is applied. Using the Laplace transform, equation (4.30) becomes

$$T_{\mathrm{R}_\beta\mathrm{Y}} = \frac{Y(s)}{R_\beta(s)} = \frac{L_\mathrm{c}\cos(\gamma_0)\big(Is^2 + mgL\sin(\gamma_0)\big)}{Is^2 + cs + \big(k_\gamma - mgL\sin(\gamma_0)\big)} \tag{4.31}$$

where R_β is rotation β in the Laplace domain, $T_{\mathrm{R}_\beta \mathrm{Y}}$ is the transmissibility of the HINS to the rotational motion R_β.

Response to rotational motion α

According to Figure 4.13c, the mechanics is under the excitation of $\boldsymbol{\alpha} = [\alpha,\ 0,\ 0]^\top$ about X-axis. Because the mechanics is tilting, the rotation has a projection in the Ω' plane, and its scale is

$$\begin{aligned} \alpha_{\mathrm{n}} &= \|\mathbf{proj}_{\mathbf{n_1}}\boldsymbol{\alpha}\| = \|\frac{\mathbf{n_1}\cdot\boldsymbol{\alpha}}{\|\mathbf{n_1}\|^2}\cdot\mathbf{n_1}\| \\ &= -\alpha\sin(\gamma_0) \end{aligned} \tag{4.32}$$

where the minus symbol denotes the clockwise rotation of the frame in the Ω' plane. In this case, the ω in equation (4.19) is

$$\omega = \theta + \alpha\sin(\gamma_0) \tag{4.33}$$

Because the mechanics tilts about X-axis, the component of the gravitational force is affected by the tilting. For space-fixed rotations, the tangent vector $\mathbf{t_1}$ containing tilting γ_0, α and rotation ω is

$$\mathbf{t_1} = R_y(\gamma_0)R_z(\alpha)R_z(\omega)\cdot\mathbf{t_0} = -\begin{bmatrix}\sin(\omega)\cos(\gamma_0)+\cos(\omega)\sin(\gamma_0)\sin(\alpha)\\ \cos(\omega)\cos(\gamma_0)\\ \sin(\omega)\sin(\gamma_0)-\cos(\gamma_0)\sin(\alpha)\cos(\omega)\end{bmatrix} \tag{4.34}$$

The vector $\mathbf{G}$ has a projection $\mathbf{g_t}$ on the vector $\mathbf{t_1}$. Combining with equation (4.33), the scalar of the projected vector is

$$g_{\mathrm{t}} = \|\mathbf{g_t}\| = \|\mathbf{proj}_{\mathbf{t_1}}\mathbf{G}\| = mg\big(\sin(\omega)\sin(\gamma_0)-\cos(\gamma_0)\sin(\alpha)\cos(\omega)\big) \tag{4.35}$$

Applying Newton's second law of rotation about the hinge O in the Ω' plane, the sum of torque about the hinge O is given by

$$I\ddot{\theta} = \sum\tau = -\tau_{\mathrm{s}} - \tau_{\mathrm{d}} + I\ddot{\alpha}_{\mathrm{n}} + g_{\mathrm{t}}L \tag{4.36}$$

Combining equations (4.32), (4.33), (4.35) and (4.36), the transfer function between θ and α can be found as

$$\begin{aligned} I\ddot{\theta} &= -c\dot{\theta} - k_\gamma\theta + I\ddot{\alpha}\sin(\gamma_0) \\ &\quad + mgL\cdot\big(\sin(\theta+\alpha\sin(\gamma_0))\sin(\gamma_0)-\cos(\gamma_0)\sin(\alpha)\cos(\theta+\alpha\sin(\gamma_0))\big) \end{aligned} \tag{4.37}$$

Applying approximations $\sin(\theta) \approx \theta, \cos(\theta) \approx 1, \sin(\alpha\sin(\gamma_0)) \approx \alpha\sin(\gamma_0)$ and $\cos(\alpha\sin(\gamma_0)) \approx 1$, equation 4.37 is simplified to

$$\begin{aligned} I\ddot{\theta} &= -c\dot{\theta} - k_\gamma\theta + I\ddot{\alpha}\sin(\gamma_0) \\ &\quad + mgL\cdot\left(\theta\sin(\gamma_0) + \alpha\sin^2(\gamma_0) - \alpha\cos(\gamma_0) + \theta\alpha^2\cos(\gamma_0)\sin(\gamma_0)\right) \end{aligned} \tag{4.38}$$

where the items $\alpha\sin^2(\gamma_0)$ and $\theta\alpha^2\cos(\gamma_0)\sin(\gamma_0)$ are neglected considering the small quantities. Substituting equation (4.22) into (4.38), yields

$$T_{\mathrm{R}_\alpha\mathrm{Y}} = \frac{Y(s)}{R_\alpha(s)} = \frac{-L_\mathrm{c}\sin(\gamma_0)Is^2 + mgLL_\mathrm{c}\cos(\gamma_0)}{Is^2 + cs + \left(k_\gamma - mgL\sin(\gamma_0)\right)} \tag{4.39}$$

where R_α is rotation α in the Laplace domain. $T_{\mathrm{R}_\alpha\mathrm{Y}}$ is the transmissibility of the HINS to the rotational motion R_α.

Figure 4.14 shows the Bode plots of equations (4.24), (4.31) and (4.39). The parameters used are listed in Table 4.2 The transfer function T_{WY} (solid blue curve) shows that the HINS is a perfect estimator for displacement w above the resonance frequency around 0.7 Hz because of the flat transfer function. However, the transfer functions $T_{\mathrm{R}_\beta\mathrm{Y}}$ (dash red curve) and $T_{\mathrm{R}_\alpha\mathrm{Y}}$ (dotted yellow curve) show that the HINS is also the estimator of rotational motions β or α. Concerning the transfer function $T_{\mathrm{R}_\beta\mathrm{Y}}$, the magnitude of the flat transfer function is scaled by the factor of $L_\mathrm{c}\cos(\gamma_0)$ in equation (4.31). Also, the transfer functions $T_{\mathrm{R}_\beta\mathrm{Y}}$ has zeros due to the gravitational force. The type of zeros (real or conjugate complex zeros) depends on the tilting direction, and the position depends on the tilting angle γ_0. Compared the transfer functions T_{WY} and $T_{\mathrm{R}_\beta\mathrm{Y}}$, it shows that depending on the amplitude of the excitations, the measurement of the HINS can be dominated by the relative motion y with respect to the

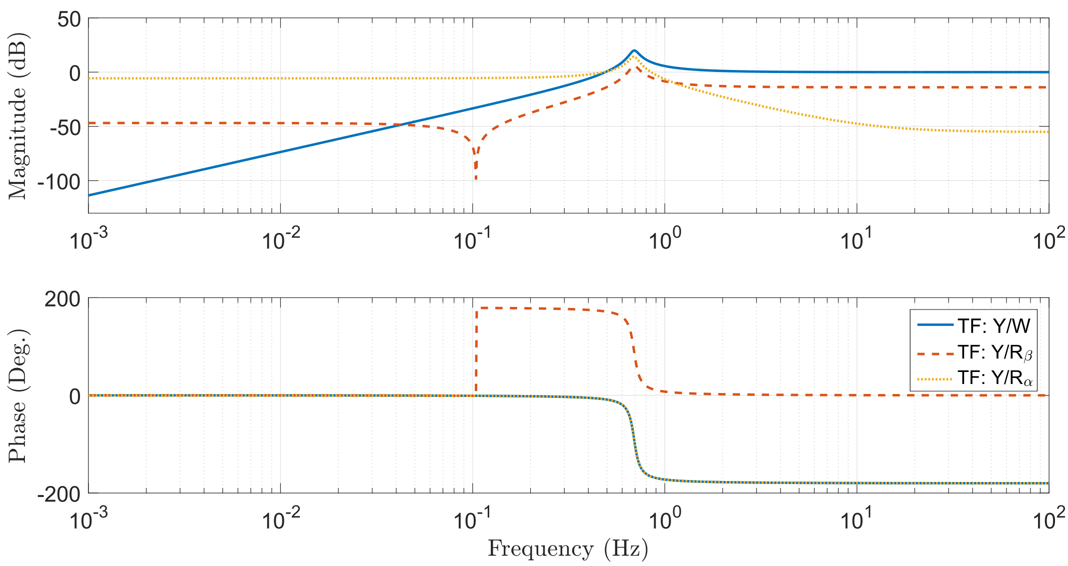

Figure 4.14: Bode plots of the transfer functions of the HINS: solid blue curve: TF between Y and W, dash red curve: TF between Y and R_β, dotted yellow curve: TF between Y and R_α

rotational motion β below 0.04 Hz. The transfer function $T_{\mathrm{R}_\alpha \mathrm{Y}}$ has zeros as well, the type of zeros (real or conjugate complex zeros) depends on the tilting direction, and the position depends on the tilting angle γ_0. It shows that the HINS tends to act as a tilt-meter at low frequency below 0.7 Hz. Therefore, care has to be given when interpreting the response of the HINS at low frequency which actually combines the response to both tilting and translational excitations.

Table 4.2: Assumed parameters in Bode plots of HINS (Figure 4.14) and VINS (Figure 4.25).

Parameters	HINS and VINS		Units
	Symbol	Value	
Tilting angle	γ_0	0.5	[°]
Proof-mass	m	0.3	[kg]
Pendulum length	L	0.16	[m]
Frame length	L_{c}	0.16	[m]
Inertia of the pendulum	$I = mL^2$	0.0077	[kgm^2]
Resonance frequency	f_0	0.7	[Hz]
Stiffness	$k_\gamma(k)^{(a)} = I(2\pi f_0)^2$	0.1486	[Nm/rad]
Damping coefficient	c	0.0034	[Nms/rad]

(a) k_γ for HINS, k for VINS.

Adjustment of resonance frequency

According to the dynamic equations of the mechanics, when the damping is small, the resonance frequency f_0 can be simplified to

$$f_0 = \frac{1}{2\pi}\sqrt{\frac{k_\gamma - mg\sin(\gamma_0)L}{I}} \tag{4.40}$$

where k_γ is the stiffness of the joint under the axial load when the mechanics is tilted, it can be estimated by equation (4.5) and the parameters are listed in Table 4.2. Equation (4.40) indicates that the resonance frequency of the mechanics is tunable by adjusting the inertial moment of the pendulum and the tilting angle. Figure 4.15 indicates the resonance frequency with respect to the tilting angle. The inertial moment is simplified to $I = mL^2$ in equation (4.40). Table 4.3 lists the main parameters to model the mechanics. The geometries of the strips in the hinge are listed to estimate the rotational stiffness of the hinge.

When $\gamma_0 = 0$, the mechanics is horizontal positioned and its rotational stiffness provides restoring force for oscillations. The resonance frequency equals to 0.3 Hz in this case. When $\gamma_0 < 0$, the mechanics is tilted towards to the ground, and the resonance frequency increases because of the restoring force of gravity. When $\gamma_0 > 0$, the mechanics is oppositely

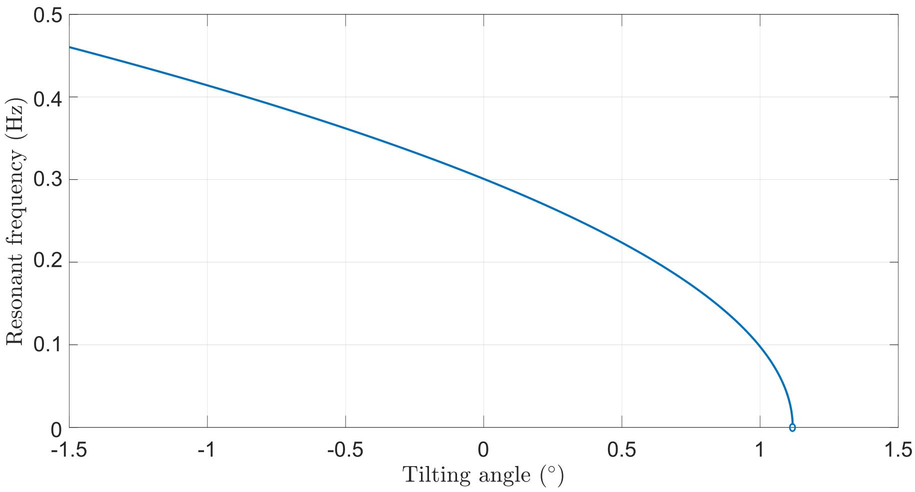

Figure 4.15: The effect of tilting angle to the resonance frequency of the structure.

tilted, as suggested by the configuration in Figure 4.12b, the effect of gravity cancels out a part of the restoring force, thus resonance frequency is decreased. When $\gamma_0 > \arcsin(\frac{k_\gamma}{mgL})$, the mechanics starts to become unstable. Therefore, choosing the tilting angle of the mechanics is a trade-off between the resonance frequency and the stability.

Figure (4.16) presents the structures for these adjustments. The proof-mass (3) at the bottom side of the pendulum (1) can move along the pendulum to adjust the mass centre and the inertial moment, it also has two cylinder screws (4) to balance the mechanics on left and right. Once the pendulum is aligned, the three screws below the frame can be used to adjust the tilting angle between the frame and the ground.

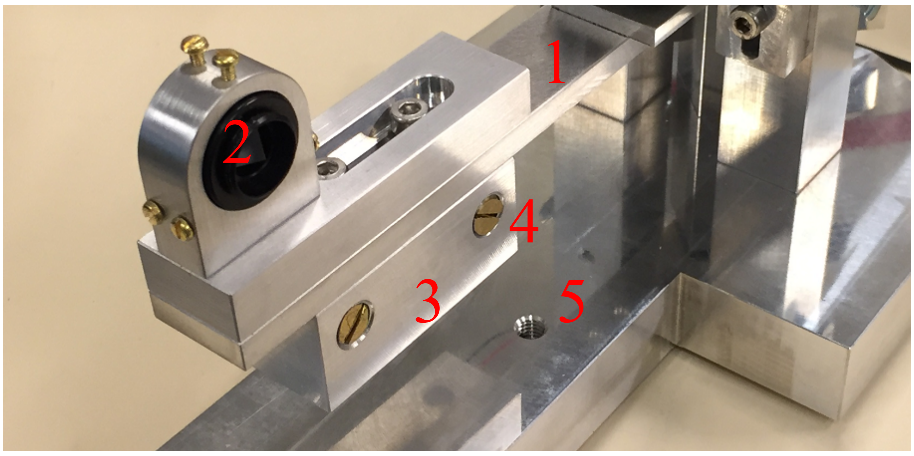

Figure 4.16: Components for adjusting the resonance frequency: 1: pendulum, 2: corner cube, 3: proof mass, 4: two brass screws, 5: base.

Table 4.3: Main parameters of the mechanics model.

Parameters	Symbol	Value	Unit
Young's modulus	E	200e9	[Pa]
Strip length	l	5e-3	[m]
Strip width	w	1.25e-2	[m]
Strip thickness	t	3.8e-5	[m]
Mass	m	0.3	[kg]
Pendulum length	L	0.16	[m]

4.2.2 Experimental characterisation

Once a HINS is assembled, it is tested inside a vacuum chamber as the setup shown in Figure 4.17. The pressure inside the chamber is 4 mbar during the tests.

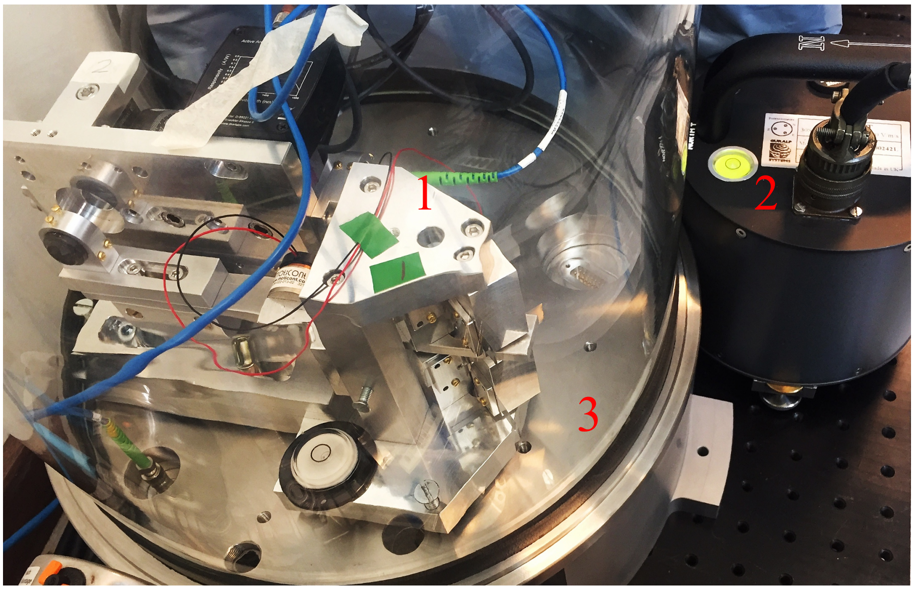

Figure 4.17: The setup to test the HINS: 1: HINS, 2: Güralp 6T seismometer, 3: The vacuum chamber.

The Quality Factor (Q factor) describes how much of energy of the oscillator is lost due to friction in one cycle of oscillation [142]. The relationship between the Q factor and the damping ratio ζ of the oscillator is

$$\zeta = \frac{1}{2Q} \tag{4.41}$$

In order to identify the Q factor and the resonance frequency of the mechanics, the ring-down experiment is performed. The pendulum of the HINS is excited by an impulse from the outside of the chamber. The signal of the HINS is recorded by the data acquisition system, NI PXIe-4497, and is shown in Figure 4.18.

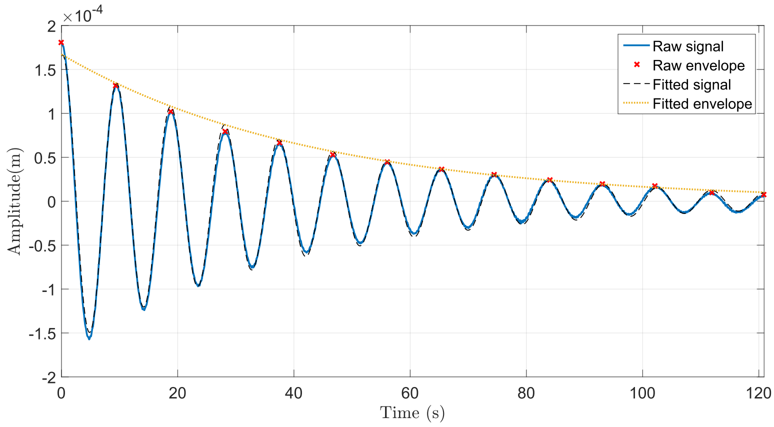

Figure 4.18: Signal of the HINS from the ring-down experiment.

The blue curve in Figure 4.18 shows the raw data from the ring-down experiment. The curve can be fitted by the general solution of a simple linear homogeneous differential equation of order 2, which is

$$y(t) = Ae^{-2\zeta\omega_0 t}\cos(\sqrt{1-4\zeta^2}\omega_0 t + \phi) \tag{4.42}$$

where $y(t)$ is the oscillation of the pendulum, A and ϕ are constants to express the gain and the phase offset. $\omega_0 = 2\pi f_0$ and f_0 is the resonance frequency. The dashed black curve in the figure is fitted signal with respect to equation (4.42) The item $Ae^{-2\zeta\omega_0 t}$ is the envelope of the fitted signal, which is the dotted yellow curve in the figure. Consequently, the Q factor $Q \simeq 14.51$ and resonance frequency $f_0 \simeq 0.11$ can be estimated from the ring-down experiment.

Moreover, the performance of the HINS is preliminarily assessed by comparing with a

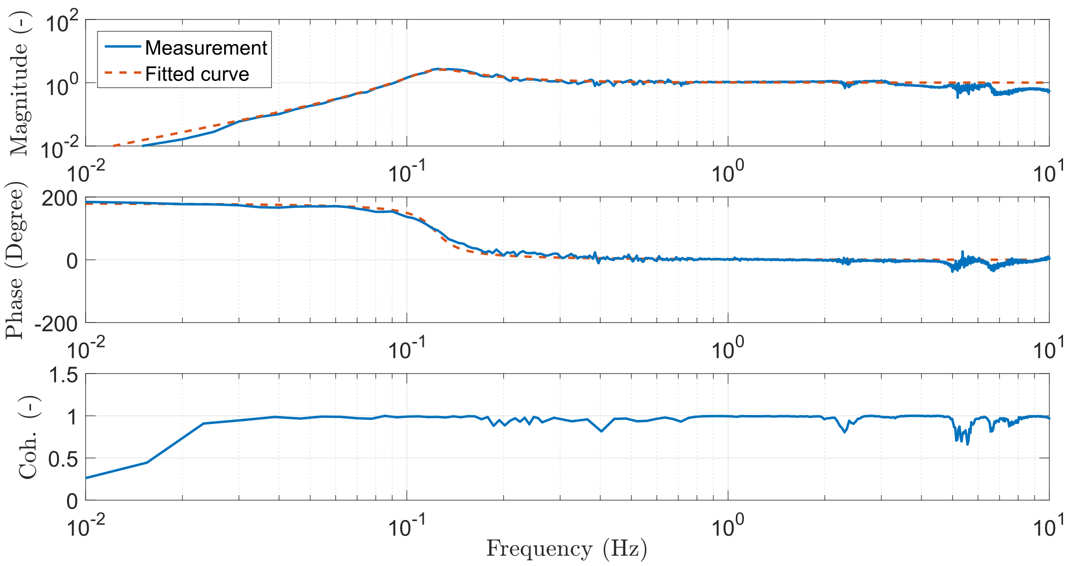

Figure 4.19: Bode plot of transfer function and the coherence between signals of the HINS and Güralp 6T seismometer.

benchmark sensor Güralp 6T seismometer (2) by the setup in Figure 4.17. The two inertial sensors are placed next to each other, and the excitation to both inertial sensors is seismic motion. The signals are recorded with sampling frequency of 10 kHz. Figure 4.19 shows that the transfer function and the coherence between the signals measured by the HINS and the Güralp 6T seismometer. As the Güralp 6T seismometer has a flat frequency response over the range of 0.03 to 100 Hz, it means that the sensitivity of the HINS can be characterised by a linear single DOF model. A second order high pass filter (dash red curve) with a pair of complex conjugate poles at $-0.115 \pm 0.682j$ (the resonance frequency $f_0 = 0.11$ and quality factor Q=3) is produced to represent the sensitivity of the HINS (solid blue curve). In order to avoid the overshoot around the resonance of HINS, the actuator of HINS is shunted with a resistor of 200 ohms leading to the fact that the poles are well damped. As depicted in the coherence plot, this model is valid from 0.03 to 10 Hz. Therefore, the experimental observation thus validates the working principle of HINS.

4.3 VINS mechanics

Figure 4.20a presents the prototype of the VINS, the interferometric readout (1) is mounted on the top of the mechanics (2). The pendulum (3) is modified for mounting a corner cube (4). Two tunable masses (5) are located on the side of the pendulum to adjust the inertia of the

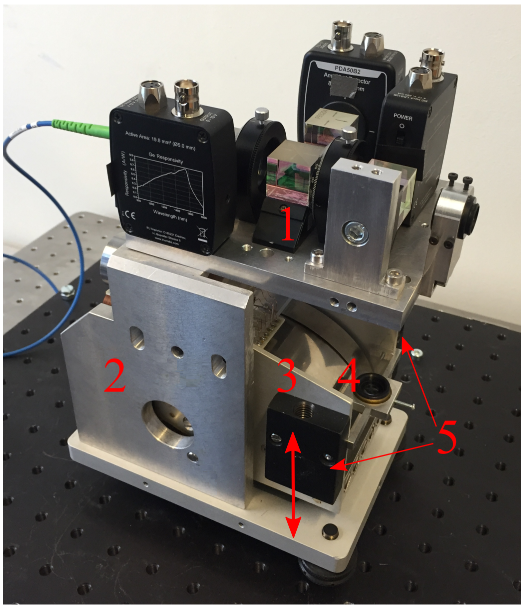

(a)

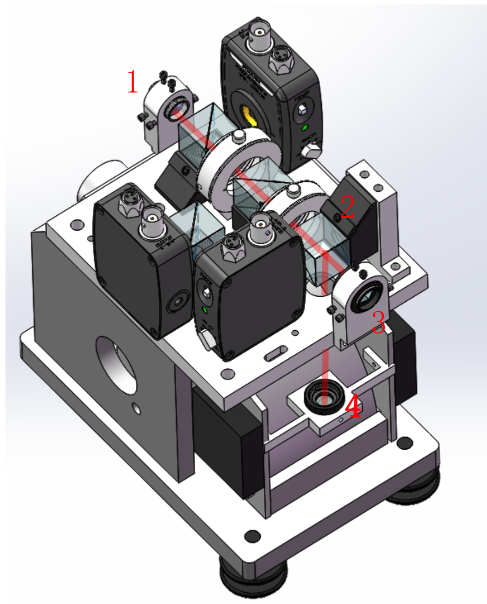

(b)

Figure 4.20: Prototype of the VINS and its optical path to corner cubes: (a) Prototype of the HINS: 1: interferometric readout, 2: mechanics of STS1-V seismometer, 3: pendulum with a corner cube, 4: tunable mass; (b) Optical path in the HINS: 1: laser collimator, 2: PBS2, 3: fixed CC, 4: movable CC mounted on the pendulum. Double arrow indicates the direction of the pendulum motion.

pendulum, and their weights are modified for adding the mass of the corner cube. Figure 4.20a presents the CAD model of the VINS. A laser beam travels from the laser collimator (1) and goes to PBS2 (2). PBS2 separates this laser beam. The reference beam goes to the fixed corner cube (3) and the measurement beam goes to the movable corner cube (4). Consequently, the motion of the pendulum is measured by the interferometric readout. The original VCAs of the STS1-V still work, thus they remain in the modified design.

4.3.1 Modelling

The VINS can be modelled by a horizontal pendulum oscillating vertically. As discussed previously, the pendulum has a cross-strips hinge and a leaf spring.

Alignment of the pendulum

The leaf spring pendulum of STS1-V uses a leaf-spring to compensate the weight of the pendulum. Figure 4.21 presents the leaf spring modelled by a zero-length spring.

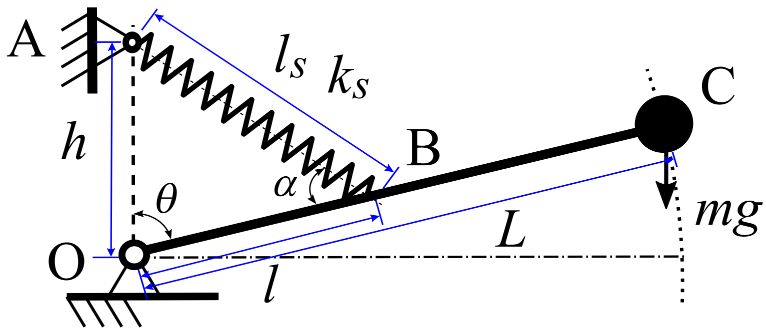

Figure 4.21: The model of the leaf spring pendulum for balancing gravity: O: the centre of rotation, A: the equivalent mounting point of the zero-length spring and B: the mounting point of the spring, C: the centre of the proof-mass. L: the length of the pendulum, l_s: the length of the equivalent zero-length spring, m: the proof-mass, k_s: the stiffness of the equivalent zero-length spring, l: the length between point A and B, h the distance between point A and O.

The point O is the position of the cross-spring hinge. Because the stiffness of the leaf spring is much greater than that of the cross-spring hinge, the stiffness of the cross-spring hinge is not taken into consideration. The angular motion of the pendulum is θ. Because the leaf spring is equivalent to a zero-length spring, the torque generated by the force of the zero-length spring is

$$\begin{aligned} \tau_s &= F_s l \sin(\alpha) \\ &= k_s l_s l \sin(\alpha) \end{aligned} \tag{4.43}$$

In the triangle OAB, the relationship between angle θ and α can be found

$$\sin(\alpha) = \frac{h}{l_s}\sin(\theta) \tag{4.44}$$

Merging equations (4.43) and (4.44) yields

$$\tau_s = k_s hl\sin(\theta) \tag{4.45}$$

The torque caused by mg about the point O τ_g is

$$\tau_g = mgL\sin(\theta) \tag{4.46}$$

When the spring compensates the gravity, it yields

$$\begin{aligned} \tau_g &= \tau_s \\ mg &= \frac{hl}{L}k_s \end{aligned} \tag{4.47}$$

this indicates that the gravity is compensated independently with the angle θ.

Tuning the leaf spring is tricky in practise. The stiffness k_s is fixed for a chosen leaf spring. One method is to tune the length h. Therefore, it is necessary to adjust the clamping of the leaf spring for balancing gravity. Otero's prototype [73] used this method. Alternatively, the inertia of the pendulum can be adjusted with respect to the parameters m and L, which is the mechanism used by the mechanics of STS1-V.

Figure 4.22 presents the modification of the pendulum to mount a corner cube on the

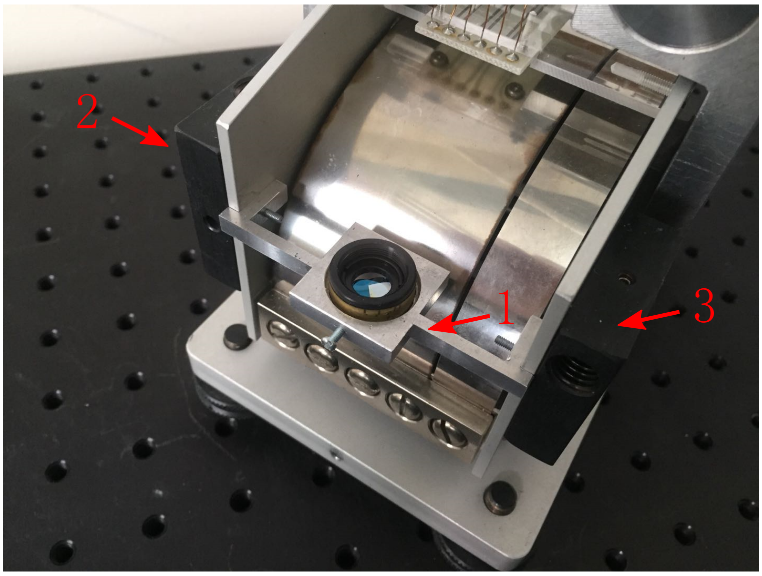

Figure 4.22: The modification to mount a corner cube on the pendulum: 1: mounting frame with corner cube; 2,3: adjustable mass on the pendulum.

pendulum, the mass of the frame with corner cube (1) and the screws are 23.6 g and 1 g. The same amount of mass 24.6 g is removed from the adjustable mass (2,3) of the pendulum. The mass has movable screws inside it, by changing its position, the inertia of the pendulum can be adjusted to align the pendulum.

Response to translational motion w_y

Figure 4.23 presents the mechanics under translational excitation. O presents the cross-spring hinge of the mechanics. If the pendulum is aligned correctly, its equilibrium point is the dash-dot line. The mechanics is sensitive to translational motion along Y-axis and rotational motion about Z-axis (see Figure 4.24). However, because of the alignment, the equilibrium point of the pendulum is not horizontal, this is shown by the dash line in the figure. γ_0 is denoted as the initial tilting of the pendulum.

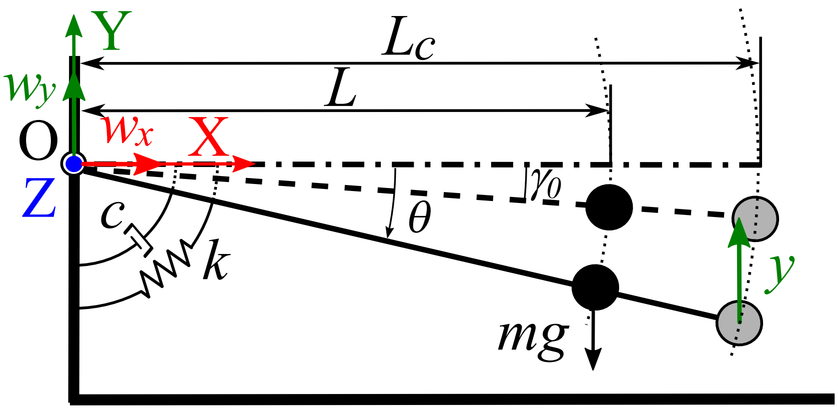

Figure 4.23: The model of the leaf spring pendulum under translational excitation: The joint O presents the cross-spring hinge allowing vertical oscillations. Black dots present the mass centre of the pendulum, and grey dots present the mounting position of the corner cube. The dashed line denotes the initial position of the pendulum. L: the length between the hinge and the mass centre, L_c: the length between the hinge and the mounting position of the corner cube, m: the proof-mass, k: the stiffness of the structure, c: the damping of the structure.

Applying Newton's second law of rotation about the hinge O when the system is excited by translational motion w_y along Y-axis, the sum of torque about the hinge O is given by

$$I\ddot{\theta} = \sum \tau = -\tau_s - \tau_d + F_{W_y} L\cos(\theta) + mgL\cos(\theta) \tag{4.48}$$

where $\tau_s = k_\gamma \theta$ is the torque generated by the rotational spring, $\tau_d = c\dot{\theta}$ is the rotational damping torque, $F_{W_y} = m\ddot{w}_y$ is the reaction force at the proof-mass. Therefore, the dynamic equation can be derived by

$$I\ddot{\theta} = -c\dot{\theta} - k\theta + m\ddot{w}_y L\cos(\theta) + mgL\cos(\theta) \tag{4.49}$$

$$y = -L_c(\theta - \gamma_0) \tag{4.50}$$

where I is the moment of the inertia with respect to the rotation centre O. The relative angle θ in the oscillation regime is small. The relative motion y is the motion of the corner cube along Y-axis and is assumed linear in the oscillation regime. Substituting equation (4.50) into (4.49), yields

$$I\ddot{y}+c\dot{y}+k(y-L_{\mathrm{c}}\gamma_0) = -mLL_{\mathrm{c}}(\ddot{w}_{\mathrm{y}}\cos(\gamma_0)+\ddot{w}_{\mathrm{y}}\frac{y}{L_{\mathrm{c}}}\sin(\gamma_0)+g\cos(\gamma_0)+g\frac{y}{L_{\mathrm{c}}}\sin(\gamma_0)) \tag{4.51}$$

where approximations $\sin(\frac{y}{L_{\mathrm{c}}}) \approx \frac{y}{L_{\mathrm{c}}}$ and $\cos(\frac{y}{L_{\mathrm{c}}}) \approx 1$ is applied.

At the equilibrium, $k\gamma_0 = mgL\cos(\gamma_0)$, equation (4.51) then becomes

$$I\ddot{y} + c\dot{y} + \big(k + mgL\sin(\gamma_0)\big)y = -mLL_{\mathrm{c}}\ddot{w}_{\mathrm{y}}\cos(\gamma_0) \tag{4.52}$$

where the coefficient $\frac{y}{L_{\mathrm{c}}}\sin(\gamma_0)$ for $\ddot{w}_{\mathrm{y}}$ is neglected considering both y and γ_0 are small quantities. Expressing equation (4.52) in the Laplace domain is

$$T_{\mathrm{WY}} = \frac{Y(s)}{W_{\mathrm{y}}(s)} = \frac{-mLL_{\mathrm{c}}\cos(\gamma_0)s^2}{Is^2 + cs + \big(k + mgL\sin(\gamma_0)\big)} \tag{4.53}$$

Equation (4.53) indicates that the suspension of the sensor is stiffened due to the sine coupling of the gravity and the vertical ground motion is less sensed because of the cosine coupling. The tilt-horizontal coupling is not considered here because the initial inclination γ_0 is assumed to be small.

If the pendulum is perfectly aligned, the inclination angle $\gamma_0 = 0$, the pendulum is immune to the horizontal motion w_{x} along X-axis. However, with the inclination angle γ_0, the pendulum is sensitive to the motion. Because the sensor is designed to measure vertical motion only, the transfer function between the relative motion y and the horizontal motion w_{x} is not discussed. There are applications using the method to measure the horizontal motion. Symmetric triaxial seismometers use three leaf spring pendulums with an angle $\gamma_0 = 35.26°$ [143]. The three readouts of the pendulums measure three signals. Consequently, the vertical motion and orthogonality horizontal motion can be obtained from the signals.

Response to rotational motion γ

Figure 4.24 shows the model of the scenario when the sensor is subjected only to a rotational excitation γ. All other notations remain the same as those in Figure 4.23.

In this case, the dynamic equation is

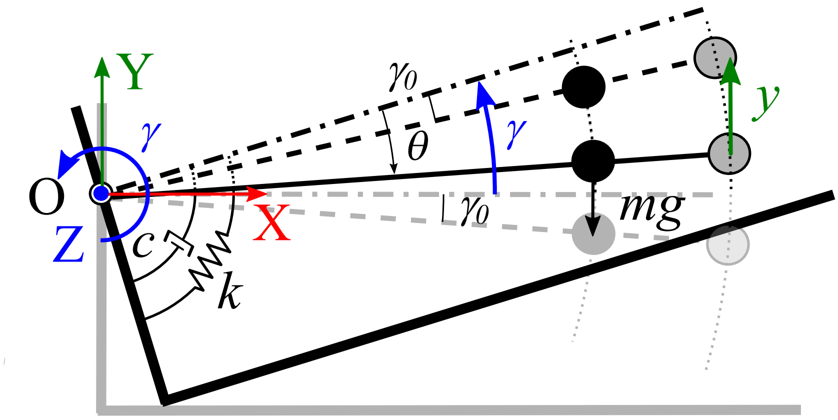

Figure 4.24: The model of the leaf spring pendulum under rotational excitation: The joint O presents the cross-spring hinge allowing vertical oscillations. Black dots present the mass centre of the pendulum, and grey dots present the mounting position of the corner cube. The dashed line denotes the initial position of the pendulum.

$$I\ddot{\theta} = -c\dot{\theta} - k\theta + I\ddot{\gamma} + mgL\cos(\gamma - \theta) \tag{4.54}$$

Substituting equation (4.50) into (4.54), yields

$$I\frac{\ddot{y}}{L_c} + c\frac{\dot{y}}{L_c} + k(\frac{y}{L_c} - \gamma_0) = -I\ddot{\gamma} - mgL\cos(\gamma + \frac{y}{L_c} - \gamma_0) \tag{4.55}$$

Expanding $\cos(\gamma + \frac{y}{L_c} - \gamma_0)$ gives

$$\cos(\gamma+\frac{y}{L_c}-\gamma_0) = \cos(\gamma)\big(\cos(\frac{y}{L_c})\cos(\gamma_0)+\sin(\frac{y}{L_c})\sin(\gamma_0)\big)-\sin(\gamma)\sin(\frac{y}{L_c}-\gamma_0) \tag{4.56}$$

Considering that γ, y and γ_0 are small quantities, equation (4.56) is simplified to

$$\cos(\gamma + \frac{y}{L_c} - \gamma_0) = \cos(\gamma_0) + \frac{y}{L_c}\sin(\gamma_0) + \gamma\sin(\gamma_0) \tag{4.57}$$

where an approximations $\sin(\frac{y}{L_c}) \approx \frac{y}{L_c}$ and $\cos(\frac{y}{L_c}) \approx 1$ are applied.

Substituting equation (4.57) into equation (4.55), yields

$$I\frac{\ddot{y}}{L_c} + c\frac{\dot{y}}{L_c} + k(\frac{y}{L_c} - \gamma_0) = -I\ddot{\gamma} - mgL\big(\cos(\gamma_0) + \frac{y}{L_c}\sin(\gamma_0) + \gamma\sin(\gamma_0)\big) \tag{4.58}$$

At equilibrium, the same as for the translational excitation case, equation (4.58) then turns into

$$I\ddot{y} + c\dot{y} + \big(k + mgL\sin(\gamma_0)\big)y = -IL_c\ddot{\gamma} - mgLL_c\gamma\sin(\gamma_0) \tag{4.59}$$

In the Laplace domain, equation (4.59) can be expressed by

$$T_{\mathrm{R}_\gamma\mathrm{Y}} = \frac{Y(s)}{R_\gamma(s)} = \frac{-(IL_c s^2 + mgLL_c\sin(\gamma_0))}{Is^2 + cs + \big(k + mgL\sin(\gamma_0)\big)} \tag{4.60}$$

There is one frequency at which the right hand terms cancels out, leading to a complete loss of the sensitivity transfer function at this particular frequency, termed zero of the sensor sensitivity. It is noted that the location of this frequency is proportional to the initial inclination and this phenomenon only occurs when the VINS is subject to rotational motions.

Figure 4.25 shows the Bode plots of equations (4.53) and (4.60). The parameters used are given in Table 4.2. The VINS is used to measure vertical motion. Its transfer function $T_{\mathrm{W_yY}}$ (solid blue curve) shows that the VINS is a perfect estimator to measure vertical displacement w_y because of the flat transfer function above the resonance frequency, 0.7 Hz. However, the VINS is sensitive to rotational motion γ. The transfer function $T_{\mathrm{R}_\gamma\mathrm{Y}}$ (dash red curve) is also flat about the resonance frequency to estimate the rotational motion γ, and its magnitude is scaled by the factor L_c in equation (4.60). Moreover, $T_{\mathrm{R}_\gamma\mathrm{Y}}$ has zeros around 0.1 Hz. Compared the transfer functions $T_{\mathrm{W_yY}}$ and $T_{\mathrm{R}_\gamma\mathrm{Y}}$, it shows that measurements of VINS can be affected by the rotational motion γ in the low-frequency domain, which was reported in [144].

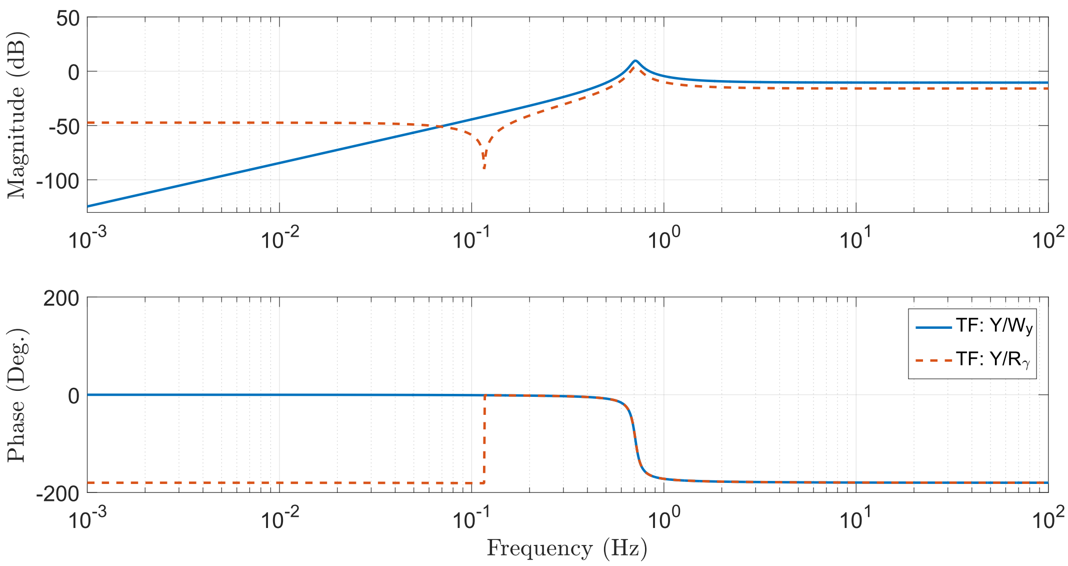

Figure 4.25: The transfer function of the VINS between the relative motion and the different inputs: solid blue curve: TF between Y and W_y, dash red curve: TF between Y and R_γ.

When the damping is small, the resonance frequency of the pendulum can be estimated by

$$f_0 = \frac{1}{2\pi}\sqrt{\frac{k + mgL\sin(\gamma_0)}{I}} \tag{4.61}$$

According to the equation, the initial inclination of γ_0 affects the resonance frequency of the VINS.

4.3.2 Experimental characterisation

The assembled VINS is assessed with experiments. Figure 4.26 shows the assembled VINS (1) inside a vacuum chamber (3). The chamber holds the air pressure of 4 mbar during measurements.

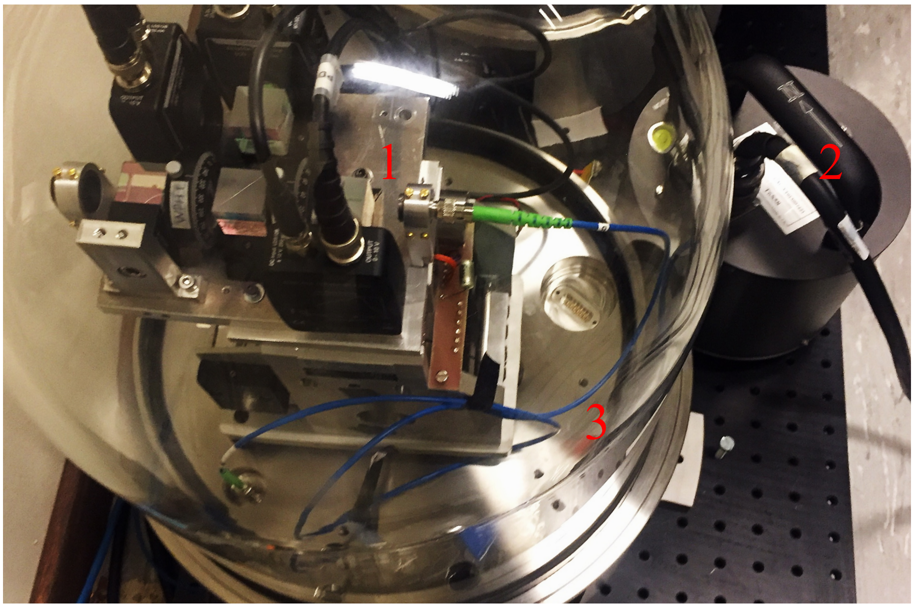

Figure 4.26: The setup to test the VINS: 1: the VINS, 2: Güralp 6T seismometer, 3: The vacuum chamber.

Firstly, the Q factor and the resonance frequency is measured with the ring-down

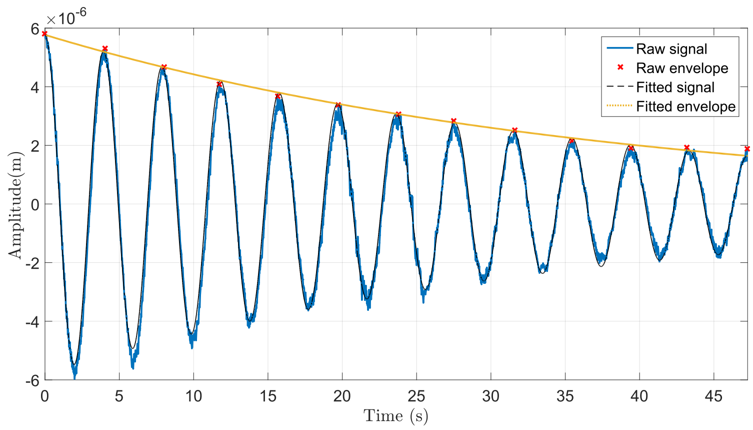

Figure 4.27: Signal of the VINS from the ring-down experiment.

experiment. Figure 4.27 shows the response of the VINS to an impulse excitation. The solid blue curve is the raw data of the measurement. Using the fitting methods presented in Section 4.2.2, the fitted signal is shown by the dash black curve and the fitted envelope is shown by the dotted yellow curve. The estimation of the Q factor is 30 and the resonance frequency is 0.26 Hz.

The performance of the developed VINS is preliminarily assessed by comparing it with the Güralp 6T seismometer which is shown in Figure 4.26. The Güralp 6T seismometer (3) and the VINS (1) are placed next to each other to measure the same seismic motion. Figure 4.28 plots the transfer function and the coherence between the VINS and the Güralp 6T seismometer. As the sensitivity of the Guralp has a flat frequency response over the range of 0.1 to 100 Hz, it alternatively means that the sensitivity of the VINS can be characterised by a linear single DOF model as can be seen from the magnitude and the phase plots. A second order high pass filter (dash red line) with a pair of complex conjugate poles at $-0.027 \pm 1.633j$ (the resonance frequency $f_0 = 0.26$ and quality factor Q=30) is produced to represent the sensitivity of the VINS (solid blue curve). As depicted in the coherence plot, this model is valid only from 0.1 to 10 Hz. Below 0.1 Hz, the sensitivity of the VINS decreases whereas incoherent noises are recorded causing the drop of the coherence between the two inertial sensors. Nevertheless, it is shown that the developed VINS is capable of capturing the ground motion in the frequency range between 0.1 and 10 Hz.

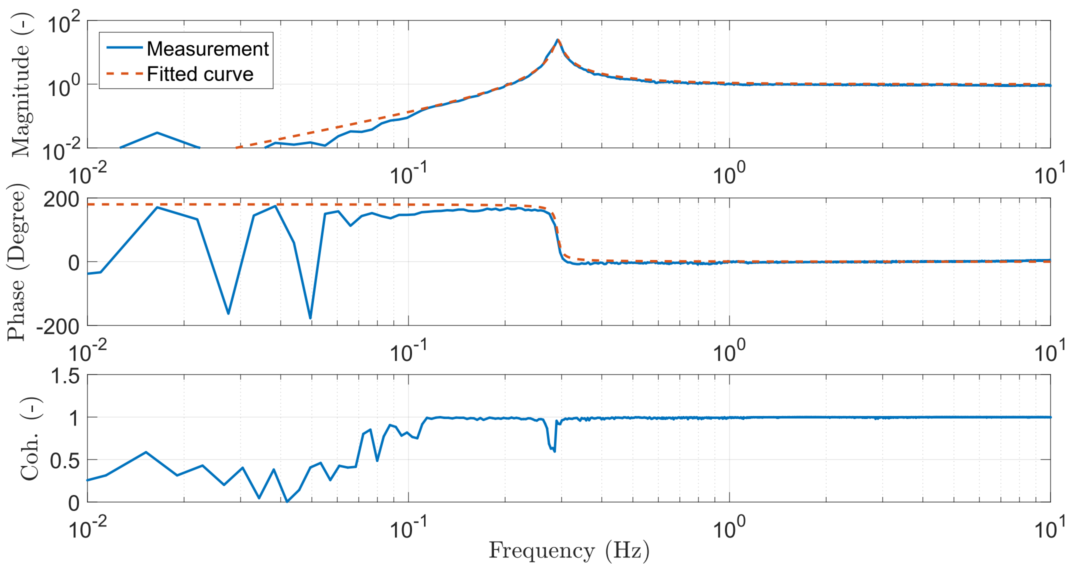

Figure 4.28: Bode plot of transfer function and the coherence between signals of the VINS and Güralp 6T seismometer.

4.4 Assembly of inertial unit

Figure 4.29 shows the layout of an inertial unit consisting of a VINS and a HINS placed in a vacuum chamber. The size of the vacuum chamber is carefully selected to fit the

HINS and VINS. In order to electrically and optically access the components inside and outside the vacuum chamber, the vacuum box is equipped with two optical feedthroughs and a multi-channel electric feedthrough. Appendix F presents the vacuum system with feedthroughs.

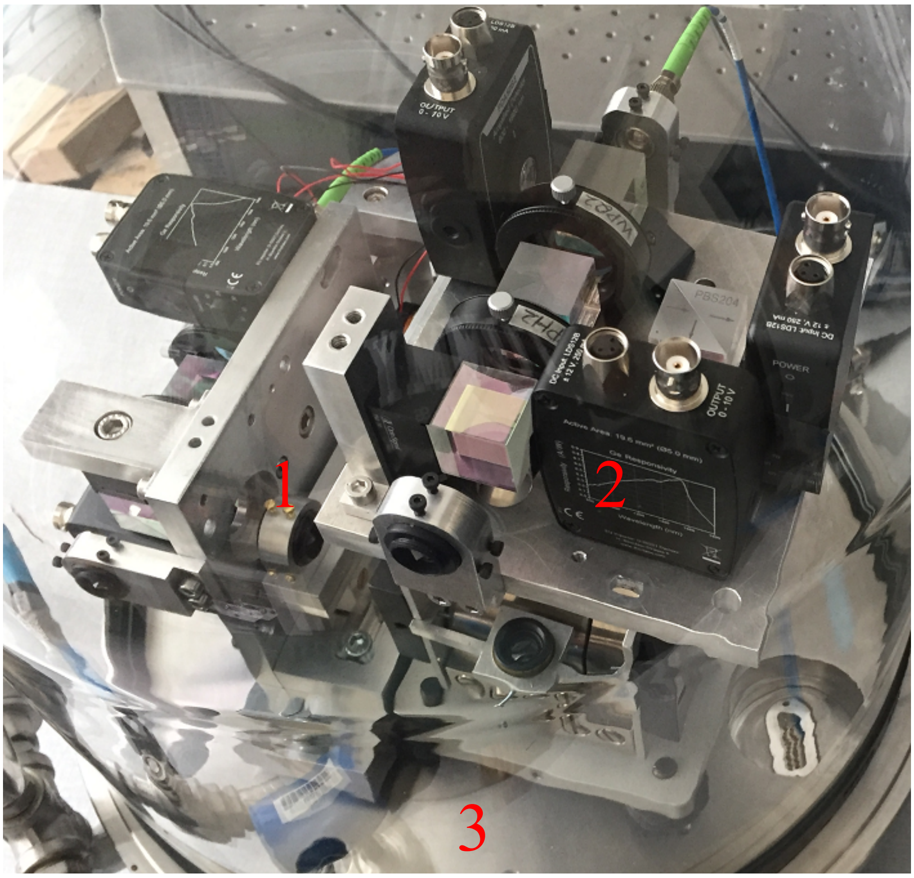

Figure 4.29: Inertial unit assembled from a VINS and a HINS: 1: the HINS, 2: the VINS, 3: vacuum chamber.

One inertial unit measures both vertical motion and horizontal motion. Two inertial units have been assembled for the huddle test, which is presented in Chapter 6.

4.5 Conclusion

This chapter showed the development of inertial sensor mechanics. Various forms of mechanics for implementing inertial sensors have been reviewed. It was found that the Lehman pendulum (in Horizontal Interferometric Inertial Sensor (HINS)) and leaf spring pendulum (in Vertical Interferometric Inertial Sensor (VINS)) combining cross-spring hinges are good candidates. The dynamic behaviours of the mechanics used for the VINS and HINS were studied which allows investigating their sensitivities to excitations in different directions. Especially, the dynamic behaviour of the Lehman pendulum was analysed with the effect of negative-stiffness. It was shown that both mechanics are capable of well reacting to pure translational excitations.

However, they are found to be sensitive to some extent to rotational excitations. The Liquid Absolute Tilt-meter (LAT) shown in Appendix A is under the development. It is used to measure the tilting signal for removing that in measurements.

Moreover, the HINS and VINS are tested, the ring-down experiment proved that the resonance frequency of the assembled HINS and VINS can reach to 0.11 and 0.26 Hz, receptively. Also, their performances were assessed by comparing with a benchmark inertial sensor, the Güralp 6T seismometer, and the results showed that the developed sensors are good to measure seismic vibration.

Chapter 5

Inertial sensor characterisation

This chapter presents the characterisation of the inertial sensor. In Section 5.1, a full model of the inertial sensors combining with optoelectronic system, mechanical system, and noise sources. In Section 5.2, different noise sources from the data acquisition system, photodetectors, laser source and mechanical system are simulated for the model. Meanwhile, possibilities to decrease the effect of noises were discussed. Section 5.3 presents the noise budgeting for the interferometric readout, the horizontal interferometric inertial sensor and the vertical interferometric inertial sensor.

5.1 Inertial sensor modelling

Figure 5.1 presents the measurement system: a laser source, an inertial unit (one HINS and one VINS) and a data acquisition system (DAQ). The laser source generates laser beams to the inertial unit. The three photodetectors measure laser beams with respect to the input motion, and the output voltage signals. The DAQ records the signals from the inertial unit via six channels (three channels for one inertial sensor). All three instruments contain different noise sources.

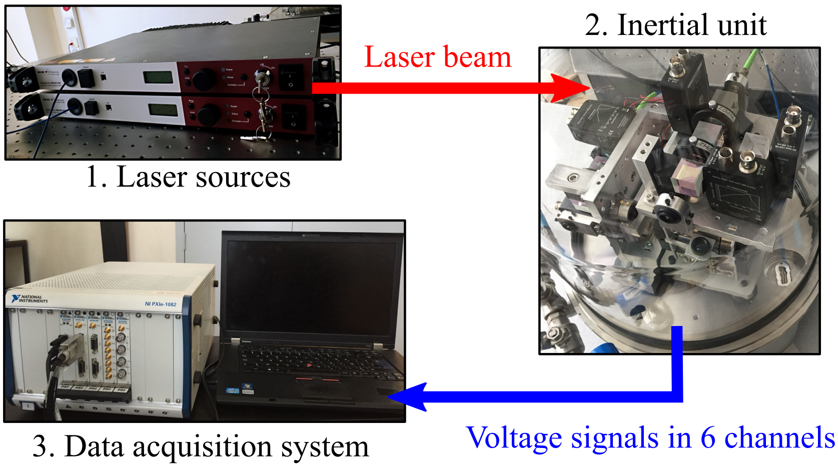

Figure 5.1: The instruments used in measurements: 1. laser source: Koheras X15, 2. sensor: VINS, 3. data acquisition system: NI PXIe-4497.

Figure 5.2 presents the system with main noise sources. The three instruments shown in Figure 5.1 are represented by four blocks. The first block represents the laser source. The flow of laser beam is denoted by red lines with arrows. The second block shows the mechanics of the sensor, which converts the input motion w to relative motion y. The blue lines with arrows indicate the signal flows containing the measurement of y.

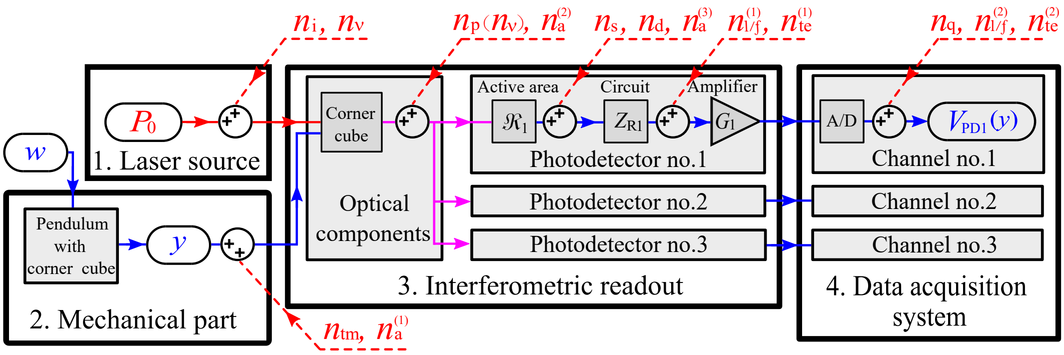

Figure 5.2: Diagram of noise contribution during measurements: red arrows (solid lines): the direction of laser beam, blue arrows: the direction of measured information, pink arrows: laser beam containing information, red arrows (dash lines): noise sources; n_{tm}: thermomechanical noise, n_{a}: ambient noise, n_{i}: laser intensity noise, n_{f}: laser frequency noise, n_{p}: phase noise with respect to the laser frequency noise, n_{s}: shot noise, n_{d}: dark current noise, $n_{1/f}$: $1/f$ noise, n_{te}: thermoelectric noise, n_{q}: quantisation noise; The index (1), (2) and (3) present the same type of noise with different values.

The third block presents the interferometric readout of the inertial sensor. It consists of optical components and three photodetectors. Concerning the optical components, one of the key component is the movable corner cube which combines the laser beam (solid red lines) with the information of motion (solid blue lines). The combined beam (denoted by the purple lines) is interfered in this optical system and finally measured by the three photodetectors. The photodetectors used are switchable gain amplified photodiodes. The subsystems of the first photodetector (PD1, see Figure 3.10) is shown in the figure, these are the active area, circuit and amplifier. The received laser intensity is converted consecutively into a photocurrent by the active area and into a voltage by the circuit and the amplifier.

The fourth block represents the data acquisition system, which converts the analogue signals into digital signals and records them. Three channels are used to record signals from one sensor. Taking the signal from the first channel as an example, the recorded signal without noise is

$$V_{\mathrm{PD1}} = G_1 Z_{\mathrm{R1}} \Re_1 \cdot \frac{P_0}{8}\Big(1 + \cos(2\phi_{\mathrm{y}})\Big) \quad (\mathrm{V}) \tag{5.1}$$

where, V_{PD1} indicates the signal recorded by the DAQ, and is used to distinguish it from analogue signal $V^{\mathrm{a}}_{\mathrm{PD1}}$ in the following discussion. P_0 is the pure laser intensity without noise, and ϕ_{y} is the measured phase information. $\Re_1$ (in the unit of A/W) is the responsivity of the active area of PD1, Z_{R1} (in the unit of V/A) is the resistance of the circuit of PD1, and G_1 is the gain factor of PD1, which is one selected among eight selectable gain factors from 0 to 70 dB with the interval of 10 dB.

Noise sources can be added into equation (5.1) step by step. Concerning the laser source (the first block), it generates a pure laser intensity of P_0, as well as the intensity noise and the frequency noise. The noisy outputs with laser intensity noise can be written as

$$P_{\mathrm{n}} = P_0 + n_{\mathrm{i}} \quad (\mathrm{W}) \tag{5.2}$$

where, P_{n} is the noisy output and the intensity noise n_{i} originates from the laser intensity fluctuation. The frequency noise n_ν originates from the laser frequency fluctuation. Because the laser frequency noise influences measurements by the Optical Path Difference (OPD) of the interferometer, and it is converted into phase noise $n_{\mathrm{p}}(n_\nu)$ in the interferometric readout. The methods to simulate the noise sources are discussed in Section 5.2.3.

In the mechanics (the second block), not only the input motion w excites the pendulum, but also ambient noise $n_{\mathrm{a}}^{(1)}$ and the thermomechanical noise n_{tm}. Therefore, the relative motion between the corner cube and the support is

$$y_{\mathrm{n}} = y + n_{\mathrm{a}}^{(1)} + n_{\mathrm{tm}} \quad (\mathrm{m}) \tag{5.3}$$

where, y_{n} is the motion with noise, the thermomechanical noise n_{tm} is the thermal fluctuation of the pendulum, in the unit of m (Section 5.2.4), and ambient noise $n_{\mathrm{a}}^{(1)}$ is the unwanted excitations to the pendulum (for example the air fluctuations), assumed in the unit of m (Section 5.2.5).

In the interferometric readout (the third block), both optical components and photodetectors inject noises into the measurement. Concerning the optical system, the motion of the corner cube is converted into the phase of the laser beam. Meanwhile, the optical system senses phase noise and ambient noise. Therefore, the phase can be expressed as

$$\phi_{\mathrm{y_n}} = \frac{2\pi n y_{\mathrm{n}}}{\lambda} + n_{\mathrm{p}}(n_\nu) + n_{\mathrm{a}}^{(2)} \quad (\mathrm{rad}) \tag{5.4}$$

where, $\phi_{\mathrm{y_n}}$ is the noisy phase with respect to the motion of the corner cube y, $\lambda = 1550$ nm is the wavelength of the laser beam and $n \simeq 1$ is the index of refraction. $n_{\mathrm{p}}(n_\nu)$ is the phase noise caused by the laser frequency noise (Section 5.2.3) and $n_{\mathrm{a}}^{(2)}$ is environment variations, such as temperature, cause unwanted phase fluctuations.

The working principle of the interferometric readout is introduced in Chapter 3. It can be simulated by the Jones matrices in the time domain with respect to both of the motion and noise sources. The MATLAB script about the model is presented in Appendix G. Consequently, the laser intensity received by the first photodetector is

$$P_{\mathrm{PD1n}} = \frac{P_{\mathrm{n}}}{8}\Big(1 + \cos(2\phi_{\mathrm{y_n}})\Big) \quad (\mathrm{W}) \tag{5.5}$$

where, P_{PD1n} is the noisy laser intensity reaching PD1. Electrical noise sources are presented in the measurements (block of Photodetector no.1). While the active area converts laser intensity to photocurrent, it injects shot noise, dark current noise and ambient noise into measurements. Therefore, the noisy photocurrent I_{PD1} in PD1 is

$$I_{\mathrm{PD1}} = \mathfrak{R}_1 P_{\mathrm{PD1n}} + n_{\mathrm{d}} + n_{\mathrm{s}} + n_{\mathrm{a}}^{(3)} \quad (\mathrm{A}) \tag{5.6}$$

where, dark current noise n_{d} is unwanted leakage current from the photodetector, shot noise n_{s} originates from the discrete nature of electric charge and ambient noise $n_{\mathrm{a}}^{(3)}$ is the unwanted excitation by the environment, such as natural light. Dark current noise, shot noise and ambient noise are assumed in the unit of A in the equation and they are discussed in Section 5.2.2. Moreover, thermoelectric noise and $1/f$ noise affect the measurement by

$$V_{\mathrm{PD1}}^{\mathrm{a}} = G_1\Big(Z_{\mathrm{R1}} I_{\mathrm{PD1}} + n_{\mathrm{te}}^{(1)} + n_{1/f}^{(1)}\Big) \quad (\mathrm{V}) \tag{5.7}$$

where, $V_{\mathrm{PD1}}^{\mathrm{a}}$ is the noisy analogue voltage output of PD1, thermoelectric noise $n_{\mathrm{te}}^{(1)}$ and $1/f$

noise $n_{1/f}^{(1)}$ are electronic noise in the unit of V. They originate from the electronics of the photodetector. Because the DAQ has the same noise sources, thermoelectric noise $n_{\mathrm{te}}^{(1)}$ and $1/f$ noise $n_{1/f}^{(1)}$ are discussed together hereafter.

Concerning the data acquisition system (the fourth block), three channels are used to record the signals from the three photodetectors. In the first channel, the analogue-to-digital converter (A/D) converts the analogue signal to digital one but generates quantisation noise n_{q}. Meanwhile, $1/f$ noise and thermoelectric noise originating from the DAQ are added to the measurement. Therefore, the recorded noisy digitalised signal is

$$V_{\mathrm{PD1}} = V_{\mathrm{PD1}}^{\mathrm{a}} + n_{\mathrm{q}} + n_{\mathrm{te}}^{(2)} + n_{1/f}^{(2)} \quad (\mathrm{V}) \tag{5.8}$$

where V_{PD1} is the recorded noisy signal, quantisation noise n_{q} is random fluctuations during quantisation processes of the A/D, thermoelectric noise $n_{\mathrm{te}}^{(1)}$ originates from thermal fluctuations of electronics and $1/f$ noise $n_{1/f}^{(1)}$ is electronic noise with a $1/f$ power spectral density. The added quantisation noise, thermoelectric noise and $1/f$ noise are in the unit of V and are discussed in Section 5.2.1.

Merging equations 5.2 to 5.8, a general equation containing the above noise sources is

$$\begin{aligned} V_{\mathrm{PD1}} = G_1\Big[Z_{\mathrm{R1}}\big[\Re_1\Big(\frac{P_0 + n_{\mathrm{i}}}{8}\big(1 + \cos(2\frac{2\pi n(y + n_{\mathrm{a}}^{(1)} + n_{\mathrm{tm}})}{\lambda} + n_{\mathrm{p}}(n_\nu) + n_{\mathrm{a}}^{(2)})\big)\Big) \\ + n_{\mathrm{s}} + n_{\mathrm{d}} + n_{\mathrm{a}}^{(3)}\big] + n_{1/f}^{(1)} + n_{\mathrm{te}}^{(1)}\Big] + n_{\mathrm{q}} + n_{1/f}^{(2)} + n_{\mathrm{te}}^{(2)} \quad (\mathrm{V}) \end{aligned} \tag{5.9}$$

where y is relative motion between the corner cube and the support, and V_{PD1} is the final recorded signal. Following the same method, the signals in the other two photodetectors can be modelled.

5.2 Noise sources

Some noise (such as ambient noise) can be reduced with proper treatment, however, most of them (such as electric noise) still affect measurements. Based on Figure 5.2, a model has been developed to simulate the propagation of noise in the time domain. The noise sources in the time domain are generated, and the Amplitude Spectral Density (ASD) of the simulated noises are presented in the following discussion.

5.2.1 Data acquisition system noise

The data acquisition system used in the thesis is NI PXIe-4497, which is a 24 bits DAQ. The noise floor of the DAQ can be measured by connecting a 50 Ω terminator and recording the signal directly. It is shown as the solid black curve in Figure 5.3. As in the previous discussion, the noise sources contributing to this noise floor are quantisation noise, $1/f$ noise and thermoelectric noise, which can be expressed by

$$n_{\mathrm{DAQ}} = n_{1/f} + n_{\mathrm{te}} + n_{\mathrm{q}} \quad (\mathrm{V}) \tag{5.10}$$

where, n_{DAQ} is the noise floor of the DAQ, and is defined as the DAQ noise in this thesis.

Owing to the fact that the noise floor of the data acquisition system inevitably contributes to all measurements, it is introduced before other noise sources in this section and used as a reference to evaluate other noises. The parameters used to simulate the noise floor are given by its specifications [145]. The sampling frequency f_s is 10 kHz. The noise floor of the DAQ is measured by a channel disconnected from inputs, the ASD of the measurement is shown by the solid black curve in Figure 5.3.

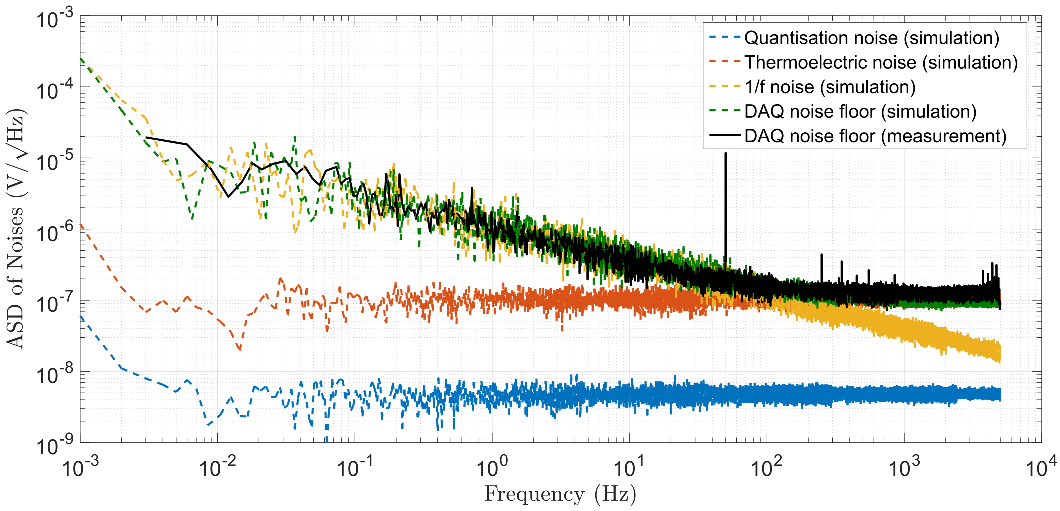

Figure 5.3: Simulation and measurement of DAQ noise: The ASD of DAQ noise can be regarded as two parts. One part has a slope of -0.5 below 100 Hz and is dominated by $1/f$ noise. The second part of the noise floor is flat above 100 Hz. As shown in the figure, the thermoelectric noise dominates the noise floor above 100 Hz.

The modelled DAQ noise n_{DAQ} is the dash green curve, which equals to the ASD of the measured DAQ noise. The modelled DAQ noise is used in the simulation is the addition of the three noises, and the noises in the three channels are incoherent. Moreover, DAQ noise is used to compare the other noise sources in the following discussions.

Quantisation noise

The quantisation noise is the rounding error between the analog input voltage and the output digitised value, which is introduced by the analog-to-digital converter (A/D). It is dominated by sampling frequency and bits of the A/D. The Amplitude Spectral Density (ASD) of the theoretical quantisation noise $\mathrm{A}_{\mathrm{n_q n_q}}$ is given by [146]

$$\mathrm{A}_{\mathrm{n_q n_q}} = \frac{q}{\sqrt{12 f_{\mathrm{n}}}} \quad (\mathrm{V}/\sqrt{\mathrm{Hz}}) \tag{5.11}$$

where $q = 2\Delta V/2^{n+1}$ is the quantisation interval, $\Delta V = 10$ V is half the voltage range, $n = 24$ is the number of bits available in the DAQ and $f_{\mathrm{n}} = f_{\mathrm{s}}/2 = 5$ kHz is the Nyquist frequency. The simulation of quantisation noise of the DAQ is given by Figure 5.3 as the dash blue curve. Because quantisation noise is the white noise, it can be modelled in the time domain by

$$n_{\mathrm{q}} = \bar{\mathrm{A}}_{\mathrm{n_q n_q}} \cdot n_0 \cdot \sqrt{B} \tag{5.12}$$

where $\bar{\mathrm{A}}_{\mathrm{n_q n_q}}$ is the mean value of the ASD of quantisation noise and $B = f_{\mathrm{s}}/2$ is its bandwidth. n_0 is a sequence of the white noise, which has an interval $t_{\mathrm{s}} = 1/f_{\mathrm{s}}$ and a length $L = T/f_{\mathrm{s}}$, where T is the duration of the simulation in the unit of s. The white noise is assumed to be normally distributed with the mean $\mu = 0$ and the standard deviation $\sigma = 1$. The white noise n_0 is simulated by the **wgn** function of MATLAB, which generates white Gaussian noise. The quantisation noise in the time domain is obtained by scaling the white noise n_0 with $\bar{\mathrm{A}}_{\mathrm{n_q n_q}} \cdot \sqrt{B}$, and its ASD is the dash blue curve in Figure 5.3.

Thermoelectric noise

Thermoelectric noise or Johnson noise [147] is generated by thermal fluctuations of electrons passing through resistive components of the circuits. The ASD of thermoelectric noise $\mathrm{A}_{\mathrm{n_{te} n_{te}}}$ is given by

$$\mathrm{A}_{\mathrm{n_{te} n_{te}}} = 2\sqrt{k_{\mathrm{B}} T \mathrm{Re}(Z_{\mathrm{DAQ}})} \quad (\mathrm{V}/\sqrt{\mathrm{Hz}}) \tag{5.13}$$

where $k_{\mathrm{B}} = 1.380\,648\,52 \times 10^{-23}$ J/K is the Boltzmann's constant, $T = 297.15$ K is the Kelvin temperature in laboratory conditions. $\mathrm{Re}(Z_{\mathrm{DAQ}})$ is the real part of the impedance of the channel. According to the specification [145], the impedance of the channel is equivalent to a resistor $R = 10$ MΩ and a capacitor $C = 35$ pF in parallel, and it is

$$Z_{\mathrm{DAQ}} = \frac{R}{1 + j\omega RC} \quad (\Omega) \tag{5.14}$$

where ω is the angular frequency. The real part of the impedance is $\mathrm{Re}(\mathrm{Z_{DAQ}}) = 6.93 \times 10^5\ \Omega$. The simulation of thermoelectric noise in the frequency domain is presented by Figure 5.3 as the dash red curve. Thermoelectric noise in the time domain can be modelled by band-limited white noise, and it is

$$n_{\mathrm{te}} = \bar{\mathrm{A}}_{\mathrm{n_{te}n_{te}}} \cdot n_0 \cdot \sqrt{B} \tag{5.15}$$

where $\bar{\mathrm{A}}_{\mathrm{n_{te}n_{te}}}$ is the mean value of the ASD of thermoelectric noise and $B = f_{\mathrm{s}}/2$ is its bandwidth. n_0 is a sequence to represent white noise, which is discussed with equation (5.12). The ASD of thermoelectric noise is shown by the dash red curve in Figure 5.3.

$1/f$ noise

$1/f$ noise, or Flicker noise, corresponds to fluctuations in diverse types of electronic components [148]. The main characteristic of the $1/f$ noise is that its power spectral density is inversely proportional to the frequency. The ASD model of the $1/f$ noise $\mathrm{A_{n_{1/f}n_{1/f}}}$ can be expressed as

$$\mathrm{A_{n_{1/f}n_{1/f}}} = \frac{K}{\sqrt{f^a}} \quad (\mathrm{V}/\sqrt{\mathrm{Hz}}) \tag{5.16}$$

where K is a constant related to the circuit, f is the frequency and a is a coefficient between 0 and 2, and is usually closer to 1. Therefore, it has a characteristic slope of its Power Spectral Density (PSD) as -1 and a characteristic slope of its ASD as -0.5. Moreover, this noise is often the dominant source in the frequency domain.

Because $1/f$ noise $\mathrm{n}_{1/f}$ is coloured noise, its ASD curve is modelled according to the measurement of the DAQ noise (solid black curve) below 100 Hz in Figure 5.3, and its ASD is converted into the time domain. The function to generate $\mathrm{n}_{1/f}$ in MATLAB is given in Appendix G.2. The ASD of $\mathrm{n}_{1/f}$ is presented by the dash yellow curve in Figure 5.3.

5.2.2 Photodetector noise

The applied photodetector (PD) is PDA50B2 from Thorlabs [100]. Its active area is made of germanium (Ge), which reacts to near-infrared laser beams from 800 to 1800 nm. Its responsivity is 0.85 A/W for the 1550 nm laser. The photodetector works in the photo-conductive mode, and tends to produce a larger dark current than the one that works in the photo-voltaic mode. This is the reason for why the dark current is presented in the model. The simulation of the noise floor of the first photodetector n_{PD1} in Volt is

$$n_{\mathrm{PD1}} = G_1 \left[Z_{\mathrm{R1}}(n_{\mathrm{s}} + n_{\mathrm{d}} + n_{\mathrm{a}}) + n_{1/f} + n_{\mathrm{te}} \right] \quad (\mathrm{V}) \tag{5.17}$$

where shot noise n_s, dark current noise n_d and ambient light noise n_a are regarded as current fluctuations. They are converted into voltage signals by the resistance of the photodetector Z_R1. Thermoelectric noise n_te can be estimated with respect to the photodetector's circuit and $1/f$ noise is estimated by measurements. All noises are amplified by G_1. n_PD1 is the noise floor of photodetector, and is defined as the PD noise in this thesis.

Dark current noise

Dark current noise is the statistical variation of the charge generation of the photodetector even when no photons are entering. The ASD of dark current noise $\mathrm{A_{n_d n_d}}$ can be defined as [149]

$$\mathrm{A_{n_d n_d}} = \sqrt{I_\mathrm{SAT}(e^{\frac{qV}{k_\mathrm{B}T}} - 1)} \quad (\mathrm{A}/\sqrt{\mathrm{Hz}}) \tag{5.18}$$

where I_SAT is the reverse saturation current, which varies with temperature and is not a constant for a given device [150]. V is the applied bias voltage, $q = 1.60 \times 10^{-19}$ C is the electron charge, $k_\mathrm{B} = 1.380\,648\,52 \times 10^{-23}$ J/K is the Boltzmann's constant and $T = 297.15$ K is the Kelvin temperature.

Concerning the dark current noise, it relates to the type of the photodetectors: the photo-conductive or the photo-voltaic type. Generally, the photo-voltaic type has a better sensitivity by minimising dark current, and the photo-conductive type has an extended response by a reverse bias [70]. However, the bias voltage is responsible for current leakage even when no laser is detected. Photo-voltaic detectors, on the other hand, do not require a bias voltage, and do not present the current leakage. Therefore, there is a trade-off between using the photo-conductive and photo-voltaic detectors.

The photo-conductive detectors are used in the prototype for the extended response. However, the reverse saturation current and the applied bias voltage are not given in the specifications of the photodetector, so the current dark noise is not modelled directly. Alternatively, the PD noise including dark current noise is measured by the experiment discussed in Section 5.2.2.

Shot noise

Shot noise, or Schottky noise, is caused by the discrete nature of photons and electrical charges across potential barriers, such as diodes, transistors or p–n junctions [149]. Two photons with the same energy will not create the same number of electron-hole pairs. Consequently, the photo-current generated fluctuates. The ASD of shot noise is given by [151]

$$\mathrm{A_{n_s n_s}} = \sqrt{2qI_\mathrm{PD}} \quad (\mathrm{A}/\sqrt{\mathrm{Hz}}) \tag{5.19}$$

where $I_{\rm PD}$ is the average photo-current that crosses the barrier. Shot noise is proportional to the square root of the photo-current, because a higher current causes more random motion which leads to a higher shot noise. The ASD of shot noise is measured by experiments discussed in Section 5.2.2.

PD noise identification

The identification of PD noise includes two tasks; the first task is to select the best gain factor. The photodetector is measured without a laser beam, therefore, the shot noise owing to the laser is exclusive in measurements.

Figure 5.4 presents the scheme of the experiment to measure the noise floor of the photodetector. The photodetector is located inside a vacuum chamber, which decreases air fluctuations and blocks ambient light, therefore, the shot noise is minimised and can be neglected. The laser source is outside the chamber and the laser beam is fed through the chamber by a polarisation-maintaining optical fibre. The signals of the two photodetectors are recorded by two channels of the DAQ. The vacuum system and the feedthroughs for optical and electrical communication between inside and outside of the chamber are presented in Appendix F. The signal from the photodetector is recorded by the DAQ, and processed by MATLAB.

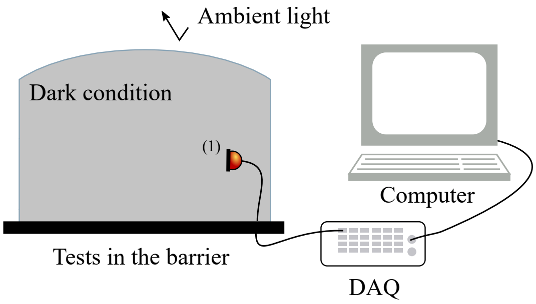

Figure 5.4: Scheme of experiment to measure the photodetector noise without laser: (1) photodetector in measurements.

The gain factors settings can be 0 to 70 dB in 10 dB steps, and the ASD of noise floors measured at 0 to 50 dB are shown in Figure 5.5. Meanwhile, the DAQ noise (dash black curve) is presented in the figure for comparison. The noise floors measured at 30 dB (purple curve), 40 dB (green curve) and 50 dB (cyan curve) are shown in the figure. They are dominated by the $1/f$ noise, in frequencies below 400 Hz, and by the thermoelectric noise, above 400 Hz. The difference of their amplitude is caused by their gain factors with difference 10 dB. Their curves. Because they are higher than the DAQ noise, they are not used in measurements.

The noise floors measured at 0 dB (blue curve), 10 dB (red curve) and 20 dB (yellow curve) are not higher than the DAQ noise, and thus their ASD are dominated by the DAQ noise. Because a high gain of the photodetector means that reaching it maximum output

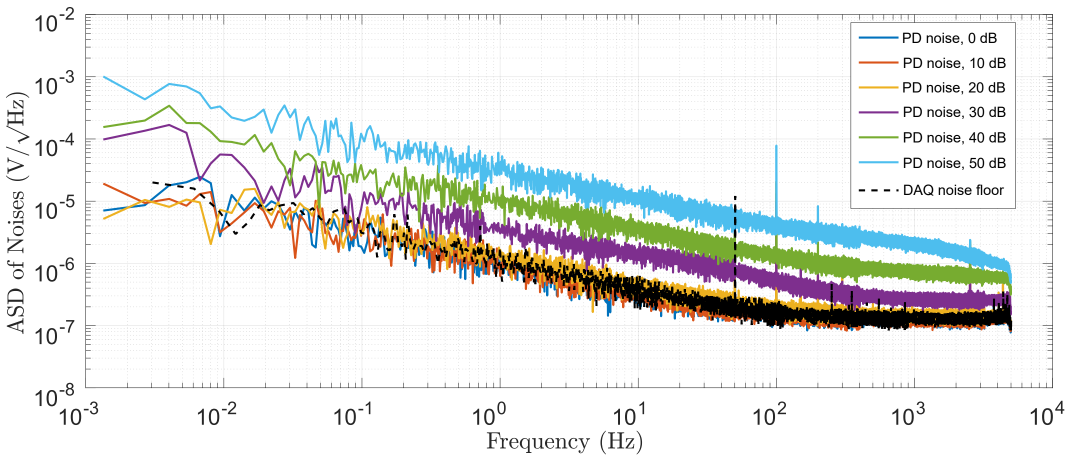

Figure 5.5: Noise floors of photodetector with different gain factors.

requires low laser intensity, the gain factor of the photodetector is selected as 20 dB.

The second task is to evaluate PD noise when the laser is switched on. As shown in Figure 5.6, the experiments follow the working principle of the huddle test, which will be discussed in Section 6.1. The laser beam passes through the collimator (4) and is divided by a non-polarising beam splitter (3) into two equal beams. The first photodetector (1) measures one beam and the second photodetector (2) measures the other. The coherent part of the two signals evaluates the laser intensity which is discussed in Section 5.2.3, and the incoherent parts of the two signals are noises in individual photodetectors. The photodetectors are located inside a vacuum chamber which blocks ambient light. Therefore, the measured PD noise includes shot noise, dark current noise, ambient light noise, thermoelectric noise and $1/f$ noise.

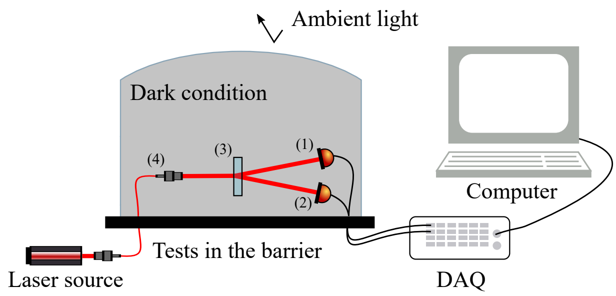

Figure 5.6: Scheme of experiment to measure the photodetector noise with laser: (1) the first photodetector in measurements, (2) the second photodetector in measurements, (3) non-polarising beam splitter (50:50), (4) laser collimator with polarisation-maintaining optical fibre.

Figure 5.7 shows the ASD of the measured and simulated PD noise at 20 dB. The DAQ noise (dash black curve) is shown in the figure for the comparison. The PD noise without laser (solid yellow curve) is the minimum voltage, which is equivalent to the photodetector measuring destructive interference in the interferometric readout. With laser, the maximum voltage of the photodetector is 10 V, which is equivalent to the photodetector measuring

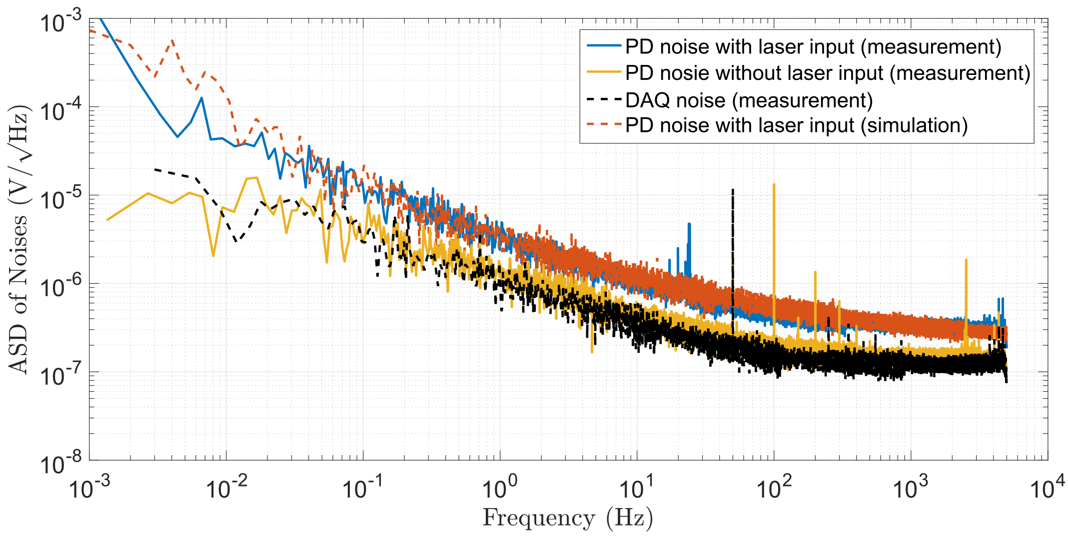

Figure 5.7: Noise floors of photodetector at 20dB with different inputs.

constructive interference in the interferometric readout. In order to generate a high voltage level around 9.6 V, the laser laser intensity is 1.6 mW. The PD noise with laser (solid blue curve) is 5 times higher than the PD noise without laser, this difference is provided by shot noise. When photodetectors measure interference in the interferometric readout, the ASD of the PD noise varies between the solid yellow curve and dash blue curve. In order to simulate PD noise including shot noise, the simulated PD noise is based on the measured PD noise with laser. Because of the same gap between the solid blue curve and the dash black curve from 0.02 to 5 kHz, the PD noise including shot noise can be simulated by

$$n_{\mathrm{PD1}} = c_1(n_{1/f} + n_{\mathrm{te}}) \quad (\mathrm{V}) \tag{5.20}$$

where $c_1 = 5$ is the ratio to generate the gap between the dash blue curve and the dash black curve, the parameters of $1/f$ noise and thermoelectric noise are discussed in Section 5.2.1 and 5.2.1. It is worth noting that the PD noise and DAQ noise in the three channels are incoherent.

Ambient noise to photodetector

The photodetector also senses ambient light. Figure 5.8 presents the experiment which measures ambient light. The cover of the vacuum chamber is removed, so the natural light propagates through the cover and influences the photodetector.

Figure 5.9 presents the measurement of natural light. The DAQ noise (solid black curve) is shown in the figure for the comparison. The measurement of natural light (blue curve) shows that the photodetector reacts to natural light. Therefore, all measurements in the thesis are performed in the dark condition, as a result, natural light is not included in the simulation.

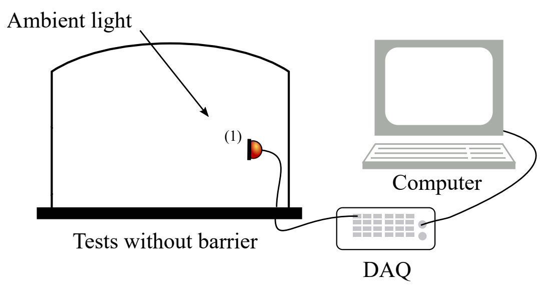

Figure 5.8: Scheme of experiments to measure ambient light: (1) photodetector in measurements.

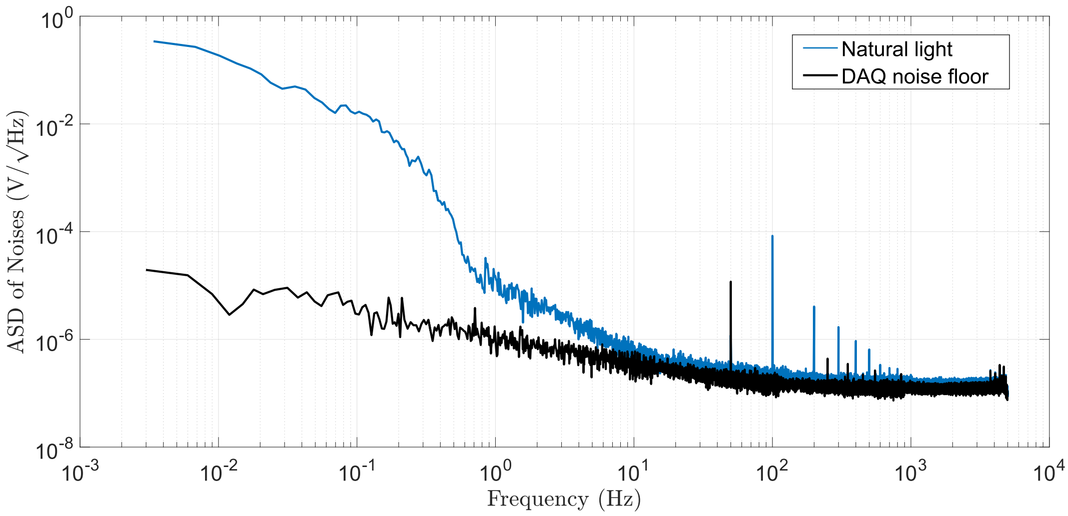

Figure 5.9: Noise floors of photodetector at 20dB with different inputs.

5.2.3 Laser noise

The laser used in this thesis is Koheras X15 from NKT Photonics [152]. It emits 1550.12 nm laser beam with maximum intensity of 30 mW, and with laser intensity noise and laser frequency noise.

Intensity noise

Laser intensity noise (or amplitude noise) is the fluctuation of the laser intensity, and is a typical noise generated by a single-frequency laser source. The intensity noise is represented in equation (5.2) by additional fluctuations of the intensity n_{i}. The origin of intensity noise has been investigated in reference [153]. In practice, the Relative Intensity Noise (RIN) is often used to express the relationship between pure intensity and the noise. The RIN(dB) is often described in dB or dB/Hz. It is calculated by [154]

$$\mathrm{RIN(dB)} \equiv 10\log_{10}\left(\frac{\langle n_{\mathrm{i}}(t)^2\rangle}{{P_0}^2}\right) \quad \mathrm{(dB)} \tag{5.21}$$

where, the $\langle\,\rangle$ denote the time average, $\langle n_{\mathrm{i}}(t)^2\rangle$ is the mean-square of the assumed Gaussian noise distribution. Moreover, $n_{\mathrm{i}}(t)$ can be converted into signal-sided power spectral density $\mathrm{P}_{\mathrm{n_i n_i}}$, the RIN(dB/Hz) with respect to its PSD of the noise is [154]

$$\mathrm{RIN(dB/Hz)} = \frac{\mathrm{RIN(dB)}}{B} = \frac{\mathrm{P}_{\mathrm{n_i n_i}}}{{P_0}^2} \quad \mathrm{(dB/Hz)} \tag{5.22}$$

where B is the bandwidth of the measurement expressed in Hz. The RIN(dB/Hz) from 0.1 to 10 MHz measured by the manufacturer are given in Appendix E. However, as this thesis focuses on the frequency range from 0.01 to 10 Hz, in order to obtain the ASD of the intensity noise, the setup shown in Figure 5.6 has be used to measure the intensity noise by huddle tests.

Figure 5.10 presents the ASD of the intensity noise (solid blue curve) measured by two photodetectors working at 20 dB. As in the previous discussion about Figure 5.6, the incoherent parts of the two signals are the noises from each photodetector. The coherent part of the two signals is the noisy intensity P_{n} measured by the two photodetectors. Its DC component is the voltage with respect to P_0 and the AC components are voltages with respect to noise intensity. According to equation (5.9), the converting factor between the laser intensity and the voltage is $c_2 = G_1 Z_{\mathrm{R_1}} \mathfrak{R}_1$.

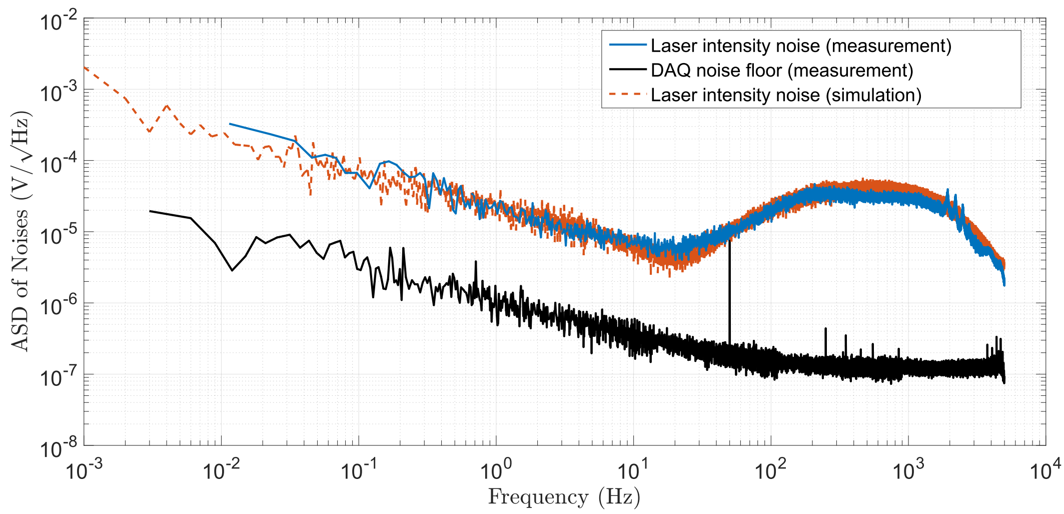

Figure 5.10: Intensity noise measured by the huddle test of two photodetectors.

The shape of the ASD is caused by the laser source, which is out of the discussion. The laser intensity is 1.6 mW. The DAQ noise is the dash black curve in the figure for the comparison. For the frequencies less than 20 Hz, the voltage of intensity noise is almost 20 times higher than the ASD of DAQ noise. The simulated intensity noise is modelled by filtering white noise, and its ASD is shown by the dash red curve in the figure. The function of the filter and the code to obtain the simulated intensity noise by MATLAB is given in Appendix G.4.

Intensity noise treatment

Because the intensity noise in the three photodetectors of an interferometric readout are coherent, it can be reduced by data processing. Three photodetectors are used in the interferometric readout to reduce the intensity noise. A simulation is performed to compare the data processing with quadrature signals of two photodetectors and three photodetectors. The simulation is based on the model shown in Figure 5.2. The input motion y in the time domain is defined by

$$y = \frac{\lambda}{T}t + 1 \times 10^{-15}n \quad (\mathrm{m}) \tag{5.23}$$

where t is the time series from 0 to T, and it has internal t_s =0.0001 s. $T =$ 1000 s is the duration of the simulation, and n is white noise with mean value equals 1. The first item $\frac{\lambda}{T}t$ in the right side presents a linear motion from 0 to λ in the simulation. According to equation (3.7), its phase is $\frac{2\pi}{T}t$, which varies from 0 to 2π to generate a full Lissajous circle. Therefore, extra simulated calibration signals are unnecessary in the simulation. The second item $1 \times 10^{-15}n$ introduces a broadband noise floor for the comparison.

Assuming the intensity noise is the only noise source in measurements, the voltage signals measured by the three photodetectors are

$$V_{\mathrm{PD1}} = G_1 Z_{\mathrm{R}_1} \Re_1 \cdot \frac{P_0 + n_\mathrm{i}}{8}\big(1 + \cos(2\phi_\mathrm{y})\big) \tag{5.24}$$

$$V_{\mathrm{PD2}} = G_2 Z_{\mathrm{R}_2} \Re_2 \cdot \frac{P_0 + n_\mathrm{i}}{8}\big(1 + \sin(2\phi_\mathrm{y})\big) \tag{5.25}$$

$$V_{\mathrm{PD3}} = G_3 Z_{\mathrm{R}_3} \Re_3 \cdot \frac{P_0 + n_\mathrm{i}}{8}\big(1 - \sin(2\phi_\mathrm{y})\big) \tag{5.26}$$

where ϕ_y is the phase with respect to y. $G_1 \simeq G_2 \simeq G_3 \simeq 10$ are gain factors of the three photodetectors, respectively. $Z_{\mathrm{R}_1} \simeq Z_{\mathrm{R}_2} \simeq Z_{\mathrm{R}_3} \simeq 1.51 \times 10^3$ V/A are the resistance of the circuit. $\Re_1 \simeq \Re_2 \simeq \Re_3 \simeq 0.85$ A/W are factors of responsivity. The non-linearities, losses and other noises are not considered in this simulation.

According to equations (3.44) and (3.45) in Chapter 3.4, the DC gains and offsets from the three signals can be estimated from the calibration. The DC components of the laser intensity noise are ignored in this discussion. The three normalised signals are

$$N_{\mathrm{PD1}} = \frac{V_{\mathrm{PD1}} - \bar{b}_1}{\bar{g}_1} = (1 + \frac{n_\mathrm{i}}{P_0})\cos(2\phi_\mathrm{y}) + \frac{n_\mathrm{i}}{P_0} \tag{5.27}$$

$$N_{\mathrm{PD2}} = \frac{V_{\mathrm{PD2}} - \bar{b}_2}{\bar{g}_2} = (1 + \frac{n_\mathrm{i}}{P_0})\sin(2\phi_\mathrm{y}) + \frac{n_\mathrm{i}}{P_0} \tag{5.28}$$

$$N_{\mathrm{PD3}} = \frac{V_{\mathrm{PD3}} - \bar{b}_3}{\bar{g}_3} = -(1 + \frac{n_\mathrm{i}}{P_0})\sin(2\phi_\mathrm{y}) + \frac{n_\mathrm{i}}{P_0} \tag{5.29}$$

where $\bar{g}_1 = \bar{b}_1 = G_1 Z_{R_1} \Re_1 P_0/8, \bar{g}_2 = \bar{b}_2 = G_2 Z_{R_2} \Re_2 P_0/8$ and $\bar{g}_3 = \bar{b}_3 = G_3 Z_{R_3} \Re_3 P_0/8$ are the DC gains and offsets from the signals V_{PD1}, V_{PD2} and V_{PD3} respectively.

When two photodetectors are used in measurements, quadrature signals can be found in equation (5.27) and (5.28) as

$$Q_{\sin} = N_{\mathrm{PD2}} \tag{5.30}$$

$$Q_{\cos} = N_{\mathrm{PD1}} \tag{5.31}$$

where $Q_{\sin}$ and $Q_{\cos}$ are the quadrature signals from measurements by two photodetectors.

As no phase offset is present in the simulation, the ellipse fitting is not required for this data processing. In practice, the **atan2** function in MATLAB is used to recover the measured phase. However, in order to simplify the discussion, $2\phi_{\mathrm{y}}$ is assumed within $(-\frac{\pi}{2}, \frac{\pi}{2})$, and the arctangent function is used

$$2\hat{\phi_{\mathrm{y}}} = \arctan\big(\frac{Q_{\sin}}{Q_{\cos}}\big) = \arctan\big(\frac{(1+\frac{n_{\mathrm{i}}}{P_0})\sin(2\phi_{\mathrm{y}}) + \frac{n_{\mathrm{i}}}{P_0}}{(1+\frac{n_{\mathrm{i}}}{P_0})\cos(2\phi_{\mathrm{y}}) + \frac{n_{\mathrm{i}}}{P_0}}\big) \tag{5.32}$$

where, $2\hat{\phi_{\mathrm{y}}}$ is the measured phase. Applying the series expansion around $n_i \simeq 0$, equation (5.32) gives

$$\begin{aligned} 2\hat{\phi_{\mathrm{y}}} &= \arctan\big(\frac{\sin(2\phi_{\mathrm{y}})}{\cos(2\phi_{\mathrm{y}})}\big) + \frac{\cos(2\phi_{\mathrm{y}}) - \sin(2\phi_{\mathrm{y}})}{P_0} n_{\mathrm{i}} + \mathrm{O}(n_{\mathrm{i}}^2) \\ &= 2\phi_{\mathrm{y}} + \frac{\cos(2\phi_{\mathrm{y}}) - \sin(2\phi_{\mathrm{y}})}{P_0} n_{\mathrm{i}} \end{aligned} \tag{5.33}$$

where $\mathrm{O}(n_{\mathrm{i}}^2)$ is disregarded because of $n_{\mathrm{i}} \simeq 0$. Likewise, the equation shows that the contribution of the intensity noise depends on the measured phase.

In order to eliminate the item of intensity noise contribution $\frac{n_{\mathrm{i}}}{P_0}$, quadrature signals can be obtained from the subtraction of the three signals, and they are

$$\begin{aligned} Q_{\sin} &= N_{\mathrm{PD1}} - N_{\mathrm{PD3}} \\ &= \sqrt{2}(1+\frac{n_{\mathrm{i}}}{P_0})\sin(2\phi_{\mathrm{y}} + \frac{\pi}{4}) \end{aligned} \tag{5.34}$$

$$\begin{aligned} Q_{\cos} &= N_{\mathrm{PD1}} - N_{\mathrm{PD2}} \\ &= \sqrt{2}(1+\frac{n_{\mathrm{i}}}{P_0})\cos(2\phi_{\mathrm{y}} + \frac{\pi}{4}) \end{aligned} \tag{5.35}$$

where $Q_{\sin}$ and $Q_{\sin}$ are quadrature signals obtained by using three photodetectors. The measured phase is

$$
\begin{aligned}
2\hat{\phi}_y &= \arctan\left(\frac{Q_{\sin}}{Q_{\cos}}\right) = \arctan\left(\frac{\sqrt{2}(1+\frac{n_i}{P_0})\sin(2\phi_y+\frac{\pi}{4})}{\sqrt{2}(1+\frac{n_i}{P_0})\cos(2\phi_y+\frac{\pi}{4})}\right) - \frac{\pi}{4} \\
&= \arctan\left(\frac{\sin(2\phi_y+\frac{\pi}{4})}{\cos(2\phi_y+\frac{\pi}{4})}\right) - \frac{\pi}{4} \\
&= 2\phi_y
\end{aligned} \tag{5.36}
$$

where $\pi/4$ is applied to compensate the extra $\pi/4$ in sine and cosine functions. As shown by equation (5.36), the laser intensity noise is effectively removed by using three photodetectors.

Figure 5.11 shows the model to simulate the data processing by using two or three photodetectors. In order to simplify the discussion, only the DAQ noise including $1/f$ noise, thermoelectric noise and quantisation noise and intensity noise are applied in the model. The ASD of simulated DAQ noise is presented in Figure 5.3 and the ASD of the simulated intensity noise is presented in Figure 5.10. Moreover, they are incoherent in different channels.

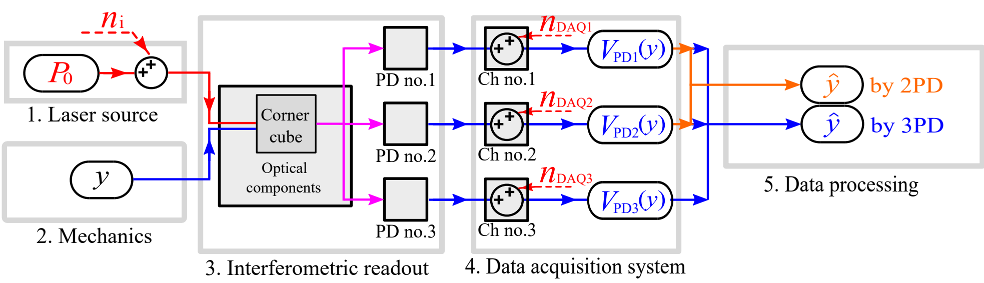

Figure 5.11: Diagram of the model to simulate the measurement by using two photodetectors and three photodetectors: unmarked symbols and lines are as the same as in Figure 5.2. The fifth section is the data processing to recover the measured relative displacement. The orange lines with arrows: the data processing with two photodetectors; $\hat{y}$ in orange is the measured relative motion by using two photodetectors; $\hat{y}$ in blue is the measured relative motion by using three photodetectors; n_{DAQi} i= 1, 2, 3 are the DAQ noise in the three channels and they are incoherent.

Figure 5.12 shows the comparison of simulated measurements by using interferometric readout with two or three photodetectors. The ASD of the input y (in equation (5.23)) is dash black curve in the figure. Its noise floor from 0.01 to 5 kHz has the amplitude 1×10^{-15} m, which is the contribution of the second item in equation (5.23). The motion is measured by the simulation system with DAQ noise and intensity noise. The dash red curve shows the ASD of the motion measured by two photodetectors, and the shape of the curve contains the residual of intensity noise. The solid blue curve shows the ASD of the motion measured by three photodetectors. Because the amplitude of the DAQ noise is higher than the noise floor of the input signal, the DAQ noise dominates its noise floor.

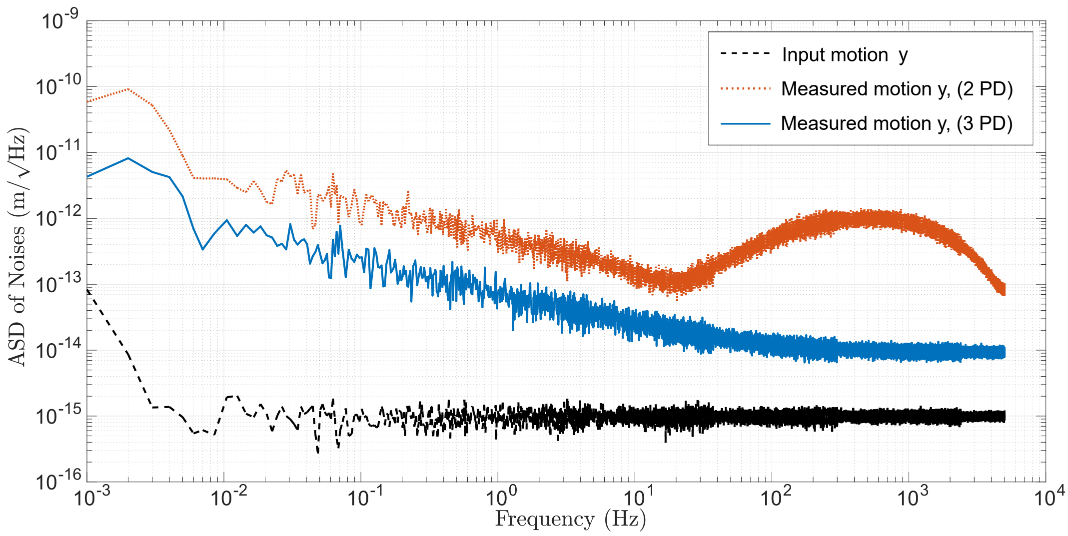

Figure 5.12: Comparison between the effect of intensity noise in the simulated measurements done by using two photodetectors and three photodetectors.

In conclusion, obtaining quadrature signals from subtraction helps to reduce the laser intensity noise. If the laser intensity noise is less than the DAQ noise, the use of an extra photodetector is not necessary. In this thesis, three photodetectors are used for the interferometric readout.

Frequency noise and phase noise

Another noise arising from the laser source is laser frequency noise for example the thermal effect and mechanical vibration of components [155]. Therefore, the central frequency of single-frequency laser sources is accompanied by a frequency noise. The central frequency with noise can be measured by a Frequency Discriminator (FD) method or self-heterodyne method [154]. In practice, interferometers with equal arms are unaffected by the noise. Alternatively, laser frequency noise can be converted into phase noise which affects measurements. The relationship between phase noise and laser frequency noise is [156]

$$\mathrm{A}_{\mathrm{n_p n_p}} = 2\pi \frac{n \cdot L_{\mathrm{OPD}}}{c} \mathrm{A}_{\mathrm{n_\nu n_\nu}} \quad (\mathrm{rad}/\sqrt{\mathrm{Hz}}) \tag{5.37}$$

where, $\mathrm{A}_{\mathrm{n_p n_p}}$ is the ASD of the phase noise, $\mathrm{A}_{\mathrm{n_\nu n_\nu}}$ is the ASD of the laser frequency noise, $n \simeq 1$ is the refractive index in propagation, $c = \lambda\nu = 299\,792\,458$ m/s is the speed of the laser beam, and L_{OPD} is the length of optical path difference (OPD).

The phase noise of the laser source is measured by the manufacturer with respect to 1 m OPD, which is shown in Appendix E. Figure 5.13 shows the ASD of the phase noise from 1 Hz to 10 kHz by the circle-marked red curve. Its ASD below 1 Hz is estimated with respect to the slope of -0.5 according to the technical report [157]. Therefore, the ASD of the phase noise with respect to 1 m OPD is presented by the solid blue curve. Due to the assembly of the VINS and HINS, the static OPD of VINS is around 10 cm and the static OPD of HINS is around 1 cm. Therefore, the phase noise with respect to 0.1 m OPD (solid red curve) and 0.01 m OPD (solid yellow curve) estimated by equation (5.37) are shown in the figure for the comparison.

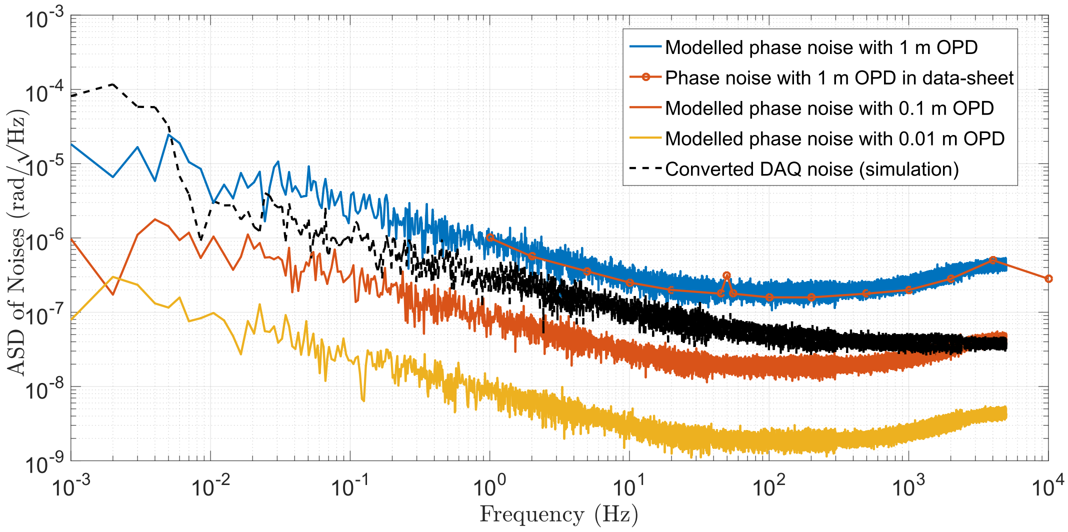

Figure 5.13: Phase noise simulated with different OPD.

In order to compare the phase noise with DAQ noise, the simulated DAQ noise (in Figure 5.12) is converted into the unit of rad/$\sqrt{\mathrm{Hz}}$. The converting factor is $2\pi/\lambda$. When compared to the curves of DAQ noise, phase noise with 0.1 m OPD and phase noise with 0.01 m OPD, demonstrates that DAQ noise is still higher than the phase noise. Therefore, it is assumed that the interferometric readout is insensitive to frequency noise and the related phase noise. The method to generate phase noise in the simulation is given in Appendix G.3. In the future, if the DAQ and PD are improved with a lower noise floor, the OPD of VINS and HINS have to be modified to ensure the phase noise is low in the system.

5.2.4 Mechanics noise

Thermomechanical noise n_{tm} is the thermal fluctuation of the proof-mass and it is a dominant noise source in inertial sensors. According to the different working condition, the thermomechanical noise can be simulated in terms of different dissipation effects [137]. Concerning viscous damping, several sources including gas and eddy current give the damping force proportional to velocity. The ASD of the fluctuation is

$$\mathrm{A}_{\mathrm{n_{tm}n_{tm}}} = \sqrt{\frac{4k_{\mathrm{B}}Tm\omega_0/Q}{(k - m\omega^2)^2 + (m\omega_0/Q)^2\omega^2}} \quad (\mathrm{m}/\sqrt{\mathrm{Hz}}) \tag{5.38}$$

where $k_{\mathrm{B}} = 1.380\,648\,52 \times 10^{-23}$ J/K is the Boltzmann's constant, $T = 297.15$ K is the Kelvin temperature and ω is the angular frequency. According to the mechanics, the proof mass m, the quality factor (Q factor), the resonance frequency in rad and the stiffness can be found.

The thermomechanical noise can be also simulated in terms of internal damping, which is caused by the dissipation of the material. The ASD of the fluctuation is

$$\mathrm{A}_{\mathrm{n_{tm}n_{tm}}} = \sqrt{\frac{4k_{\mathrm{B}}Tk/Q}{\omega[(k-m\omega^2)^2+k^2/Q^2]}} \quad (\mathrm{m}/\sqrt{\mathrm{Hz}}) \tag{5.39}$$

The selection of the estimations depends on the type of damping, with viscous damping, equation (5.38) is valid. Otherwise, equation (5.39) is more realistic. Normally, when the inertial sensor works in air, the former is dominant and this is the reason why the high resolution inertial sensors are preferred operating in vacuum [137]. In the vacuum, the latter is dominant. The relationship between the Q factor of folded pendulum and vacuum levels were studied by Acernese *et al.* [158], and it shows that the value of Q factor increase with higher vacuum level. However, because the inertial sensors mounted with the voice coil actuator (VCA), the Q factor is found to be limited by viscous damping related the eddy currents and is independent to the pressure.

Because the proof mass is $m = 0.3$ kg, the quality factor (Q factor) is $Q = 3$ and the resonance frequency is $f_0 = 0.11$ Hz, the stiffness $k = m(2\pi f_0)^2 = 0.14$ N/m and the resonance $\omega_0 = 2\pi f_0 = 0.69$ rad can be found. The ASD of the thermomechanical noise (dash blue curve) is simulated in Figure 5.14, its value is shown by the left vertical axis. When the measured relative motion is converted to the absolute motion, the thermomechanical noise is reshaped by multiplying by the inverse transmissibility, of the mechanics T_{WY}^{-1}, which is

$$T_{\mathrm{WY}}^{-1} = \frac{W(s)}{Y(s)} = \frac{s^2 + \frac{2\pi f_0}{Q}s + (2\pi f_0)^2}{-s^2} \tag{5.40}$$

The inverse transmissibility (solid red curve) is given in Figure 5.14, its value is shown by the right vertical axis. The ASD of the reshaped thermomechanical noise (solid blue curve) can be estimated by the original noise multiplied by the inverse transmissibility, its value is shown by the left vertical axis. Consequently, the thermomechanical noise presented in input motion has a slope of -2.5 in the frequency domain.

There are several aspects to increase the Q factor thus to reduce thermomechanical noise. The first is about the use of the VCA. If the VCA is removed or the effect of the eddy current treated by shielding or using superconducting material [159], the Q factor related the eddy current can be increased. The second is about the pressure, high vacuum level helps to increase the Q factor. The Q factor of the mechanics in the high vacuum will be tested in the future. The third is to use high Q factor material [160]. For example fused silica [161, 162, 163]) or silicon nitride photonic crystal [164] can be used for the mechanics. The

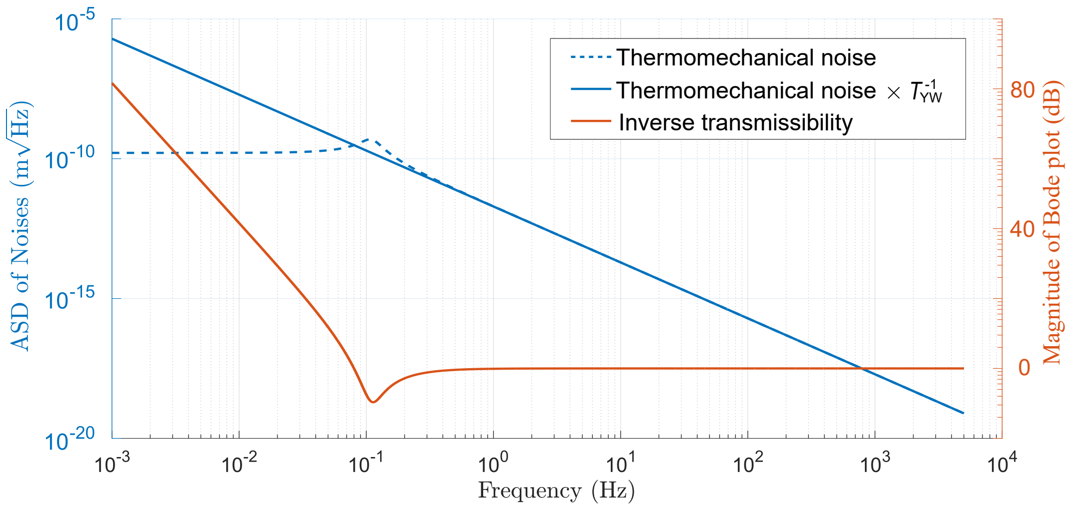

Figure 5.14: Simulated thermomechanical noise and the inverse transmissibility of the mechanics: The left axis (blue) is in the unit of $\mathrm{m}/\sqrt{\mathrm{Hz}}$ to show the ASD of thermomechanical noise, the right axis (red) is in the unit of dB to show the inverse transmissibility of the mechanics.

fourth is to decrease the temperature. van Heijningen [159] predicted the performance of the inertial sensor operating at cryogenic temperatures.

5.2.5 Ambient noise

The effect of ambient noise on photodetectors is discussed in Section 5.2.2. Moreover, the pendulum and the optical components are sensitive to unwanted seismic vibration, temperature and pressure fluctuations. All can excite the pendulum with extra motion, and cause extra relative motion between optical components [165]. In order to reduce the seismic noise, an isolation system or rigid optical components holders are required, to reduce the temperature and pressure influence, the sensors can be placed in vacuum chambers. Another option is to remove the effect of ambient fluctuations by monitoring signals [166, 167, 168]. In addition, the optical elements have to be placed in a compact [169] monolithic holder made of a material with a low thermal expansion coefficient for example Zerodur, fused silica [170].

5.3 Noise budgeting

The noise sources in the data acquisition system, in the photodetectors, in the laser source and in the mechanics are discussed here. According to the model of the noise sources, their effects on the resolution of the inertial sensor can be estimated with the noise budget and characterised by the blocked-mass test.

The blocked-mass test is a method to identify the noise floor of inertial sensors by restricting the motion of the proof-mass. By recalling equation 2.9 in Section 2.1, the resolution of the inertial sensor can be estimated by

$$A_r = \frac{A_{nn}}{|T_{WY}|} \tag{5.41}$$

where A_r is the ASD of the resolution, A_{nn} is the ASD of the interferometric readout noise in m/$\sqrt{\text{Hz}}$ and T_{WY} is the transmissibility of the HINS or VINS. Actually, the blocked-mass test includes no noise from the mechanics, but noises from its interferometric readout. The resolution of the interferometric readout is introduced in Chapter 3 and the parameters of the transmissibility of the HINS and VINS are given in Chapter 4.

As the relative motion between the pendulum and the frame is restricted, the non-linearities with respect to the pendulum motion are reduced in the test. The inertial sensors under development are to be used in isolation systems. When the isolation performance increases, the pendulum motion decreases, according, the blocked-mass test predicts the best resolution can be achieved.

5.3.1 Interferometric readout

Firstly, the output of interferometric readout from the blocked-mass test is studied. The setup and the measurement are shown in Section 3.5.2. Figure 5.15 shows the diagram of the model to simulate the measurement with different noise sources. They are intensity noise n_i, phase noise n_τ, PD noise n_{PDi} and DAQ noise n_{DAQi} i$= 1, 2, 3$. Moreover, the PD noise and DAQ noise in different channels are incoherent. The relative motion $y = 0 \cdot t$ is the input signal which equals to zero in the simulation. It indicates that the corner cube is blocked at the initial position. t is the time series of the simulation increasing from 0 to T, and it has internal t_s =0.0001 s. $T =$ 1000 s is the duration of the simulation. With the presence of noise, the measured $\hat{y}$ is dominated by the noise. Therefore, the ASD of the measured $\hat{y}$ with individual noise can represent the ASD of the noise in the unit of m/$\sqrt{\text{Hz}}$. By using this method, the ASD of phase noise n_τ, PD noise n_{PD} and DAQ noise n_{DAQ} can be simulated.

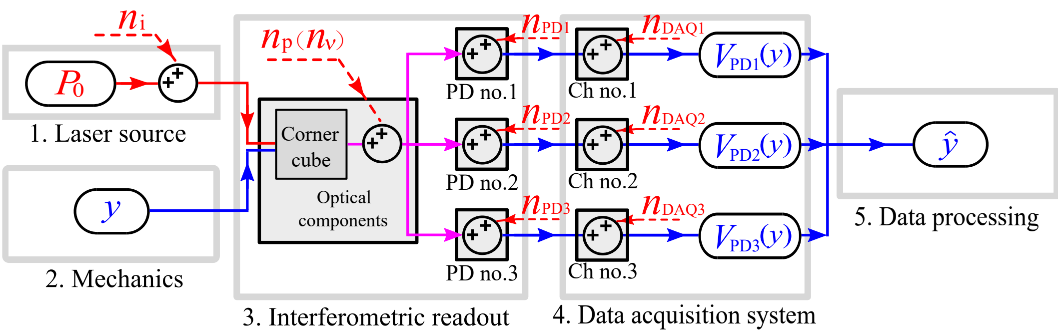

Figure 5.15: Diagram of the model to simulate the measurement and estimate the noise floor: unmarked symbols and lines are as the same as in Figure 5.2. The fifth section is the data processing to recover the measured relative displacement. n_{PDi} and n_{DAQi} i$= 1, 2, 3$ are the PD noise and DAQ noise in the three channels and they are incoherent.

Figure 5.16 shows the ASD of measurement and simulation of the interferometric readout. For the comparison, the solid blue curve shows the measured interferometric resolution (discussed in Section 3.5.2). The ASD of the DAQ noise (dash red curve) is shown in Figure 5.3 with the input relative motion y and noise sources $n_{\mathrm{q}}, n_{1/f}^{(2)}$ and $n_{\mathrm{te}}^{(2)}$). Following the same idea, the PD noise (solid yellow curve) can be simulated with the input relative motion y and the PD noise including noise sources $n_{\mathrm{s}}, n_{\mathrm{d}}, n_{1/f}^{(1)}$, and $n_{\mathrm{te}}^{(1)}$). The noise sources in the laser source are intensity noise n_{i} and frequency noise n_{ν}. According to the previous discussion, only the frequency noise may affect measurements, and it presents as phase noise in the interferometric readout. The estimation of the phase noise (dash purple curve) is simulated with an optical path difference of 10 mm. Its amplitude is lower than the noise dominated by the DAQ noise. The addition of the DAQ noise, the PD noise and the phase noise, it gives the theoretical interferometric readout resolution (solid black curve).

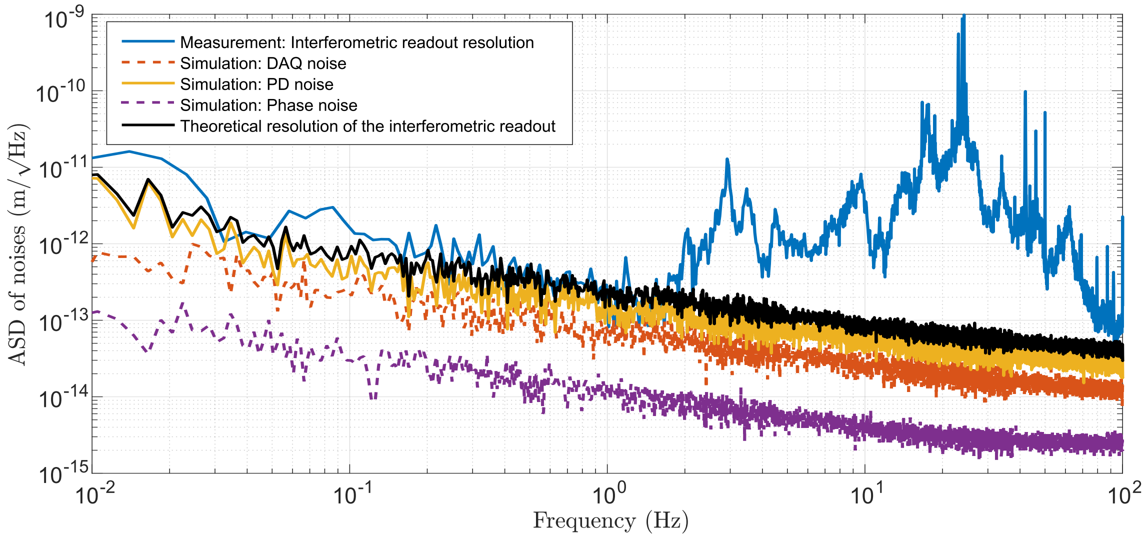

Figure 5.16: Noise budgeting of the interferometric readout from blocked-mass test.

Comparing the theoretical resolution and the measured resolution, it shows that from 0.01 to 2 Hz, the resolution of the interferometric readout is dominated by the PD noise, from 2 to 100 Hz, the measured resolution is dominated by the seismic noise. The seismic noise can be reduced by three processes. The first one is to perform the experiments where the ground motion is low. The second one is to improve the isolation performance of the experimental table. The third is to improve the mounting of the interferometric readout by using a monolithic frame or rigid optics holders, which helps to reduce the effect of seismic noise in the high frequency range [85].

5.3.2 Inertial sensor

According to equation (5.41), the resolution of VINS and HINS can be estimated by using the resolution of the interferometric readout multiplied by their inverse transmissibility. The transmissibility of the mechanics of the VINS and HINS are identified in Chapter 4. It is assumed that the inertial sensors work without the problem of tilt-horizontal coupling in the discussion.

Figure 5.17 present the noise budget of the HINS. According to equation (5.41), the noise of the interferometric readout is multiplied by the inverse transmissibility of the HINS. The solid blue curve is the measured interferometric resolution multiplied by the inverse transmissibility of the mechanics of the HINS, the curve between 0.01 to 0.11 Hz is increased. Following the same idea, the simulated interferometric noise multiplied by the inverse transmissibility of the HINS (solid black curve) is shown in the figure as well. When the pendulum is free in measurements, thermomechanical noise (dash green curve) affects the mechanics. Therefore, thermomechanical noise shown in the figure is to be considered in the overall noise floor. In conclusion, the theoretical noise floor of the HINS (dash red curve) is obtained by adding the thermomechanical noise and interferometric readout noise. It is dominated by the PD noise from 1 to 100 Hz and by the thermomechanical noise from 0.01 to 1 Hz.

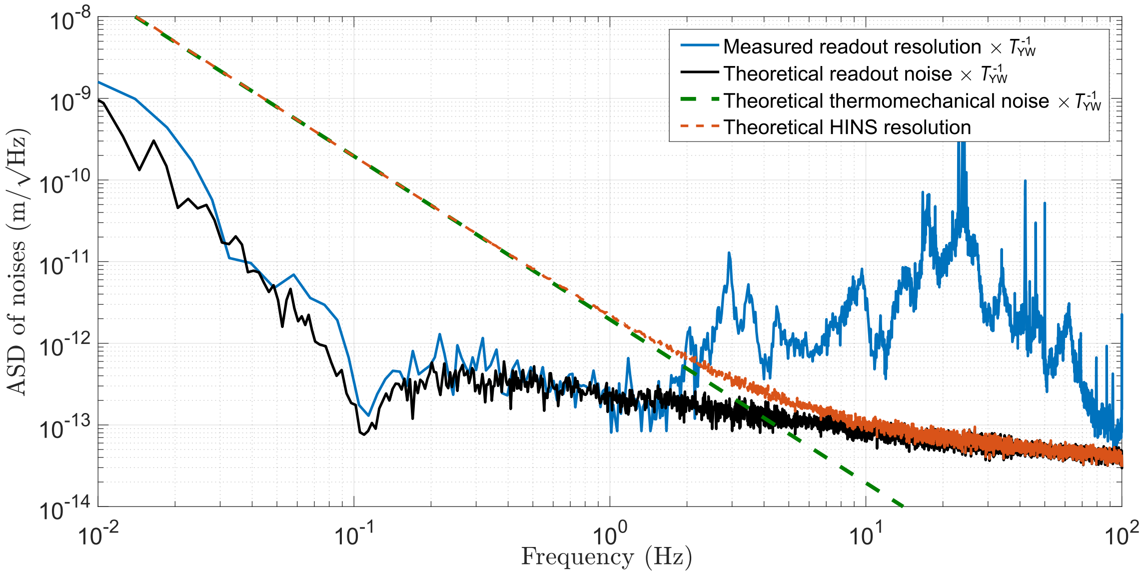

Figure 5.17: Theoretical resolution of the HINS.

The VINS has the same noise sources as the HINS. Figure 5.18 shows previously discussed noises reshaped with the inverse transmissibility of the mechanics of the VINS, the same as the theoretical resolution of the HINS. The theoretical resolution of the VINS (dash red curve) is dominated by the PD noise from 1 to 100 Hz and by the thermomechanical noise from 0.01 to 1 Hz.

The same type of mechanics is used in the accelerometer developed by Zumberge [92] and Otero [73]. Figure 5.19 shows a comparison between the resolution of the VINS (solid red curve) and prototypes, iSTS1 (solid blue curve) and iSeis (solid purple curve). As introduced in Section 2.1, the theoretical resolution of the VINS measuring acceleration is estimated. The figure shows the Power Spectral Density (PSD) of the resolution in the unit

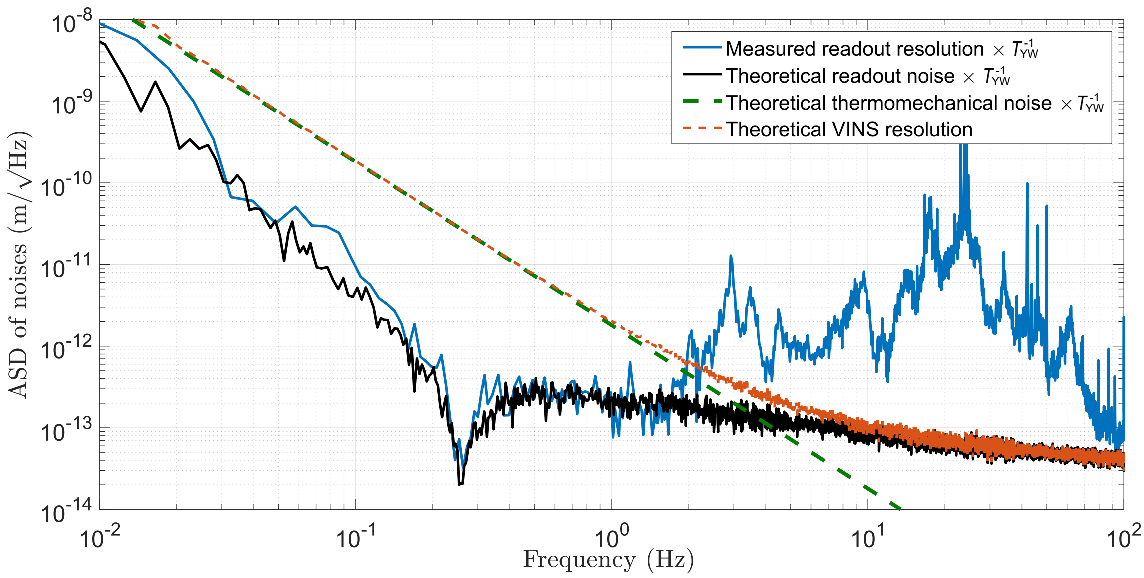

Figure 5.18: Theoretical resolution of the VINS.

of $(\mathrm{m/s^2})^2/\mathrm{Hz}$. Because of the similar mechanics, the resonance frequencies are close to each other. The different noise performance of the interferometric readouts and their different resonance frequencies contribute to the differences of the curves. The black curve is the Low Noise Model (LNM) estimated by the measurements from Global Seismographic Network (GSN), and it indicates the minimum acceleration of the ground. Since the curves of the three theoretical resolutions are lower than the black curve, the three prototypes are possible to measure the LNM.

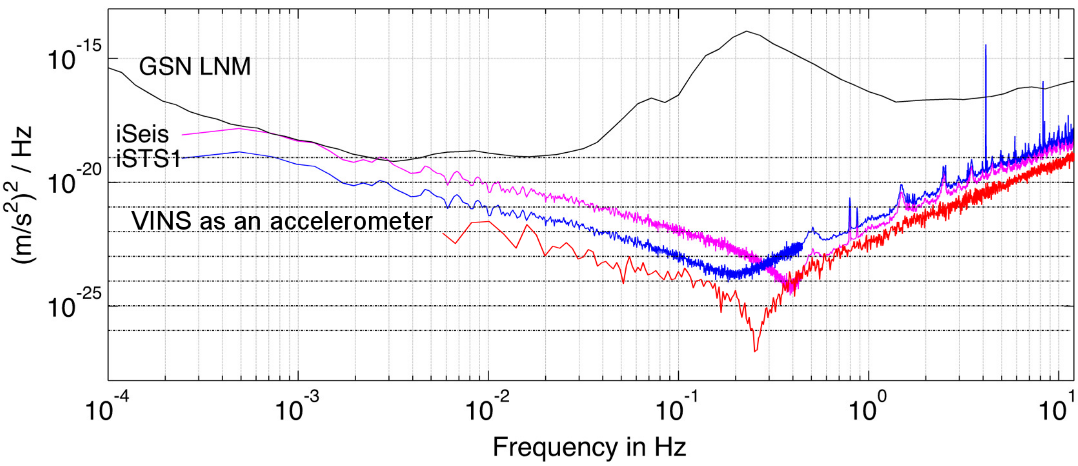

Figure 5.19: Comparison of the theoretical resolution of the VINS, iSeis and the iSTS1 [73]

Figure 5.20 shows the theoretical resolution of the HINS (solid blue curve) and VINS(dash red curve). The theoretical resolution of the VINS and the HINS is dominated by the thermomechanical noise in low frequencies and is dominated by the photodetector noise in high frequencies. Meanwhile, the geophone GS-13 (dash-dot grey curve) and seismometer T-240 (dash-dot black curve) are the best commercial inertial sensors used in the aLIGO (See

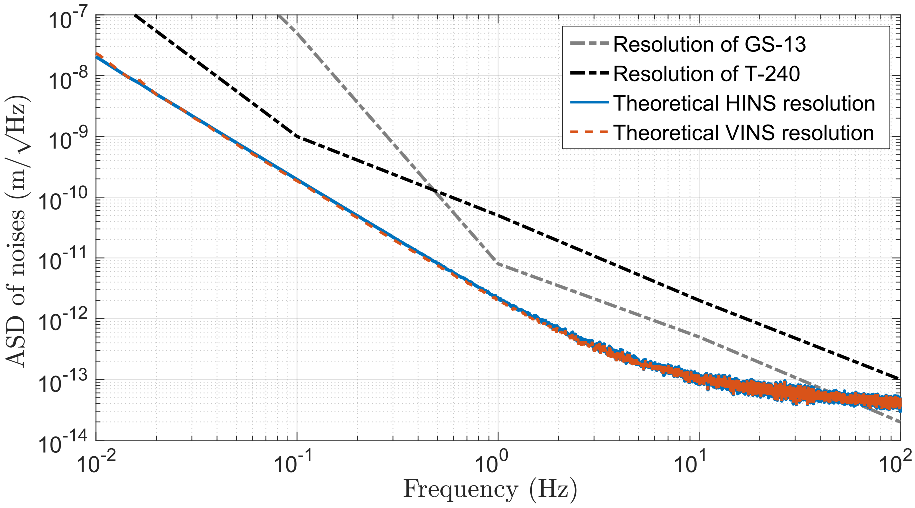

Figure 5.20: Comparison among the resolution of the HINS, VINS, geophone GS-13 and seismometer T-240 [38].

Figure 1.10). Their resolution are given in the figure for comparison. Both the resolution of the VINS and the HINS is better than the resolution of sensors GS-13 and T-240 from 0.01 to 30 Hz.

As mentioned at the beginning of the section, the tilt-horizontal coupling is not discussed. To make sure the inertial sensors are not affected by the tilting signal, the signal from a high-resolution tilt-meter is required to compare the signals. The resolution should be better than the level of thermomechanical noise, for example at least 0.1 $\mathrm{nrad}/\sqrt{\mathrm{Hz}}$ at 0.1 Hz. The development of the Liquid Absolute Tilt-meter (LAT) is presented in Appendix A.

5.4 Conclusion

This chapter presented a full model of VINS and HINS combining both the optoelectronic systems and the mechanical systems. Different noise sources were established for the simulation. Meanwhile, possibilities to decrease the effect of noises in measurements were discussed. The model was used as the basis for making noise budgeting. The predicted resolution based on this simulation matched well with that estimated by the experimental blocked-mass test. It was shown that the resolution below 1 Hz is dominated by the thermomechanical noise. The resolution from 1 to 100 Hz is currently limited by unwanted internal vibrations of the interferometric readout. Therefore, improvements are suggested in terms of reducing both noises. The internal vibration can be reduced by improving the mounting of the optical components. The thermomechanical noise can be reduced by increasing the Q factor, the priorities are the eddy current, the vacuum level, the material and the temperature. Once both noises are sufficient low, the noise of photodetector will limit the resolution. The improvement can be done by replacing the current Germanium (Ge) based photodetectors by the indium gallium arsenide (InGaAs) based one, which is reported having a better noise performance.

Chapter 6

Huddle test

This chapter discusses the resolution of the inertial sensors estimated by the huddle test. In Section 6.1, the working principle of the huddle test is demonstrated. Section 6.2 presents the results of the huddle test. In Section 6.3, the reasons cause high residual from the huddle test are discussed, which includes the reasons cause non-linearities in the measurement and incoherent excitations.

6.1 Working principle

The huddle test [171, 172] is often used to determine the incoherent noise of signals measured by multiple sensors. When at least two sensors are placed close to each other, they sense the same motion. However, due to the presence of unknown noise in both sensors, the two signals are not identical. The method will allow to extract the spectrum of the incoherent part of the signal, which will be considered as the resolution of the tested sensors.

Figure 6.1 presents a simplified working principle of the huddle test. Two inertial sensors are put side by side to measure ground motion W. Both inertial sensors are disturbed by incoherent noise sources N_1 and N_2.

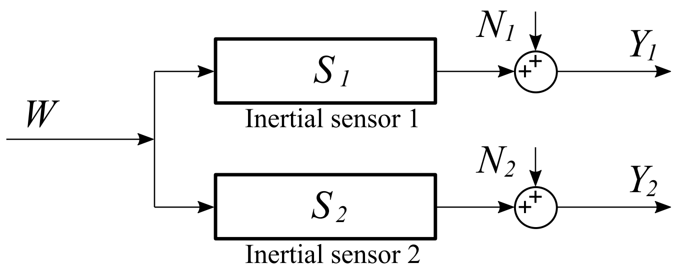

Figure 6.1: Working principle of huddle tests: W is ground motion, S_1 and S_2 are the sensitivities of the two sensors, N_1 and N_2 are noise sources and Y_1 and Y_2 are signals of the two sensor.

The outputs of two inertial sensors Y_1 and Y_2 can be expressed by

$$Y_1 = S_1 W + N_1 \tag{6.1}$$

$$Y_2 = S_2 W + N_2 \tag{6.2}$$

where W is ground motion, S_1 and S_2 are sensitivities of the two sensors. Substituting equation (6.1) into (6.2), the relationship between two measurements is

$$Y_2 = HY_1 + N \tag{6.3}$$

where $H = S_2/S_1$ and $N = N_2 - HN_1$. Since n_1, n_2 and y_1 are not correlated, the PSD of the signal can be calculated from equation (6.3) by

$$\mathrm{P}_{\mathrm{y_2y_2}} = H^2\mathrm{P}_{\mathrm{y_1y_1}} + H^2\mathrm{P}_{\mathrm{n_1n_1}} + \mathrm{P}_{\mathrm{n_2n_2}} \tag{6.4}$$

where H can be estimated by $\mathrm{P}_{\mathrm{y_1y_2}}/\mathrm{P}_{\mathrm{y_1y_1}}$. $\mathrm{P}_{\mathrm{y_1y_1}}$ and $\mathrm{P}_{\mathrm{y_2y_2}}$ are the PSD of the signal respectively measured by the first and the second sensor. $\mathrm{P}_{\mathrm{y_1y_2}}$ is the cross power spectral density between the two signals. $\mathrm{P}_{\mathrm{n_1n_1}}$ and $\mathrm{P}_{\mathrm{n_2n_2}}$ are the PSD of two sensor noises, respectively. It is can be found that, the first item in the right, $H^2\mathrm{P}_{\mathrm{y_1y_1}}$, is the PSD of the coherent signal from the huddle test. The second item in the right contains PSD of both sensors' noises. Assuming that the two sensors are of the same kind, the PSD of noise $\mathrm{P}_{\mathrm{n_1n_1}}$ can be considered to be same as that of $\mathrm{P}_{\mathrm{n_2n_2}}$. Therefore, the PSD of noise from one sensor is estimated by

$$\mathrm{P}_{\mathrm{nn}} = \frac{\mathrm{P}_{\mathrm{y_2y_2}} - H^2\mathrm{P}_{\mathrm{y_1y_1}}}{1 + H^2} \tag{6.5}$$

The ASD of incoherent noise measured by the huddle test of the inertial sensors is

$$\mathrm{A_{nn}} = \sqrt{\mathrm{P_{nn}}} \tag{6.6}$$

where $\mathrm{P_{nn}}$ is the PSD of the noise of one sensor. $\mathrm{A_{nn}}$ is the ASD of the noise floor of the inertial sensor. The coherent signal estimated by the huddle test is

$$\mathrm{A_{ss}} = |H|\sqrt{\mathrm{P_{y_1y_1}}} \tag{6.7}$$

where $\mathrm{P_{ss}}$ and $\mathrm{A_{ss}}$ are respectively the PSD and ASD of the measured motion.

Hua [173] presented the data processing for the huddle test with multiple sensors. Distinct from the blocked-mass test, the huddle test estimates the resolution without blocking the proof-mass, which reveals more information about for example the noise caused by the thermomechanical noise can be studied.

6.2 Experimental result

The results of huddle tests of two HINS and two VINS are separately discussed in this section. Figure 6.2 shows the setups of the huddle test. Two vacuum chambers are put side by side on a rigid platform (7). Each of the chambers holds one VINS (1 or 3) and one HINS (2 or 4) to measure motion in the vertical and horizontal direction. Two Güralp 6T seismometers (5 and

Figure 6.2: Inertial sensors under huddle tests: (1, 3) VINS, (2, 4) HINS, (5, 6) Güralp 6T seismometers, (7) platform.

6) are put together with the interferometric inertial sensors.

The data acquisition system, NI PXIe-4497, is used to record signals of both interferometric inertial sensors and Güralp 6T seismometers. The sampling frequency is 10 kHz and the measurement lasts 1000 s. There are four pairs of signals from the measurements: the vertical motion is measured separately by the two VINS, and the two Güralp 6T seismometers (with vertical signals); the horizontal motion is measured separately by the two HINS and the two Güralp 6T seismometers (with horizontal signals). Recalling equations (6.1) to (6.7), the coherent signal and the incoherent residual can be extracted from each pair of signals.

6.2.1 Result of the HINS

Figure 6.3 shows a comparison between the coherent signals and incoherent residuals measured by the two HINS and two Güralp 6T seismometers. The solid blue and dash blue curves respectively present the coherent signal and incoherent residual obtained from the HINS measurements. Similarly, the solid red and dash red curves respectively present the signal and residual obtained from the measurements of the two Güralp 6T seismometers. The comparison between the two coherent signals (solid blue and red curves) reveals that the sensors measure the same amplitude of motion from 0.01 to 10 Hz, which implies that the HINS implements the same function as the Güralp 6T seismometer in terms of monitoring the seismic motion. The comparison between the two residuals shows that the incoherent part from the huddle test of HINS (dash blue curve) is lower than the one from the Güralp 6T seismometers (dash red curve) from 0.01 to 10 Hz. However, the residual from the huddle test of the HINS is much higher than the theoretical resolution of the HINS (solid black curve), and the difference between the signal and residual from the HINS is less than two orders below 10 Hz. The physical insight of this is investigated in Section 6.3. Figure 6.4 shows the coherence

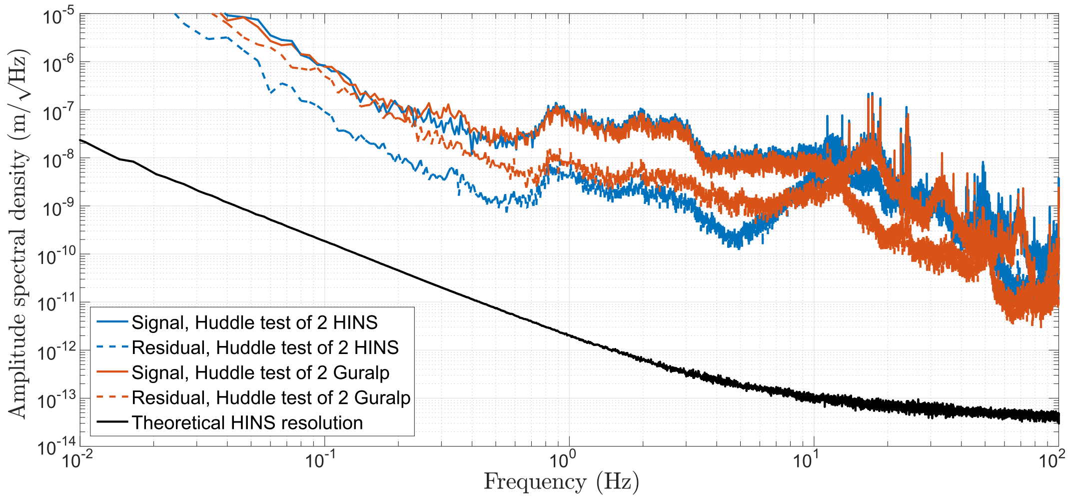

Figure 6.3: Comparison between the results from huddle test of sensors in horizontal direction.

between the signals used in Figure 6.3 from 0.01 to 20 Hz. Both of the measurements from the HINS (solid blue curve) and the measurements from the Güralp 6T seismometers are incoherent around 12 Hz, which is assumed to be caused by the flexibility of the platform ((7), in Figure 6.2). The coherence of the HINS drops below 0.03 Hz, and the possibility is the difference of the tilt-horizontal coupling as explained with Figure 4.19. The coherence of the Güralp 6T seismometers is good above 0.1 Hz, which corresponds to the presented bandwidth of the sensor in its manual. One possibility to explain the dropped coherence in the low frequencies could be the low SNR in the frequencies beyond its bandwidth.

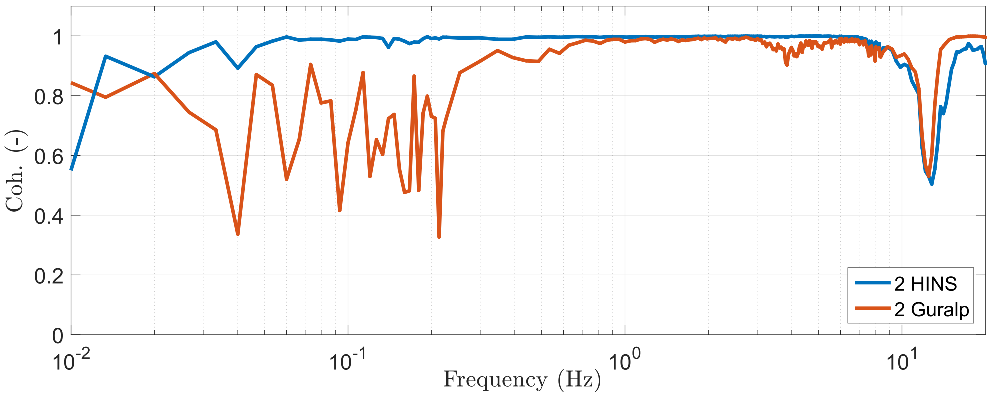

Figure 6.4: Comparison between the coherence between the same sensors in the horizontal direction.

6.2.2 Result of the VINS

Figure 6.5 shows a comparison between the huddle tests of the two VINS and two Güralp 6T seismometers. The blue curves present respectively, the coherent signal (solid blue curve) and incoherent residual (dash blue curve) processed from the two VINS. The red curves present respectively, the signal (solid red curve) and residual (dash red curve) obtained from

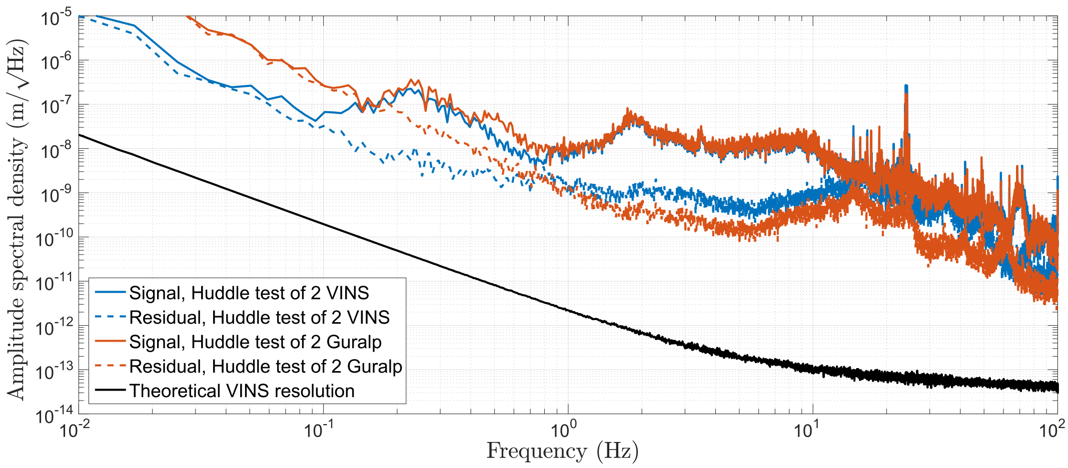

Figure 6.5: Comparison between the results from huddle test of sensors in vertical direction.

the two Güralp 6T seismometers. The coherences of the signals below 0.2 Hz are different, the explanation is that the sensitivity of the Güralp 6T seismometer drops in the frequencies beyond its bandwidth. Therefore, the signal of the Güralp 6T seismometer is dominated by noise below 0.2 Hz. The comparison between the residuals shows that the VINS has a better residual at the frequencies below 1 Hz. However, the residual of the Güralp 6T seismometer is better between 1 and 50 Hz. Compared with Figure 6.3, it shows that the residual of Güralp 6T seismometer one vertical measurement is 10 times lower than the residual on horizontal measurement. Similar to the huddle test of HINS, the key question is still that the residual of the VINS is only lower than the signal by less than two orders. The physical insight of this is investigated in Section 6.3.

Figure 6.6 presents the coherence of the signals used in Figure 6.5. It shows that the incoherence around 12 Hz, which might be caused by the flexibility of the platform. Moreover, the two coherences of the sensors drop in the frequencies below 0.1 or 0.2 Hz. The possibilities could be the sensitivity of the sensors to the tilt-horizontal coupling and the influence of the noise source.

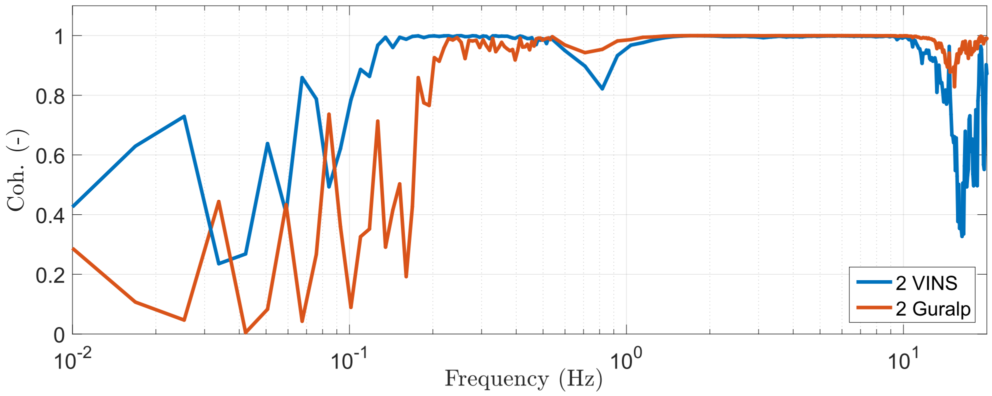

Figure 6.6: Comparison between the coherence between the same sensors in the vertical direction.

6.3 Discussion

The residual from the huddle tests should be as low as the theoretical resolution from the blocked-mass test. However, according to the experimental results in Figure 6.3 and Figure 6.5, one obvious point is that the obtained residuals are much higher than the estimated resolution. Therefore, this section attempts to explain the reasons for the high residual in huddle tests.

Section 3.4 presents the data processing from measured voltages to recover the measured displacement. Normalisation and ellipse fitting are the two key procedures. The quality of normalisation highly depends on the estimation of parameters, $\bar{g}_{\mathrm{i}}$ and $\bar{b}_{\mathrm{i}}$ in equations (3.44) and (3.45). Similarly, the estimation of parameters, $\bar{k}_1$, $\bar{k}_2$, $\sin(\bar{\phi}_0)$ and $\cos(\bar{\phi}_0)$ in equation (3.52), are vital for the ellipse fitting. All these parameters are estimated during the calibration phase and used in the measurement phase. Therefore, the errors of parameter estimation cause non-linearities in measurement, and thus leads to high errors of the gain, offset and phase offset in the data processing. In order to study their effects, $\arctan$ function is used to represent the $\arctan 2$ function (in equation (3.55)) to facilitate the series expansion. Assuming the quadrature signal $Q_{\sin}$ has the errors after data processing, equation (3.55) becomes

$$2\hat{\phi_{\mathrm{y}}} = \arctan\Big(\frac{g_0\big(\sin(2\phi_{\mathrm{y}} + \frac{\pi}{4} + \frac{\phi_2-\phi_1}{2} + \phi_0)\big) + b_0}{\cos(2\phi_{\mathrm{y}} + \frac{\pi}{4} + \frac{\phi_2-\phi_1}{2})}\Big) - \frac{\pi}{4} \tag{6.8}$$

where $g_0 \simeq 1$, $\phi_0 \simeq 0$ and $b_0 \simeq 0$ are the errors of the gain, phase and offset in the quadrature signal. Concerning g_0 and ϕ_0 are ignored, the series expansion about $b_0 \simeq 0$ in equation (6.8) is expressed as

$$\begin{aligned}2\hat{\phi_{\mathrm{y}}} &= \arctan\Big(\frac{\sin(2\phi_{\mathrm{y}} + \frac{\pi}{4} + \frac{\phi_2-\phi_1}{2})}{\cos(2\phi_{\mathrm{y}} + \frac{\pi}{4} + \frac{\phi_2-\phi_1}{2})}\Big)\\ &+ \cos(2\phi_{\mathrm{y}} + \frac{\pi}{4} + \frac{\phi_2 - \phi_1}{2})b_0 + \mathrm{O}(b_0^2) - \frac{\pi}{4}\\ &= 2\phi_{\mathrm{y}} + \frac{\phi_2 - \phi_1}{2} + \cos(2\phi_{\mathrm{y}} + \frac{\pi}{4} + \frac{\phi_2 - \phi_1}{2})b_0 + \mathrm{O}(b_0^2)\end{aligned} \tag{6.9}$$

where items $\cos(2\phi_{\mathrm{y}} + \frac{\pi}{4} + \frac{\phi_2-\phi_1}{2})b_0$ and $\mathrm{O}(b_0^2)$ contribute to the non-linearity components in the measured phase $\hat{\phi_{\mathrm{y}}}$. Concerning g_0 and b_0 are ignored in equation (6.8), the series expansion about $\phi_0 \simeq 0$ is expressed as

$$\begin{aligned}2\hat{\phi_{\mathrm{y}}} &= \arctan\Big(\frac{\sin(2\phi_{\mathrm{y}} + \frac{\pi}{4} + \frac{\phi_2-\phi_1}{2})}{\cos(2\phi_{\mathrm{y}} + \frac{\pi}{4} + \frac{\phi_2-\phi_1}{2})}\Big)\\ &+ \cos^2(2\phi_{\mathrm{y}} + \frac{\pi}{4} + \frac{\phi_2 - \phi_1}{2})\phi_0 + \mathrm{O}(\phi_0^2) - \frac{\pi}{4}\\ &= 2\phi_{\mathrm{y}} + \frac{\phi_2 - \phi_1}{2} + \cos^2(2\phi_{\mathrm{y}} + \frac{\pi}{4} + \frac{\phi_2 - \phi_1}{2})\phi_0 + \mathrm{O}(\phi_0^2)\end{aligned} \tag{6.10}$$

where items $\cos^2(2\phi_{\mathrm{y}} + \frac{\pi}{4} + \frac{\phi_2-\phi_1}{2})\phi_0$ and $\mathrm{O}(\phi_0^2)$ contribute to the non-linearity components in the measured phase $\hat{\phi_{\mathrm{y}}}$. Concerning ϕ_0 and b_0 are ignored in equation (6.8), the series expansion about $g_0 \simeq 1$ is expressed as

$$\begin{aligned}2\hat{\phi_{\mathrm{y}}} &= \arctan\Big(\frac{\sin(2\phi_{\mathrm{y}} + \frac{\pi}{4} + \frac{\phi_2-\phi_1}{2})}{\cos(2\phi_{\mathrm{y}} + \frac{\pi}{4} + \frac{\phi_2-\phi_1}{2})}\Big) + \mathrm{O}((g_0 - 1)^2) - \frac{\pi}{4}\\ &+ \cos(2\phi_{\mathrm{y}} + \frac{\pi}{4} + \frac{\phi_2 - \phi_1}{2})\sin(2\phi_{\mathrm{y}} + \frac{\pi}{4} + \frac{\phi_2 - \phi_1}{2})(g_0 - 1)\\ &= 2\phi_{\mathrm{y}} + \cos(2\phi_y + \frac{\pi}{4} + \frac{\phi_2 - \phi_1}{2})\sin(2\phi_y + \frac{\pi}{4} + \frac{\phi_2 - \phi_1}{2})(g_0 - 1) + \mathrm{O}((g_0 - 1)^2)\end{aligned} \tag{6.11}$$

where items $\cos(2\phi_y + \frac{\pi}{4} + \frac{\phi_2-\phi_1}{2})\sin(2\phi_y + \frac{\pi}{4} + \frac{\phi_2-\phi_1}{2})(g_0 - 1)$ and $O((g_0 - 1)^2)$ contribute to the non-linearity components in the measured phase $\hat{\phi}_y$.

Similarly, the effect on the measurement by a single error in the quadrature signal $Q_{\cos}$ can be derived. A derivation including the effect of multiple errors and phase tracking in preferred in the further investigation. Anyway, according to equations (6.9), (6.10) and (6.11), the effect of the non-linearity depends on the input and the amplitude of the errors g_0, b_0 and ϕ_0. In order to better understand the relationship between the non-linearity and the errors and the measured phase, two simulations with the different amplitude of the input and errors are conducted.

6.3.1 Influence of input level

Due to the presence of noise, the errors g_0, b_0 and ϕ_0 always exist in measurements. A simulation with the different amplitude of inputs with the same noise sources is conducted to investigate the non-linearity of measurements. Figure 6.7 shows the diagram of the simulation. The idea of the simulation is to inject the same motion w into the two models of the inertial sensor ((7) and (8)), and analyse their simulated outputs by the data processing of the huddle test (6). Equations (6.1-6.6) are used for the data processing. The noise sources include laser intensity noise, phase noise, PD noise and DAQ noise. They are as the same as models presented in Chapter 5, moreover, they are marked with a different number to express that they are incoherent.

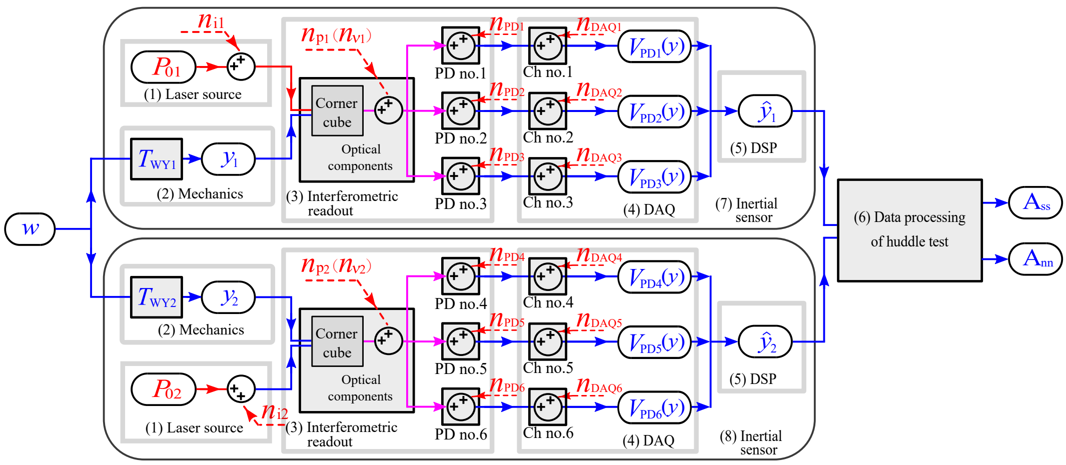

Figure 6.7: Diagram of the simulation to investigate the effect of amplitude of the input and noise on the non-linearity of the huddle test: The working principle of the simulation and unmarked items are as the same as the one shown in Figure 5.15. (5) is the data processing to recover relative displacement, (6) is the data processing of the huddle test, (7) and (8) are two models of inertial sensor in the simulation. Noise sources: n_i: laser intensity noise, n_f: laser frequency noise, n_p: phase noise with respect to the laser frequency noise, n_{DAQ}: PD noise, n_{DAQ}: DAQ noise. The noise sources are marked with numbers to show the incoherence.

$P_{01} = P_{02} = 4$ mW are laser intensity used in the simulation. $T_{\mathrm{WY1}} = T_{\mathrm{WY2}}$ are the transmissibilities of the mechanics assumed equal to each other. Therefore, the relative motion of the proof-mass is the same, $y_1 = y_2 = y$. The MATLAB code to generate y in the time domain is given in Appendix G.5.

Figure 6.8 shows a comparison between the two simulated huddle tests. In the first simulation (HT1), the input is $y_1 = y_2 = y$, the ASD of the signal A_{ss} (solid blue curve) and the ASD of the residual A_{nn} (dash blue curve) have about a 4 orders difference. In the second simulation (HT2), the input is $y_1 = y_2 = \frac{y}{100}$, whose amplitude is 2 orders lower than the amplitude of the input in HT1. Therefore, the ASD fo the signal A_{ss} from HT2 (solid red curve) is 2 orders lower than the ASD of the signal from HT1. With this lower input, the ASD of the residual A_{nn} from HT2 (dashed red curve) is lower than the residual from HT1. The data processing for HT1 and HT2 are the same.

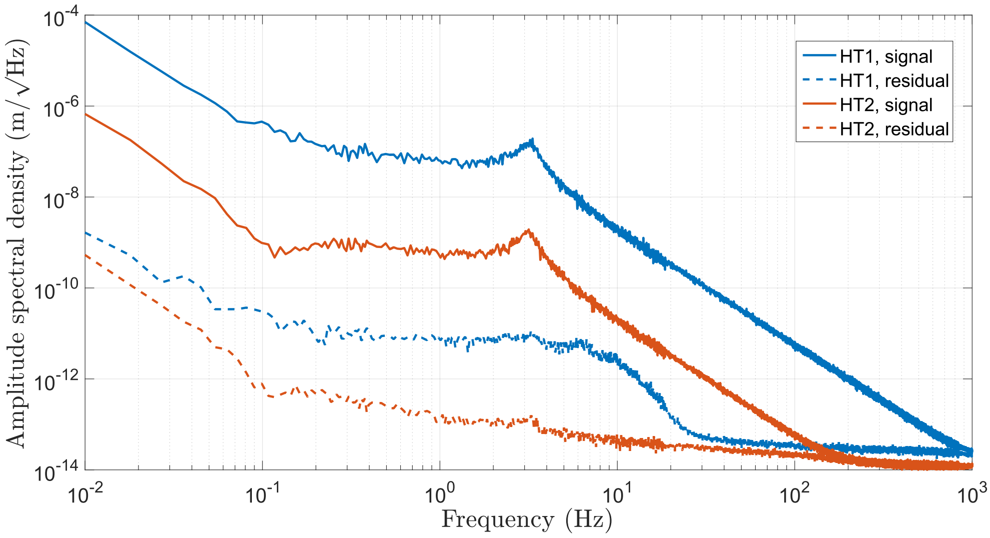

Figure 6.8: Comparison between the huddle test simulation with different input amplitude.

The comparison between the results of HT1 and HT2 indicates that the presence of the noise sources (the laser intensity noise, phase noise, PD noise and DAQ noise) introduces non-linearities in measurements. Moreover, with the same amplitude of noise, the input with high amplitude brings more non-linearities thus leading to a high level of residual, which is predicted by equations (6.9), (6.11) and (6.10). Therefore, performing huddle tests in a seismically quiet place or on an isolated table is one possibility to reduce the level of the input and lead to a lower residual. A similar result was given by Kirchhoff *et al.* [171] with huddle test of geophones.

6.3.2 Influence of parameter estimation

According to equations (6.9), (6.10) and (6.11), the errors g_0, b_0 and ϕ_0 contribute to the non-linearity. The parameter variations between calibration and measurement result in high values of errors. The parameters fluctuate for different reasons: (i) the electrical components have performance shifts during long-term operation; (ii) environmental changes (temperature, pressure, ground motion) affect the optical system and (iii) the variation of the fringe contrast. The interferometric readout is easy to have non-linearities by misalignments [174]. However, the misalignment cannot be avoided because the mechanical systems of VINS and HINS provide only a quasi-translation motion to the corner cube. Therefore, the motion of the movable corner cube changes the alignment of the two reflected beams, which causes the undesirable variation of the fringe contrast and leads to non-linearities.

Figure 6.9 shows a combination of the simplified mechanics with the simplified interferometric readout. The laser beam from the collimator goes to a beam splitter (BS). BS separates the incident beam into two which go to the two corner cubes (CC1 and CC2). The purple lines mark the perfect incident optical paths. CC1 is fixed, and CC2 oscillates with the joint and pendulum of the mechanics. The green lines mark the perfect reflected optical paths from CC1 and CC2. The re-combined beams finally reach the photodetector. Because of the quasi-translation motion, CC2 guarantees that the reflected beam is parallel to the incident beam but the position of the reflected beam shifts with the motion. The red lines show the misaligned reflected beam from CC2. The green spot from CC1 and the red spot from CC2 interferes only in the overlapped region. The photodetector measures the whole power from the interfered region and non-interfered regions. The linear measurement is the variation of the fringe in the interfered region regarding the translation. However, due to parasitic motion, the photodetector detects the variation of fringe contrast, and the larger the amplitude of the motion, the greater the variation of fringe contrast. As the motion of the calibration is often larger than the motion in the measurement, it causes errors of parameter estimation, which causes non-linearities in measurement.

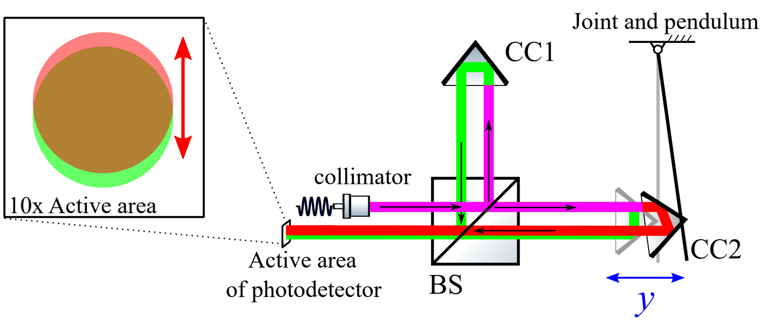

Figure 6.9: Variation of the fringe contrast caused by the motion of the corner cube: BS is the beam splitter, CC1 and CC2 are the fixed corner cube and the movable corner cube; Purple lines are the prefect incident optical path, green lines are the prefect reflected optical path and the red lines are the misaligned reflected optical path; y is the quasi-translation motion of CC2 with the pendulum. In the 10 times zoom-in active area of the photodetector, the green spot shows the prefect position of the beam reflected by CC1, the red spot shows the position of the beam reflected CC2 with the arrows showing the motion of the laser spot and the overlapped region of the two spots is the interference area.

Figure 6.10 compares the results of the simulated huddle tests with and without the deficient parameter estimation. The diagram of the simulation is shown by Figure 6.7. In the third simulation (HT3), the input is $y_1 = y_2 = \frac{y}{100}$, which is as the same as the input in HT2. Therefore, the impact of the input with high amplitude is removed. As mentioned in the previous discussion, the parameters fluctuate with different reasons. In order to simplify the simulation, only the measured voltage $V_{\mathrm{PD2}}(y)$ is assumed to have the errors of parameter estimation, because of the error, it is assumed that the maximum voltage measured by PD2 in the calibration phase is 1% less than the maximum voltage in the measurement phase. The ASD of the signal from HT3 (solid green curve) is the same as the ASD of the signal from HT2 (solid red curve). However, the residual from HT3 (dotted green curve) is higher than the residual from the HT2 (dash red curve). The comparison shows that the deficient parameter estimation causes a high residual.

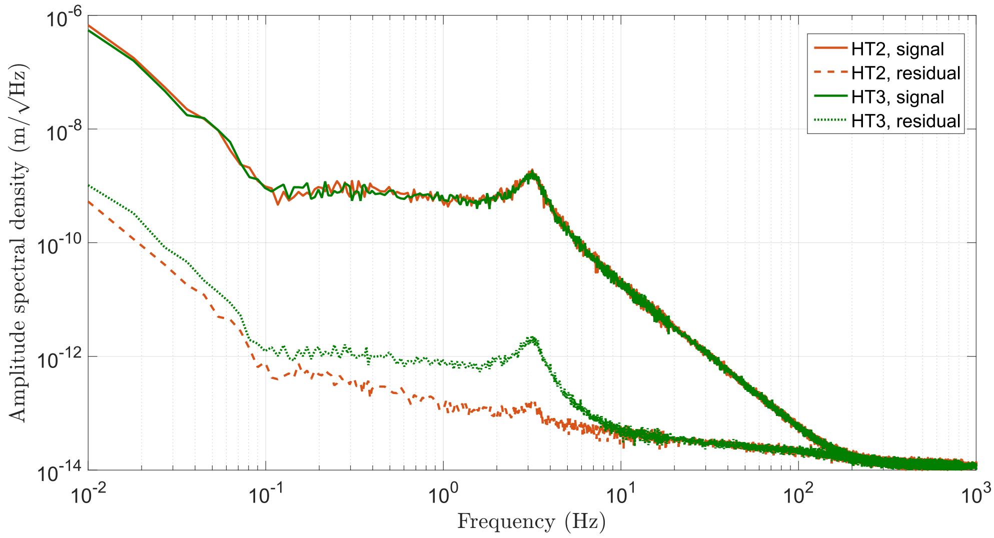

Figure 6.10: Comparison between the huddle test simulation with amplitude difference.

In practice, the reason for parameter estimation errors is complicated; the variation of parameters is not as simple as the example used in the simulation; all photodetectors including PD2 have such problems. In order to clarify the contribution of individual reason and find more physical insight, measurements are suggested to be performed in the condition with less parameter variations, which includes (i) making interferometric readout more robust to the variation, (ii) creating a stable environment, (iii) keeping calibrating during measurements (also is called online calibration) and (iv) improving the linearity of the proof-mass motion.

6.3.3 Influence of incoherent excitations

In order to study the non-linearity caused by the incoherent excitations on individual mechanical system, a setup with one mechanics of the HINS measured by the two interferometric readouts is assembled. Figure 6.11 shows the setup in measurements. The mechanics of HINS (1) is used to provide motion. Two corner cubes of the two interferometric readouts (5 and 7) are mounted opposite one another on the end of the pendulum (4). The benefit of the setup is that the motion of the pendulum always results in the coherent signals measured by the two interferometric readouts.

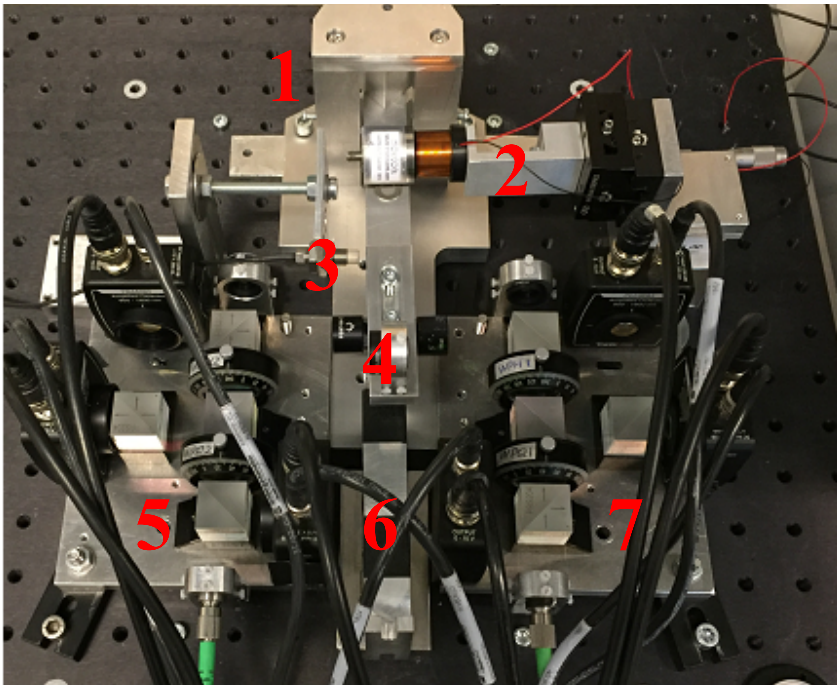

Figure 6.11: Setup of the huddle test with two interferometric readouts: 1. mechanics of HINS, 2. an voice coil for decreasing the motion of the pendulum, 3. an Eddy current sensor for monitor the position of the pendulum, 4. the end of the pendulum with two corner cubes (for two interferometric readout), 5. the first interferometric readout under tests, 6. a shield to block the reflections between two interferometric readout, 7. the second interferometric readout under tests.

Figure 6.12 presents the huddle test of the signals measured by the two interferometric readouts of the setup. The resolution identified from the blocked-mass test (dotted black

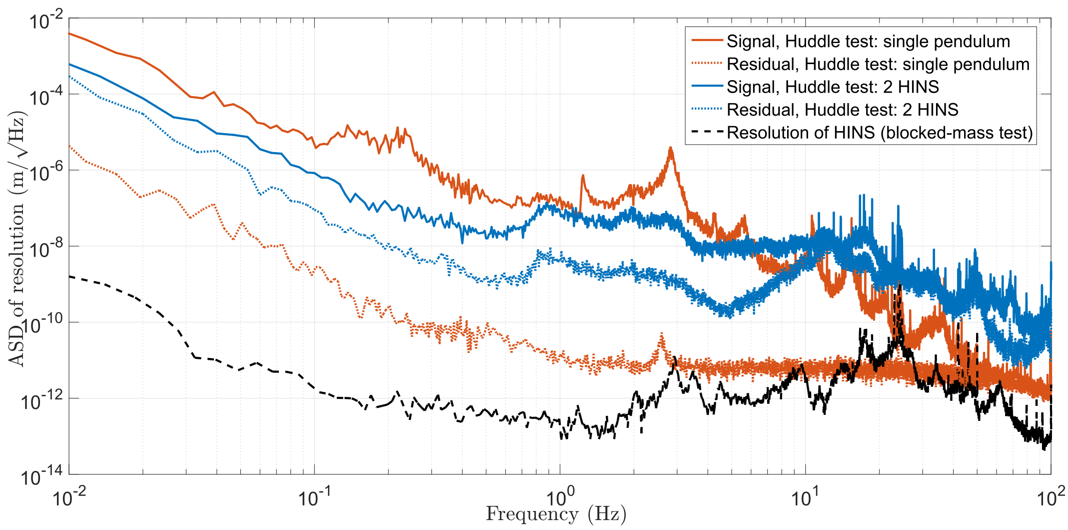

Figure 6.12: The huddle test of two interferometric readouts with one HINS pendulum.

curve) is presented in the figure for comparison. The curve precludes the thermomechanical noise because the induced noise is coherent for this setup. Meanwhile, the signal (solid blue curve) and the residual (dotted blue curve) obtained from the huddle test of the two HINS (see Figure 6.3) are shown for comparison with the results measured by the setup. The solid red curve presents the ASD of the measured displacement. Because the location and time are different, the amplitude of the motion from 0.01 to 6 Hz is even higher than the ground motion of the huddle test of HINS. On the contrary, the residual (dotted red curve) measured by the setup is even lower than the one from the huddle test of two HINS. The difference below 10 Hz between the residual and the signal is about 4 orders, and the difference below 2 Hz between the residual and the estimated resolution of the HINS is about 2 orders. Moreover, the residual measured by the setup from 2 and 60 Hz is close to the estimated resolution which is limited by the internal vibration of the optical components. The residual from 15 to 25 Hz is even lower than the estimated resolution because the estimated resolution at the frequency band may contain the internal vibration of the poorly blocked corner cube. However, as the two corner cubes are mounted on the same pendulum, their unwanted vibration is actually coherent in the signals and can be extracted from the signals.

Figure 6.13 shows the coherence of the signals measured by the setup (solid red curve). The coherence between the two interferometric readouts (solid red curve) perfectly equals to 1 from 0.01 to 20 Hz, which is better than the coherence of the signals from the huddle test of HINS, because both of the thermomechanical noise and the excitation of rotational motion are coherent in this case. From 10 to 20 Hz. However, because of the distance between the locations of the two HINS on the platform.

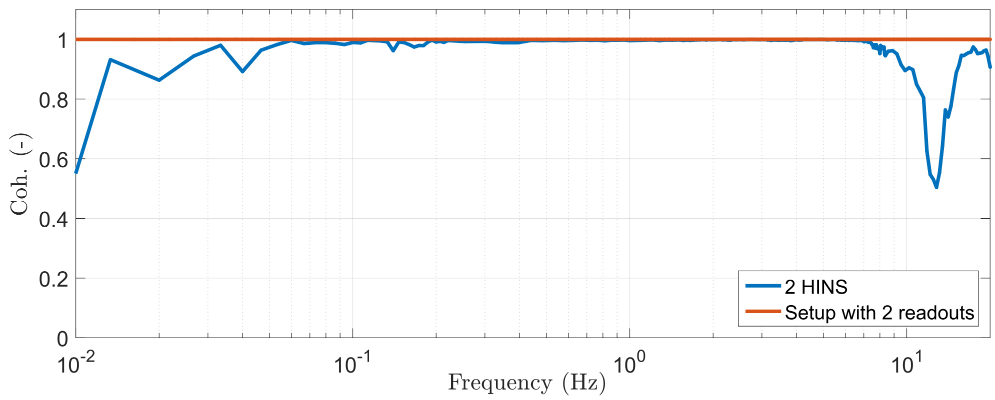

Figure 6.13: Comparison between the coherence of the measurements in Figure 6.12.

In order to reduce the residual caused by incoherent excitations, several measures are suggested, (i) performing the test in a stable environment, which reduces temperature and pressure fluctuations that cause incoherent movement of individual proof-mass. (ii) providing pure translation as the input, which reduces the incoherent signals due to tilting or flexibility of the platform and (iii) using multiple sensors in the huddle test, which helps to extract the more coherent signals from the signals [171].

6.4 Conclusion

This chapter discussed the huddle test of the HINS and VINS. The first section briefly introduced the data processing of the huddle test and showed that huddle test can be used to estimated the resolution of the sensors with free proof-mass. The second section compared the residual from the huddle test with the estimated resolution from the blocked-mass test. It shown that the residual from the huddle test is high. In order to understand the reason for a high residual, simulations and experiments are performed to get more physical insight in the third section. The comparison between the simulations HT1 and HT2 showed that the presence of noise injects non-linearities and the high amplitude of the input aggravates the non-linearities, which result in a high residual. The comparison between the simulations HT2 and HT3 showed that the errors from the parameter estimation causes non-linearities and thus a high residual. The comparison between the huddle test of two HINS and the huddle test of two interferometric readouts measuring one mechanics shows that the incoherent excitation causes a high residual from the huddle test.

However, it is necessary to investigate the dominant factor in the residual of the huddle test. There are two ways to proceed. One is to develop equation (6.8) in Section 6.3. The derivation only includes the influence of an error of one signal and does not include phase tracking. In order to improve the result, the effect of multiple errors and the phase tracking should be included. The other is to improve the huddle test. Generally, The result can be improved in aspects of (i) decreasing the amplitude of the input, (ii) improving the quality of parameter estimation in data processing, (iii) avoiding incoherent excitations to the sensors and (iv) using multiple sensors in the test improve the estimated resolution of the developed sensor by the huddle test.

Chapter 7

Summary and future work

Large ground-based instruments such as the Laser Interferometer Gravitational-Wave Observatory (LIGO) and the Compact Linear Collider (CLIC) needs to be decoupled from the Earth's ever-present seismic motion which would otherwise destroy the functionalities of these extremely sensitive instruments. Active vibration isolation is often sought to decrease the effect of ground motion in the low-frequency domain and its performance is essentially determined by the quality of the employed inertial sensors in terms of resolution and dynamic range. This thesis focused on the development of high-resolution inertial sensors for low-frequency applications.

During the course of the research, both horizontal and vertical inertial sensors with interferometric readouts (the HINS and VINS) are developed, which are placed in a vacuum chamber in a compact fashion. Several tests including ring-down test, blocked-mass test, huddle test were performed to analyse the performance of the developed sensors. The results demonstrated that the developed sensors fulfil the requirements to monitor seismic motions and its performance is beyond than the state of the art commercial sensors. The framework of this thesis can be also considered as a good starting point for further performance improvement in the future.

7.1 Summary

In Chapter 2, the development route of inertial sensors was discussed and determined. The working principles of passive and active inertial sensors were analysed at the beginning. For low-frequency applications, it was found that inertial sensors measuring the displacement quantity are superior in terms of the achievable sensitivity compared to those measure velocity or acceleration quantities. For this type of inertial sensor, its performance can be improved by reducing the resonance frequency of its mechanics and improving the resolution of its readout from the design viewpoint. In order to better regulate the dynamic behaviours of inertial sensors such as extending its bandwidth or increasing its dynamic range, active methods can be used. This is done by including an actuator in the design and driving this actuator properly with the readout signals. However, this method comes with a side-effect, which injects the actuator noise to the output signal of the sensor.

Chapter 3 discussed the development of the readout of the inertial sensors. Different readouts for measuring relative displacements were reviewed. It was found that long-range interferometric readouts are superior among candidates in terms of the resolution and the measurement range. The working principle of the developed long-range interferometric readout with three photodetectors was presented by using Jones matrices. Meanwhile, the importance of the employed data-processing was analysed in terms of noise and non-linearities reduction. The performance of the interferometric readout was also experimentally investigated in comparison with a benchmark eddy current sensor (Lion Precision, U8B). It was shown that the interferometric outperforms the eddy current sensor in terms of the resolution, and also it behaves linearly in a measurement range of 0.4 µm. With a block-mass test, the resolution of the readout was identified as 2e-13 $\mathrm{m}/\sqrt{\mathrm{Hz}}$ at 1 Hz.

Chapter 4 showed the development the mechanics of the interferometric inertial sensor. Various forms of mechanics for implementing inertial sensors were reviewed. It was found that the Lehman pendulum (in Horizontal Interferometric Inertial Sensor (HINS)) and the leaf spring pendulum (in Vertical Interferometric Inertial Sensor (VINS)) combining cross-spring hinges are good candidates as mechanics. The dynamic behaviours of both vertical and horizontal inertial sensors, realised with the leaf spring pendulum and Lehman pendulum, were studied which allows investigating their sensitivities to excitations in different directions. Especially, the dynamic behaviour of the Lehman pendulum was analysed with the effect of negative-stiffness. It was shown that both mechanics are capable of well reacting to pure translational excitations. However, they are found to be also sensitive to some extent to rotational excitations. The resonance frequencies of the assembled HINS and VINS can receptively reach to 0.11 and 0.26 Hz with a careful tuning. Moreover, their performance was assessed by comparing with benchmark inertial sensors, the Güralp 6T seismometers, and it was demonstrated that the sensitivity of both sensors is good enough to measure seismic vibration.

Chapter 5 presented a full model of VINS and HINS combining both the optoelectronic systems and the mechanical systems. Different noise sources were established for the simulation. Meanwhile, possibilities to decrease the effect of noises in measurements were discussed.The simulation was used as the basis for making noise budgeting. It is found that the predicted resolution based on this simulation matched well with that estimated by the experimental blocked-mass test. It was shown that the resolution below 1 Hz is dominated by the thermomechanical noise and the resolution from 1 to 100 Hz is currently limited by unwanted internal vibrations of the interferometric readout.

In Chapter 6, the performance of the developed inertial sensors was experimentally investigated by the huddle test. Two benchmark inertial sensors, the Güralp 6T seismometer, were used for comparison. The current experimental results showed that the residual was much higher than the resolution estimated through the blocked-mass experiment. The reasons was concluded as the effect of non-linearities and incoherent excitations. Three possibilities were putted forward for the high residual: (1) the high amplitude of excitation, (2) the deficient parameter estimation, and (3) the influence of incoherent excitations. Some simulations were conducted which confirmed that a high level of excitations or a deficient parameter estimation can degrade the huddle test results. A setup with two readouts pointing to one mechanic was prepared in order to investigate the influence of incoherent excitations to the huddle test results. It is found that the residual measured by the setup is two orders lower than that from the huddle test of HINS. The reason behind is that the two interferometric readouts in this case measure essentially the motion of the proof-mass in the same fashion just with different signs. Thus, the input signals to them were always coherent. Therefore, it was reasonable to conclude that the residual from the huddle test can be reduced by (i) lowing the level of the input motion, (ii) performing the test in a stable environment, or (iii) reducing incoherent excitations (for example the thermomechanical noise).

7.2 Suggestions for future research

During the course of the research, it became clear that further developments are possible in the field of design and experiment.

Further improvement of the mechanics

The mechanics presented in the thesis can be improved in future, and they are the primary objects of improvements. As stated in Chapter 5, the assembly of interferometric readout and mechanics introduce optical path difference which leads to high phase noise. The material of the mechanics contributes to the thermomechanical noise in the low frequencies. Moreover, as stated in Chapter 6, the quasi-translation motion of the assembled corner cube is responsible for the unexpected non-linearities in the measurement. Therefore, future improvements can focus on the mechanics including, (i) the optimisation of the assembly to minimise the optical path difference, (ii) the investigation of the mechanics to reduce the thermomechanical noise and (iii) the replacement of mechanics with more linear motion.

Further improvement of the interferometric readout

This thesis presented a high-resolution interferometric readout with the extended measurement range. As suggested by the noise budgeting analysis, it is clear that the resolution of the prototype is limited by the noise of the applied photodetector and the flexibilities of the optical components. Therefore, the improvements can be done from two aspects, (i) replace the current Germanium (Ge) based photodetectors by the indium gallium arsenide (InGaAs) based one, which is reported having a better noise performance. (ii) mount optical components of the interferometric readout more rigidly for example by using monolithic design [85].

Development of chamber providing cryogenic and high-vacuum environment

This thesis presented the estimated resolution from the blocked-mass test and the huddle test. The comparison between the two results showed that the residual measured from the huddle test is higher than the resolution from the blocked-mass test. The reasons were concluded as the effect of non-linearities and incoherent excitations. In order to avoid deficient parameter estimation and incoherent excitations, a chamber providing the cryogenic and high-vacuum environment is suggested, which gives a stable environment by reducing temperature and pressure fluctuations. The parameter variation related to these fluctuations and the undesired incoherent excitation is expected to be reduced when conducting experiments in the future.

Development of seismic isolator

Following the previous discussion, the amplitude of the excitation is another reason for causing a high residual. As stated in Chapter 6, the huddle test is performed on the ground, where the ground motion is fully transmitted to the sensors. A well-isolated platform can help in improving the huddle test results in the future.

Appendix A

Liquid absolute tilt-meter (LAT)

Once we have horizontal inertial sensors, the sensors suffer from the tilt-horizontal coupling due to the working principle of the sensors. To solve the problem, we need a high-resolution tilt-meter to measure the tilting signal of the platform, and therefore remove the tilting signal from the signal of the horizontal sensor. The undergoing development of a prototype of liquid absolute tilt-meter (LAT) is discussed hereafter.

A.1 Working principle

Auto-collimators are commonly used in industry to measure the relative angle in a non-contact fashion [175]. Figure A.1 shows a brief working principle of its optical system. A collimated laser beam goes to the BS and then goes to the reflector. If the reflector is at the initial position (marked by 1 in the figure), the reflected beam goes to the centre of the four-quadrature photodetector (Quad-PD). When the reflector is tilted (marked by 2 in the figure), the reflected

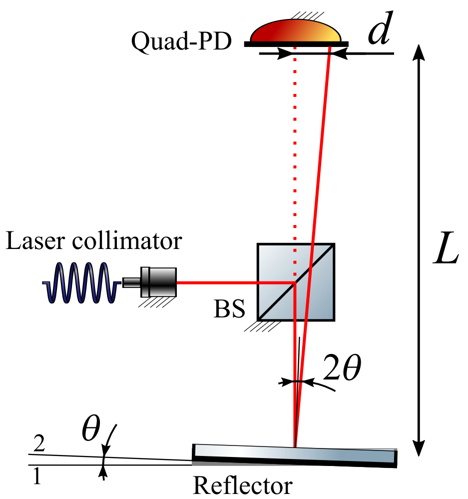

Figure A.1: Working principle of angular measurement: BS: Non-polarisation Beam Splitter, Quad-PD: four quadrature photodetector, θ: rotational angle of the reflector from the initial position 1 to the current position 2, L: distance between reflector and Quad-PD, d: position of the centre of the laser spot.

beam goes to a new position on the active area of the Quad-PD. At BS, the refraction at the coating is ignored. The difference between the laser spot and the centre is d. Alternative laser position detectors can be the Charge-Coupled Device (CCD) camera or the Lateral Effect Photodiode (LEP) [67]. The distance from the reflector and the Quad-PD is L, and the relationship between the tilting angle and the laser position is

$$\begin{aligned} d &= L \cdot \tan(2\theta) \\ &= 2L \cdot \theta \end{aligned} \tag{A.1}$$

where the approximation $2\theta = \tan(2\theta)$ is applied for the angle 2θ is small.

A prototype was developed by our colleagues [176] for implementing the above working principle in order to measure the deflection of micro-components. Following this idea and inspired by the truth that liquid surface is perpendicular to the gravity in the low-frequency domain, the LAT is being developed at hand aiming to measure the absolute tilt deflection of macro structures [177]. The reflector in Figure A.1 is replaced by mercury. Since the liquid surface is perpendicular to the gravity and the optical system tilts with the container of the liquid, equation (A.1) is still valid for the system. As far as we know, similar systems are under development by Azaryan *et al.* [178]. The sensitivity of the LAT is

$$\mathrm{S}_1 = 2L = \frac{d}{\theta} \tag{A.2}$$

where the sensitivity $\mathrm{S}_1 = 900$ mm/rad according to the design of the LAT. Figure A.2 shows the Computer-Aided Design (CAD) model of the LAT, the whole structure is held by the frame (1). The laser beam propagates from the collimator (2) and is expanded and separated by the beam expander and splitters (3). The transmitted beam propagates to the reference Quad-PD

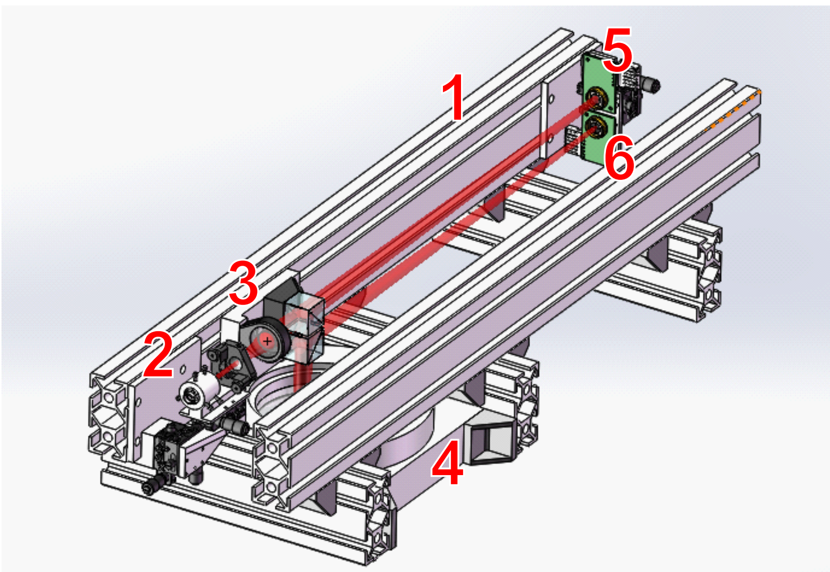

Figure A.2: Model of the LAT: 1: frame of the LAT, 2: laser collimator, 3: Beam expander and splitters, 4: container of mercury, 5: reference Quad-PD 6: measurement Quad-PD. Red lines: laser beams.

(5) to detect the shifting of the structure. The reflected beam propagates to the mercury and is reflected back to the measurement Quad-PD (6) to measure the tilting angle of the frame.

A.2 Four-quadrature photodetector (Quad-PD)

A Quad-PD (First Sensor, QP50-6-TO8 [179]) is used as the detector in the LAT to measure the position d in equation (A.2). The type of Quad-PD has four equivalent active areas, which is shown in Figure A.3. The big black circle with black crossing is to represent the Quad-PD with four quadrature sections. The diameter of the Quad-PD is 8mm. When a laser points the active area of the Quad-PD, the laser spot is divided into four segments and fall into the four quadrature sections of the Quad-PD. The voltage measured by different sections can be expressed as

$$V_{\mathrm{n}} = A_{\mathrm{n}} \cdot I \cdot \mathfrak{R} \cdot G \tag{A.3}$$

$$V_{\mathrm{SUM}} = \sum V_{\mathrm{n}} \quad n = 1,\ 2,\ 3 \text{ and } 4 \tag{A.4}$$

where A_{n} is the is the area of the laser spot segment occupied on the section of the Quad-PD. The collimated beam diameter of the is 3.4 mm, so the entire area of the laser spot is 9.08 mm^2. I is the laser power intensity from the laser source (Thorlabs, S1FC637 [180]) suggested as 10 mW/cm^2. $\mathfrak{R}$ is the responsivity of the Quad-PD, which is 0.4 A/W for 632 nm laser. G is the gain factor which converts the photocurrent into the voltage, which is $10\,000$ V/A. The position of the laser spot can be calculated by

$$\begin{aligned} x_{\mathrm{d}} &= \frac{V_1 + V_4 - V_2 - V_3}{V_{\mathrm{SUM}}} \cdot c \\ &= \frac{A_1 + A_4 - A_2 - A_3}{A_{\mathrm{SUM}}} \cdot c \end{aligned} \tag{A.5}$$

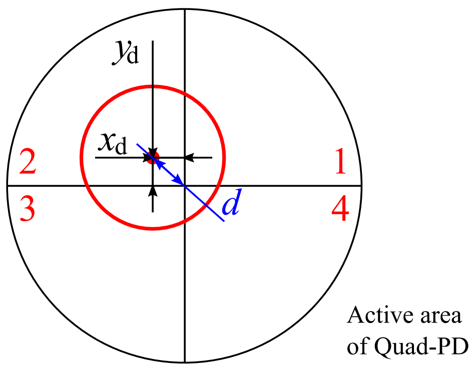

Figure A.3: Working principle of four-quadrature photodetector: red circle: laser spot, black circle: active area of the photodetector, 1, 2, 3 and 4 are the four sections of the photodetector, $d(x_{\mathrm{d}},\ y_{\mathrm{d}})$: position of the laser spot.

$$
\begin{aligned}
y_{\mathrm{d}} &= \frac{V_1 + V_2 - V_3 - V_4}{V_{\mathrm{SUM}}} \cdot c \\
&= \frac{A_1 + A_2 - A_3 - A_4}{A_{\mathrm{SUM}}} \cdot c
\end{aligned} \tag{A.6}
$$

where c is converting factor from measurement to displacement in the unit of m/(-), x_{d} indicate the position on Right-Left (RL) direction of the Quad-PD and y_{d} indicate the position on Top-bottom (TB) direction of the Quad-PD. The benefit of the data processing is that measurement is insensitive to intensity fluctuations of the laser source. However, the distribution of the laser intensity on the spot influence measurements.

A.3 Resolution estimation

Figure A.4 shows the prototype to identify the value of converting factor c. The laser generates 3 mW laser beam which directly propagates to the Quad-PD. Because a Quad-PD is the same on the RL direction and TB direction, the measurement of factor c is performed on RL direction by finely changing the position of the Quad-PD by a manual positioning stage, the corresponding measured values are recorded.

Figure A.4: Prototype to identify the converting factor c: 1: frame of the setup, 2: laser collimator, 3: Quad-PD, 4: laser source.

Figure A.5 shows the position of the laser spot on the Quad-PD against the measured

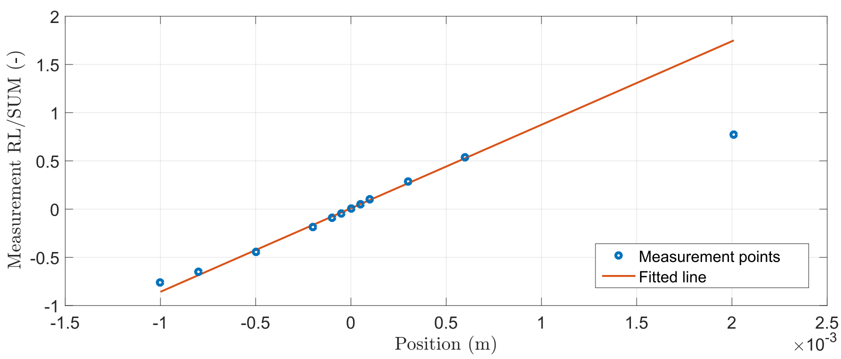

Figure A.5: Position of the laser spot on the Quad-PD against the measured value.

value by equation(refequ.ap.e3), it shows that the measurement is linear within $[-0.75, 0.75]\times 10^{-3}$ m. By ignoring the measurement point at -1e^{-3} m and -2e^{-3} m, the remaining 10 points can be used to calculate the converting factor, c = 1.15e^{-3}. The points at-1e^{-3} m and -2e^{-3} m show the non-linearity of measurements. Because of the laser spot in Figure A.3, the Quad-PD cannot correctly measure laser spot when it fully falls in a half active area, so the signal of RL and TB position shows non-linearity. If only the range of $[-0.75, 0.75]\times 10^{-3}$ m, the measurement range of the LAT is $[-834, 834]$ µrad.

Once the factor c and sensitive S_1 are know, the factor S between the Quad-PD outputs and the measured angle is

$$\mathrm{S} = c/\mathrm{S}_1 \tag{A.7}$$

where $\mathrm{S} = 1.467$ is in the unit of rad/(-). Therefore, the resolution of the LAT can be estimated by

$$\mathrm{R}_\theta = \frac{\mathrm{R}}{S} \tag{A.8}$$

where R is the resolution of the Quad-PD measured at the point $x_\mathrm{d} = 0$ in Figure A.5. Figure A.6 shows the ASD of the estimated resolution of the LAT on RL (solid blue curve) and TB (solid red curve) directions. The DAQ noise (dash black curve) is shown in the figure for a comparison. Right now, the resolution of the LAT reaches 1 nrad/$/\sqrt{\mathrm{Hz}}$ at 1 Hz. Peaks around 10 to 1000 Hz is the seismic noise, in low-frequencies, the resolution is dominated by the DAQ noise. The length of the optical path between the liquid surface and the Quad-PD can be increased to improve the resolution.

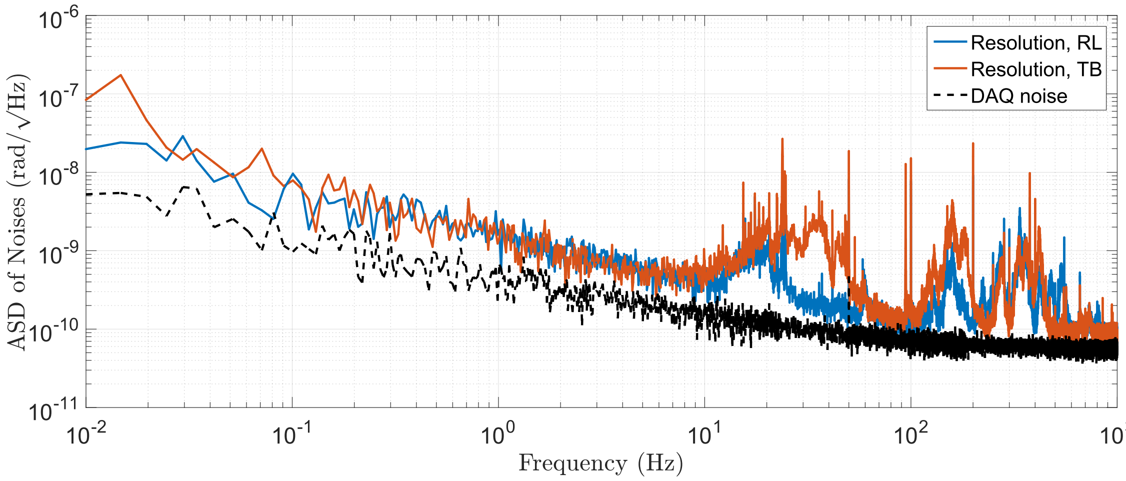

Figure A.6: Estimated resolution of the LAT.

Figure A.7 shows the prototype of the LAT including the container with mercury inside. More experiments will be performed to identify the performance of the inertial sensor.

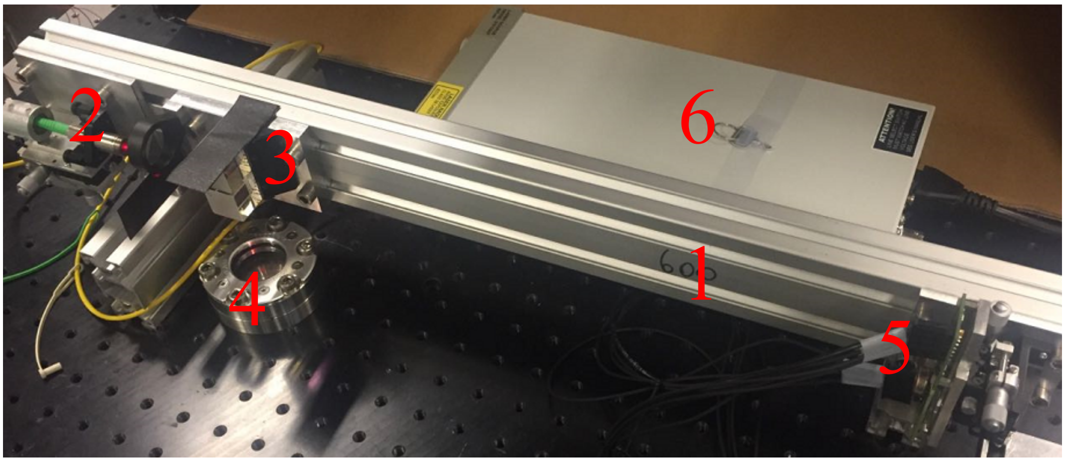

Figure A.7: Prototype of LAT: 1: frame of the LAT, 2: laser collimator, 3: Beam expander and splitters, 4: container of mercury, 5: reference Quad-PD 6: measurement Quad-PD.

Appendix B

Polarisation

The state of polarisation is an important feature of a laser beam, and its direction can be defined by the oscillation of the electric field. Figure B.1 presents the three typical polarisation states of the laser beam.

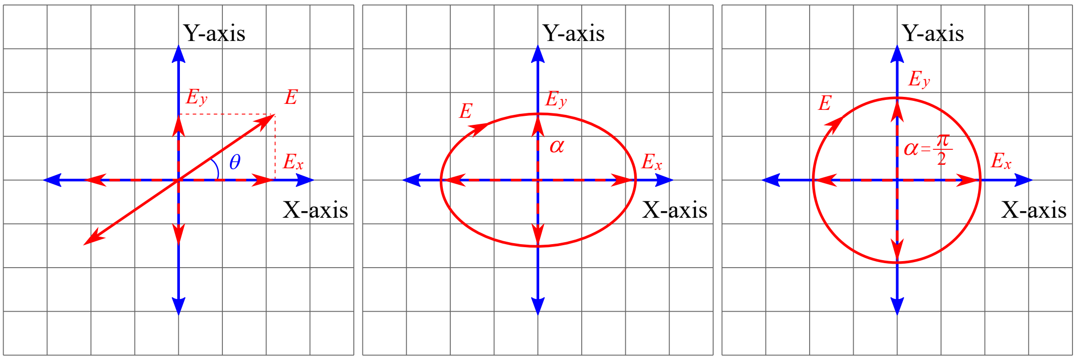

(a) Linear polarisation. **(b)** Elliptical polarisation. **(c)** Circular polarisation.

Figure B.1: The polarisation states of laser beams (The figures are perpendicular to the direction of beam propagation): the solid red curves are the oscillation of electric field; the dashed red lines are components of the electric field oscillation; the blue arrow is the reference axis.

Figure B.1a presents a linearly polarised laser beam. A pair of orthogonal axes (horizontal x-axis and a vertical y-axis) can be defined in the figure. The angle between the linear polarisation state and the x-axis is θ. Therefore, the electric field of a laser beam (presented by equation (3.6)) projects onto the x-axis and the y-axis, which are E_x and E_y, respectively. Using the Jones vector [1], a laser beam with the linear polarisation state can be expressed by

$$E = \begin{bmatrix} E_x \\ E_y \end{bmatrix} = E_0 \, e^{i(\omega t + \phi_L)} \begin{bmatrix} \cos(\theta) \\ \sin(\theta) \end{bmatrix} \tag{B.1}$$

Figure B.1b presents an elliptically polarised laser beam, which can be expressed by

[1]Jones calculus is only valid for the fully polarised beam. Otherwise, the Mueller calculus is required.

two orthogonal linear polarisation states E_x and E_y. The amplitude of the electric fields are unequal, and the phase difference between electric fields E_x and E_y is α. The Jones vector of an elliptical polarisation state is

$$E = \begin{bmatrix} E_x \\ E_y\, e^{i\alpha} \end{bmatrix} = \begin{bmatrix} E_{x0}\, e^{i(\omega t+\phi_L)} \\ E_{y0}\, e^{i(\omega t+\phi_L+i\alpha)} \end{bmatrix} \tag{B.2}$$

where E_{x0} and E_{y0} are initial electric field of E_x and E_y, respectively. If the magnitude of the initial electric field equals to each other, $|E_{x0}| = |E_{y0}|$, and the vertical electric field E_y has a specific phase lag, $\alpha = \pi/2$ rad, equation (B.2) becomes

$$E = E_{x0}\, e^{i(\omega t+\phi_L)} \begin{bmatrix} 1 \\ i \end{bmatrix} \tag{B.3}$$

Thus, the elliptical polarisation state becomes a circular polarisation. Figure B.1c shows a left-hand circularly polarised laser beam. If the horizontal electric field E_x has the specific phase lag, $\alpha = \pi/2$ rad, the circular polarisation rotates clockwise and is called the right-hand circular polarisation state, which is expressed by

$$E = E_{x0}\, e^{i(\omega t+\phi_L)} \begin{bmatrix} i \\ 1 \end{bmatrix} = E_{x0}\, e^{i(\omega t+\phi_L)} \begin{bmatrix} 1 \\ -i \end{bmatrix} \tag{B.4}$$

The quarter-wave plate is a polarising optical component which affects the polarisation state of the incident laser beam. Figure B.2 presents an example showing the effect on the polarisation state. A quarter-wave plate (solid black circle) has a fast axis (solid black line) and a slow axis (dotted black line). The fast and slow axis of the quarter-wave plate is on the y- and x-axis, respectively.

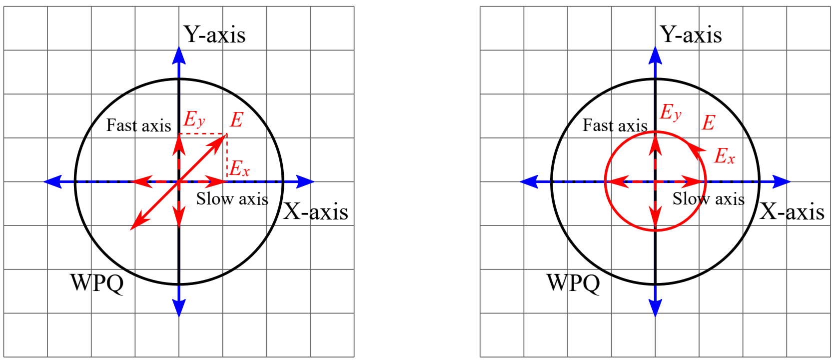

(a) Incident laser beam at WPQ. **(b)** Transmitted laser beam at WPQ.

Figure B.2: The effect of the quarter-wave plate.

Figure B.2a shows a linear polarisation state of incident laser beam that has equal projections E_x and E_y on the x- and y-axis (dashed red lines). Figure B.2b shows the polarisation state of the transmitted laser beam on the quarter-wave plate. The outputting electric field from the slow axis is delayed by a phase lag, $\pi/2$ rad, compared to the electric field from the fast axis. Thus the main function of a quarter-wave plate is to convert a linear polarisation state to circular polarisation state [99].

The half-wave plate is also a polarising optical component. Figure B.3 presents an example showing its effect on the polarisation state. Similar to a quarter-wave plate, a half-wave plate (solid black circle) also has a fast axis (solid black line) and a slow axis (dotted black line). The outputting electric field from the slow axis is delayed by a phase lag, π rad, when compared to the electric field from the fast axis [99].

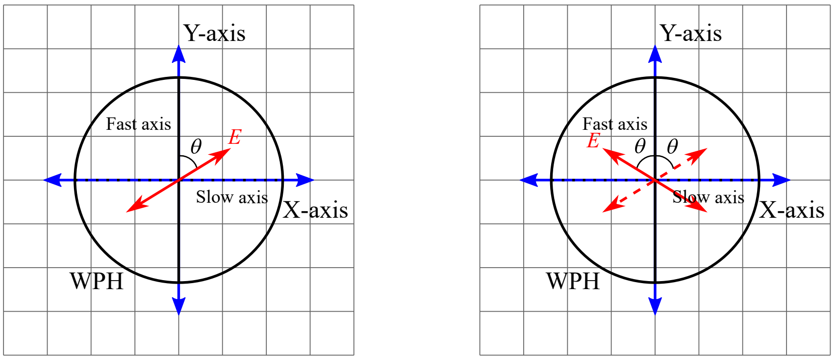

(a) Incident laser beam at WPH. **(b)** Transmitted laser beam at WPH.

Figure B.3: The effect of the half-wave plate.

Figure B.3a shows an incident laser beam with a linear polarisation state which has an angle θ to the fast axis. Figure B.2b shows the transmitted laser beam with the mirrored polarisation state from the half-wave plate. The angle between the electric field of the incident laser beam (dashed red line) and the transmitted laser beam (solid red line) is 2θ. Therefore, the main function of the half-wave plate is to rotate the incident linear polarisation state with a specific angle.

When an optical system contains many polarising components, propagation direction of an incident beam varies with transmission, refraction and reflection. Therefore, using x-axis and y-axis it is complex to define polarisation states of laser beams. As an alternative, p-polarisation (parallel polarisation) and s-polarisation (perpendicular, 'senkrecht' in German, polarisation) can be defined, and are respectively, parallel and perpendicular to the plane of incidence.

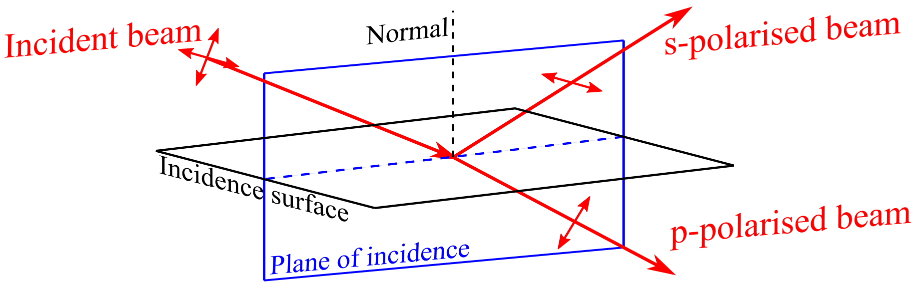

Figure B.4: P- and s-polarisation of incidence plane.

As shown in figure B.4, the incident surface of a polarising beam splitter separates the incident beam with both p- and s-polarisation states. Generally, the transmitted or refracted beam is p-polarised, and the reflected beam is s-polarised. The p- and s-polarisation states indicate the polarisation states of beams in the whole optical system, which simplifies the description of a complex optical system.

Appendix C

Phase tracking

The algorithms of four-quadrant inverse tangent and phase tracking are used for the data processing of the long-range interferometric readout. By recalling Figure 3.6 in Section 3.2.1, the relationship between measured phase and displacement of the corner cube y is

$$\phi = \frac{4\pi y}{\lambda} \tag{C.1}$$

where ϕ is the phase with respect to two times of relative displacement y because of reflection, λ is the wavelength of the laser source. It is obvious that a large relative displacement causes a large variation of the phase. When the relative displacement is smaller than 775 nm, the variation of the phase is 2π and can be expressed within $(-\pi,\ \pi]$. Thanks to the interferometric readout, the measurement by two photodetectors can be expressed by

$$\begin{aligned} a &= r \cdot \sin(\phi) \\ b &= r \cdot \cos(\phi) \end{aligned} \tag{C.2}$$

where $r = \sqrt{a^2 + b^2}$ is the amplitude and a and b are sine and cosine value of the measured phase. The phase ϕ can be recovered by four-quadrant inverse tangent by

$$\operatorname{atan2}(a, b) = \begin{cases} \arctan(\frac{a}{b}), & \text{if } b > 0\,, \\ \arctan(\frac{a}{b}) + \pi, & \text{if } b < 0 \text{ and } a \geqslant 0\,, \\ \arctan(\frac{a}{b}) - \pi, & \text{if } b < 0 \text{ and } a < 0\,, \\ +\frac{\pi}{2}, & \text{if } b = 0 \text{ and } a > 0\,, \\ -\frac{\pi}{2}, & \text{if } b = 0 \text{ and } a < 0\,, \\ \text{undefined}, & \text{if } b = 0 \text{ and } a = 0\,. \end{cases} \tag{C.3}$$

where $\arctan$ function returns value in the range of $(-\pi/2,\ \pi/2)$. When the relative motion is larger than 775 nm, the phase measured by the interferometric readout exceeds the range $(-\pi,\ \pi]$. According to the working principle of the interferometric readout, the measured phase stays in the range but with multiple intervals 2π. This wrapped phase ϕ_{w} can be expressed by

$$\phi_{\mathrm{w}} = \mathrm{W}\{\phi\} \tag{C.4}$$

where W{ } indication the operation of wrapping the phase by the interferometric readout. Because the measured phase from the interferometric readout is the wrapped phase, phase tracking is required and is performed by the **unwrap** function of MATLAB. The unwrapped phase ϕ_{u} can be expressed by

$$\phi_{\mathrm{u}} = \mathrm{U}\{\phi_{\mathrm{w}}\} = \phi_{\mathrm{w}} + 2\pi \cdot k \tag{C.5}$$

where U{ } indication the operation of unwrapping the phase and k is an integer. After obtaining the unwrapped phase, the relative displacement can be recovered by equation C.1.

Appendix D

Optical components list

The commercial components used in the interferometric readout are listed hereafter.

Table D.1: Components of the interferometric readout

No.	Components	Abbreviation	Company	Product code	Pieces
1	Laser Source	\	NKT Photonics	Koheras X15	1
2	Collimator	\	Thorlabs	F240APC-1550	1
3	Polarising Beam Splitter Cube	PBS	Thorlabs	PBS204	3
4	Non-polarising Beam Splitter Cube	BS	Thorlabs	BS018	1
5	Prism Holder	\	OptoSigma	PAD-20	4
6	Quarter-Wave Plate	WPQ	Thorlabs	WPQ10E-1550	1
7	Half-Wave Plate	WPH	Thorlabs	WPH10E-1550	1
8	Circular Optic Holder	\	OptoSigma	MPHN-25.4R-N	2
9	Corner Cube	CC	Thorlabs	PS974M-C	2
10	Photodetector	PD	Thorlabs	PDA50B2	3

Appendix E

Laser specification

Koheras ADJUSTIK$^{\mathrm{TM}}$System
Product type K822-175-112
Test report for serial no. 15500360

NKT Photonics
the power of light

Product specification

System		
Parameter	Value	Unit
Power setpoint	30	mW
Power range	0.29 ... +30	mW
Wavelength setpoint	1550.12	nm
Wavelength tuning	–440 ... +510	pm
Power stability (after warmup and stabilization, over 2 hours)	0.01	dB

Figure E.1: Specification of the laser source.

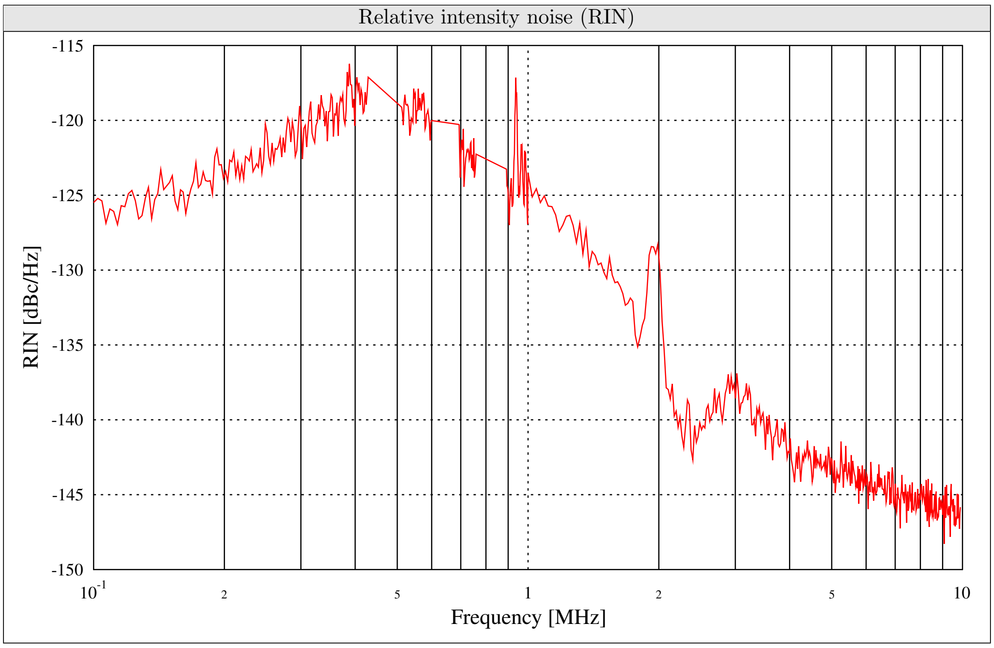

Figure E.2: Measured laser relative intensity noise.

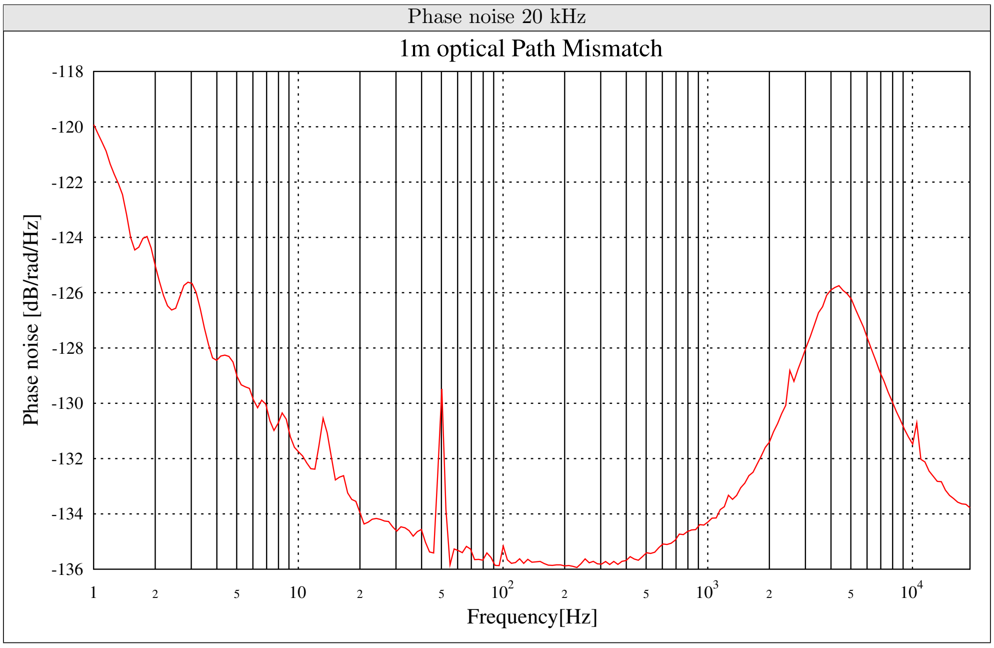

Figure E.3: Measured laser frequency noise.

Appendix F

Vacuum system

The vacuum system consists of two main components, the vacuum chamber and pump. Figure F.1 presents the pump, EVISA E40.3 HV[1], used in the vacuum system. The pump can supply vacuum levels as low as 0.5 mbar.

Figure F.1: The pump, EVISA E40.3 HV.

The vacuum chambers used in the project are glass bell jar chambers, SF MODEL BJ-12-SF[2]. One of them is shown in Figure F.2, and its specification is listed by Table F.1.

[1] `https://drive.google.com/file/d/0B3djDaGyLz4gSng4N1BLVjBNT0E/view`
[2] `https://www.appliedvacuum.co.uk/products/vacuum-bell-jar-chambers-degassing-systems`

Figure F.2: The chamber, SF MODEL BJ-12-SF.

The vacuum chamber is suitable for use at pressures as low as 0.01 mbar. Therefore, the vacuum chamber holds pressure from ambient pressure (1013 mbar) to medium vacuum (1 to 10^{-3} mbar). The mean free path at medium vacuum and room temperature is from 0.1 to 100 mm. The pendulum of the mechanical part known, therefore, the Knudsen number of the inertial sensors in the chamber is

$$\mathrm{Kn} = \frac{\lambda}{L} \tag{F.1}$$

where $\lambda = 1$ mm is the mean free path estimated at 0.1 mbar, and $L = 16$ mm is the length of the pendulum. Therefore, $\mathrm{Kn} = 0.006\,25 < 0.1$ and the pendulum works in the viscous region. [181]

The photodetectors require channels for power input and signals output. Therefore the electrical feed-throughs are used (see Figure F.3), and are mounted on the service ports (KF50) of the chamber. There are two types of electrical feed-through. One is KF50-SUBD-15-BASIC[3], with 15 pins. The connectors used for the feed-through are Sub-D-15 connectors.

[3] http://www.vacom-shop.de/epages/VacomShop.sf/en_GB/?ObjectPath=/Shops/Store.VacomShop/Products/346305

Table F.1: Specification of the vacuum chamber.

Glass Bell Jar OD × ID × H	315 mm × 301 mm × 356 mm
304 Stainless Steel Base Plate OD × THK	350 mm × 15 mm
Height of supporting leg	86 mm
Feet diameter	60 mm × 15 mm
3 Service ports	2 × KF50 & 1 × KF25
Overall height	531 mm
Weight	22 kg
Minimal pressure	0.01 mbar

The number of pins is sufficient for the use of one inertial sensor in one chamber. The other is KF50-MPC2-41-DE-CE-SSG[4], with 41 pins. The connectors are the type of MIL-26482. The connector is used to connect two inertial sensors in one chamber.

In addition, inertial sensors need laser beams for measurements. Therefore, optical fibre feed-throughs are required (see Figure F.4). One type, T-SM1310-FCAPC with a KF50 plate [5], is to be mounted on KF50 ports, and the other, W-SM1310-FCAPC with a KF25 plate[6], is for KF25 ports. Their core channels are the same, and pass 1550 nm.

Concerning the use of two inertial sensors in one chamber, the employed feed-throughs are one T-SM1310-FCAPC with a KF50 plate, one W-SM1310-FCAPC with a KF25 plate and one KF50-MPC2-41-DE-CE-SSG.

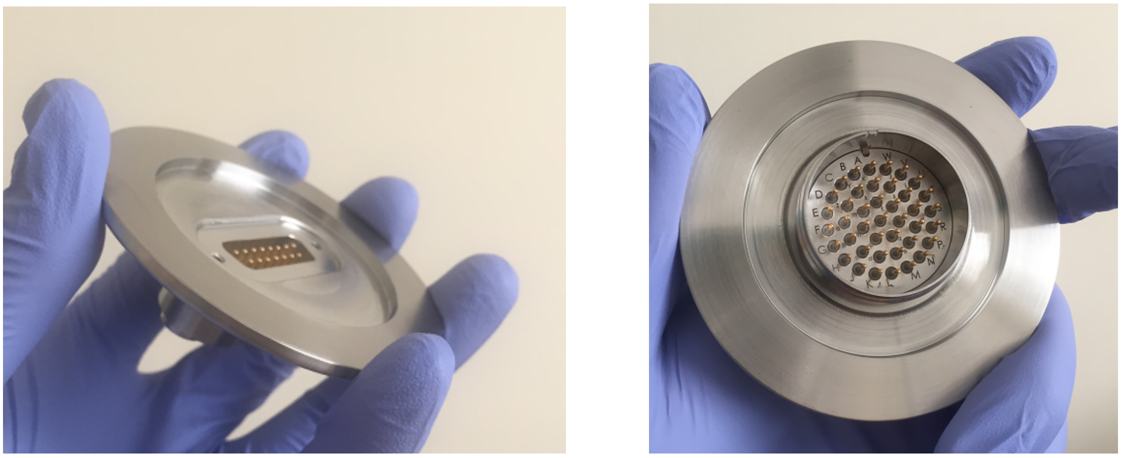

(a) KF50-SUBD-15-BASIC.

(b) KF50-MPC2-41-DE-CE-SSG.

Figure F.3: Electrical feed-throughs.

[4]http://www.vacom-shop.de/epages/VacomShop.sf/en_GB/?ObjectPath=/Shops/Store.VacomShop/Products/302097

[5]http://www.vacom-shop.de/epages/VacomShop.sf/en_GB/?ObjectPath=/Shops/Store.VacomShop/Products/323941

[6]http://www.vacom-shop.de/epages/VacomShop.sf/en_GB/?ObjectPath=/Shops/Store.VacomShop/Products/303913

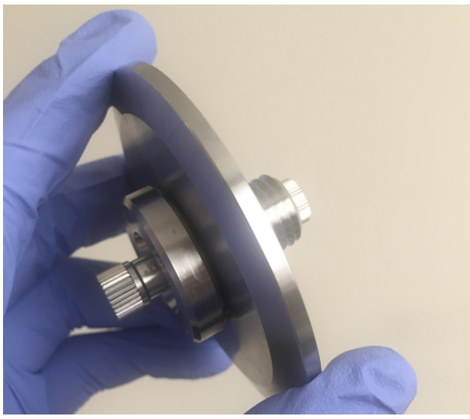

(a) T-SM1310-FCAPC with a KF50 plate.

(b) W-SM1310-FCAPC with a KF25 plate.

Figure F.4: Optical fibre feed-throughs.

Appendix G

Key original script

Key original MATLAB functions are shown hereafter:

G.1 Interferometric readout simulation

The function of the code is to return the field of the laser measured by the three photodetectors in Figure 3.10. The inputs are the parameters of the laser source includes laser intensity, intensity noise and frequency noise, and parameters of the orientation of the wave plates and corner cubes. The returned values are the field without noise, with frequency noise, with intensity noise or with both noise.

```
function [E_PD1_p, E_PD2_p, E_PD3_p, E_PD1_f, E_PD2_f, E_PD3_f, E_PD1_I, E_PD2_I,
E_PD3_I, E_PD1_If, E_PD2_If, E_PD3_If] = interferometer_n(time,I0,O_LS,O_WPQ,O_WPH,
O_CC,phi,dB_I,

% output: E_PD_p pure output, _f with phase noise, _I with intensity noise, _If with both
% time: time series
% I0: Laser intensity
% O_LS: angle of collimator
% O_WPQ: angle of WPQ
% O_WPH: angle of WPH
% O_CC: angle of CC
% phi: sequence of input phase
% dB_I: RIN

% 1/4 waveplates, rotated 45 degrees.
WPQ0 = [exp(1i*pi/4) 0;0 exp(-1i*pi/4)];
R1 = [cos(O_WPQ) sin(O_WPQ);-sin(O_WPQ) cos(O_WPQ)];
R1in = [cos(-O_WPQ) sin(-O_WPQ);-sin(-O_WPQ) cos(-O_WPQ)];
WPQ1 = R1in*WPQ0*R1;
% 1/2 waveplates, rotated 22.5 degree.
```

```
WPH0 = [1i 0; 0 -1i];
R2 = [cos(O_WPH) sin(O_WPH);-sin(O_WPH) cos(O_WPH)];
R2in = [cos(-O_WPH) sin(-O_WPH);-sin(-O_WPH) cos(-O_WPH)];
WPH1 = R2in*WPH0*R2;
% Jones Matrices for PBS and BS.
PBS_H = [1 0;0 0];
PBS_V = [0 0;0 1];
BS = (1/sqrt(2))*[1 0;0 1];

% create laser source

E_source = [sqrt(I0)*cos(O_LS)*ones(1,length(phi));sqrt(I0)*sin(O_LS)*ones(1,length(phi))];
% orignal laser power
E_inter = WPH1*BS*WPQ1*PBS_H*E_source; % at the entry of the PBS2
CC0 = [1i 0; 0 -1i];
R3 = [cos(O_CC) sin(O_CC);-sin(O_CC) cos(O_CC)];
R3in = [cos(-O_CC) sin(-O_CC);-sin(-O_CC) cos(-O_CC)];
CC1 = R3in*CC0*R3;
E_PBS2_reflection = PBS_V*CC1*PBS_V*E_inter; % reference arm

%% Output fields E_PD 123 without noise, and creat matrices in cells

E_PBS2_transmission = cell(1,length(phi));
E_after_PBS2 = cell(1,length(phi));
E_PD1 = cell(1,length(phi));
E_PD2 = cell(1,length(phi));
E_PD3 = cell(1,length(phi));
% OPD_noise = 4*pi/lambda*fd;

for i = 1:1:length(phi)
    E_PBS2_transmissioni = PBS_H*CC1*exp(1i*(phi(i)))*PBS_H*E_inter(:,i); % measurement arm
    E_after_PBS2i = E_PBS2_transmissioni+E_PBS2_reflection(:,i); % combination of laser from 2 arms
    E_PD1i = PBS_V*WPQ1*BS*WPH1*E_after_PBS2i; % field on PD1, PD2 and PD3
    E_PD2i = PBS_V*BS*WPH1*E_after_PBS2i;
    E_PD3i = PBS_H*BS*WPH1*E_after_PBS2i;
end

E_PD1_p = sqrt(abs(cellfun((v)v(1),E_PD1)).^2+abs(cellfun((v)v(2),E_PD1)).^2); % pick values from the cells for data
```

```
E_PD2_p = sqrt(abs(cellfun((v)v(1),E_PD2)).^2+abs(cellfun((v)v(2),E_PD2)).^2);
E_PD3_p = sqrt(abs(cellfun((v)v(1),E_PD3)).^2+abs(cellfun((v)v(2),E_PD3)).^2);

%% Output fields E_PD 123 with frequency noise

Noise_phi=noise_phase(time); % phase noise generator

E_source_f = [sqrt(I0)*cos(O_LS)*ones(1,length(phi));sqrt(I0)*sin(O_LS)*ones(1,length(phi))];
E_inter = WPH1*BS*WPQ1*PBS_H*E_source_f;
E_PBS2_reflection = PBS_V*CC1*PBS_V*E_inter;
E_PBS2_transmission = cell(1,length(phi));
E_after_PBS2 = cell(1,length(phi));

for i = 1:1:length(phi)
    E_PBS2_transmissioni = PBS_H*CC1*exp(1i*(phi(i)+Noise_phi(i)))*PBS_H*E_inter(:,i);
    E_after_PBS2i = E_PBS2_transmissioni+E_PBS2_reflection(:,i);
    E_PD1i = PBS_V*WPQ1*BS*WPH1*E_after_PBS2i;
    E_PD2i = PBS_V*BS*WPH1*E_after_PBS2i;
    E_PD3i = PBS_H*BS*WPH1*E_after_PBS2i;
end

E_PD1_f = sqrt(abs(cellfun((v)v(1),E_PD1)).^2+abs(cellfun((v)v(2),E_PD1)).^2);
E_PD2_f = sqrt(abs(cellfun((v)v(1),E_PD2)).^2+abs(cellfun((v)v(2),E_PD2)).^2);
E_PD3_f = sqrt(abs(cellfun((v)v(1),E_PD3)).^2+abs(cellfun((v)v(2),E_PD3)).^2);

%% Output fields E_PD 123 with intensity noise

n_I = dB_I*noise_i(time,phi)/c; % c: coverting factor, generate intensity noise
E_intensity_noise =
[cos(O_LS)*(I0*ones(1,length(phi))+n_I).^.5;sin(O_LS)*(I0*ones(1,length(phi))+n_I).^.5];
% with intensity noise
E_source_n = E_intensity_noise;
E_inter = WPH1*BS*WPQ1*PBS_H*E_source_n; % at the entry of the PBS2
E_PBS2_reflection = PBS_V*CC1*PBS_V*E_inter; % reference arm

for i = 1:1:length(phi)
    E_PBS2_transmissioni = PBS_H*CC1*exp(1i*(phi(i)))*PBS_H*E_inter(:,i);
    E_after_PBS2i = E_PBS2_transmissioni+E_PBS2_reflection(:,i);
    E_PD1i = PBS_V*WPQ1*BS*WPH1*E_after_PBS2i;
    E_PD2i = PBS_V*BS*WPH1*E_after_PBS2i;
    E_PD3i = PBS_H*BS*WPH1*E_after_PBS2i;
```

```
end

E_PD1_I = sqrt(abs(cellfun((v)v(1),E_PD1)).^2+abs(cellfun((v)v(2),E_PD1)).^2);
E_PD2_I = sqrt(abs(cellfun((v)v(1),E_PD2)).^2+abs(cellfun((v)v(2),E_PD2)).^2);
E_PD3_I = sqrt(abs(cellfun((v)v(1),E_PD3)).^2+abs(cellfun((v)v(2),E_PD3)).^2);

%% Output fields E_PD 123 with intensity + frequency noise

E_source_n =
[cos(O_LS)*(I0*ones(1,length(phi))+n_I).^.5;sin(O_LS)*(I0*ones(1,length(phi))+n_I).^.5];
% with intensity noise
E_inter = WPH1*BS*WPQ1*PBS_H*E_source_n_f;
E_PBS2_reflection = PBS_V*CC1*PBS_V*E_inter;

for i = 1:1:length(phi)
    E_PBS2_transmissioni = PBS_H*CC1*exp(1i*(phi(i)+Noise_phi(i)))*PBS_H*E_inter(:,i);
    E_after_PBS2i = E_PBS2_transmissioni+E_PBS2_reflection(:,i);
    E_PD1i = PBS_V*WPQ1*BS*WPH1*E_after_PBS2i;
    E_PD2i = PBS_V*BS*WPH1*E_after_PBS2i;
    E_PD3i = PBS_H*BS*WPH1*E_after_PBS2i;
end

E_PD1_If = sqrt(abs(cellfun((v)v(1),E_PD1)).^2+abs(cellfun((v)v(2),E_PD1)).^2);
E_PD2_If = sqrt(abs(cellfun((v)v(1),E_PD2)).^2+abs(cellfun((v)v(2),E_PD2)).^2);
E_PD3_If = sqrt(abs(cellfun((v)v(1),E_PD3)).^2+abs(cellfun((v)v(2),E_PD3)).^2);
end
```

G.2 $1/f$ noise generator

The function of the code is to return a sequence representing $1/f$ noise in the time domain.

```
function [output] = one_f_noise(input,q,n,time)

% input: sequence, to know the data length of the simulation
% output: sequence of simulated 1/f noise
% q: quantization interval
% time: time series
% n: fitting factor to make the simulated 1/f noise fits the measured 1/f
% noise in ASD

dt = time(10)-time(9); %time interval
x = input;
%% 1/f noise simulation
```

```
N=length(x); % data points
Fs = 1/dt; % sampling frequency
df = Fs/length(x); % frequency interval
freq = 0:df:Fs/2; % bandwidth
noise_f_asd = q/sqrt(12)*abs(wgn(length(x)/2+1, 1, 0))./(freq.^.5);
%% filter to make 0.5 slope in ASD
f_asd_po = noise_f_asd;
f_asd_po(2:end-1) = f_asd_po(2:end-1)/2;
f_asd_po(1) = f_asd_po(2);
f_psd_ne = flip(conj(f_asd_po(2:end-1)));
f_psd = [f_asd_po f_psd_ne];
noise_f_t = real(ifft(f_psd)*N*df);
%%
output= noise_f_t/n; %output adjusted with n to fit the measurement.
end
```

G.3 Phase noise generator

The function of the code is to return a sequence representing phase noise in the time domain. A filter is made according to the ASD of the given phase noise from the manufacturer (Appendix F). Then, generated white noise passes through the filter and is transformed to the phase noise in the time domain.

```
function [output] = noise_phase(time)

% output: sequence of simulated phase noise
% time: time series


inputSignal = c1*c2*wgn(length(time),1,0); % c1=0.67e-4, adjust c1 to meet phase noise at 1m OPD, c2 = 0.1, 0.01 for 0.1m and 0.01m OPD
s = tf('s');
transF = zpk([-2*pi*10 -2*pi*1e3],[0 -2*pi*1e4 -2*pi*1e4],(2*pi*1e4)^2/(2*pi*10*2*pi*1e3));
Noise_phi = lsim(transF,inputSignal,time);
output = Noise_phi(1:length(time))';
end
```

G.4 Intensity noise generator

The function of the code is to return a sequence representing intensity noise in the time domain. A filter is made according to the ASD of the given intensity noise from measurement in Section 5.2.3. In order to match the measured curve, function of oustaloup-recursive-approximation for fractional order differentiator [182] is used as a part of the filter. Then, generated white noise passes through the filter and is transformed to the phase noise in the time domain.

```
function [output] = noise_phase(time)
% output: sequence of simulated phase noise
% time: time series

inputSignal = c3*wgn(length(time),1,0); % c3=0.67e-2, adjust c3 to meet ASD of intensity noise
s = tf('s');
transF1=0.25*ora_foc(-0.5,5,0.001*2*pi,1000*2*pi); % ora_foc: oustaloup-recursive-approximation for fractional order differentiator
transF2 = zpk([-2*pi*1],[-2*pi*200,-2*pi*2000,-2*pi*2000],8e7);
transF = transF1+transF2;
Noise_inte = lsim(transF,inputSignal,time);
output = Noise_inte(1:length(phi))';
end
```

G.5 Ground motion generator

The function of the code is to return a sequence representing ground motion in the time domain.

```
function [output] = noise_gm(time)
% output: sequence of simulated phase noise
% time: time series

w1 = 0.001;
c1 = 2;
w2 = 20;
c2 = 0.2;

sys_1 =ora_foc(-0.5,5,0.00001*2*pi,1000*2*pi); % ora_foc: oustaloup-recursive-approximation for fractional order differentiator
sys_2 =10*tf([0 0 1],[1 c2*w2 w2^2]);
sys_dis = sys_1*sys_2;
in_w1=0.0005*wgn(length(time),1,0);
ground_motion =lsim(sys_dis,in_w1,time);
output = ground_motion';
end
```

Bibliography

[1] E. Stuhlinger, "Why explore space," *Letters of Note*, vol. 6, 1970.

[2] D. K. Shaeffer, "MEMS inertial sensors: A tutorial overview," *IEEE Communications Magazine*, vol. 51, no. 4, pp. 100–109, 2013.

[3] R. Poole, *Earthrise: How man first saw the Earth*. Yale University Press, 2010.

[4] NASA, "Earthrise," Feb. 2015, (accessed: Apr. 02, 2020). [Online]. Available: https://www.nasa.gov/multimedia/imagegallery/image_feature_1249.html

[5] J. M. Hill, "The large binocular telescope," *Applied optics*, vol. 49, no. 16, pp. D115–D122, 2010.

[6] R. Nan, "Introduction to FAST: five hundred meter Aperture Spherical radio Telescope," in *Ground-based and Airborne Telescopes II*, L. M. Stepp and R. Gilmozzi, Eds., vol. 7012, International Society for Optics and Photonics. SPIE, 2008, pp. 559 – 570. [Online]. Available: https://doi.org/10.1117/12.791288

[7] K. Christiaens, "Large binocular telescope," Sep. 2012, (accessed: Apr. 06, 2020). [Online]. Available: https://www.spacepage.be/artikelen/sterrenkunde/observatoria-wereldwijd/large-binocular-telescope

[8] LIGO, "New LIGO documentary videos released," Oct. 2019, (accessed: Apr. 06, 2020). [Online]. Available: https://www.ligo.caltech.edu/WA/news/ligo20191015

[9] Z. Chen, "China revises regulation to better protect world's largest telescope," Jan. 2019, (accessed: Apr. 06, 2020). [Online]. Available: http://www.chinadaily.com.cn/a/201901/22/WS5c46de8ea3106c65c34e5df8.html

[10] CERN, "CERN's new einstein observatory to explore black holes, big bang," May. 2011, (accessed: August. 06, 2020). [Online]. Available: https://phys.org/news/2011-05-cern-einstein-observatory-explore-black.html

[11] A. Einstein, "Approximative integration of the field equations of gravitation," *Sitzungsber. Preuss. Akad. Wiss. Berlin (Math. Phys.)*, vol. 1916, pp. 688–696, 1916.

[12] A. Abramovici, W. E. Althouse, R. W. Drever, Y. Gürsel, S. Kawamura, F. J. Raab, D. Shoemaker, L. Sievers, R. E. Spero, K. S. Thorne *et al.*, "LIGO: The laser interferometer gravitational-wave observatory," *science*, vol. 256, no. 5055, pp. 325–333, 1992.

[13] B. Caron, A. Dominjon, C. Drezen, R. Flaminio, X. Grave, F. Marion, L. Massonnet, C. Mehmel, R. Morand, B. Mours *et al.*, “The VIRGO interferometer,” *Classical and Quantum Gravity*, vol. 14, no. 6, p. 1461, 1997.

[14] G. M. Harry, L. S. Collaboration *et al.*, “Advanced LIGO: the next generation of gravitational wave detectors,” *Classical and Quantum Gravity*, vol. 27, no. 8, p. 084006, 2010.

[15] B. P. Abbott, R. Abbott, T. Abbott, M. Abernathy, F. Acernese, K. Ackley, C. Adams, T. Adams, P. Addesso, R. Adhikari *et al.*, “Observation of gravitational waves from a binary black hole merger,” *Physical review letters*, vol. 116, no. 6, p. 061102, 2016.

[16] M. Punturo, M. Abernathy, F. Acernese, B. Allen, N. Andersson, K. Arun, F. Barone, B. Barr, M. Barsuglia, M. Beker *et al.*, “The einstein telescope: a third-generation gravitational wave observatory,” *Classical and Quantum Gravity*, vol. 27, no. 19, p. 194002, 2010.

[17] M. Le Louarn, N. Hubin, M. Sarazin, and A. Tokovinin, “New challenges for adaptive optics: extremely large telescopes,” *Monthly notices of the Royal Astronomical society*, vol. 317, no. 3, pp. 535–544, 2000.

[18] P. Spanò, F. Zerbi, C. Norrie, C. Cunningham, K. Strassmeier, A. Bianco, P. A. Blanche, M. Bougoin, M. Ghigo, P. Hartmann *et al.*, “Challenges in optics for extremely large telescope instrumentation,” *Astronomische Nachrichten: Astronomical Notes*, vol. 327, no. 7, pp. 649–673, 2006.

[19] R. Gilmozzi, “Science, technology and detectors for extremely large telescopes,” *Experimental Astronomy*, vol. 19, no. 1-3, pp. 5–13, 2005.

[20] F. W. Kan and J. Antebi, “Seismic hazard: analysis and design of large ground-based telescopes,” in *Ground-based and Airborne Telescopes II*, L. M. Stepp and R. Gilmozzi, Eds., vol. 7012, International Society for Optics and Photonics. SPIE, 2008, pp. 960 – 969. [Online]. Available: https://doi.org/10.1117/12.791243

[21] J. Kim, P. Hinz, O. Durney, T. Connors, M. Montoya, and C. Schwab, “Testing and alignment of the LBTI,” in *Optical and Infrared Interferometry II*, W. C. Danchi, F. Delplancke, and J. K. Rajagopal, Eds., vol. 7734, International Society for Optics and Photonics. SPIE, 2010, pp. 660 – 671. [Online]. Available: https://doi.org/10.1117/12.857342

[22] F. Fan, Y. Li, H. Qian, and E. Zhu, “Seismic responses of the supporting structure of FAST under multiple-support excitations,” *Advances in Structural Engineering*, vol. 18, no. 5, pp. 675–685, 2015.

[23] E. Daw, J. Giaime, D. Lormand, M. Lubinski, and J. Zweizig, “Long-term study of the seismic environment at LIGO,” *Classical and Quantum Gravity*, vol. 21, no. 9, p. 2255, 2004.

[24] B. A. Bolt, W. Horn, G. A. MacDonald, and R. Scott, *Geological Hazards: Earthquakes-tsunamis-volcanoes-avalanches-landslides-floods*. Springer Science & Business Media,

2013.

[25] B. C. Bigelow, N. P. Loewen, E. van Vuuren, and W. S. Burgett, "A survey of enclosure suspension and rotation systems for 3-15m telescopes," in *Ground-based and Airborne Telescopes VI*, H. J. Hall, R. Gilmozzi, and H. K. Marshall, Eds., vol. 9906, International Society for Optics and Photonics. SPIE, 2016, pp. 124 – 141. [Online]. Available: https://doi.org/10.1117/12.2231530

[26] J. Fanson, P. J. McCarthy, R. Bernstein, G. Angeli, D. Ashby, B. Bigelow, A. Bouchez, W. Burgett, E. Chauvin, A. Contos, F. Figueroa, P. Gray, F. Groark, R. Laskin, R. Millan-Gabet, A. Rakich, R. Sandoval, M. Pi, and N. Wheeler, "Overview and status of the Giant Magellan Telescope project," in *Ground-based and Airborne Telescopes VII*, H. K. Marshall and J. Spyromilio, Eds., vol. 10700, International Society for Optics and Photonics. SPIE, 2018, pp. 319 – 332. [Online]. Available: https://doi.org/10.1117/12.2313340

[27] E. H. Anderson, R. M. Glaese, and D. Neill, "A comparison of vibration damping methods for ground based telescopes," in *Ground-based and Airborne Telescopes II*, L. M. Stepp and R. Gilmozzi, Eds., vol. 7012, International Society for Optics and Photonics. SPIE, 2008, pp. 184 – 198. [Online]. Available: https://doi.org/10.1117/12.790195

[28] F. Matichard, B. Lantz, R. Mittleman, K. Mason, J. Kissel, B. Abbott, S. Biscans, J. McIver, R. Abbott, S. Abbott *et al.*, "Seismic isolation of advanced LIGO: Review of strategy, instrumentation and performance," *Classical and Quantum Gravity*, vol. 32, no. 18, p. 185003, 2015.

[29] S. Aston, M. Barton, A. Bell, N. Beveridge, B. Bland, A. Brummitt, G. Cagnoli, C. Cantley, L. Carbone, A. Cumming *et al.*, "Update on quadruple suspension design for advanced LIGO," *Classical and Quantum Gravity*, vol. 29, no. 23, p. 235004, 2012.

[30] G. Zhao, A. Paknejad, A. Deraemaeker, and C. Collette, "$\mathscr{H}_\infty$ optimization of an integral force feedback controller," *Journal of vibration and control*, vol. 25, no. 17, pp. 2330–2339, 2019.

[31] C. Collette, S. Janssens, P. Fernandez-Carmona, K. Artoos, M. Guinchard, C. Hauviller, and A. Preumont, "Inertial sensors for low-frequency seismic vibration measurement," *Bulletin of the seismological society of America*, vol. 102, no. 4, pp. 1289–1300, 2012.

[32] C. Collette, S. Janssens, and K. Artoos, "Review of active vibration isolation strategies," *Recent patents on Mechanical engineering*, vol. 4, no. 3, pp. 212–219, 2011.

[33] Streckeisen, *Portable Very-Broad-Band Tri-axial Seismometer, STS-2 Manual*, STS2LPV2, G Streckeisen AG, Switzerland. [Online]. Available: https://www.passcal.nmt.edu/webfm_send/488

[34] Nanometrics, *Trillium 240 Seismometer User Guide*, 15672R3, Nanometrics, Inc., Canada. [Online]. Available: https://www.passcal.nmt.edu/webfm_send/220

[35] Geotech, *Short-period Seismometer: Model S-13 and GS-13*, DS-18300,

Geotech Instruments, LLC., United States. [Online]. Available: http://www.geoinstr.com/ds-s13.pdf

[36] Sercel, *Geophones Specifications: Seismometers, L-4C*, Sercel Inc., United States. [Online]. Available: https://www.sercel.com/products/Lists/ProductSpecification/Geophones_specifications_Sercel_EN.pdf

[37] C. Collette and F. Matichard, "Sensor fusion methods for high performance active vibration isolation systems," *Journal of sound and vibration*, vol. 342, pp. 1–21, 2015.

[38] B. Lantz and J. Kissel, "Sensor noise estimates for advanced LIGO seismic isolation systems," LIGO at Stanford, United States, Tech. Note LIGO-T900450, Feb., 2017.

[39] LIGO Scientific Collaboration, "Instrument science white paper 2019," SLAC National Accelerator Lab., Menlo Park, CA (United States), Tech. Note LIGO-T1900409, Nov., 2019.

[40] L. Linssen, A. Miyamoto, M. Stanitzki, and H. Weerts, "Physics and detectors at clic: Clic conceptual design report," CERN, the European Organization for Nuclear Research, Tech. Rep. ANL-HEP-TR-12-01, March., 2012.

[41] K. Artoos, C. Collette, M. Guinchard, M. Sylte, B. Bolzon, O. Capatina, A. Jeremie, and C. Hauviller, "Ground vibration and coherence length measurements forthe CLIC nano-stabilization studies," no. CERN-ATS-2009-126. CLIC-Note-795, p. 3, Apr., 2009. [Online]. Available: https://cds.cern.ch/record/1223610

[42] J. Havskov and G. Alguacil, *Instrumentation in earthquake seismology*. Springer, 2004, vol. 358.

[43] A. Bertolini, R. DeSalvo, F. Fidecaro, and A. Takamori, "Monolithic folded pendulum accelerometers for seismic monitoring and active isolation systems," *IEEE transactions on geoscience and remote sensing*, vol. 44, no. 2, pp. 273–276, 2006.

[44] F. Acernese, R. De Rosa, G. Giordano, R. Romano, S. Vilasi, and F. Barone, "Low frequency-high sensitivity horizontal inertial sensor based on folded pendulum," in *Journal of Physics: Conference Series*, vol. 363, no. 1. IOP Publishing, 2012, p. 012001.

[45] F. Barone and G. Giordano, "The UNISA folded pendulum: A very versatile class of low frequency high sensitive sensors," *Measurement*, vol. 118, pp. 339–347, 2018.

[46] D. S. Nyce, *Linear position sensors*. Wiley Online Library, 2004.

[47] J. Watchi, S. Cooper, B. Ding, C. M. Mow-Lowry, and C. Collette, "Contributed review: A review of compact interferometers," *Review of scientific instruments*, vol. 89, no. 12, p. 121501, 2018.

[48] P. Rodgers, "A note on the response of the pendulum seismometer to plane wave rotation," *Bulletin of the Seismological Society of America*, vol. 59, no. 5, pp. 2101–2102, 1969.

[49] F. Matichard and M. Evans, "Tilt-free low-noise seismometry," *Bulletin of the seismological society of America*, vol. 105, no. 2A, pp. 497–510, 2015.

[50] S. Lambotte, L. Rivera, and J. Hinderer, "Vertical and horizontal seismometric observations of tides," *Journal of Geodynamics*, vol. 41, no. 1-3, pp. 39–58, 2006.

[51] Streckeisen, *Very-broad-band Feedback Seismometers, STS-1V/VBB and STS-1H/VBB*, STS1-VBB, Rev. 1, G Streckeisen AG, Switzerland. [Online]. Available: http://www.software-for-seismometry.de/textfiles/Seismometry/STS-1_datasheet.pdf

[52] M. Kelley, "Prototyping a tilt-free seismometer, final report," LIGO, California Institute of Technology and Massachusetts Institute of Technology, Tech. Rep. LIGO-T1500218, Sep., 2015.

[53] M. Afrough, "A thermal enclosure prototype for a suspended inertial sensor," Master's thesis, Department of Physics and Astronomy, University of Mississippi, University, MS, 2017.

[54] K. Venkateswara, C. A. Hagedorn, M. D. Turner, T. Arp, and J. H. Gundlach, "A high-precision mechanical absolute-rotation sensor," *Review of Scientific Instruments*, vol. 85, no. 1, p. 015005, 2014.

[55] T. Forbriger, "About the nonunique sensitivity of pendulum seismometers to translational, angular, and centripetal acceleration," *Bulletin of the Seismological Society of America*, vol. 99, no. 2B, pp. 1343–1351, 2009.

[56] N. Ackerley, M. Beer, I. Kougioumtzoglou, E. Patelli, and S. Au, "Principles of broadband seismometry," *Encyclopedia Earthquake Engineering*, vol. 1941, pp. 1–35, 2014.

[57] E. Wielandt and G. Streckeisen, "The leaf-spring seismometer: Design and performance," *Bulletin of the Seismological Society of America*, vol. 72, no. 6A, pp. 2349–2367, 1982.

[58] A. Araya, K. Kawabe, T. Sato, N. Mio, and K. Tsubono, "Highly sensitive wideband seismometer using a laser interferometer," *Review of scientific instruments*, vol. 64, no. 5, pp. 1337–1341, 1993.

[59] A. J. Fleming, "A review of nanometer resolution position sensors: Operation and performance," *Sensors and Actuators A: Physical*, vol. 190, pp. 106–126, 2013.

[60] M. S. Longuet-Higgins, "A theory of the origin of microseisms," *Philosophical Transactions of the Royal Society of London. Series A, Mathematical and Physical Sciences*, vol. 243, no. 857, pp. 1–35, 1950.

[61] M. Martino, A. Danisi, R. Losito, A. Masi, and G. Spiezia, "Design of a linear variable differential transformer with high rejection to external interfering magnetic field," *IEEE Transactions on magnetics*, vol. 46, no. 2, pp. 674–677, 2010.

[62] H. Tariq, A. Takamori, F. Vetrano, C. Wang, A. Bertolini, G. Calamai, R. DeSalvo, A. Gennai, L. Holloway, G. Losurdo *et al.*, "The linear variable differential transformer (LVDT) position sensor for gravitational wave interferometer low-frequency controls," *Nuclear Instruments and Methods in Physics Research Section A: Accelerators, Spectrometers, Detectors and Associated Equipment*, vol. 489, no. 1-3, pp.

570–576, 2002.

[63] S. Braccini, C. Bradaschia, R. Del Fabbro, A. Di Virgilio, I. Ferrante, F. Fidecaro, R. Flaminio, A. Gennai, A. Giassi, A. Giazotto *et al.*, "Low noise wideband accelerometer using an inductive displacement sensor," *Review of scientific instruments*, vol. 66, no. 3, pp. 2672–2676, 1995.

[64] M. R. Nabavi and S. N. Nihtianov, "Design strategies for eddy-current displacement sensor systems: Review and recommendations," *IEEE Sensors Journal*, vol. 12, no. 12, pp. 3346–3355, 2012.

[65] L. K. Baxter, *Capacitive sensors: Design and Applications*. Wiley-IEEE Press, 1997.

[66] A. Bertolini, R. DeSalvo, F. Fidecaro, M. Francesconi, S. Marka, V. Sannibale, D. Simonetti, A. Takamori, and H. Tariq, "Readout system and predicted performance of a low-noise low-frequency horizontal accelerometer," *Nuclear Instruments and Methods in Physics Research Section A: Accelerators, Spectrometers, Detectors and Associated Equipment*, vol. 564, no. 1, pp. 579–586, 2006.

[67] A. Mäkynen, "Position-sensitive devices and sensor systems for optical tracking and displacement sensing applications," Ph.D. dissertation, Oulu University, Oulu, 2000.

[68] Heidenhain, *Exposed Linear Encoders*, LIP 382, DR. JOHANNES HEIDENHAIN GmbH, Germany. [Online]. Available: https://www.heidenhain.de/fileadmin/pdb/media/img/208960-2F_Exposed_Linear_Encoders_en.pdf

[69] S. Hellegouarch, L. Fueyo Roza, K. Artoos, P. Lambert, and C. Collette, "Linear encoder based low frequency inertial sensor," *International Journal of Optomechatronics*, vol. 10, no. 3-4, pp. 120–129, 2016.

[70] J. D. Ellis, *Field guide to displacement measuring interferometry*. Washington USA: SPIE Press, 2013.

[71] J. VAN HEIJNINGEN, "Interferometric readout for a monolithic accelerometer, towards the fm/rthz," in *Technology and Instrumentation in Particle Physics 2014*, vol. 213. SISSA Medialab, 2015, p. 097.

[72] M. Usher, C. Guralp, and R. Burch, "The design of miniature wideband seismometers," *Geophysical Journal International*, vol. 55, no. 3, pp. 605–613, 1978.

[73] J. D. Otero, "Development and characterization of an observatory-class, broadband, non-fedback, leaf-spring interferometric seismometer," Ph.D. dissertation, University of California, San Diego, 2009.

[74] M. A. Zumberge, J. Berger, M. A. Dzieciuch, and R. L. Parker, "Resolving quadrature fringes in real time," *Applied optics*, vol. 43, no. 4, pp. 771–775, 2004.

[75] M. J. Downs and K. Raine, "An unmodulated bi-directional fringe-counting interferometer system for measuring displacement," *Precision engineering*, vol. 1, no. 2, pp. 85–88, 1979.

[76] M. Pisani, "Multiple reflection michelson interferometer with picometer resolution,"

Opt. Express, vol. 16, no. 26, pp. 21 558–21 563, Dec 2008. [Online]. Available: http://www.opticsexpress.org/abstract.cfm?URI=oe-16-26-21558

[77] C. Joenathan, A. Bernal, Y. Woonghee, R. M. Bunch, and C. Hakoda, "Dual-arm multiple-reflection michelson interferometer for large multiple reflections and increased sensitivity," *Optical Engineering*, vol. 55, no. 2, p. 024101, 2016. [Online]. Available: http://dx.doi.org/10.1117/1.OE.55.2.024101

[78] Z. Zhou, J. Winterflood, L. Ju, and D. Blair, "Investigation of a laser walk-off angle sensor and its application to tilt measurement in gravitational wave detectors," *Physics Letters A*, vol. 280, no. 4, pp. 197–203, 2001.

[79] M. Downs and W. Rowley, "A proposed design for a polarization-insensitive optical interferometer system with subnanometric capability," *Precision Engineering*, vol. 15, no. 4, pp. 281–286, 1993.

[80] K. Raine and M. J. Downs, "Beam-splitter coatings for producing phase quadrature interferometer outputs," *Optica Acta: International Journal of Optics*, vol. 25, no. 7, pp. 549–558, 1978. [Online]. Available: http://dx.doi.org/10.1080/713819816

[81] D. Ponceau, P. Millier, and S. Olivier, "Subnanometric Michelson interferometry for seismological applications," in *Optical Sensors 2008*, F. Berghmans, A. G. Mignani, A. Cutolo, P. P. Meyrueis, and T. P. Pearsall, Eds., vol. 7003, International Society for Optics and Photonics. SPIE, 2008, pp. 251 – 260. [Online]. Available: https://doi.org/10.1117/12.777491

[82] S. Aston, "Optical read-out techniques for the control of test-masses in gravitational wave observatories," Ph.D. dissertation, Unviersity of Birmingham, Birmingham, 2011. [Online]. Available: http://etheses.bham.ac.uk/1665/

[83] M. Bradwshaw, "nEUCLID: a new homodyne interferometer with space applications," Ph.D. dissertation, University of Birmingham, Birmingham, 2015.

[84] V. Greco, G. Molesini, and F. Quercioli, "Accurate polarization interferometer," *Review of Scientific Instruments*, vol. 66, no. 7, pp. 3729–3734, 1995. [Online]. Available: http://dx.doi.org/10.1063/1.1145429

[85] B. Ding, J. Watchi, and C. Collette, "Development of a high resolution optical inertial sensor," in *7th World Conference on Structural Control and Monitoring*. IACSM, Qingdao, China, 2018.

[86] S. J. Cooper, C. J. Collins, A. C. Green, D. Hoyland, C. C. Speake, A. Freise, and C. M. Mow-Lowry, "A compact, large-range interferometer for precision measurement and inertial sensing," *Classical and Quantum Gravity*, vol. 35, no. 9, p. 095007, 2018. [Online]. Available: http://stacks.iop.org/0264-9381/35/i=9/a=095007

[87] K. Birch, "Optical fringe subdivision with nanometric accuracy," *Precision Engineering*, vol. 12, no. 4, pp. 195–198, 1990.

[88] S. Donati, G. Giuliani, and S. Merlo, "Laser diode feedback interferometer for measurement of displacements without ambiguity," *IEEE journal of quantum electronics*,

vol. 31, no. 1, pp. 113–119, 1995.

[89] S. Donati, *Photodetectors*. Prentice Hall PTR, 1999, vol. 1.

[90] Y.-S. Jang and S.-W. Kim, "Compensation of the refractive index of air in laser interferometer for distance measurement: A review," *International Journal of Precision Engineering and Manufacturing*, vol. 18, no. 12, pp. 1881–1890, 2017.

[91] K. Harding, *Handbook of optical dimensional metrology*. CRC Press, 2016.

[92] M. Zumberge, J. Berger, J. Otero, and E. Wielandt, "An optical seismometer without force feedback," *Bulletin of the seismological society of America*, vol. 100, no. 2, pp. 598–605, 2010.

[93] F. Acernese, G. Giordano, R. Romano, and F. Barone, "Compact tunable monolithic sensors for vibration monitoring and control of structures and very low frequency large band characterization of sites," in *15th World Conference in Earthquake Engineering*, 2012, pp. 24–28.

[94] B. J. Slagmolen, D. A. Shaddock, M. Gray, and D. McClelland, "Frequency stability of spatial mode interference (tilt) locking," *IEEE journal of quantum electronics*, vol. 38, no. 11, pp. 1521–1528, 2002.

[95] D. A. Shaddock, "Advanced interferometry for gravitational wave detection," Ph.D. dissertation, Australian National University, Canberra ACT, 2000.

[96] H. Kogelnik and T. Li, "Laser beams and resonators," *Proceedings of the IEEE*, vol. 54, no. 10, pp. 1312–1329, 1966.

[97] C. Bond, D. Brown, A. Freise, and K. A. Strain, "Interferometer techniques for gravitational-wave detection," *Living reviews in relativity*, vol. 19, no. 1, p. 3, 2016.

[98] J. Liu and R. Azzam, "Polarization properties of corner-cube retroreflectors: theory and experiment," *Applied optics*, vol. 36, no. 7, pp. 1553–1559, 1997.

[99] E. Hecht *et al.*, *Optics*. Addison Wesley San Francisco, 2002, vol. 4.

[100] Thorlabs, *PDA50B2 Ge Switchable Gain Detector User Guide*, TTN135074-D02, Rev. D, Thorlabs Inc., United States. [Online]. Available: https://www.thorlabs.de/drawings/d6220742a19cc65a-4037283B-C5E6-A546-5300DC2E21E266F0/PDA50B2-Manual.pdf

[101] T. Požar and J. Možina, "Enhanced ellipse fitting in a two-detector homodyne quadrature laser interferometer," *Measurement Science and Technology*, vol. 22, no. 8, p. 085301, 2011.

[102] P. L. Rosin, "A note on the least squares fitting of ellipses," *Pattern Recognition Letters*, vol. 14, no. 10, pp. 799–808, 1993.

[103] Cedrat Technologies, *APA100M, Amplified piezo actuators*, cedrat Technologies, France. [Online]. Available: https://www.cedrat-technologies.com/fileadmin/datasheets/APA100M.pdf

[104] Thorlabs, *User guide, MDT693B and MDT694B open-loop piezo controllers*, TTN011225-D02, Rev.E Thorlabs, United states. [Online]. Available: https://www.thorlabs.com/drawings/320194fcf435c52f-A8E1C120-DD34-4355-7B2530B25213ED3E/MDT693B-Manual.pdf

[105] L. Precision, *Eddy-current Sensors*, LL02-0030, Lion Precision, United States. [Online]. Available: https://www.lionprecision.com/wp-content/uploads/2019/04/EddyCurrentSensorCatalog_LionPrecision-1.pdf

[106] A. Wanner, "Seismic attenuation system (AEI-SAS) for the AEI 10 m prototype," Ph.D. dissertation, Gottfried Wilhelm Leibniz Universität Hannover, Hannover, 2013.

[107] N. Lobontiu, *Compliant mechanisms: design of flexure hinges*. CRC press, 2002.

[108] L. J. LaCoste Jr, "A new type long period vertical seismograph," *Physics*, vol. 5, no. 7, pp. 178–180, 1934.

[109] H. Bradner, "A note on zero length springs," *American Journal of Physics*, vol. 40, no. 7, pp. 1040–1041, 1972.

[110] C. Collette, F. Nassif, J. Amar, C. Depouhon, and S.-P. Gorza, "Prototype of interferometric absolute motion sensor," *Sensors and Actuators A: Physical*, vol. 224, pp. 72–77, 2015.

[111] A. Bertolini, N. Beverini, G. Cella, R. DeSalvo, F. Fidecaro, M. Francesconi, and D. Simonetti, "Geometric anti-spring vertical accelerometers for seismic monitoring," *Nuclear Instruments and Methods in Physics Research Section A: Accelerators, Spectrometers, Detectors and Associated Equipment*, vol. 518, no. 1-2, pp. 233–235, 2004.

[112] A. Bertolini, G. Cella, R. DeSalvo, and V. Sannibale, "Seismic noise filters, vertical resonance frequency reduction with geometric anti-springs: a feasibility study," *Nuclear Instruments and Methods in Physics Research Section A: Accelerators, Spectrometers, Detectors and Associated Equipment*, vol. 435, no. 3, pp. 475–483, 1999.

[113] D. L. Platus, "Negative-stiffness-mechanism vibration isolation systems," in *Vibration Control in Microelectronics, Optics, and Metrology*, C. G. Gordon, Ed., vol. 1619, International Society for Optics and Photonics. SPIE, 1992, pp. 44 – 54. [Online]. Available: https://doi.org/10.1117/12.56823

[114] G. Cella, V. Sannibale, R. DeSalvo, S. Marka, and A. Takamori, "Monolithic geometric anti-spring blades," *Nuclear Instruments and Methods in Physics Research Section A: Accelerators, Spectrometers, Detectors and Associated Equipment*, vol. 540, no. 2-3, pp. 502–519, 2005.

[115] W. Wittrick, "The theory of symmetrical crossed flexure pivots," *Australian Journal of Chemistry*, vol. 1, no. 2, pp. 121–134, 1948.

[116] H. Zhao and S. Bi, "Stiffness and stress characteristics of the generalized cross-spring pivot," *Mechanism and Machine Theory*, vol. 45, no. 3, pp. 378–391, 2010.

[117] D. Kang and D. Gweon, “Analysis and design of a cartwheel-type flexure hinge,” *Precision Engineering*, vol. 37, no. 1, pp. 33–43, 2013.

[118] X. Pei, J. Yu, G. Zong, S. Bi, and H. Su, “The modeling of cartwheel flexural hinges,” *Mechanism and Machine Theory*, vol. 44, no. 10, pp. 1900–1909, 2009.

[119] B. S. Melton, “Earthquake seismograph development: A modern history—part 1,” *Eos, Transactions American Geophysical Union*, vol. 62, no. 21, pp. 505–510, 1981.

[120] J. Walker, “How to build a simple seismograph to record earthquake waves at home,” *Scientific American*, vol. 241, no. 1, p. 152, 1979.

[121] Y. K. Yong, T.-F. Lu, and D. C. Handley, “Review of circular flexure hinge design equations and derivation of empirical formulations,” *Precision engineering*, vol. 32, no. 2, pp. 63–70, 2008.

[122] W. O. Schotborgh, F. G. Kokkeler, H. Tragter, and F. J. van Houten, “Dimensionless design graphs for flexure elements and a comparison between three flexure elements,” *Precision Engineering*, vol. 29, no. 1, pp. 41–47, 2005.

[123] J. W. Ryu and D.-G. Gweon, “Error analysis of a flexure hinge mechanism induced by machining imperfection,” *Precision Engineering*, vol. 21, no. 2-3, pp. 83–89, 1997.

[124] A. Hines, L. Richardson, H. Wisniewski, and F. Guzman, “Optomechanical inertial sensors,” *Applied Optics*, vol. 59, no. 22, p. G167, Jun 2020. [Online]. Available: http://dx.doi.org/10.1364/AO.393061

[125] A. Bertolini, “High sensitivity accelerometers for gravity experiments,” Ph.D. dissertation, University of Pisa, Pisa PI, 2001.

[126] D. G. Blair, J. Liu, E. F. Moghaddam, and L. Ju, “Performance of an ultra low-frequency folded pendulum,” *Physics letters A*, vol. 193, no. 3, pp. 223–226, 1994.

[127] F. Acernese, G. Giordano, R. Romano, R. De Rosa, and F. Barone, “Mechanical monolithic horizontal sensor for low frequency seismic noise measurement,” *Review of scientific instruments*, vol. 79, no. 7, p. 074501, 2008.

[128] Z. Li, W. J. Wu, P. P. Zheng, J. Q. Liu, J. Fan, and L. C. Tu, “Novel capacitive sensing system design of a microelectromechanical systems accelerometer for gravity measurement applications,” *Micromachines*, vol. 7, no. 9, p. 167, 2016.

[129] R. Middlemiss, A. Samarelli, D. Paul, J. Hough, S. Rowan, and G. Hammond, “Measurement of the earth tides with a MEMS gravimeter,” *Nature*, vol. 531, no. 7596, pp. 614–617, 2016.

[130] B. A. Boom, A. Bertolini, E. Hennes, R. A. Brookhuis, R. J. Wiegerink, J. F. J. van den Brand, M. G. Beker, A. Oner, and D. van Wees, “Nano-g accelerometer using geometric anti-springs,” in *2017 IEEE 30th International Conference on Micro Electro Mechanical Systems (MEMS)*, 2017, pp. 33–36.

[131] W. Jiang and J. Henshall, “A novel finite element model for helical springs,” *Finite Elements in Analysis and Design*, vol. 35, no. 4, pp. 363–377, 2000.

[132] W. P. Johnson, "Spring suspension for a low-frequency geophone," 1969, US Patent 3,451,040.

[133] G. Bowden, "Calibration of geophone microseismic sensors," SLAC National Accelerator Lab., Menlo Park, CA (United States), Tech. Rep. SLAC-TN-05-023, Oct., 2003.

[134] S. J. Cooper, "Breaking the seismic wall: how to improve gravitational wave detectors at low frequency," Ph.D. dissertation, University of Birmingham, Birmingham, 2020.

[135] K. Bertsche, W. A, and W. W, "Calibration of sercel L4C geophone," SLAC National Accelerator Lab., Menlo Park, CA (United States), Tech. Rep., Oct., 2010.

[136] N. Chen, X. Chen, Y. Wu, C. Yang, and L. Xu, "Spiral profile design and parameter analysis of flexure spring," *Cryogenics*, vol. 46, no. 6, pp. 409–419, 2006.

[137] P. R. Saulson, "Thermal noise in mechanical experiments," *Physical Review D*, vol. 42, no. 8, p. 2437, 1990.

[138] D. F. Wilkes, "Rolamite: A new mechanical design concept," Sandia Corporation, Albuquerque, NM (United States), Tech. Rep. B67-10611, Dec., 1967.

[139] B. Ding, G. Zhao, J. Watchi, and C. Collette, "Huddle test of optical inertial sensors combined with slightly damped mechanics," in *Conference on Noise and Vibration Engineering 2018*. LMSD, Leuven, Belgium, 2018, pp. 1471 – 1479.

[140] E. Wielandt and P. Bormann, "Seismic sensors and their calibration," *New Manual of Seismological Observatory Practices*, vol. 1, p. 46, 2002.

[141] J. H. Ginsberg, *Advanced engineering dynamics*. Cambridge University Press, 1998.

[142] K. Y. Yasumura, T. D. Stowe, E. M. Chow, T. Pfafman, T. W. Kenny, B. C. Stipe, and D. Rugar, "Quality factors in micron-and submicron-thick cantilevers," *Journal of microelectromechanical systems*, vol. 9, no. 1, pp. 117–125, 2000.

[143] V. Graizer, "The response to complex ground motions of seismometers with galperin sensor configuration," *Bulletin of the Seismological Society of America*, vol. 99, no. 2B, pp. 1366–1377, 2009.

[144] G. Zhao, B. Ding, J. Watchi, A. Deraemaeker, and C. Collette, "Experimental study on active seismic isolation using interferometric inertial sensors," *Mechanical Systems and Signal Processing*, vol. 145, p. 106959, 2020.

[145] National Instruments, *NI 449x Specifications*, 372125F-01, National Instruments, United States. [Online]. Available: https://www.ni.com/pdf/manuals/372125f.pdf

[146] A. V. Oppenheim, *Discrete-time signal processing*. Pearson Education India, 1999.

[147] J. B. Johnson, "Thermal agitation of electricity in conductors," *Physical review*, vol. 32, no. 1, p. 97, 1928.

[148] M. S. Keshner, "1/f noise," *Proceedings of the IEEE*, vol. 70, no. 3, pp. 212–218, 1982.

[149] P. Areni and J. G. Webster, *Sensor and signal conditioning*. John Wiley & Sons, Inc,

1991.

[150] T. F. Bogart, J. S. Beasley, and G. Rico, *Electronic devices and circuits*. Pearson/Prentice Hall New Jersey, 2004.

[151] Y. M. Blanter and M. Büttiker, "Shot noise in mesoscopic conductors," *Physics reports*, vol. 336, no. 1-2, pp. 1–166, 2000.

[152] NKT Photonics, *Koheras ADJUSTIK low-noise, single-frequency fiber laser*, nKT Photonics, Denmark. [Online]. Available: https://www.nktphotonics.com/wp-content/uploads/sites/3/2015/04/koheras-adjustik.pdf?1592831019

[153] K. Petermann, *Laser diode modulation and noise*. Springer Science & Business Media, 2012, vol. 3.

[154] L. A. Coldren, S. W. Corzine, and M. L. Mashanovitch, *Diode lasers and photonic integrated circuits*. John Wiley & Sons, 2012, vol. 218.

[155] W. Koechner, *Solid-state laser engineering*. Springer, 2013, vol. 1.

[156] A. Dandridge and A. Tveten, "Phase noise of single-mode diode lasers in interferometer systems," *Applied Physics Letters*, vol. 39, no. 7, pp. 530–532, 1981.

[157] NKT Photonics, *Laser Phase Noise, Application note on phase noise in single frequency lasers*, v 1.0NKT Photonics, Denmark.

[158] F. Acernese, R. De Rosa, G. Giordano, R. Romano, S. Vilasi, and F. Barone, "Mechanical monolithic sensors for mechanical damping of a suspended mass," in *Sensors and Smart Structures Technologies for Civil, Mechanical, and Aerospace Systems 2011*, vol. 7981. International Society for Optics and Photonics, 2011, p. 798156.

[159] J. V. van Heijningen, "A fifty-fold improvement of thermal noise limited inertial sensitivity by operating at cryogenic temperatures," *Journal of Instrumentation*, vol. 15, no. 06, p. P06034, 2020.

[160] S. D. Penn, G. M. Harry, A. M. Gretarsson, S. E. Kittelberger, P. R. Saulson, J. J. Schiller, J. R. Smith, and S. O. Swords, "High quality factor measured in fused silica," *Review of Scientific Instruments*, vol. 72, no. 9, pp. 3670–3673, 2001.

[161] Y. Pan, D. Wang, Y. Wang, J. Liu, S. Wu, T. Qu, K. Yang, and H. Luo, "Monolithic cylindrical fused silica resonators with high Q factors," *Sensors*, vol. 16, no. 8, p. 1185, 2016.

[162] O. Gerberding, F. G. Cervantes, J. Melcher, J. R. Pratt, and J. M. Taylor, "Optomechanical reference accelerometer," *Metrologia*, vol. 52, no. 5, p. 654, 2015.

[163] F. Guzman, L. M. Kumanchik, R. Spannagel, and C. Braxmaier, "Compact fully monolithic optomechanical accelerometer," *arXiv preprint arXiv:1811.01049*, 2018.

[164] A. G. Krause, M. Winger, T. D. Blasius, Q. Lin, and O. Painter, "A high-resolution microchip optomechanical accelerometer," *Nature Photonics*, vol. 6, no. 11, p. 768, 2012.

[165] N. Bobroff, "Recent advances in displacement measuring interferometry," *Measurement Science and Technology*, vol. 4, no. 9, p. 907, 1993. [Online]. Available: http://stacks.iop.org/0957-0233/4/i=9/a=001

[166] P. Kren and P. Balling, "Common path two-wavelength homodyne counting interferometer development," *Measurement Science and Technology*, vol. 20, no. 8, p. 084009, 2009. [Online]. Available: http://stacks.iop.org/0957-0233/20/i=8/a=084009

[167] M. Pisani, A. Yacoot, P. Balling, N. Bancone, C. Birlikseven, M. Çelik, J. Flügge, R. Hamid, P. Köchert, P. Kren *et al.*, "Comparison of the performance of the next generation of optical interferometers," *Metrologia*, vol. 49, no. 4, p. 455, 2012.

[168] S. Xu, L. Chassagne, S. Topcu, L. Chen, J. Sun, and T. Yan, "Polarimetric interferometer for measuring nonlinearity error of heterodyne interferometric displacement system," *Chin. Opt. Lett.*, vol. 11, no. 6, p. 061201, Jun 2013. [Online]. Available: http://col.osa.org/abstract.cfm?URI=col-11-6-061201

[169] C.-M. Wu, S.-T. Lin, and J. Fu, "Heterodyne interferometer with two spatial-separated polarization beams for nanometrology," *Optical and Quantum Electronics*, vol. 34, no. 12, pp. 1267–1276, 2002. [Online]. Available: http://dx.doi.org/10.1023/A:1021355410552

[170] T. Schuldt, M. Gohlke, D. Weise, U. Johann, A. Peters, and C. Braxmaier, "Compact laser interferometer for translation and tilt metrology," *International Journal of Optomechatronics*, vol. 1, no. 2, pp. 168–179, 2007. [Online]. Available: http://dx.doi.org/10.1080/15599610701385537

[171] R. Kirchhoff, C. M. Mow-Lowry, V. Adya, G. Bergmann, S. Cooper, M. Hanke, P. Koch, S. Köhlenbeck, J. Lehmann, P. Oppermann *et al.*, "Huddle test measurement of a near johnson noise limited geophone," *Review of Scientific Instruments*, vol. 88, no. 11, p. 115008, 2017.

[172] L. G. Holcomb, "A direct method for calculating instrument noise levels in side-by-side seismometer evaluations," *HISTORY*, vol. 2, no. 1, 1989.

[173] W. Hua, "Low frequency vibration isolation and alignment system for advanced LIGO," Ph.D. dissertation, Stanford University, Stanford, CA, 2005.

[174] T. Eom, J. Kim, and K. Jeong, "The dynamic compensation of nonlinearity in a homodyne laser interferometer," *Measurement Science and Technology*, vol. 12, no. 10, p. 1734, 2001.

[175] R. D. Geckeler, A. Just, M. Krause, and V. V. Yashchuk, "Autocollimators for deflectometry: Current status and future progress," *Nuclear Instruments and Methods in Physics Research Section A: Accelerators, Spectrometers, Detectors and Associated Equipment*, vol. 616, no. 2-3, pp. 140–146, 2010.

[176] A. Chau, "Theoretical and experimental study of capillary condensation and of its possible application in micro-assembly," Ph.D. dissertation, Université libre de Bruxelles, 2007.

[177] B. Lantz, R. Schofield, B. O'reilly, D. Clark, and D. DeBra, "Requirements for a ground rotation sensor to improve advanced ligo," *Bulletin of the Seismological Society of America*, vol. 99, no. 2B, pp. 980–989, 2009.

[178] N. Azaryan, J. Budagov, M. Lyablin, A. Pluzhnikov, B. Di Girolamo, J.-C. Gayde, and D. Mergelkuhl, "The compensation of the noise due to angular oscillations of the laser beam in the precision laser inclinometer," *Physics of Particles and Nuclei Letters*, vol. 14, no. 6, pp. 930–938, 2017.

[179] First Sensor, *First Sensor Evaluation Boards Data Sheet: Quad Sum and Difference Amplifier*, QP50-6-42u SD2 First Sensor, Germany. [Online]. Available: https://www.first-sensor.com/cms/upload/datasheets/QP50-6-42u_SD2_5000010.pdf

[180] Thorlabs, *User guide, Fiber-Coupled Laser Sources Operating Manual*, 2298-D11, Rev.U Thorlabs, United states. [Online]. Available: https://www.thorlabs.com/drawings/1b054cc4b2474a84-A6065E38-FCD0-E14D-E3DECAADE94E5E7A/S1FC637-Manual.pdf

[181] S. Bianco, M. Cocuzza, S. Ferrero, E. Giuri, G. Piacenza, C. Pirri, A. Ricci, L. Scaltrito, D. Bich, A. Merialdo *et al.*, "Silicon resonant microcantilevers for absolute pressure measurement," *Journal of Vacuum Science & Technology B: Microelectronics and Nanometer Structures Processing, Measurement, and Phenomena*, vol. 24, no. 4, pp. 1803–1809, 2006.

[182] Y. Chen, "Oustaloup-recursive-approximation for fractional order differentiators," 2003, (accessed: Dec. 06, 2019). [Online]. Available: https://www.mathworks.com/matlabcentral/fileexchange/3802-oustaloup-recursive-approximation-for-fractional-order-differentiators